



The
University
Of
Sheffield.

**Development and characterisation of a zebrafish larval model to investigate
mechanisms for pathophysiology of intracranial hypertension in
cryptococcal meningitis**

By: Zhaklin Chalakova

A thesis submitted in partial fulfilment of the requirements for the degree of
Doctor of Philosophy

The University of Sheffield
Faculty of Medicine
Department of Infection, Immunity & Cardiovascular Disease

Submission Date: June 2023

Abstract

Cryptococcosis is a fungal infection caused by members of the genus *Cryptococcus*. Worldwide, the most prevalent pathogen of this genus is the encapsulated saprophyte species *Cryptococcus neoformans*. Cryptococcosis most commonly occurs as an opportunistic airborne lung infection which can disseminate to most organ systems. The central nervous system appears particularly susceptible to developing a pathology from the infection, with more than half of cryptococcosis patients diagnosed with cryptococcal meningitis despite infection in multiple organs. Cryptococcal meningitis (CM) is a meningoencephalitis (infection of the brain parenchyma and meninges) which globally accounts for 19% (13-24) of AIDS-related mortality (Rajansingham et al., 2022). In 2020, reports show annual incidence of 152 000 cases of cryptococcal meningitis, resulting in 112 000 cryptococcal-related deaths, almost half of which are in eastern and southern Africa (Rajansingham et al., 2022). 50-70% of CM cases present with a pathologically elevated intracranial pressure (intracranial hypertension) (Graybill *et al.*, 2000; Jarvis *et al.*, 2014; Kagimu et al., 2022;).

This thesis aims to improve our understanding of intracranial hypertension in CM to help identify potential targets for treatment, by developing and testing new models of intracranial hypertension in CM. Three different approaches were used – theoretical, *in vitro* rheology and *in vivo* in zebrafish. Zebrafish was chosen as the core experimental system in which to develop new models due to its physiology, tractability for live imaging and susceptibility to cryptococcosis. In zebrafish larvae, the dynamic nature of cranial vasculature compartments and the CSF during infection was examined using wide field and light sheet microscopy techniques. The physical properties of tissues and fluids when interacting with cryptococcal yeast cells was modelled with theoretical and *in vitro* rheological measurements. *In vitro* it was found that viscosity of fluids may increase in the presence of heat killed *C. neoformans*, but whether this change is pathologically significant requires further investigation. Using a model of cryptococcal infection in zebrafish larvae, a “pulsation” phenomenon was identified, consisting of vasodilation and constriction in the cranial vasculature with an impact on vessel wall permeability. The findings in this work, are reflective of the CM pathology as seen in human patients and suggest impaired CSF and blood flow homeostasis may contribute to intracranial hypertension in CM.

Acknowledgements

I would like to thank my supervisor Simon Johnston, who against all reason seems to enjoy my bizarre train of thought and never stopped helping me catch it and pin it down with writing. Thank you, Simon, for really asking me how I am when I was struggling.

I would like to thank Rhoda, for always challenging my way of thinking, even if it broke my brain a few times, only to rebuilt better anew. Thank you, Rhoda, for reminding me my heart is a scientist and I deserve to be here.

I want to thank my comrades in the PhD trenches - Jacob, Ffion, Olivier, Eliot, Dan, playing DnD with you was the most accepted and understood I have ever felt. You all got me through the worst of times and made the best of times beautifully odd and the crying from laughter kind of fun. I would not change it for the world. I can only hope we can fight life from separating us.

Chris, you are a ball of sunshine and disease, and the most amazing father. I will miss you so much, it already hurts.

Mahrukh, your sharp inappropriate humour beats even mine, I bow to thee. Please remember me when you become president.

Stella, the Eastern European mum to my Eastern European mum. Thank you for always violently shoving confidence down my throat, it felt like home.

I want to thank my mum, for helping me miss her less by showering me with so much love that it felt like she was here.

Thank you, Charlie, for feeding me and standing by me, for feeling my anxiety with me. You gave me the most wonderful home, where I felt safe and loved. You did not have a whole girlfriend for a while, but you still remained patient with me for years now.

And last but not least, thank you Boo, for purring next to me and giving me kisses in all the lonely all-nighters. It was a pleasure greeting the sun with you so many times.

Table of Contents

<i>Abstract</i>	1
<i>Acknowledgements</i>	2
<i>Table of Contents</i>	3
<i>List of Tables</i>	7
<i>List of Figures</i>	7
<i>Abbreviations</i>	10
<i>Declaration</i>	11
Chapter 1: Introduction	12
1.1 Intracranial pressure in health	12
1.1.1 Intracranial pressure – early history and dogma.....	12
1.1.2 CSF physiology and contribution to intracranial pressure	14
1.1.3 Cardiovascular and respiration influence on intracranial pressure	21
1.1.4 The physics of CSF flow and intracranial pressure.....	26
1.2 Intracranial pressure in HIV positive-associated cryptococcal meningitis	31
1.2.1 Epidemiology, treatments, and determinants of mortality	31
1.2.2 Pathophysiology of cryptococcal meningitis.....	35
1.2.3 The influence of inflammation on IH in HIV positive associated CM.....	37
1.3 In vivo models of cryptococcosis or cryptococcal meningitis	38
1.3.1 Cryptococcal meningitis research in mammals, gaps in models	38
1.3.2 Cryptococcal meningitis research in zebrafish models	44
1.3.3 Gap in existing animal models of cryptococcal meningitis.....	50
1.4 Thesis aims and objectives.	52
Chapter 2: Materials and Methods	54
2.1 Zebrafish Husbandry	54
2.1.1 Ethics statement	54
2.1.2 Maintenance and breeding	54
2.1.3 Anaesthesia	55
2.1.4 Dechoriation.....	55
2.2 Cryptococcus culture	55
2.2.1 Agar plate culture of Cryptococcus.....	56
2.2.2 Broth culture of Cryptococcus	56
2.2.3 Large volume, long-term culture for rheological measurements.....	57
2.3 Infection of zebrafish embryos and larvae.	57
2.3.1 Preparation of glass microinjection needle for injection	57
2.3.2 Calibration of injection volume.....	58
2.3.3 Injection of zebrafish larvae and embryos	58
2.3.4 Injecting zebrafish larvae with dextran fluorescent dye.....	59
2.3.5 Quantification of colony forming units in injection inoculum	59
2.3.6 Quantification of zebrafish fungal burden colony forming units.	59
2.3.7 Drug Treatments of zebrafish larvae	60
2.3.8 Survival analysis	60

2.4	Microscopy	60
2.4.1	Mounting for widefield fluorescence microscopy	60
2.4.2	Mounting for light sheet microscopy	61
2.4.3	Widefield fluorescence microscopy	61
2.4.4	Light sheet microscopy	61
2.5	Image analysis	62
2.5.1	Fungal burden quantification	62
2.5.2	Head size measurement	62
2.5.3	Quantification of vessel size change in time	62
2.5.4	Quantification of vascular bed volume in 3D	62
2.5.6	Dextran fluorescence in brain quantification	63
2.6	Rheological measurements	65
2.7	Purification of <i>Cryptococcus</i> polysaccharide capsule	65
2.8	Statistical analysis	65
2.8.1	Survival analysis	65
2.8.2	Testing for normality	65
2.8.3	Analysis of difference between groups, tests used:	66
2.8.4	Assessing correlation	66
2.8.5	Power Calculations	66
Chapter 3: Developing the zebrafish larvae model to study the dispersal of cryptococci in the CNS and the pathophysiology of cryptococcal meningitis.		67
3.1	Summary	67
3.2	Introduction	68
	Summary of gaps in treatments and understanding of human patients CM pathology	68
	Suitability of the zebrafish animal model for this work (see section 1.3 of Introduction for more detail)..	70
3.3	Objectives	72
3.4	Localisation of brain ventricles <i>C. neoformans</i> KN99 infection and impact on the CNS...	72
3.4.1	Injection into the brain ventricle of 2dpf is technically challenging and not suitable for testing the null hypothesis.	72
3.4.2	Ventricular infection leads to cranial and ventricular deformation but no dissemination to brain tissue.	79
3.4.3	Cranial deformation in the zebrafish larvae ventricular infection model is linearly related to fungal burden.	85
3.4.4	17% of ventricular infections led to dissemination to the spinal canal.	87
3.4.5	It was not possible to assess if non-viable <i>C. neoformans</i> would cause cranial deformation in ventricular infection.	90
3.4.6	Pharmacological manipulation of cranial blood volume did not alter cranial deformation in ventricular infection.	92
3.5	Dissemination and localisation of systemic <i>C. neoformans</i> infection in the CNS from cranial vasculature	95
3.5.1	<i>C. neoformans</i> systemic infection in zebrafish larvae better represents dissemination as seen in patients but does not lead to persistent cranial deformation as seen in ventricular infection.	96
3.5.2	The <i>C. neoformans</i> dissemination event could not be clearly identified from time lapse images.....	99
3.6	Discussion	107
3.6.1	Injection into the brain ventricle of 2dpf is technically challenging and not suitable for examining the brain infection.	107

3.6.2 Ventricular infection leads to cranial and ventricular deformation but no dissemination to brain tissues.....	107
3.6.3 Cranial deformation in the zebrafish larvae ventricular infection model is linearly related to fungal burden.	109
3.6.4 Ventricular infection leads to dissemination to the spinal canal which does not have a uniform distribution across the length of the spine.....	110
3.6.5 It is not possible to assess if non-viable <i>C. neoformans</i> would cause cranial deformation in ventricular infection.	111
3.6.6 Pharmacological manipulation of cranial blood volume did not influence cranial deformation in infection.	112
3.6.7 <i>C. neoformans</i> systemic infection in zebrafish larvae better represents dissemination as seen in patients but does not lead to persistent cranial deformation as seen in ventricular infection.	113
3.6.8 <i>C. neoformans</i> events of dissemination from zebrafish larvae cranial vasculature are highly technically challenging to capture in long-term time-lapse imaging.....	114

Chapter 4: *C. neoformans* systemic infection affects cranial vasculature dynamics, size, and blood brain barrier permeability. 116

4.1 Summary	116
4.2 Introduction	117
4.3 Objectives	119
4.4 Results.....	119
4.4.1 “Pulsations” - acute cranial vascular volume fluctuations observed during cryptococcal infection.	119
4.4.2 Intensity and frequency of “pulsations” at higher temporal resolution.	123
4.4.3 Quantification and automated analysis of vessel pulsations from wide-field fluorescence time lapse was not possible.	123
4.4.4 Implementation of light sheet imaging and high time resolution (<1s) allows for accurate automated quantification of vessel volume fluctuations.....	128
4.4.5 Characterisation of pulsation intervals and synchronicity across vascular tree.....	133
4.4.6 Vascular wall shape is disrupted in infection to apparently accommodate passing of <i>C. neoformans</i> masses.	137
4.4.7 Volume of cranial vasculature is increased by cryptococcal infection.....	141
4.4.8 Cranial vasculature permeability increases in cryptococcal infection.....	145
4.5 Discussion	148
4.5.1 Implementation of light sheet imaging and shorter imaging intervals allows for accurate automated quantification of vessel volume fluctuations.....	148
4.5.2 Characterisation of pulsation intervals and synchronicity across vascular tree.....	149
4.5.3 Vascular wall shape is disrupted in infection to apparently accommodate passing of <i>C. neoformans</i>	150
4.5.4 Volume of cranial vasculature is increased by cryptococcal infection.....	151
4.5.5 Cranial vasculature permeability was increased by infection.....	152
4.5.6 Experimental set up for injecting inert beads into the zebrafish larvae bloodstream is an important control that needs development and validation.	154
4.5.7 Summary.....	155

Chapter 5: Impact of cryptococcal infection on CSF properties and optimisation of the zebrafish model to study CSF flow in infection 156

5.1 Summary	156
5.2 Introduction	156
CSF flow in human physiology.....	156

Viscosity of CSF in health and cryptococcal infection	157
CSF flow in zebrafish larvae.....	160
5.3 Objectives	164
5.4 Results Section 1: CSF properties in infection.....	164
5.4.1 The presence of <i>C. neoformans</i> does not alter the shear flow profile but increases fluid viscosity. 164	
5.4.2 Viscosity of YPD increases with increased concentration of cryptococcal yeast.	167
5.5 Results Section 2: Zebrafish larvae as a tractable model for the assessment of velocity and directionality of flow of cryptococci in brain ventricles.....	169
5.5.1 Observations show circular flow of <i>C. neoformans</i> in the D/M ventricle in zebrafish ventricular infection	169
5.5.2 Dissemination from cranial vasculature into the CSF allows for examination of CSF flow in the zebrafish vascular infection model.....	171
5.6 Discussion	175
5.6.1 Viscosity increase observed <i>in vitro</i> could be physiologically relevant, despite large differences with spinal fungal burden in patients.	175
5.6.2 Zebrafish larvae as a tractable model for the assessment of velocity and directionality of flow of cryptococci in brain ventricles	176
Chapter 6: Final Discussion.....	179
6.1 Introduction	179
6.1.1 High fungal burden and low toxicity of ventricular infection zebrafish model of cryptococcal meningitis.....	180
6.1.2 Is brain ventricle dissemination unidirectional?.....	181
6.1.3 Colonisation of brain tissues by cryptococci.....	183
6.2 A summary theoretical model of cranial pressure in the presence of <i>C. neoformans</i>.....	186
6.2.1 Existing knowledge base and assumptions of summary model.....	186
6.2.2 <i>C. neoformans</i> pathogenic presence in the context of theoretical model of pressure	191
6.2.3 <i>C. neoformans</i> presence in the CNS resulting in pathological influence that may not be due to intracranial pressure increase.	193
6.3 Final conclusion	194
Supplementary Videos: Legends and Links.....	195
Appendix 1.....	199
References	223

List of Tables

Table 1. 1 Components of CSF system – comparison across humans and animal models.....	49
--	----

List of Figures

Figure 1. 1 Graphical summary of current understanding of human CSF flow, secretion, and reabsorption.....	24
Figure 2. 1 Example analysis process in ImageJ for measuring dextran fluorescence in the brain: analysis of data from figure 4.16	64
Figure 3. 1 Experimental approaches tested for zebrafish larvae brain ventricle microinjection.	75
Figure 3. 2 In comparison to injection at 1dpf in the mesencephalic ventricle, injection into the hindbrain ventricle of 2dpf is more challenging technically and results in higher mortality.	77
Figure 3. 3 Phenotypes arising from ventricular injection – cranial deformation in the majority of larvae	81
Figure 3. 4 Ventricular infection at 1dpf results in cranial and ventricular deformation. Infection is contained within the ventricular chambers and degree of deformation linearly correlates with fungal burden.....	82
Figure 3. 5 Frequency distribution of ventricular infection cranial deformation measurements show a bimodal distribution.....	84
Figure 3. 6 CFU fungal burden in the cranium of larvae with dorsal cranial deformation.....	86
Figure 3. 7 3dpi ventricular infection phenotypes: localisation of infection in the spinal canal	88
Figure 3. 8 Non-viable <i>C. neoformans</i> were cleared from brain ventricles.....	91
Figure 3. 9 Pharmacological manipulation of cranial blood volume did not change cranial deformation following ventricular infection.....	94
Figure 3. 10 <i>C. neoformans</i> systemic infection in zebrafish larvae results in dissemination to the CNS but does not lead to persistent cranial deformation as seen in ventricular infection.	98
Figure 3. 11 Secondary fungaemia in the CNS captured 6 hours after blood systemic circulation inoculation. Point of dissemination and mechanisms of endothelial cell wall crossing not identified.....	100

Figure 3. 12 Pathogen dissemination event from cranial vasculature captured 20hpi to possibly disrupting the vascular endothelium.....	102
Figure 3. 13 Pathogen dissemination event from cranial vasculature captured in still images.	105
Figure 4. 1 Acute vascular volume fluctuations are seen in infected cranial vasculature. ...	121
Figure 4. 2 Acute vascular volume fluctuations are not observed in zebrafish larvae without infection.	122
Figure 4. 3 Acute vascular volume fluctuations are seen in infected cranial vasculature in 2s image capture interval time-lapses.....	126
Figure 4. 4 Results from initial attempts of “pulsations” quantification (widefield, 5min/image for 20hrs). Failure at automated vessel area measurements	127
Figure 4. 5 “Pulsations” quantification in widefield microscopy at high resolution and 2s/image – resolution improves automated vessel area measurements.	130
Figure 4. 6 “Pulsations” quantification in light sheet imaging allows for accurate automated measurements of vessel area.	131
Figure 4. 7 Successful quantification of differences in vascular dynamics in infection and control through automated vascular area quantification in time.....	132
Figure 4. 8 Area fluctuation of separate vessel groups in the same infected larva – Evidence of synchronicity across pulsations	134
Figure 4. 9 Time interval of a single pulsation event and range of volume fluctuation – vessel group 1	135
Figure 4. 10 Time interval of a single pulsation event and range of volume fluctuation – vessel group 2	136
Figure 4. 11 Vessel architecture disruption in infection – vessel 1, single event.....	138
Figure 4. 12 Vessel architecture disruption in infection – vessel 1, 8 events	139
Figure 4. 13 Vessel architecture disruption in infection – vessel 2, single event.....	140
Figure 4. 14 Cranial vasculature volume quantification in 3D – before and after tubular enhancement	142
Figure 4. 15 Cranial vasculature in volume quantification in 3D – volume of vasculature in bigger in infection and is not correlated to infection burden.....	143
Figure 4. 16 Permeability of cerebral vasculature is increased in infection	146
Figure 4. 17 Pathogen fluorescence does not skew data shown in Fig. 4.16.....	147

Figure 5. 1 Shear flow and quantification of shear rate and shear stress	157
Figure 5. 2 Diagram of directionality of CSF flow in a healthy zebrafish larva	163
Figure 5. 3 Flow profile of shaken and still <i>C. neoformans</i> liquid culture showed no difference in flow profile across growth conditions.	166
Figure 5. 4 There is a positive linear correlation of <i>C. neoformans</i> YPD liquid culture viscosity and cfu/n	168
Figure 5. 5 Observations show circular flow of <i>C. neoformans</i> in the D/M ventricle in zebrafish ventricular infection	170
Figure 5. 6 Flow velocity of <i>C. neoformans</i> in the brain ventricles can be examined in the systemic infection model.	173
Figure 6. 1 A simplified model of the dynamics of intracranial pressure.....	189

Abbreviations

- ACSF** – artificial CSF
- AMCtA** - Anterior mesencephalic central artery
- AQP** - Aquaporin
- ART** – antiretroviral therapy
- BBB** - Blood-brain barrier
- BCSFB** - Blood-CSF barrier
- CC** - Central canal of the spinal cord
- cfu** - Colony forming units
- CM** - Cryptococcal meningitis
- CNR** - Contrast to noise ratio
- CNS** – Central nervous system
- CP** - Choroid plexus
- CPP** – cerebral perfusion pressure
- CS** - Confluence of sinuses
- CSF** - Cerebrospinal fluid
- D/M** - Diencephalic/mesencephalic ventricle
- DAmB** – amphotericin B deoxycholate
- DLV** - Dorsal longitudinal vein
- DoC** - Duct of Cuvier
- dpf** - Days post fertilisation
- dpi** - Days post infection
- ICC** – intracranial compliance
- ICH** - intracerebral haemorrhage
- ICP** - intracranial pressure
- IH** - intracranial hypertension
- iNPH** - Idiopathic normal pressure hydrocephalus
- IRIS** – immune reconstitution syndrome
- LAmB** – liposomal amphotericin B
- LMICs** – low- to middle income countries
- LP** - Lumbar puncture
- MAP** – mean arterial pressure
- MIP** – maximum intensity projection

MRV – magnetic resonance venography
MsV - Mesencephalic vein
mTBI – minor traumatic brain injury
NPH - Normal pressure hydrocephalus
OP – opening pressure
PCM – Pulmonary cryptococcosis mouse
PVS – Perivascular space
RICP - Raised intracranial pressure
RV - Rhombencephalic ventricle
SAS - Subarachnoid space
SSS - Superior sagittal sinus
TBI – traumatic brain injury
TV - Telencephalic ventricle
VPS – ventriculoperitoneal shunt
VR or VRS - Virchow-Robin space, perivascular space

Declaration

I, the author, confirm that the Thesis is my own work. I am aware of the University's Guidance on the Use of Unfair Means (www.sheffield.ac.uk/ssid/unfair-means). This work has not previously been presented for an award at this, or any other, university.

Chapter 1: Introduction

Cryptococcal Meningitis (CM) is a subacute meningoencephalitis, caused by dissemination of *Cryptococcus* species from the lung. CM is the most common cause of adult meningitis in many areas of the world that have high rates of HIV infection (French *et al.*, 2002; Williamson *et al.*, 2016;). Despite the availability of antifungals, in 2020, global mortality from cryptococcal meningitis was estimated at 112 000 cases out of 152 000 diagnosed (Rajasingham *et al.*, 2022). More than 50% of HIV- infected CM patients have some degree of intracranial hypertension (IH), an abnormally increased pressure in the spaces surrounding the brain and the spinal cord (Graybill *et al.*, 2000; Jarvis *et al.*, 2014). Elevated ICP is defined as opening pressure higher than 250mm H₂O. Symptoms of intracranial hypertension can include altered mental status, papilledema and blindness, impaired hearing, general neurological deterioration, and coma (Williamson *et al.*, 2016). Therefore, treatment of CM should include management of intracranial pressure as well as administration of anti-fungal drugs to treat the infection (Papas *et al.*, 2005; Dammert *et al.*, 2008; de Vedia *et al.*, 2013; Wijewardana *et al.*, 2011). Serial lumbar punctures can be an effective treatment but is not available for many patients in low- and middle-income countries (LMICs) (Lawrence *et al.*, 2019). Therefore, there is a need for identifying new, potentially non-invasive, treatments that can be implemented in LMICs.

To understand how intracranial hypertension arises in CM we firstly need to have a knowledge of the components of the CNS and how they function in health to sustain normal IP, and secondly knowledge of cryptococcosis as a disease and the associated CNS pathology. Therefore, in this introductory chapter to my thesis I will outline how ICP physiology works in health to then explain how the system is altered in the CM pathology.

1.1 Intracranial pressure in health

1.1.1 Intracranial pressure – early history and dogma

The two main systems that are seen to contribute to creating pressure in the cranium is the cerebral spinal fluid (CSF) system and blood circulation (Kapskowitz *et al.*, 2016). Changes in volume of fluid or tissue in the cranium and obstructions of spaces of outflow are the widely accepted mechanisms of what leads to developing IH pathologies (Rekate *et al.*, 2009; Koleva and De Jesus 2020). Furthermore, CSF secretion and absorption is dependent on the cranial

vasculature (Boron and Boulpaep 2017), which increases the complexity of understanding how IP is determined.

Efforts to understand intracranial pressure can be traced back to a 5000-year-old Imhotep Egyptian papyrus describing cases of traumatic brain injury (Blomstedt 2014; Breasted, 1930). However, most of our current understanding of intracranial pressure was established around 200 years ago, at the time of Alexander Monro.

Alexander Monro (1733- 1817) was a professor of Anatomy and Surgery at the University of Edinburgh (Rabelo *et al.* 2021). In 1783 he published his book *Observations on the Structure and Functions of the Nervous System: with Illustrated Tables*, in which he described the volumes inside the skull as static or hardly variable. Monro claimed that the introduction of any foreign volume into the cranium would result in the expulsion of the same volume of blood, to compensate for the change in the system (Monro A. 1783). In 1824, his student George Kellie (1770- 1829) furthered Monro's work with his findings from the dissection of two cadavers, who died after a storm in Leith, Edinburgh. Kellie envisioned the adult skull as an incompressible structure that is independent of atmospheric pressure and is almost completely occupied by the brain (Kellie G., 1824). He claimed the integrity of the skull to be strictly related to intracranial volume i.e., the introduction of any new volume would result in the displacement of another equivalent volume, be that blood or brain tissue (Kellie G, 1824).

An essential aspect of the Monro-Kellie doctrine was introduced in 1828 by John Abercrombie (1780- 1844). He hypothesised that cranial depression should result in decreased blood flow and cause compression of the brain (Abercrombie J., 1828). However, Abercrombie's theory was left incomplete as it lacked the aspect of a key component of the cranial cavity, the CSF. In 1842, the English physician George Burrows pointed out the need to account for all three cranial component volumes: blood, brain, and CSF. Burrows stated that the compensation for pathological increase in cranial volume can come from displacement of any of the three components. He was also the first one to consider the measure of pressure in his analysis. In the 20th century the neurosurgeon Harvey Cushing (1869-1939) supported Burrow's discoveries regarding the importance of the CSF in intracranial dynamics and demonstrated the importance of the doctrine in clinical practice (Lundberg, 1983). In the 21st century the Monro-Kellie doctrine is widely accepted, especially regarding the constant intracranial volume and rigid skull. There is some work that challenges the lack of elasticity of the skull (Mascarenhas

et al. 2021), but in relation to intracranial pressure physiology, the cranium is still widely accepted as a rigid structure.

Thus, the modern and updated Monro-Kellie doctrine accepts that in health the cranium components (blood, brain, and CSF) have a constant volume. Any abnormal increase or decrease in volume of any of those components results in a compensatory displacement of matter in equal volume, to maintain healthy intracranial pressure and prevent pathological brain compression. This doctrine established the fundamental principles of intracranial pressure homeostasis and allowed for the investigation of ICP in pathology.

In this introduction I will summarise the current understanding of IP. As intracranial pressure is generally a measurement of the fluid pressure that CSF generates, I have structured my review of the literature around the CSF compartment, with the other components of ICP, such as the vascular compartment, being described as influencing CSF flow dynamics.

1.1.2 CSF physiology and contribution to intracranial pressure

1.1.2.1 *The CSF and its function*

Cerebral spinal fluid (CSF) is a colourless, watery liquid that is largely produced in the choroid plexus of the lateral ventricles of the vertebrate brain. CSF flows through the brain ventricles and the central canal of the spinal cord, known as the first system of CSF flow (Boron and Boulpaep 2017). Holes in the 4th ventricle (Foramens of Luschka and Monroe) allow for the CSF to leave the ventricular system and enter the subarachnoid space (Boron and Boulpaep 2017) (Fig. 1.1). The second system of CSF flow is where the subarachnoid space allows the CSF to circulate in proximity to all brain tissue and the spinal cord. The third system of CSF flow is from the subarachnoid space and consists of controlled transport of CSF through the pia matter and into the interstitium of the brain where the CSF interconnects with the interstitial fluid (ISF) that surrounds the individual brain cells (Iloff *et al.*, 2012; Bothwell *et al.*, 2019). Thus, the CSF reaches almost all parts of the CNS, from that alone it is clear that its presence must be imperative for sustaining neuronal tissue homeostasis.

We know that the CSF functions as a protector of the brain and spine, it acts to absorb shock and cushion those tissues from hitting cranial bones in impact injury (Boron and Boulpaep 2017; Adigun and Al-Dhahir 2021). Another mechanical function of the CSF is to alleviate

strain from the neck in carrying the mass of the brain, by suspending it and providing buoyancy which reduces brain's effective weight from true 1500 gm to a net of 25 mg (Adigun and Al-Dhahir 2021). The CSF also acts as a transporter of nutrients and signalling molecules throughout the CNS (Spector *et al.*, 1997; Tricoire *et al.*, 2003). The CSF functions also to clear aggregation of protein by-products of neuronal function, this role of the CSF has been heavily investigated recently for its role in neurological disease pathology (Shibata 2000; Iliff 2012; Kress 2014; Louveau 2015; Trumbore 2016; Weller 2018). The physiology of CSF protein clearance is also the least understood as it involves the flow of the CSF through the brain interstitium (third system of flow). This requires CSF flow from the sub-arachnoid spaces around brain vasculature (perivascular spaces), into the interstitium of the brain and out through perivascular spaces of veins. This path of the CSF is termed the glymphatic system, which was only discovered in 2013 by Iliff *et al* (Fig. 1.1 – 3,4).

1.1.2.2 CSF secretion

Total CSF production in humans is ~ 500ml/day, therefore there is turnover of the entire 150ml volume of CSF around three times a day. It is estimated that 80% of CSF is secreted at the choroid plexus in the brain ventricles, the other 20% comes from secretion at the level of blood vessels imbedded within the brain parenchyma (the blood brain barrier) (Kimelberg *et al.*, 2004; Orešković *et al.*, 2010; Redzic *et al.*, 2011; Brinker *et al.* 2014). CSF secretion is thought to be driven by both an osmotic and a hydrostatic gradient across the BBB and choroid plexus (Bothwell *et al.*, 2019).

Choroidal Secretion

The choroid plexuses are found in four locations in mammals: the two lateral ventricles, the third and fourth ventricle. Evidence from mammalian animal models suggests that the 4th ventricle choroid plexus is the largest producer of CSF (MacAulay *et al.*, 2022). The choroid plexuses consist of high density of fenestrated capillaries surrounded by an epithelial layer of selectively permeable ependymal cells. The ventricles are lined with ciliated ependymal cells which have restrict what crosses into the CNS from blood circulation and becomes CSF (see figure 1, 1) (Brightman *et al.*, 1969; Cserr *et al.*, 1977; Jones *et al.*, 1987; Whish *et al.*, 2015). Research in mice shows that the ependymal cells at the choroid plexus epithelium differ in that they possess tight junctions that severely restrict fluid-phase transport. Junction proteins in the choroid plexus in mice include Claudin -1, -2, -3, -11, -19, occludin and ZO-1 (MacAulay *et*

al., 2022). Claudin 3 is seen as a key molecule of the tight junctions of the BBB in humans, it is specifically localised in the choroid plexus and not in the rest of the CNS (Kominsky et al., 2007; Ohtsuki et al., 2008). Claudin 1 and 2 have been detected in pre- and postnatal human embryonic brain (Kratzer et al. 2012). Overall claudin 3 has been seen to be persistently express during development, whether claudin 1 is upregulated in embryonic stages, diminishing in later age, and claudin 2 seen to increase expression with age (Steinemann et al., 2016). The consensus is that claudin molecules in the choroid plexus have varied expression across development and perform different functions in the selective permeability of brain barriers.

The order of tissue and fluid in the choroid plexus from blood to CSF filled ventricular space is:

1. Blood
2. Fenestrated endothelium of capillaries surrounded by loose connective tissue
3. Filtrate from capillaries (mostly a-cellular blood plasma)
4. Choroidal ependymal epithelium with protruding microvilli and cilia into the ventricles
5. CSF and ventricular space

(Boron and Boulpaep, 2017; MacAulay *et al.*, 2022) (Fig. 1.1 - 1)

The plexuses receive blood supply from the anterior and posterior choroidal arteries, which are branches of the internal carotid artery and the posterior cerebral artery (MacAulay *et al.*, 2022). Blood flow to the plexuses (per unit mass tissue) is ~10-fold greater than the average cerebral blood flow (Boron and Boulpaep, 2017). The capillaries of the choroid plexus are outside of the BBB and the choroid plexus, together with its ependymal epithelium, forms a blood-CSF barrier. The choroidal epithelium cells are connected with tight junctions and have transporters and channels that are thought to allow an isosmotic secretion of CSF (Boron and Boulpaep, 2017).

Osmotic theory of CSF secretion

After the capillary endothelium filters blood from cells, the choroidal epithelium produces CSF from that filtrate via a net transfer of NaCl and NaHCO₃, resulting in water movement by osmosis. CSF has a lower concentration of K⁺ than plasma does, and it contains almost no protein. There is a net secretion of Na⁺ and Cl⁻ from plasma to CSF. There is a net secretion of K⁺ towards the plasma, with some reabsorption into the CSF. The choroidal epithelial cells

take up K^+ from the CSF by the Na/K/Cl cotransporter on the apical membrane (apical = facing the CSF), creating a movement towards the plasma, but most of it recycles back into the CSF creating a K^+ cycle. Large fluctuations of K^+ in the plasma only show small changes of CSF [K^+]. K^+ concentrations in the subarachnoid space are much lower than choroidal CSF, suggesting a larger K^+ removal in brain embedded capillaries in comparison to the choroid plexus ependymal cells. Water transport is driven by a small osmotic gradient favouring CSF formation. Aquaporin 1 channels are expressed in both the apical and basal membranes of the choroidal epithelium. Overall, the sustaining an ion homeostasis of the CSF is essential for healthy brain function and it largely about K^+ . The choroid plexus sustains ion concentration homeostasis in the CSF even if there are large variations of ion concentration in plasma (Boron and Boulpaep 2017) and there is some evidence of the CSF being produced against an osmotic gradient (MacAuley 2021).

Extra-choroidal secretion

At least 10-20% of secretion of CSF (10-20%) happens at the blood brain barrier (BBB) (Bothwell *et al.*, 2019) and there is evidence suggesting that the extra choroidal secretion may have an even larger contribution than widely accepted (Hladky *et al.*, 2016). The BBB is the physical interface between neuronal tissue and the blood circulation. It is a part of the neurovascular unit (NVU), which is term used to describe the relationship between brain cells and their blood vessels, a relationship which involves both cellular and molecular elements that regulate cerebral blood flow and the function of the BBB (Sweeney *et al.*, 2018). The BBB consists of the vascular wall endothelial cells, the tight junctions in-between them, and the cells surrounding the vascular wall. It is important to keep in mind that the BBB is not the same in all regions throughout the brain and the regional differences mostly come from what surrounds the vascular wall and the type of vessel. Vessels in the Virchow-Robin (perivascular) spaces are suspended in a CSF filled subarachnoid space and do not come into contact with the brain tissue directly but are close to the pial layer of the parenchyma, which is made of astrocytic feet than can pick up compounds from the CSF via aquaporin-4 channels (AQP4) (Fig.1.1 - 3) (Sweeney *et al.*, 2018; Mestre *et al.*, 2020). The BBB in perivascular spaces (BCSFB not in the CP; Figure 1.1, 3) consists of the endothelium with tight junctions, smooth muscle cells around the endothelium, CSF and the astrocyte feet forming the pia matter. Vessels that are embed close to the parenchyma (mostly capillaries and venules) are surrounded by classical capillary BBB, which in its components includes pericytes and has no CSF in between

endothelial cells and astrocytes (Fig. 1.1 – 4). This is where the majority of gas exchange and nutrient delivery happens for the brain. The BBB of capillaries and venules consists of an endothelium with tight junctions, pericytes enveloping the endothelium, and astrocyte feet enveloping pericytes (Sweeney *et al.*, 2018) (Fig. 1.1 – 4). The ability of the capillary endothelium BBB to diffuse fluid is not supported by much evidence, as opposed to the arterial (perivascular) BBB. The capillary endothelium has a very low osmotic water permeability there is no evidence of the presence of AQP channels (MacAuley *et al.*, 2022).

Interstitial fluid (ISF) is produced by secretion across the BBB, and it fills the extracellular space between neurons and glia in the brain parenchyma (Redzic 2011; Hladky *et al.*, 2016; Boron and Boulpaep 2017). In the “glymphatic system” model, CSF enters the parenchymal extracellular space via perivascular spaces and mixes with the ISF, to then drain into the perivenular spaces (Fig. 1.1 – 5) (Abbot *et al.*, 2018; Mestre *et al.*, 2020). The purpose of this fluid mix is thought to be for the transport and saturation of compounds such as melatonin across all brain regions, not just spaces in contact with SAS or ventricular CSF (Abbot *et al.*, 2018).

1.1.2.3 CSF flow

See Figure 1.1 for a graphical summary of different types of CSF flow.

There are multiple suggested motile forces directing flow of CSF in the CNS. In the brain ventricles ependymal cell cilia synchronous beating facilitates CSF flow (Roales -Bujan *et al.*, 2012). The flow through the ventricles is pulsatile, unidirectional and is thought to be driven by arterial pulsations which in turn are dependent on blood pressure and heart rate (Bradley *et al.*, 2015; Madhok *et al.*, 2018). In mammalian models, CSF has been seen to move at the same speed as the arterial wall pulse within perivascular spaces, with the pulse driving influx of CSF in those spaces (Mestre *et al.*, 2018). In the glymphatic system, CSF flow has been demonstrated as a form of convection of net bulk substrate from one place to another, which is driven by a build-up of volume in one end of the tissue that transfers and equalises across the tissue through convection. In addition, both diffusion and convective type flows coexist within the glymphatic system (Koundal *et al.*, 2020). In the central canal (CC) of the spine, CSF flow has been shown to have bidirectional character driven mainly by breathing (Dreha-Kulaczewski *et al.* 2018). Forced inspiration results in CSF flow from the whole spine towards

the brain ventricles. Following expiration there is a change in direction of flow of lower level spinal CSF (below level of the heart) towards caudal end of the CC (Dreha-Kulaczewski *et al.* 2018) (Fig. 1.1, yellow arrows).

1.1.2.4 CSF reabsorption

The arachnoid granulations (AG or AV for arachnoid villi) act as an avenue for CSF reabsorption into the dural sinuses and venous blood circulation through a pressure-dependent gradient. The AGs are tubular network structures that act as an interface between the SAS and the Dural sinuses, where CSF drains into and returns to the venous flow (Boron and Boulpaep 2017). There are also arachnoid villi protruding from the SAS into epidural spinal veins, which are thought to mimic what is happening in the cranium (Pollay 2010). In the glymphatic system model, new mechanisms of CSF reabsorption have been suggested in the form of the CSF draining into the perivenular spaces where it gets absorbed by the venous vasculature within the brain parenchyma (Mestre *et al.*, 2020). There is also a rise in interest in a recently discovered meningeal lymphatic drainage at the base of the skull, that is thought to represent a major efflux route for the CSF (Louvea *et al.*, 2015). CSF reabsorption is also seen to be driven by the circadian rhythm, with an increase in reabsorption through the lymphatic system in the waking cycle (Mestre *et al.*, 2020).

1.1.2.5 Changes to CSF flow in disease pathology

Increased intracranial pressure is reported as a symptom or complication in several CNS pathologies, for example hydrocephalus, idiopathic intracranial hypertension, traumatic brain injury, intracerebral haemorrhage (ICH) and subarachnoid haemorrhage.

Hydrocephalus is characterised by a pathological increase in the volume of the CSF and enlargement of the brain ventricles. Hydrocephalus was first described to be of two types, communicating and non-communicating (obstructive), but since its initial characterisation in 1910s there have been many more classifications proposed (Rekate *et al.*, 2009). Currently there are four classifications accepted: obstructive, communicating, hypersecretory, and normal pressure hydrocephalus (NPH), excluding genetic hydrocephaly or spinal dysraphism (Koleva and De Jesus 2020).

Obstructive hydrocephalus can arise as a result of physical obstruction of flow in the ventricular system such as a tumour in the interventricular foramen, but more often obstruction is seen around the base of the skull in the foramina of Monro, the aqueduct of Sylvius, the fourth ventricle, and foramen magnum (Koleva and De Jesus 2020). Communicating hydrocephalus is a pathology of impaired CSF reabsorption often at the level of subarachnoid granulations, most commonly caused by haemorrhagic blockages or inflammation during meningitis (Koleva and De Jesus 2020). More traditionally known as a form of communicating hydrocephalus, hypersecretory hydrocephalus is a problem of abnormally increased CSF secretion. The condition is considered quite rare and commonly caused by plexus papilloma tumours in children (Rekate et al., 2009).

Hydrocephalus fits the Monroe-Kelly hypothesis quite well, until we consider a version of the disease known as normal pressure hydrocephalus (NPH), where lumbar puncture measurements show slightly high or normal levels of IP in the presence of ventricular dilation (Boron and Boulpaep 2017). NPH is considered a chronic version of communicating hydrocephalus, where the pathology comes from reabsorption problems. The pathophysiology of idiopathic NPH (iNPH) is mysterious, reports of disease-causing mechanisms have been heterogenous, and a single cause has not been identified (Passos-Neto *et al.*, 2022). The symptoms of NPH mimic Alzheimer's disease (AD) and Parkinson's disease, which often leads to misdiagnosis, especially due to the high prevalence of the disease in elderly people, with a median age of onset of 70 years old (Andersson et al., 2019). It is suggested that the condition is overlooked and the prevalence amongst elderly people with AD is much higher than currently recognised (Andersson et al., 2019). Treatment of NPH by introducing a ventriculoperitoneal shunt has a very high rate of success (Nakajima et al., 2021).

Our understanding of the pathophysiology of hydrocephalus is based on research into the arachnoid granulations on the assumption that this is where most CSF reabsorption occurs. However, the contribution of reabsorption from the meningeal lymphatics and the glymphatic system (venous outflow) (see 1.1.2.4) needs to be included. New evidence challenges arachnoid granulations as the main route of CSF outflow from the CNS and claims that the primary efflux route is the meningeal lymphatics, which reduce in capacity for supporting reabsorption with age (Mesquita, Fu and Kipnis 2018; Ma et al., 2017; Louveau et al., 2015; Absinta et al., 2017, Aspelund et al., 2015). It is important to appreciate these new findings and how they fit in our understanding of hydrocephalus pathogenesis and more importantly if there

is potential in manipulating those structures pharmacologically to improve clearance of CSF. The implication of the glymphatic system in neuroradiological disorders is already being evidenced. Altered AQP4 expression is evident in brain tissue from patients with NPH (Eide et al., 2018). Glymphatic MRI scans of patients with NPH show reduced CSF tracer entry and clearance (Ringsad et al., 2018, 2019).

More recent studies have found significant neuroradiological similarities between iNPH patients and (AD) patients particularly in the sizes of the basal cisterns and Sylvian fissure (Passos-Neto *et al.*, 2022; Yamada *et al.*, 2016). Epidemiological analyses have identified older age to be the most common risk factor for developing NPH, similar to AD. It is possible the development of the two pathologies has commonalities (Passos-Neto *et al.*, 2022). There is a lot of work suggesting pathological changes of CSF flow homeostasis strongly contribute to the aetiology of AD, and decreased CSF flow is associated with cognitive deficits in elderly patients (Attier-Zmudka *et al.*, 2019). Dysfunction in protein aggregates clearance through of the glymphatic system in particular has been suggested as a major driver of the pathology of AD (Han *et al.*, 2021).

It is important to examine how our understanding of IH disease pathophysiology has evolved in conditions like hydrocephalus, because obstruction hypotheses might be oversimplifying what occurs in pathology and there may be new mechanisms that contribute to IH development such as the above mentioned AQP expression changes. New ideas of aetiology for IH pathologies may contribute to also identifying new mechanisms for pathological increase in pressure in CM. Cryptococcal meningitis also has a history of being misdiagnosed as vascular dementia or AD pathology (Steiner et al., 1984; Aharon-Peretz et al., 2004; Alla, Doss and Sullivan 2004; Hoffmann et al., 2009; Chishimba et al., 2022), so there may be some mechanistical overlap between NPH, AD, dementia and CM worth exploring.

1.1.3 Cardiovascular and respiration influence on intracranial pressure

1.1.3.1 Heart rate and blood pressure

ICP is not constant, it normally varies between 6-25 mmH₂O. There are cyclical pressure changes occurring in the cranium during the cardiac cycle (Wagshul, Eide, Madsen 2011) with ICP fluctuating in response to cardiac systole and diastole (Madhok *et al.*, 2018). At heart contraction (systole), there is a wave of blood coming into the neurovascular compartment and

therefore intracranial pressure increases (P1). During P1 the brain expands inwards, compressing the ventricles, and outwards, compressing the subarachnoid space (SAS) (Fig.1.1) (Bradley, 2015). The inward pulsation causes the CSF to go from lateral ventricles to the third and fourth ventricles, leading to drainage of the SAS into the venous system (Bradley, 2015). This is then followed by a response of intracranial compliance resulting in a drop in pressure (P2) (Madhok *et al.*, 2018). There is a third pressure wave, which is related to diastole and decrease in brain volume during venous drainage (P3). If P1 is larger than P2 and P3 there is an exponential increase in IP, which quickly leads to pathology. The exponential is coming from exponential like phenomenological relationship observed but not an actual mathematically defined relationship (see section 1.1.4 Physics of CSF flow and Intracranial pressure).

Arterial pulsations are also thought to drive CSF flow within the subarachnoid space (Mestre *et al.*, 2018). The arterial pulse wave is dependent on HR, BP, and arterial wall elasticity (Messas *et al.*, 2013). Hypertension is seen to reduce the responsiveness of CSF flow to vascular dynamics in perivascular spaces (Mestre *et al.*, 2018). Furthermore, blood pressure would affect CSF secretion and reabsorption in the glymphatic system as it is not dependent on an osmotic gradient (AQP4 channels). There is some speculation whether CSF secretion at the choroid plexus is completely dependent on osmosis or that it may be that arterial pressure also affects CSF secretion at the level of the ventricles (MacAuley 2021). Overall, pathology of the vascular compartment of the CNS or changes in BP would likely significantly affect CSF flow and production.

1.1.3.2 Respiration

The respiratory cycle also has a marked impact on IP. Using MRI and echo-planar imaging to distinguish between the temporal and spatial events related to respiration (as opposed to cardiac output) demonstrated that velocity of CSF movement through the cerebral aqueduct is impacted greatly by the cardiac component (Takizawa *et al.*, 2017). In contrast, the respiratory cycle is more impactful on brain mass and medulla oblongata displacement (Takizawa *et al.*, 2017; Bordoni *et al.*, 2018). Spinal CSF dynamics, in particular, are highly sensitive to respiratory performance and instantaneously reflect intrabdominal and intrathoracic volume, and associated pressure changes. As stated above, forced inspiration and expiration therefore lead to upward and downward CSF flow in the spinal canal, respectively (Aktas *et al.*, 2019). It is,

therefore, important to consider the dynamics respiration, how they add complexity on the influence of blood pressure, venous return, and heart rate on intracranial and intraspinal pressure.

Figure 1.1 Graphical summary of current understanding of human CSF flow, secretion, and reabsorption

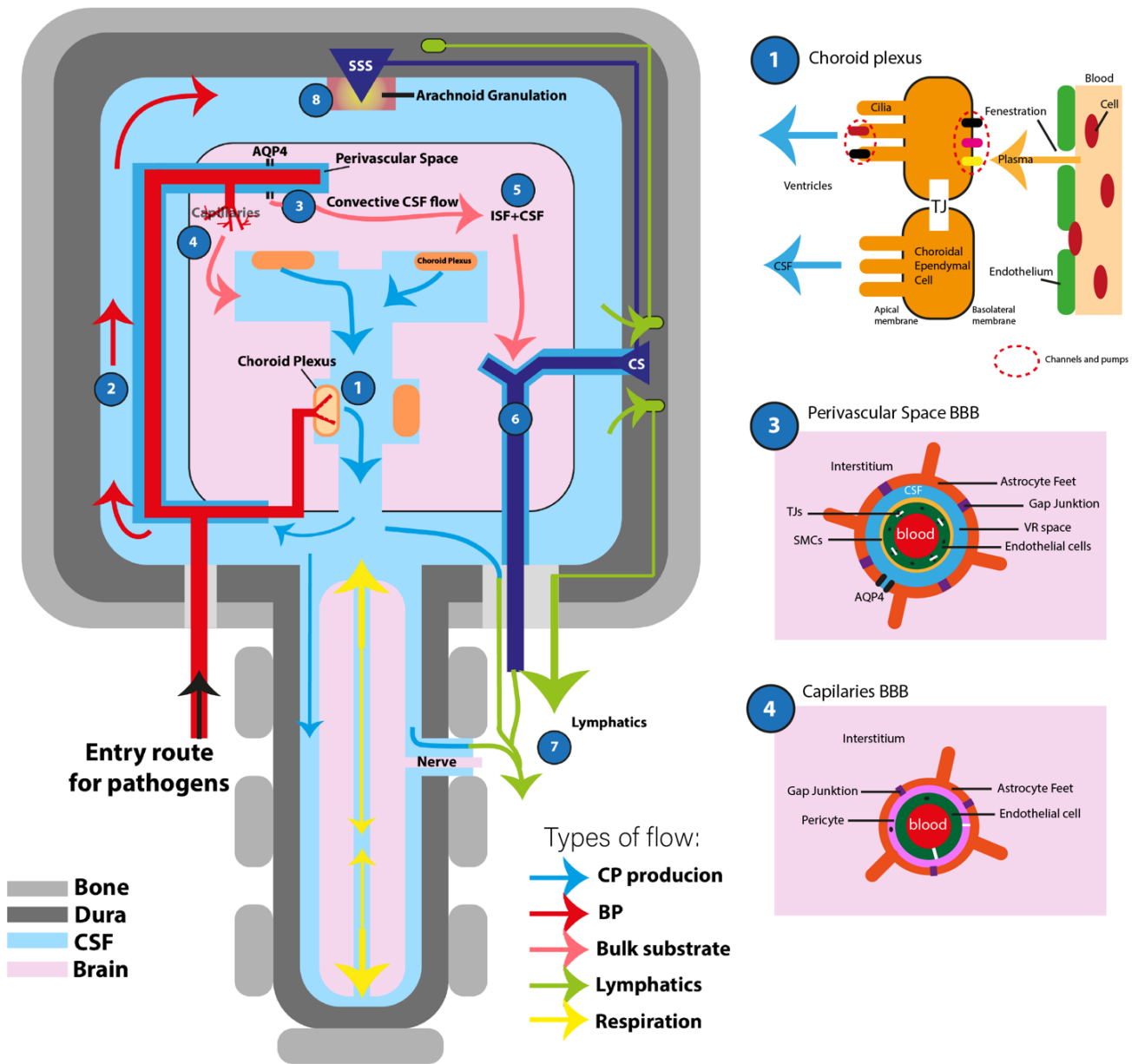


Figure 1. 1 Graphical summary of current understanding of human CSF flow, secretion, and reabsorption

1. Unidirectional CSF Flow Dogma: Choroidal secretion: 80% of CSF gets produced in the Choroid Plexus (CP). The flow of CSF is from the CP towards the spine or out of the foramina of Luschka and Magendie into the SAS
 2. Regional flow: Arterial wall pulsations drive CSF flow around the SAS and specifically deep into the perivascular spaces
 3. CSF in perivascular spaces enters brain parenchyma/ interstitium through AQP4 channels on astrocyte feet
 4. Interstitial flow: permeability across at BBB capillaries produces some ISF/CSF that flows back into ventricles
 5. Interstitial flow: CSF that enters through perivascular spaces undergoes convective flow within the parenchyma and mixes with ISF
 6. CSF drainage: After 5, CSF exits by reabsorption into the venous circulation, which drains either through dural sinuses or through meningeal or cervical lymphatics (7)
 8. CSF drainage: CSF in the SAS can be reabsorbed through arachnoid granulations into dural sinuses
 9. CSF pulsatile flow in the ventricles not shown;
- *Figure inspired by Mestre et al., 2020 and Sweeney et al., 2019

1.1.4 The physics of CSF flow and intracranial pressure

When the Monroe-Kellie doctrine was established in the late 1800s, it claimed that the volume of blood, CSF and brain in the cranium remain constant, as the skull is a rigid structure encapsulating its components (Monroe 1783; Kellie 1824). The series of animal experiments and clinical observations that followed described a system with dynamic volume changes. Cerebral compression experiments suggested a non-linear relationship between volume of cranial components and pressure, and complex interplay between heart rate and cerebral pressure pathology (Kocher 1901). Based on those observations, the Swiss neurosurgeon Theodor Kocher defined 4 stages of cranial compression. Stage one is asymptomatic initial expansion of mass compressing the brain, which is followed by stage two - beginning of intracranial pressure elevation. In stage three Kocher defines a “capillary anaemia” and blood pressure increase, with rhythmic alterations in consciousness due to fluctuating cerebral perfusion. In the terminal stage Kocher describes a fall in blood pressure, bradycardia, and occurrences of deep coma. Henry Cushing defined the triad of widened pulse pressure (increasing systolic, decreasing diastolic), bradycardia, and irregular respirations, as the vasopressor response (Cushing 1901), now known as the Cushing’s triad. The vasopressor response is thought to be as a result of mechanical distortion of the medulla, and it is now clear that it is a late sign of intracranial hypertension and is seen as a preterminal event (Wan, Ang and Wang 2008). Although they may not be as relevant in early to mid-stages of an IP pathology, Cushing’s characterisations point out the complex relationship between blood pressure and intracranial pressure, it is not just a physical relationship, but the two factors also influence each other through the CNS regulation of the physiological response.

Interest in the vasopressor response, led to research aiming at characterising the change in intracranial pressure with gradual increase in cranial compression. In the 1950s, and 60s, a trend in experimental design emerged which involved recording intracranial pressure from several points in the cranium of mammalian models, usually supratentorial space (subdural), cisterna magna or ventricles (ventricular space) and cerebral and spinal subarachnoid spaces (Langfitt et al., 1965). Pressure was recorded by inserting a catheter attached to a transducer, the unit of pressure used was not pascals (Pa) but millimetres of mercury (mmHg) or water (mmH₂O), which is a measurement of CSF opening pressure (OP) exerted on a column of mercury. In a report assessing recordings from 26 primates, a curious empirical relationship was observed between volume and pressure. Intracranial pressure was artificially elevated by inserting a double-wall balloon into the extradural space and filling it gradually with water (up

to 10ml) to mimic an abnormal mass growing in the cranium and exercising cranial compression (Langfitt et al., 1965). The volume-pressure curves from four animals showed an exponential like phenomenological relationship, the pressure did not initially increase with the introduction of a new volume but after a certain volume it appeared to “exponentially” increase (Langfitt et al., 1965). The authors speculated on what causes this relationship to occur, much like other physicians before them, they propose that when a pathological mass is introduced in the cranium (tumour, haemorrhage) the brain has a compensatory mechanism of returning to homeostatic volume in the form of emptying the venous and sinus compartments. That compensation is hypothesised to be limited, judging by the fact that IP eventually rises with increase in pathological growth. The compensatory mechanism of venous outflow was initially just a speculation, direct evidence of the venous outflow in response to abnormal increase in volume was shown in research in the 80s and 90s, utilising more modern techniques such transcranial Doppler sonography and MRI imaging to establish a linear relationship between ICP increase in patients and venous blood outflow velocity in the straight sinus (Hassler et al., 1988; Shoser et al, 1999; Alperin et al., 2000). The ratio of introduced volume and the pressure change induced (dV/dP) is now termed intracranial compliance (ICC). There is a large ICC in a healthy brain, therefore the ability to accommodate abnormal new mass (e.g., a newly growing tumour) is initially high (high ICC) and then it declines in an exponential manor. ICC in pathology however does not seem to be as simple as in Langfitts balloon volume experiments, for example it has been observed that in mild traumatic brain injury (mTBI), in comparison to healthy volunteers, venous outflow in patients happens via alternative routes to the jugular vein and sinuses. In mTBI, venous outflow seemed to happen through the secondary pathways which have higher resistance and cause and decrease in ICC, and redirected flow was observed in patients who did not exhibit clinical symptoms of pressure (Pomschar et al., 2013). Therefore, compliance may be reduced by pathological mechanisms that redirect flow as well as introduce abnormal volumes.

When discussing the volume-pressure gradients in ICP it is important to note that there is some debate whether pressure is equal across the cranio-spinal axis and if opening pressure (OP) at the lumbar level represent the whole system. It is generally accepted and taught that CSF is actively and largely formed in the choroid plexus of the brain ventricles, and it flows from the ventricles unidirectionally towards the cisterna magna (see 1.1.2). The exact volumes are undetermined, but ventricular CSF flows into the spinal canal and the subarachnoid cisterns around the brain and from there CSF is mixed with interstitial fluid of the parenchyma.

Reabsorption from the subarachnoid space through the arachnoid villi (AV) into the Dural sinuses is to be only possible if OP is 20-50 mmH₂O, allowing for a pressure gradient to be created across SA space and dural sinuses (Pollay et al., 2010). There is now evidence of a contribution of the skull lymphatics in reabsorbing subarachnoid CSF. CSF in the interstitial space and the perivascular spaces gets reabsorbed by the venioles and veins at the BCSFB and BBB. No matter the path or the volumes, CSF physiology is based on the idea of secretion (passive and osmotic), re-absorption and unidirectional flow from zones of secretion into zones of reabsorption.

Much of the canonical physiology of intracranial pressure assumes that pressure equalises across the whole of the CSF, as it assumes that the cranium is a closed system filled with incompressible material (brain, CSF and blood are assumed incompressible) – these are principles of Pascal’s law of homogeneous pressure distribution in a closed fluid-containing environment (Preuss et al., 2013). However, it has been shown that CSF has a directional flow in the cisterna magna, and to have a directional flow there needs to be a gradient from high to low pressure in a system (Poiseuille’s principles). Without a hydrostatic pressure gradient there is no CSF circulation nor passive CSF reabsorption (Klarica et al., 2013). There is evidence of a hydrostatic pressure gradient across subarachnoid space and dural sinuses, which allows CSF reabsorption (Cutler et al., 1968; Klarica et al., 2013), but the gradients of pressure that sustain CSF circulation are poorly understood. When pressure is measured while the person is lying down, there can be little to no difference seen between the pressure in the ventricles, supratentorial subarachnoid space and lumbar spine (Davson, Welch and Segal 1987). However, others have reported a difference of pressure between ventricles and subarachnoid space, termed transmante pressure gradient, with subarachnoid space having slightly higher pressure (Hoff and Barber 1974; ReKate 2009). In a sitting (upright) position, multiple studies demonstrate that the OP to be on the level of atmospheric pressure in the cervical and foramen magnum regions, and on the level of the lumbar region – higher than atmospheric pressure (i.e., higher the further from cisterna magna) (Klarica et al., 2013). In upright position, for there to be a flow towards the spine, there must be forces opposing the pressure gradient with higher pressure at the caudal end of the spinal canal – with some *in vivo* and supporting *in vitro* evidence suggesting that unidirectional pressure driven flow from site of secretion to sites of reabsorption may not be even possible (Klarica et al., 2013).

Instead, fluid mixing and CSF crossing compartments is hypothesised to occur through a pulse pressure mechanism, where there is a localised, rapid change in pressure resulting in a narrow region of travelling pressure difference through the CSF (shockwave) (Greitz et al., 1991; Preuss et al., 2013). CSF has been commonly shown to have pulsatile flow with a pulse wave the amplitude of which is termed CSF pulse pressure, and which is influenced by heartbeat and how it impacts cerebral vasculature (Mascalchi et al., 1988). ICP has been shown to be pulsatile in rhythm with a peak in systole and a valley in diastole which is synchronous with the heart rate, this corroborates the clinical evidence linking CSF motion in the ventricular system to arterial pulsations (Linninger et al., 2005). The pulse wave theory describes the following cycle of events that drive CSF flow across compartments (Preuss et al., 2013):

1. Blood enters vessels around and within the parenchyma. Or in general vasculature expands at systole, with more potential to distend/higher compliance in veins (compliance of veins is 10-20 higher than that of arteries).
2. The larger blood vessels in the cranium around the cortex (grey matter), the subarachnoid space and skull restrict outward expansion – most of the blood volume in the outward blood vessels have a net inward push on the parenchyma towards the ventricles; ISF is simultaneously pushed towards the ventricles. *
3. A shockwave of pressure pushes on the ventricles and CSF flows towards the cisterna magna and later the pulse wave allows for the arrival of CSF into the supratentorial subarachnoid space.

* The process of expansion of the parenchyma causes a push of the CSF in the supratentorial subarachnoid space into the dural sinuses; once the arteries start diastole, the shockwave from the ventricles pushes new CSF into the subarachnoid space around the brain.

Pulsatile CSF flow is very different than the laminar flow model in the cerebral aqueduct. Some work speculates that pulsatile CSF flow might be involved in communicating hydrocephalus and iNPH pathologies (Balédent et al., 2004; Eide et al., 2006), by generating forces and pressure gradients that cause brain tissue deformation of the ventricular walls due to active distention. However, there is contradictory evidence for this, observations are published showing pressure changes across the cerebral aqueduct and the cranio-spinal axis, although maybe present, are not sufficient to cause ventriculomegaly (Eide et al., 2010; Holmlund et al., 2019).

Pulsatile CSF flow that changes with heart rate is well evidenced (Linniger et al., 2005; Wahlin et al., 2012). Therefore, it is important to understand the physics of blood flow into the cranium when examining ICP pathologies, as it appears to be the one known source of dynamic pressure changes. The measure of cerebral perfusion pressure (CPP) and mean arterial pressure (MAP), in relation to intracranial pressure, is a measure of the relationship between ICP and blood flow. CPP (mm Hg) is a net pressure gradient across the vascular wall of cranial vessels that drives oxygen transfer to cerebral tissue, and it is represented by the difference between MAP and ICP ($CPP = MAP - ICP$) (Gauer OH, 1960; Mount and Das 2022). Range of normal CPP is variable due to the variability of MAP homeostasis across individuals (Mount and Das 2022). Normal CPP is 60-80 mmHg and normal ICP is 5-10 mm Hg. If intracranial pressure increases (i.e., an increase in pathological volume) then CPP decreases, and diastolic pressure is not enough to sustain a healthy gradient across vascular walls (Mount and Das 2022). This relationship is modified by changes in blood flow. Cerebral blood flow (CBF) has an inverted relationship to blood pressure, maintaining a steady CPP in health but potentially exacerbating pathology (Mount and Das 2022). In addition, there is a pressure gradient across arachnoid granulations, that allows for reabsorption through the AV structures into dural sinuses. The mean sagittal sinus pressure in normal conditions is 90 mm H₂O and remains constant over a wide range of artificially elevated CSF OPs (Pollay 2010). The pressure difference across the AV ranges between 3-5 mm Hg (Pollay 2010). Mathematical models have suggested that the amplitudes of CSF flow (phase contrast MRI), the amplitude of ICP and MAP, and the degree of cerebrovascular dilation are all positively related (Czosnyka et al., 2018). It is of the essence to examine the cerebrovascular compartment when investigating for possible mechanisms of pathology in intracranial hypertension associated disease.

There are still many fundamental questions of the physics of intracranial pressure and CSF flow that are unanswered. Study of many of these questions has resulted in contradictory answers e.g., such as whether a hydrostatic pressure gradient exists across the CNS. This increases the difficulty of drawing conclusions about pathological mechanisms. For example, there has been a failure to produce evidence of a cranio-spinal pressure gradient - meaning the possibility of unidirectional CSF flow, according to Poiseuille's principles, is assumed not present unless/until proven otherwise. Therefore, the logical conclusion with the available evidence is to assume the cranium is a closed system with an equalised hydrostatic pressure, with flow and pressure described with consideration of Pascal's principles. The CSF compartment is a closed system with incompressible fluid in it but there is the cerebral

vasculature that surrounds the brain and is embedded in it. The cranial vasculature is another closed system of flow but, in contrast to the CSF, with a pump, which in terms of its physics can be considered a piston. Therefore, if we assume that the CSF system is incompressible and it is in contact with the vascular system, which expands and contracts, within the closed volume of the cranium the force generated by the expansion and contraction of the vasculature will propagate into the CSF system. This may generate a push, pull like CSF displacement, with volumes of CSF moving caudally or rostrally depending on whether vessels in the brain are expanding or contracting. It is important to know whether brain tissue is incompressible and if the forces of pressure from the vascular compartment will increase its density or only displace volume. If density of the tissue does increase, then we would have an increase in the hydrostatic pressure the tissue exerts on the container i.e., the skull. Classically, the brain is accepted to be incompressible and to behave as a fluid when forces of deformation are applied (Klarica et al., 2013), but recent reports claim the brain contains sufficient soft compressible material to be compressible (Hosseini-Farid et al., 2019). Brain density has been previously assessed using computer tomography (CT) and is defined by CT Hounsfield Units (CTHU). Using this method, patients with extra-axial haematoma with brain deformation, overall density was seen to increase (Nguyen et al., 2016). However, in a different pathology (blunt head trauma) there was no increase in brain density associated with high ICP and low CPP (Inaba et al., 2007). Thus, while there is some emerging evidence that suggest the brain maybe compressible it is currently not possible to draw a firm conclusion and further research is required.

1.2 Intracranial pressure in HIV positive-associated cryptococcal meningitis

1.2.1 Epidemiology, treatments, and determinants of mortality

In 2020, it was estimated there were 179 000 cases of cryptococcal antigenemia (presence of cryptococcal antigen CrAg in the blood) among HIV-positive people with CD4 counts of less than 200 cells/ μ L (stage 3 or 4/advanced HIV which is the demographic with highest risk for developing CM) (Rajansingham et al., 2022; WHO July 2017;). It was estimated that there were 152 000 cases of cryptococcal meningitis, resulting in 112 000 cryptococcal-related deaths, almost half of which are in eastern and southern Africa (Rajansingham et al., 2022). Globally, it is estimated that cryptococcal disease accounts for 19% of AIDS-related mortality (Rajansingham et al., 2022). These latest estimates are an improvement on the 2014 estimates of 181 100 cryptococcal meningitis deaths (Rajansingham et al., 2017). The mortality from cryptococcal meningitis has decreased likely due to the improved availability or antiretroviral

therapy (ART) and emphasis on preventative screening (WHO Guidelines 2017). Unfortunately, even after significant effort to improve strategies for managing global disease burden, cryptococcal meningitis mortality rates remain high (~70%) (Rajansingham et al., 2022). Furthermore, the results of the 2020 study should take into consideration the COVID-19 pandemic and how it affected diagnostic capabilities of clinical facilities across the globe, which may have resulted in underestimation of CM global disease burden (Rajansingham et al., 2022).

In 2020, when the most recent epidemiological data on CM burden was acquired, the WHO recommended short-course induction therapy of 1 week of amphotericin B deoxycholate (DAmB) administration (World Health Organisation [WHO], 2022). There is evidence showing amphotericin B deoxycholate has associated toxicity, such as anaemia, kidney impairment, and electrolyte abnormalities (Bicanic et al., 2015). Since then, results from an open-label, phase 3, randomized, controlled, noninferiority trial (the AMBITION trial) show that induction therapy with liposomal amphotericin B (LAmB) instead, reduces drug-related toxicity and produces noninferior results in mortality, fungal clearance, and disease adverse effects (Jarvis et al., 2022). Currently, there is a low availability of the substantially more expensive effective liposomal antifungal agents in developing countries (World Health Organisation [WHO], 2022). It is likely we see improvement in administration and decrease in mortality rates if liposomal antifungals become more accessible in resource limited settings. Results from the AMBITION trial show a non-inferiority to the conventional treatment schedule of 14 days of DAmB and flucytosine, with LAmB induction therapy resulting in 25% as opposed to 30% mortality from DAmB at 10 weeks (Day *et al.*, 2013; Beardsley *et al.*, 2016; Molloy *et al.*, 2018). Away from controlled clinical settings, in Eastern and Southern Africa, where the prevalence of cryptococcal meningitis is the highest globally and the clinical settings are resource limited, mortality rates from CM are more than 80% (Rajansingham et al., 2022). The lower mortality in Sub-Saharan Africa clinical trials, may have to do with the improved patient monitoring of disease progression and OP, access to pharmaceuticals and preliminary diagnosis of HIV in order to avoid ART induced IRIS (see section 1.2.4). Currently large efforts in managing the clinical burden of CM are invested in incorporating the settings that are seen to be effective in clinical trials, which would significantly reduce mortality, nonetheless even with the better efforts of disease management in clinical trials, evidence shows that there is still a risk of death in 25% of cases (Jarvis et al., 2022). In Western central Europe and North America, where there is generally access to better care for patients with CM,

mortality rates from cryptococcosis were still high in 2020, ~50% (Rajansingham et al., 2022). This suggests that there is still need for improving understanding of the disease in order to find the gaps in treatment as current disease management and treatment is not sufficient to prevent fatal outcomes.

Antifungals have variable degrees of penetration into the CNS tissue and CSF and complex pharmacokinetics (Groll et al., 2000; Ashley 2019). Lower-mortality and adverse effects associated liposomal amphotericin B (LAmB) has been shown to successfully penetrate the into the brain tissue, particularly in higher fungal infection where there are parenchymal lesions present, but in much lower concentrations than what is administered in the plasma (Groll et al., 2000; Petraitis et al., 2019; Moore et al., 2019). Flucytosine on the other hand has very high penetration into the CSF, therefore, it may compensate for the lower availability of LAmB, although some more recent investigations may be necessary to confirm how effective flucytosine is in targeting the brain alongside LAmB (Polak 1979; Block and Bennett 1972). To summarise, although the exact pharmacokinetics may need further examination, it has been seen that antifungals do cross the BBB and reach CNS parenchyma and CSF. Therefore, there are available effective antifungals that reach the CNS but mortality from CM is still high.

It is important to attempt to identify the potential gaps in our understanding of what the best disease management would be. Antifungals are not the only part of the treatment course for cryptococcal meningitis, a large body of evidence has shown that therapeutic lumbar punctures (LPs) improve survival (Kagimu et al., 2022; Lawrence et al., 2019; Perfect et al., 2010). LPs were introduced as a management of the pathologically elevated ICP/IH (>200mm H₂O) seen in ~50-70% of cryptococcal meningitis patients (Graybill *et al.*, 2000; Jarvis *et al.*, 2014; Kagimu et al., 2022;). A number of studies support the concept that increased intracranial pressure above 200mm H₂O increases chances of mortality from CM and of acute and chronic cognitive impairment (Graybill et al., 2000; Perfect et al., 2010; Brizendine, Baddley and Pappas 2013; Kagimu et al., 2022). Managing the intracranial pressure aspect of the CM pathology with LPs is effective at improving survival (Papas et al., 2005; Dammert et al., 2008; de Vedia et al., 2013; Wijewardana et al., 2011). Therapeutic LPs are only recommended in the case of initial registration of > 200 mm H₂O OP or if symptoms of IH are present (WHO guidelines 2022). However, therapeutic LPs are associated with 69% relative improvement in survival, regardless of initial intracranial pressure (Rolfes et al., 2014) and data from Adjunctive Sertraline for the Treatment of HIV-Associated Cryptococcal Meningitis (ASTRO-

CM) suggests that therapeutic LPs are improving 30-day mortality by 50% in a cohort with no symptoms of IH and < 200 mmH₂O OP (Kagimu et al., 2022). One obvious mechanism of how LPs may help alleviate symptoms, in accordance with the Monroe-Kellie hypothesis, is the removal of pathological excess volume from the cranium and alleviating pressure. However, it is unclear how LPs are helping patients with normal pressure and no symptoms of IH.

One hypothesis about how LPs may alleviate the CM condition would be if fungal burden was correlated with increase in mortality or cognitive impairment. Initial colony forming units (cfu) measurement is a good predictor of mortality at 2 weeks but less predictive at 10 weeks (Bicanic et al., 2009). CSF cryptococcal antigen is seen as a factor associated with high risk of death within 1 year of diagnosis (Wang et al. 2022), it also appears no presence of cryptococcal antigen CrAg in the CSF is correlated with decreased the risk of death. A slow rate of clearance of infection was independently associated with increased mortality at 2 and 10 weeks (Bicanic et al., 2009). Higher blood fungal burden (cryptococemia) is also a predictor of mortality (Brizendine, Baddley and Pappas 2013). Overall, it is possible that the removal of a certain amount of infected CSF from the spine through LPs can alleviate pathology by reducing fungal burden in the CNS, but this has not been measured. As CSF is secreted through filtration of blood, if LPs are coupled with antifungal therapy, which acts to alleviate cryptococcaemia, the reduction of fungal burden would be even more potent. Also, high fungal burden appears necessary but not sufficient for the development of IH (Bicanic et al., 2009). Ventriculoperitoneal (VPS) shunts are an alternative to daily LPs for patients that have severe presentation of IH, VPS are recommended if 1) refractory elevated ICP >35 cmH₂O, (2) the effect of LPs is limited, or (3) severe clinical manifestations, such as damage to cranial nerve function (Wen et al., 2022). Unfortunately, there is evidence that long-term outcomes do not differ from more conservative treatment strategies and can be post-surgical complications (Wen et al., 2022).

It seems that therapeutic LPs could be used in a preventative way to improve survival. Access to therapeutic LPs however is limited in developing countries with high prevalence of the disease. Thus, a more accessible and less invasive alternative to LPs would create a great positive impact on reducing mortality from CM. To find such an alternative we need to investigate how exactly LPs alleviate disease causing mechanisms. To identify such an alternative, it would be beneficial to improve our knowledge of cryptococcal meningitis pathophysiology, as there are still significant gaps in our understanding of IH causing

pathogenic mechanisms, host-pathogen interactions in the CNS, and pharmacology of available antifungals.

1.2.2 Pathophysiology of cryptococcal meningitis

Cryptococcal meningitis is a subacute (between acute and chronic) meningoencephalitis, meaning it is an infection of the meninges and the brain parenchyma (Williamson et al., 2017). Pathology is thought to most commonly develop by the acquisition of a *Cryptococcus* spp. cell through inhalation, followed by dissemination into different organ systems through the vasculature. It is known that cryptococcal infection can disseminate to almost all organ systems, but the pathology of CNS is the most often cause of mortality and morbidity (Williamson et al., 2017). Theories as to why the brain is more susceptible to develop pathology have to do with trapping of the organism due to the higher level of control in vascular entry and exit in/from the CNS (presence of blood and CSF barriers) and environmental factors specific to the brain that favour survival of the pathogen such as high-affinity sugar transporters around vasculature (Coehlo et al., 2014). Once in the CNS, the pathogen seems to trigger mechanisms that cause a pathological increase in intracranial pressure. The following paragraphs explore different hypotheses as to what those mechanisms could be.

Neuroradiological observations in cryptococcal meningitis patients

Neuroradiological abnormalities related to cryptococcal meningitis can include dilated perivascular spaces, dilated periventricular spaces, leptomeningeal enhancement, masses in the parenchyma, hydrocephalus, vascular events, and oedema (Lee et al. 2021). In comparison to CT, MRI imaging is the better tool for detection of cryptococcosis related lesions (Loyse et al. 2015; Charlier et al. 2008; Popovich et al. 1990; Andreula et al. 1993). The most commonly identified neurological marker in CM patients is dilated perivascular spaces (Virchow Robin space - VRS) (36% of patients Loyse et al. 2015; 46% of patients Charlier et al. 2008;). A VRS on a T2-weighted scan is defined to be dilated if it measures 2 to 3mm in diameter (Braffman et al. 1988; Heier et al. 1989). Dilated perivascular spaces are colocalising with pseudocysts and are mostly seen around the regions of the basal ganglia, thalamus, midbrain, and cerebellum (Offiah and Naseet et al., 2016). Dilated VR spaces and periventricular spaces are shown to be the 2 most relevant markers for poor neurological outcomes in CM (Lee et al. 2021). Choroid plexitis is also a feature of CM (Patronas et al., 1993; Offiah et al., 2015). The fenestrated capillaries of the CP may be an easier entry route into the CNS, with the cryptococci

unable to cross the choroidal epithelium and remain in the plexuses. It is possible growth in the CP creates a strain on the choroidal epithelium, compromising its integrity and altering CSF influx. 30% of cardiovascular events in CM have been seen to result in lacunar infarcts (Mishra *et al.*, 2018). It is possible that cryptococcal yeast cells are prone to getting trapped in smaller vasculature and this may alter the blood pressure within the cranial vasculature, which in turn affects CSF turnover, particularly in the glymphatic system.

The arachnoid granulations obstruction hypothesis

The classical obstruction hypothesis proposes that *C. neoformans* infection disrupts the re-absorption and flow of the CSF at the level of the arachnoid granulations, causing retention of CSF and increased ICP. A large number of cryptococcal cells have been found in arachnoid granulations of a small case series of CM patients, alongside with inflammatory cell infiltrates and disruption of normal architecture of granulations (Loyse *et al.*, 2010). Data from these 6 patients showed a possible correlation with the number of fungal cells found in the granulations and CSF pressure (Loyse *et al.*, 2010). Due to the limited number of studies into the mechanism of CM RICP, these preliminary findings have made the obstruction hypothesis largely accepted as the key mechanism of raised intracranial pressure in CM (Williamson *et al.*, 2016). In the classical model of IP, in the presence of arachnoid granulations obstruction, raised intracranial pressure would arise as a result of CSF retention. CSF retention most commonly manifests as a condition known as hydrocephalus, which presents with a radiological marker of abnormally enlarged ventricles (ventriculomegaly). Ventriculomegaly, however is only an occasional complication of fungal meningitis; a large portion of CM patients, although suffering from raised IP, do not present with ventriculomegaly (Tang, 1990; Park, Hospenthal and Bennett, 1999; Liu *et al.*, 2014, 2018; Loyse 2015). This suggests that CSF retention may not be similar to the one occurring in conditions of hydrocephalus. There may not be sufficient obstruction to cause enough a retention, or the retention may be manifested in a different way through dilation of Vichow-Robin spaces.

Increased CSF Viscosity Hypothesis

It is possible that raised intracranial pressure in CM is not only an issue of increase in CSF volume within the cranium, but also an issue of altered CSF properties. In CM patients, there is a high content of cryptococcal colony forming units within the CSF, this could change the properties of the fluid (Jarvis *et al.*, 2013). *C. neoformans* has polysaccharide capsule, which

is named the most important virulence factor in CM and cryptococcosis (Robertson *et al.*, 2014). It has been shown in humans that there is an independent correlation between capsule size and raise in ICP (Robertson *et al.*, 2014). Therefore, when investigating how cryptococcal infection may change the properties of the CSF, both the influence of cryptococcal cells and the polysaccharide capsule need to be considered.

1.2.3 The influence of inflammation on IH in HIV positive associated CM

Cryptococcal infection (cryptococcosis) develops initially as an infection of the lungs, airborne or yeast cells are inhaled and deposited in the lung alveoli (Velagapudi *et al.*, 2009). The initial immune response is thought to be phagocytosis of cryptococci by resident lung macrophages and dendritic cells, which leads to antigen presentation and activation of T helper cells (Rudman, Evans, Johnston 2019). This activation of the adaptive immune response can result in formation of granulomas composing of cryptococcal cells surrounded by macrophages and CD4+ T cells (Hill 1992). In immunocompromised patients the adaptive immune response is insufficient which leads to uncontrolled replication of the pathogen in the lungs and dissemination into other organ systems likely through the vasculature (Stie *et al.*, 2012; Santiago-Tirado *et al.*, 2017). In 15-20% of individuals who survive the initial disease, the administration of antiretroviral therapy (ART) and recovery of adaptive immune response causes a further complication known as immune reconstitution inflammatory syndrome (IRIS). It appears that the innate immune players continue to present antigens despite the absence of an adaptive immune response. Antigen presentation, dead and viable cryptococcal yeast accumulate and once ART mediates recovery of T cell activity there is an inflammatory flair up due to the presence of large amounts of Cryptococcus-associated antigen (Jarvis, Harrison 2018). IRIS causes an influx of inflammatory cells into the CNS, it worsens IH, and it further increases mortality (Jarvis, Bicanic and Loyse 2014). Development of IRIS in CM has been strongly associated with high CNS expression of the chemokines MCP-1(CCL2) and MIP-1 α (CCL3) at initial cryptococcal meningitis presentation and at ART initiation (Jarvis, Harrison 2018). High levels of plasma and CSF CCL2 is seen in other IH pathologies such as idiopathic intracranial hypertension (Dhungana, Sharrack, Woodroffe 2009). The balance between Th1, Th2, and Th17-type cytokines have also been shown to affect disease outcome even before IRIS development (Jarvis *et al.*, 2015).

1.3 *In vivo* models of cryptococcosis or cryptococcal meningitis

For the study of intracranial hypertension, it is necessary to investigate all physical elements of the CNS (vascular, parenchyma, CSF) as they function together and influence each other to sustain intracranial pressure in homeostasis (as discussed in section 1.1). The architectural complexity of the human CNS and the limitations of tools allowing us to observe it *in vivo*, are part of what make the pathophysiology of cryptococcal meningitis such a medical mystery. *In vitro* models have proven useful when assessing some of the simple physical relationships such as changes in fluid properties that influence flow dynamics. However, alone they cannot reliably re-create the complexity of cell and tissue interactions in the CNS. Mimicking that architectural complexity and observing it in a living system are objectives of new approaches to IH pathology investigation.

In vivo invertebrate models such as *Caenorhabditis elegans* and *Drosophila melanogaster* although powerful in their potential for real-time *in vivo* imaging, do not mimic the anatomy and physiology of the human CNS as well as vertebrates. *C. elegans* do not have a blood compartment or anything like a brain cavity (Sinclair and Hamza 2015) and *D. melanogaster* brain is cushioned by a more blood like fluid called haemolymph, the presence of CSF-like compartment has not been identified (Piyankarage, Featherstone and Shippy 2012). Vertebrates have been shown to be more suitable for developing models for studying the impact of a cryptococcal infection on the components of the CNS, due to the similarities in infection progression and CNS anatomy (**See Table 1**).

Important findings from vertebrate models are discussed in the paragraphs below. The systems described were developed with the aims of examining mechanisms of dissemination and/or immune response to the pathogen, both of which are relevant to studying IH in CM as pathogen localisation and tissue disruption can impact the pressure homeostasis of the CNS. Nonetheless, there is a gap in model systems and experimental approaches that specifically target the investigation of IH pathology.

1.3.1 Cryptococcal meningitis research in mammals, gaps in models

Mouse (*Mus musculus*) model of cryptococcosis is the most used animal model. There are multiple infection routes that have been used: intranasal, intratracheal, intravenous, intraperitoneal, intracranial (Rudman *et al.*, 2021). All infection routes have advantages when

studying different aspect of the pathophysiology of cryptococcosis, for example the intracranial is good for rapidly generating CNS pathology. However, the intranasal and intratracheal infection routes (collectively named pulmonary), have the key advantage that the resulting infection follows the assumed progression of infection in humans (Zaragoza *et al.*, 2007, Coelho *et al.*, 2019).

The pulmonary cryptococcosis mouse model is powerful for the study of cryptococcal meningitis because it replicates the progression of the infection from a lung to blood to the CNS (Zaragoza *et al.*, 2007, Coelho *et al.*, 2019). It involves all the tissues and organ systems that are affected in humans, with the same route of infection and the high architectural complexity of a mammalian CNS. The brain ventricular system in mice has the same organisation as humans, like humans they have brain embedded lateral, 3rd and 4th ventricles and a central canal which allows entry of CSF into the SA space or spinal cord (Eichelle *et al.*, 2019). Also, most of our modern understanding of CSF fluid flow in the glymphatic system was initially established and still extensively researched in mice models (Illif *et al.*, 2012, Brinker *et al.*, 2014; Lun *et al.*, 2015; Steffensen *et al.*, 2018; Mestre *et al.*, 2018; Abbott *et al.*, 2018). Mice in general are also well characterised genomically and phenotypically (Waterston *et al.*, 2002) and require less maintenance costs in comparison to other mammalian models (e.g., rat, Guinea pig, primate) which allows for larger scale studies. Also, the mouse immune system consist of innate and adaptive, with all the major immune cell types present in humans, which makes it suitable to study host-pathogen interactions (Haley, 2003). Therefore, at first glance it appears that the pulmonary cryptococcosis mouse model has a lot of advantages when it comes to CM research.

Nonetheless, there are complications when attempting to utilise the mouse model for studying intracranial pressure pathology and host-pathogen interactions in the CNS. The complexity of intracranial pressure pathology in humans is very apparent when aiming to understand how live dynamic changes such as CNS vascular wall dynamics and CSF flow in perivascular spaces, SA and ventricular spaces significantly impact IP. Mice models are quite powerful when observing CSF flow along perivascular spaces in health and infection (Shi *et al.*, 2010; Illiff *et al.*, 2012; Coelho *et al.*, 2019), but observing pathogen interactions with ventricular cilia or changes in ventricular CSF flow during infection is limited by the lack of optical transparency of the system. In particular, real-time observations of cilia driven flow in mice, has been previously done in explant culture (Eichelle *et al.*, 2019), and although important

conclusions can be drawn by this model, it is crucial to address the limitations of it, such as the inability to visualise other drivers of flow in the ventricles with higher resolution than in human imaging (see introduction 1.1.3). Furthermore, host pathogen interaction that impact flow of CSF seize *post-mortem*. Furthermore, cardiac arrest initiates an influx of CSF into the brain, this would skew conclusions of fluid distribution and tissue architecture from *post-mortem* tissue (Mestre *et al.*, 2020; Ma *et al.*, 2019). In humans, the gold standard for live CNS tissue observations is phase contrast MRI imaging, the technique however does not provide high-resolution visualisation across both space and time, not-allowing cell-cell interactions or examination, limiting its potential in our understanding of IP (Eide *et al.*, 2021). This is where *in vivo* imaging in animal models can improve our understanding of ICP dynamics, as it provides a much higher spatiotemporal resolution imaging of CNS tissues (Markicevic *et al.*, 2021).

In mice (and other mammalian models) higher resolution of imaging involves of performing invasive procedures such as craniotomy surgeries creating a cavity in the bone or regions of skull thinning circumventing anatomical disruption (Li *et al.*, 2022; Shih *et al.*, 2012). There are also new emerging techniques that are managing to chemically achieve skull transparency, such as the Through-Intact-Skull (TIS) chronic window technique (Li *et al.*, 2022). Non-invasive techniques which keep the skull intact like ultrasound, doppler and MRI are also viable, but their resolution, as in humans, is very limited and does not allow for observing pathogen interactions with tissues and cells like for example pathogen trapping in the cranial vasculature (Li *et al.*, 2022).

The skull opening skull window technique in particular is very problematic when it comes to IH research. Creating an opening in the skull will inevitably alter the pressure of the cranium, as it will no longer be a closed, fixed volume system, as in craniotomies CSF leaks out of the skull periodically, it is likely the procedure skews CSF fluid dynamics skews measurements of ICP (Cramer *et al.*, 2021; Yang *et al.*, 2009). IH causing pathologies would be partially alleviated by the “skull window” and pathological mechanisms that require study will not be examined. Skull thinning and the TIS techniques are good alternatives to craniotomy procedures specifically because they retain anatomical integrity and the ICP homeostasis. Those techniques have been powerful in studying CSF flow in perivascular spaces above the pial surface (Ilfiff *et al.*, 2013), they have helped establish research into the glymphatic system of CSF flow (see Fig. 1.1 section 2). However, the skull thinning and TIS techniques have a

major limitation as they only allow up to 300µm imaging depth into the tissue, pathologies of arterial pulsations and CSF flow in deeper brain structures remain unobserved.

No mouse model of cryptococcosis has been aimed at examining specifically the pathophysiology of cranial pressure. Instead, the major focus of pathophysiology studies has been studying the dissemination of the pathogen. Some work has been done on the real-time interactions of *C. neoformans* with the vascular compartment of the CNS *in vivo* using the skull window techniques. Intravital imaging of live *C. neoformans* interactions with the cranial vasculature in mice shows cryptococcal masses getting trapped in small vessels and cryptococci disseminating into the parenchyma from the microvasculature (Shi *et al.*, 2010). The pathogen was injected into the blood stream of the tail and was seen to pass through the cranial microvasculature of injected mice, on average, 3.4 seconds post injection (n = 8 mice), and cryptococci were observed to be trapped in the microvasculature at ~25s post injection (Shi *et al.*, 2010). That suggested that once cryptococcal masses disseminate into the blood stream from the lungs it is possible they almost immediately start having an impact on the CNS. Cryptococcal yeast cells are seen to be trapped in locations of vessel narrowing and they are shown to not slow down before trapping, suggesting a mechanical trapping rather than a receptor binding like leukocyte extravasation by rolling adhesion (Shi *et al.*, 2010). Similar sized polystyrene spheres injected in the same way were trapped in microvasculature at a similar time post injection (Shi *et al.*, 2010). Other mouse models have attempted to replicate a dissemination route from the lungs into the CNS (Coelho *et al.*, 2019, Zaragoza *et al.*, 2007, Mukherjee *et al.*, 1993). Living mice with intranasal instillation of *C. neoformans* showed dissemination into brain parenchyma in *postmortem* histology as early 3hrs post infection; the presence of yeast in the blood stream was assessed in early stages of the infection, and no cryptococcal yeast were detected (Coelho *et al.*, 2019). This remarkable finding is currently unexplained but suggests that cryptococcal infection in the brain can establish without systemic fungaemia. Similarly, it appears that in the intravenous infection model, the presence of *C. neoformans* in the circulation diminishes completely within hours post infection (Kauffman-Francis *et al.*, 2018, Shi *et al.*, 2010). *Postmortem* work in mice has shown cryptococcal masses blocking small brain vasculature, disruptions in small vessel wall architecture and formation of cryptococcal cysts around capillaries and venules (Olszewski *et al.*, 2004), supporting the idea that the smaller vasculature is likely to be the entry route of the pathogen. Post-mortem data has also shown that perivascular spaces (PVS) of cortical post-capillary venules is the major site of phagocyte-dependent entry of *C. neoformans* (Kauffman-Francis *et al.*, 2018).

Dilated PVS being the most common neuroradiological feature of patient MRIs, it is possible the pathogen has a targeted effect on these niches (36% of patients Loyse *et al.* 2015; 46% of patients Charlier *et al.* 2008).

In summary, previous work in murine models of cryptococcal meningitis shows that *C. neoformans* blood stream infection results in trapping and blockages of small brain vasculature, similar to patients (see 1.2.2). Pathogen trapping is suggested to be as a result of mechanical interactions with the vascular epithelium rather than receptor mediated ones. The pathogen is seen to disseminate from small vasculature into PVSs and parenchyma but has only been observed in *postmortem*.

Rat (*Rattus rattus*), Rabbit (*Oryctolagus cuniculus*), Guinea pig (*Cavia porcellus*) are the other established mammalian models of cryptococcosis. However, due to the refractory features of their skull tissue they have similar limitations to mouse when it comes to live *in vivo* imaging of the CNS and intracranial pressure studies.

Rats have a more complex husbandry than mice but in comparison they are larger and allow for repeated venous and CSF sampling (Krokenberger *et al.*, 2010). Rats are able to develop CM infection upon inoculation with cryptococcal pathogen and the rat model has been previously developed for the study of cryptococcal meningitis (Goldman *et al.*, 1996) Intratracheal inoculation has been shown to produce granulomatous meningitis with no parenchymal involvement, granulomatous meningitis is more reminiscent of CM in immunocompetent patients as opposed to immunocompromised (Goldman *et al.*, 1996). The inflammatory response of the CNS appeared to be delayed in comparison to other organs with disseminated infection, suggesting that the CNS requires a T cell peripheral activation to control the infection, something that would be impaired in immunocompromised individuals (Goldman *et al.*, 1996). Pleocytosis and inflammatory profile can impact permeability, integrity and fluid flow through tissues and therefore have an influence on intracranial pressure. In immunocompromised patients however, there is not much evidence of significant inflammation in the CNS (in the absence of IRIS) (see 1.2.4. CNS tissue permeability in infection has been assessed in the rat model before and it appears BBB permeability increases significantly in infection (Pai *et al.*, 2008). It is unclear whether that effect is mediated by inflammatory factors which have been shown to be active in the rat model, other factors secreted and/or mediated by the physical presence of cryptococcal yeast.

Rat models of intracranial pressure in CM have been previously developed and used to test the influence of different colony switch variants of *C. neoformans* on ICP measurements, but the model has not been used to study the mechanics of how ICP increases in pathology (Fries *et al.*, 2005). There are rat models that allow for the long-term assessment of ICP in freely moving rats (Eftekhari *et al.*, 2020), this model would be very powerful in assessing the variability of ICP in pathology and should be considered for the study of IH in CM. Overall, the rat model has great potential as powerful tool for the assessment of the impact of *C. neoformans* on ICP values over time but its use has been limited, likely due to its relative complexity and the small cryptococcosis research community.

The guinea pig and rabbit models have a similar advantage as rats over mice, for they allow repeated CSF sampling and therefore more frequent monitoring of IP, but as mentioned above they have a big disadvantage, as all other rodent models, in live *in vivo* observation studies of pressure pathologies in the CNS. Furthermore, the guinea pig and rabbit models require a much more complex and expensive husbandry in comparison to mouse and rat models, which can further prevent accessibility to the model to the cryptococcosis community and slow down progress in research. The guinea pig has been shown to be a useful pharmacokinetics model of antifungal therapeutics, as they can effectively replicate dose dependent protective response that mimics human patient observations (Kirkpatrick *et al.*, 2007), which shows the value of the model for potential pre-clinical research. The rabbit model is similar to humans in that it successfully clears cryptococcal infection when immunocompetent but upon the administration of corticosteroids it becomes susceptible to the pathogen (Perfect, Lang and Durack 2008). This would make the rabbit a strong model for pre-clinical and translational research. For exploratory research into pathophysiology however, from the rodent models the mouse model may be most suitable, due to the larger experimental N numbers that can be acquired and the more advanced animal specific technology in intravital *in vivo* imaging (e.g., chemically induced skull transparency).

Other mammalian models of cryptococcal meningitis developed have been the *Macaca fascicularis* species of non-human primates (Li *et al.*, 2019), but model is not shown to provide higher translatability to humans than murine models and there are greater ethical and financial implications than other models.

In conclusion, mammalian models have provided great insight into the pathophysiology of CM, but when it comes to *in vivo* observations of the dynamics of host-pathogen interactions across the whole CNS, existing models and techniques are limited. Murine models for example do not allow for *in vivo* examination of *C. neoformans* yeast cells flow in the CSF of brain ventricles, which would give us insight in how fungal burden is distributed across all tissues of the CNS. Also, murine models do not allow for observation of deeper brain tissue imbedded vasculature, dynamics of those vessels, particularly in infection, is likely to differ from superficial pial vessels. There is need for improving on the limitations of mammalian CM models to improve our understanding of IH pathophysiology. A strong candidate for a system that can achieve that is the zebrafish larvae infection model.

1.3.2 Cryptococcal meningitis research in zebrafish models

Zebrafish (*Danio rerio*) are a tropical freshwater fish native to South Asia (Choi *et al.*, 2021). In biomedical research, the zebrafish animal model has become an increasingly popular vertebrate alternative to murine models (Choi *et al.*, 2021), as zebrafish have a smaller size, a shorter gestation period and high fecundity. The anatomical components of the zebrafish larvae CNS are also reminiscent of the human physiology and functional in early development. Unlike other high throughput models, such as the roundworm and fruit fly, zebrafish have a brain with complex architecture (telencephalon, mesencephalon, hindbrain, spinal cord) and with interconnected ventricular cavities full of CSF, blood vessels with barriers (BBB, BCFB) and imbedded into the parenchyma, cilia directed CSF fluid flow (van Leeuwen *et al.*, 2018; Fame *et al.*, 2016) (See Table 1).

The advantages of the zebrafish model, specifically when it comes to cryptococcal meningitis research, are most apparent in the embryonic phase of the animal's development. Zebrafish larvae also lack adaptive immune system which mimics reduced numbers of CD4⁺ T cells in immunodeficiency, however, the larvae's innate immunity still shares a highly conserved framework with mammals (Tobin *et al.*, 2012). Zebrafish larvae naturally lack much pigmentation, generated transgenic strains have taken this further by increasing optical transparency of the whole animal and there are methods of even further reducing pigmentation chemically (Antinucci and Hindges 2016). This makes intravital imaging of the CNS, specifically of ventricular CSF flow, significantly simpler than in murine models, not requiring any invasive or extensive procedures. What is more, the optical transparency and the size of

the larvae, coupled with recent advancements in high-resolution microscopy, allow for visualisation of the CNS across its whole depth (Kunst *et al.*, 2019). Infection progression can also be visualised over many days from a single animal, something that is not possible in mammalian models (Gibson *et al.*, 2022). The zebrafish larvae model has already been proven powerful for the study of CSF flow in the ventricles, particularly when it comes to the contribution of motile cilia (Olstad *et al.*, 2019; Thouvenin *et al.*, 2020). What is more, the zebrafish larvae model allows for imaging pathogen invasion into the CNS, through the whole brain, with high-resolution in time and space (Tenor *et al.*, 2015). Transgenic zebrafish lines have been developed to fluorescently tag vasculature, blood and/or neuronal tissue, which allows for live *in vivo* visualisation of the dynamics of the components of the CNS (Kunst *et al.*, 2019; van Leeuwen *et al.*, 2018; Weijts *et al.*, 2018). The blood brain barrier (BBB) and blood CSF barrier (BCSFB) presence, development and function in zebrafish larvae have been studied and reporter lines are generated that allow for high-resolution observation (van Leeuwen *et al.*, 2018; Xie *et al.*, 2010).

The zebrafish larvae model has also been previously developed as a system for study host-pathogen interactions in cryptococcosis (Tenor *et al.*, 2015; Davis *et al.*, 2016; Bojarczuk *et al.*, 2016; Evans *et al.*, 2019; Singulani *et al.*, 2021; Gibson *et al.*, 2022). Particularly in the Johnston lab the model has been used in examining immune cell interactions with the pathogen and dissemination mechanisms involving the blood vasculature (Gibson *et al.*, 2022; Evans *et al.*, 2019; Bojarczuk *et al.*, 2016). In the following paragraphs I will summarise research that has developed and utilised the zebrafish larvae system for the study of cryptococcal infection.

In my literature search, I managed to identify two zebrafish model manuscripts that examined host-pathogen interactions and mechanics of *C. neoformans* invasion specifically in the CNS (Tenor *et al.*, 2015; Nielson and Davis *et al.*, 2023). Other papers looked the pathogen interacting with the immune system and other tissue in the periphery as opposed to the CNS (Nielson and Davis *et al.*, 2016; Bojarczuk *et al.*, 2016; Evans *et al.*, 2019; Singulani *et al.*, 2021; Gibson *et al.*, 2022). The work of Tenor *et al.*, proposes zebrafish larvae as a good model for studying pathogen invasion from blood to CNS, and it shows that there is early recruitment of macrophages that phagocyte infecting yeast and provide initial protection (Tenor *et al.*, 2015). The model involved introducing the infection into the bloodstream (caudal vein) at 2dpf, with varying cfu across experiments, but always less than 50 cfu/fish. They showed that the pathogen can replicate *in vivo* and establish a persistent infection even with macrophage

control. When assessing pathogen invasion into the CNS from the vasculature, they show that percentage of larvae with CNS invasion increases with higher infection burden (cfu not specified) at 4dpi (Tenor *et al.*, 2015). Local vascular infection burden positively correlated with CNS tissue invasion, and interestingly, brain-resident yeast cells were often observed outside macrophages and not eliciting macrophage recruitment (unlike yeast cells in peripheral tissues). Potential dissemination events were observed but the data presented were representative images only (Tenor *et al.*, 2015). A more recent paper that continued this work is Davis *et al.*, 2023, where the zebrafish larvae were again used to study *C. neoformans* invasion into the CNS from the cranial vasculature. The focus of the work was to examine the details of BBB crossing and the events immediately before and after. What they found is that microglia either actively transfer cryptococcal cells across the BBB or engulf a significant portion of yeast cells immediately after it crosses the BBB (Nielson and Davis *et al.*, 2023). Microglia seemed to be capable of clearing infection from the CNS before adaptive immunity develops and they sustained endothelial vascular wall integrity by preventing other dissemination mechanisms apart from phagocyte transfer (Nielson and Davis *et al.*, 2023). Previously, phagocyte transfer has only been reported to happen through macrophages, not microglia subtypes (Charlier *et al.*, 2009; Sorrel *et al.*, 2016; Santiago *et al.*, 2017). It has also been previously reported in zebrafish larvae, that ERK5 mediated enhancement of vomocytosis leads to lowering of secondary fungaemia/dissemination from systemic vasculature, which supports the idea of a prevalent Trojan Horse like dissemination mechanism (Gilbert *et al.*, 2017).

Other zebrafish models of cryptococcosis aim to examine how of immune cells control infection, particularly phagocytes such as macrophages and neutrophils. The zebrafish model of cryptococcosis developed in the Johnston lab had the aim of studying cryptococcal and macrophage cell interactions during infection *in vivo* (Bojarczuk *et al.*, 2016). The work examines the importance of macrophages in early fungemia, data showed that the majority of yeast cells are intracellular 24hpi and that larger capsule size limits control of phagocytes over infection (Bojarczuk *et al.*, 2016). The report was limited to observing macrophage-yeast interactions, overall infection burden and survival. Further work in zebrafish aimed to examine the differences between yeast and spore forms of *C. neoformans* and the respective immune response, with focus on neutrophils as well as macrophages (Nielson and Davis *et al.*, 2016). Larvae were injected intravenously or in the hindbrain, with 150-250 cfu of H99 strain *C. neoformans* at 2dpf, which was the dose used in previous zebrafish models of cryptococcosis

and which aimed to mimic dose to mass ratios that have previously been used in mice (ratio of ~4). They defined two phases of infection progression – primary and secondary fungemia, with primary being the initial inoculation and secondary being the appearance of previously intracellular (in macrophages) pathogen cells (Nielson and Davis *et al.*, 2016). The observations of host-pathogen interactions, for both spore and yeast inoculation, occurred primarily during secondary fungemia, lodging was observed of newly extracellular yeast cells into the brain vasculature and invasion of the brain tissue from infected vessels (Nielson and Davis *et al.*, 2016). In secondary fungemia, particularly in trunk vessels, a tendency for intravascular replication was identified (Davis *et al.*, 2016). Both neutrophils and macrophages were implicated in clearance of infection, macrophages were seen to be important in primary re-uptake, but neutrophils played an important role in pathogen killing in secondary fungemia (Nielson and Davis *et al.*, 2016).

As discussed above, initial reports utilising the zebrafish larvae model to study cryptococcosis had a focus on the immune cell interactions with the pathogen *in vivo*. Some other important relationships as well were seen in Tenor *et al.*, 2015, in which it was discussed how high or low fungemia impacts dissemination into the CNS. In Nielson and Davis *et al.*, 2016 pathogen trapping, and intravascular replication was observed in cranial vessels. Shifting the focus towards more physiological or system wide observations, the work Gibson *et al.* 2022, aimed to examine the impact of *C. neoformans* on the vascular physiology of the zebrafish larvae (Gibson *et al.*, 2022). This is highly relevant work when it comes to understanding the mechanisms of intracranial hypertension in CM, as the cranial vasculature plays an important role in CSF homeostasis (volumes and flow). The study showed that in a zebrafish infection model cryptococcal cells tend to get trapped in small blood vessels and form cryptococcal masses that damage the vessel walls to then disseminate into surrounding tissues (Gibson *et al.*, 2022). Observations of the infection development were focused on pathogen trapping and replication within intersegmental vessels. What was seen is that single or a very small number of cryptococcal yeast cells get trapped in a blood vessel to later develop microcolonies in that vessel (Gibson *et al.*, 2022). Dissemination of the pathogen can be accompanied by vessel rupture, but this is not a requirement suggesting, as other studies have shown, that dissemination can occur by transcytosis or intracellularly. All vessels had an increased diameter compared to uninfected fish suggesting an increase in peripheral resistance (Gibson *et al.*, 2022). Using the FRET reporter, the zebrafish transgenic line *TgBAC(ve-cad:ve-cadTS)^{uq11bh}* (hereafter VE-cadherin-TS) showed that intra-molecular tension at cell-cell

junctions between vascular endothelial cells is increased (Gibson *et al.*, 2022). It appears that there is an increased tension in the vessels during cryptococcal infection, in vessels with and without cryptococcal cells (Gibson *et al.*, 2022). There seemed to be overall global vasodilation and increase in peripheral resistance in. Experiments with 4.2 μm inert beads (similar size as the average cryptococcal yeast cell) in the zebrafish larvae however, showed no trapping in smaller vasculature but a slight increase in vascular width (Gibson *et al.*, 2022). Overall, the work showed that the occurrence of vessel occlusions is common in the zebrafish larvae model, mimicking data from patients which commonly reports infarction events (Mishra *et al.*, 2018). The proposed form of dissemination of *C. neoformans* was through vessel rupture and it was also suggested that occlusions increase peripheral resistance which may cause the reported vessel elasticity reduction (Gibson *et al.*, 2022). While this study has potential for the understanding of the mechanisms of IH in CM the majority of data points were taken from the peripheral vasculature.

As discussed, the zebrafish larvae model is powerful system for the study of cryptococcosis and other pathogens (Rosowski *et al.*, 2018), nevertheless the model has certain limitations, specifically when it comes to attempting to examine how the CNS pathology develops. Although research on CSF flow in zebrafish larvae is advancing, there is a lack of understanding on how CSF is secreted and reabsorbed and if the machinery involved is similar to mammals (van Leeuwen *et al.*, 2018; Fame *et al.*, 2016). In larvae there is a conservation of structures and genes of the BBB and BCSFB as seen in mammals (in some greater conservation in comparison to mouse models e.g., claudin 5), but whether they are involved in reabsorption and secretion has not been shown (Li *et al.*, 2022; Olstad *et al.*, 2019; van Leeuwen *et al.*, 2018; Fame *et al.*, 2016). Also, the zebrafish larval model vasculature is still in development, so there may be properties of the vessel wall that are different than mature vasculature, such as smooth muscle development where very few smooth muscle cells can be detected in the caudal vein even at 20dpf (Parker *et al.*, 2013). Fish blood pressure control in generally is less critical than in terrestrial animals due to lower gravitational influences in aqueous habitats (Parker *et al.*, 2013). Nonetheless, the translational potential of the zebrafish animal model for cardiovascular and blood flow investigation research is still quite powerful, research shows that zebrafish larvae vasculature has a very similar response to that of other mammalian models when tested model compounds which act as modulators on beta-adrenergic and renin–angiotensin systems (Margiotto-Casaluci *et al.*, 2019).

Table 1. 1 Components of CSF system – comparison across humans and animal models

	Human	Mouse	Zebrafish larvae
<i>Secretion apparatus</i>	Choroid plexus (Boroun and Boulpaep 2017)	Choroid plexus 80% (Eichele <i>et al.</i> , 2020) Extra choroidal across BBB (~20%) (Bothwell <i>et al.</i> , 2019)	Unknown Conserved choroid plexus like structures: <i>claudin5a</i> positive ependymal cells, localising with brain vasculature and protruding cilia into the ventricles (van Leeuwen <i>et al.</i> , 2018)
<i>Chambers</i>	2 Lateral Ventricles, Intraventricular Foramen, Third, Fourth Ventricles, Cisterna Magna, Central canal of the spinal cord, Subarachnoid space, Dural Sinuses (Boroun and Boulpaep 2017)	2 Lateral Ventricles, Intraventricular Foramen, Third, Fourth Ventricles, Cisterna Magna, Central canal of the spinal cord, Subarachnoid space, (Eichele <i>et al.</i> , 2020)	3 chambers – Telencephalic, Diencephalic/Mesencephalic, Rhombencephalic Central canal of the spinal cord
<i>Drivers of flow (CSF pulsatile flow and villi directed flow)</i>	Pulsatile CSF flow, directed by heartbeat (Preuss <i>et al.</i> , 2013). Ependymal cells protruding cilia into the ventricles and directing flow (Boroun and Boulpaep 2017)	Pulsatile CSF around arteries in the perivascular space (Mestre <i>et al.</i> , 2018) Ependymal cells protruding cilia into the ventricles and directing flow (Eichele <i>et al.</i> , 2020)	Pulsatile CSF flow, directed by heartbeat (Olstad <i>et al.</i> , 2019). Ependymal cells protruding cilia into the ventricles and directing flow (van Leeuwen <i>et al.</i> , 2018; Olstad <i>et al.</i> , 2019)
<i>Re-absorption apparatus</i>	Arachnoid granulations (Pollay <i>et al.</i> , 2010)	Arachnoid granulations (Eichele <i>et al.</i> , 2020) Veins and lymphatic vessels in the brain (Mestre <i>et al.</i> , 2020 and Sweeney <i>et al.</i> , 2019)	Unknown Putative arachnoid cells present 21dpf, functionality not characterised (Banerjee <i>et al.</i> , 2022)

1.3.3 Gap in existing animal models of cryptococcal meningitis

Here I highlight the most important strengths and weaknesses of the current experimental animal models in comparison to the gaps in knowledge regarding the human pathophysiology of cryptococcal meningitis. This will then form the basis of the experimental plans for the thesis. The pathophysiology of cryptococcal meningitis is difficult to understand in patients often because at the point of diagnosis (symptom presentation) and by the time any investigation can be done, the disease has progressed to severe stages. It is important to understand pathology progression and attempt to identify disease mechanisms that can be prevented before severe irreversible cognitive impairment ensues. The power of the zebrafish model is in that it allows for long term, high-resolution, *in vivo* observation of pathology progression from initial infection to more severe stages across the whole organism. In mammalian models there are restraints in spatial and temporal resolution of observation, we can mostly observe superficial parts of the CNS disease and we cannot do prolonged investigatory time-lapses. Although the architecture of the zebrafish larvae CNS is not as similar to humans as mouse or rabbit models, the simplicity of the system may actually prove useful in unravelling the complexity of the mammalian pathology.

Work utilising experimental *in vivo* mammalian models to study CNS cryptococcosis has demonstrated:

1. *C. neoformans* blood stream infection results in trapping and blockages of small brain vasculature.
2. Pathogen trapping is suggested to be as a result of mechanical interactions with the vascular epithelium rather than receptor mediated ones.
3. The pathogen is seen to disseminate from small vasculature into PVSs and parenchyma but only *post-mortem*.

Limitations of experimental mammalian models:

1. Do not allow for the observation of CSF flow in brain ventricles *in vivo*, particularly cilia mediated flow.
2. Low resolution for observation of host pathogen interactions in vascular structures of the CNS *in vivo*.
3. *In vivo* observation limited to observation of more superficial structures of the dorsal cranium.

4. Higher cost and high severity limits of regulated craniotomy procedures necessary for *in vivo* observation of host-pathogen interactions.
5. Small number of experimental repetitions performed when it comes to exploratory observations, dissemination events only captured *post-mortem*.

Work utilising experimental *in vivo* zebrafish models to study CNS cryptococcosis has demonstrated:

1. Pathogen trapping in all of the vasculature (the same size as mammalian small brain vasculature).
2. Vessel rupture not necessary for dissemination but can occur.
3. Vessel wall disruption through increase in trapped cryptococcal mass either due to accumulative trapping OR pathogen replication.
4. VE-cadherin expression is reduced the vascular endothelium in vessels with cryptococcal masses i.e., vascular wall integrity is disrupted likely due to increase in peripheral resistance.

Limitations of zebrafish models:

1. Lack of understanding on how CSF is secreted and reabsorbed.
2. Zebrafish larval model vasculature is still in development, so there may be properties of the vessel wall that are different than mature vasculature.

Gaps in knowledge that this thesis proposes to investigate with the development of new experimental *in vivo* animal models in zebrafish:

1. The longitudinal progression of CNS infection once established.
2. More robust investigation of impact of infection on cranial vasculature
 - a. Existing studies before my work was complete has only contain one or two data points showing dissemination from the cranial vasculature (Tenor et al., 2015; Gibson et al., 2022).
 - b. A recent publication (after my work was completed) (Nielson and Davis et.al, 2023) discusses dissemination from cranial vessels in a lot of detail. Data assessing vessel integrity assessment can be expanded on
3. No dynamic data collected (image capture from a single time point as opposed to time lapse data) from infected cranial vasculature.
4. No investigation of CSF flow in ventricles in infection.

1.4 Thesis aims and objectives.

In my PhD work I aimed to develop a new *in vivo* animal model and utilise it to address the question of how *C. neoformans* can cause mechanical impact on the CNS resulting in IH. As demonstrated above, a suitable *in vivo* animal model that would allow me to examine the interactions of the *C. neoformans* pathogen within and around capillary sized vessels imbedded within the brain parenchyma, and within the CSF of the brain ventricles. Fluorescent transgenic zebrafish lines are a state-of-the-art model for high resolution *in vivo* visualisation of small cranial vasculature, brain parenchyma and CSF flow (Gibson *et al.*, 2017; van Leeuwen *et al.*, 2018; Hamilton *et al.*, 2020; Lowery *et al.*, 2005; Fame *et al.*, 2016; Olstad *et al.*, 2019). Due to their transparency, zebrafish allow for non-invasive visualisation of CNS pathology development in real-time. The zebrafish infection system is also well established for experimentally examining host pathogen interactions in cryptococcosis (Tenor *et al.*, 2015; Davis *et al.*, 2016; Bojarczuk *et al.*, 2016; Evans *et al.*, 2019; Singulani *et al.*, 2021; Gibson *et al.*, 2022). Therefore, I chose the zebrafish larvae system for my *in vivo* host-pathogen interactions model. In addition, to measure changes to the biophysical properties of aqueous fluids contain cryptococci I tested the use of *in vitro* rheological measurements.

Thus, with my *in vitro* and *in vivo* models, I aimed to investigate how the CSF and cranial vasculature systems develop pathology in *C. neoformans* infection, in order to identify potential mechanisms that would contribute to raised intracranial pressure, reflective of the human condition.

To achieve my aims, I generated the following objectives:

1. Generate a zebrafish model of cryptococcal meningitis in which we can observe impact of infection in all main tissues of the CNS.
 - a. CSF
 - b. Vasculature
 - c. Parenchyma
2. Measure the location of the pathogen non-invasively in the CNS during infection progression.
3. Assess how pathogen location could contribute to a IH pathology.
4. Identify dissemination of pathogen into the CNS to assess if they precede and aid disruption of CNS tissue homeostasis.

5. Measure changes in vascular wall dynamics during cryptococcal infection of the CNS
 - a. Examine if there is a change overall vascular volume of the cranial vascular bed.
 - b. Examine if there is a change in permeability of cranial vasculature.
6. Develop a negative control experimental model.
 - a. Test if the effects of the infection are purely mechanical by injecting beads with the same procedure as pathogen was introduced into the blood stream of the zebrafish larvae.
7. To measure the changes in fluid properties in the presence of *C. neoformans* and its capsule
8. To develop the zebrafish infection model for the study of the impact of the *C. neoformans* pathogen on CSF fluid flow in the brain ventricles

There is cross-over between my objectives and the results presented in my three results chapters. However, broadly, Objectives 1-4 are addressed in Chapter 3, Objectives 4-6 in Chapter 4, and Objectives 7-8 in Chapter 5.

The aims and objectives of this thesis are to do with setting up new experimental designs and pilot studies. Group sizes for pilot studies were aimed at N of 30 as the effect size could not be determined prior to conducting initial experiments. N of 30 as a starting sample number for feasibility studies has been previously advised as a good practice (Lancaster, Dodd, and Williamson 2004). Where an N of 30 was not reached or the data presented was to do with experimental design set up (for e.g., injection, imaging, and quantification approaches), the necessary increase in sample numbers is discussed in the corresponding results and discussion sections.

Chapter 2: Materials and Methods

N.B. For detailed step by step methods for zebrafish infection with Cryptococcus and other procedures see my published methodology paper in Appendix 1.

2.1 Zebrafish Husbandry

The following zebrafish lines were used in this thesis:

- a) *Nacre (nac^{v2})* – lack melanophores throughout development but have increased numbers of iridophores; normal retinal pigment (Lister *et al.*, 1999)
- b) *Tg(kdrl:mCherry)^{S916}* - *mCherry* marker of endothelial vascular cells; (Krueger *et al.*, 2011)
- c) *Tg(kdrl:mCherry)^{is5};TgBAC(cldn5a:EGFP)^{vam2}* - GFP *claudin5a* tight junction protein marker expressed in ciliated ependymal cells in the choroid plexus vasculature; *mCherry* marker of endothelial vascular cells. (van Leeuwen *et al.*, 2018)
- d) *Tg(mpeg:mCherry-CAAX)^{sh378}* - *mCherry* reporter of macrophages and macroglia. Origin - Johnston lab (Bojarczuk *et al.*, 2016)

2.1.1 Ethics statement

All work on zebrafish was carried out according to legislation and guidelines set by UK law in the Animals (Scientific Procedures) Act 1986 under the Project Licenses P1A4A7A5E or PP7684817. Ethical approval was granted by the University of Sheffield Local Ethical Review Panel.

2.1.2 Maintenance and breeding

Adult zebrafish were maintained by University of Sheffield aquarium staff at 28°C with 14h/10h light/dark cycle within home office approved aquariums at the University of Sheffield.

Embryos and larvae for experiments were obtained by marble breeding trap (“marbling”) or pair-wise mating. Zebrafish are dawn spawners; therefore, breeding is initiated following the change from light to dark in their light cycle. To collect fertilised eggs breeding traps (meshed bottomed containers containing marbles that simulate shallower pebbled areas of open water) are introduced into aquarium tanks. Alternatively, e.g., for specific strain crosses or for precisely timed mating, male and female pairs were removed and placed into small tanks (with

slotted bottoms that allow the passage of fertilised eggs) overnight containing dividers to separate them. Pairs were divided or marble breeding traps were gently introduced into zebrafish tanks after 3pm the day prior to breeding. Breeding was initiated by light at 8am in our aquaria and, in pair mating, plastic dividers were removed. Fertilised eggs were collected before 10am by pouring the contents of a breeding trap through a tea strainer and washing them in aquarium water into 90mm petri dishes (typically reused which reduces the adhesion of the plates to embryos and larvae). Under a stereo dissecting microscope, unfertilised eggs and overage embryos were discarded (occasionally some breeding can occur the evening before the planned breeding). Fertilised eggs, embryos and larvae were maintained in E3 (NaCl 0.5mM, KCl 17 μ M, CaCl₂ 33 μ M, MgSO₄ 33 μ M) with 0.000025% methylene blue (an anti-microbial agent which reduces the loss of embryos to environmental microbes) at 28°C in an incubator with a 14-10-hour light and dark cycle. All zebrafish embryos used were at the same development stage to avoid reduce experimental variability. Throughout all zebrafish experimental procedures, the health of zebrafish was observed and any embryos or larvae with developmental defects were removed. No more than 80 embryos were kept in a single petri dish to ensure normal development and reduce the possibility of opportunistic infection.

2.1.3 Anaesthesia

Tricaine/MS222 was used as an anaesthetic before zebrafish experimental work. Larvae were anaesthetised by immersion in 0.168 mg/mL tricaine mixed in E3. Successful anaesthesia was confirmed through observing lack of locomotion. Larvae would be maintained in tricaine in E3 until the end of experimental procedure. Where required, larval recovery was completed through replacing medium with fresh E3 which did not contain tricaine.

2.1.4 Dechoriation

Zebrafish embryos have a chorion layer than impedes microinjection and imaging. Larvae come out of their chorion between 2- and 3-days post fertilisation but prior to this they need to be removed from their chorions manually. Using two pairs of Dumont #5 forceps embryos were held in place and the chorion removed by making a small hole and the tearing the chorion to release the embryo.

2.2 *Cryptococcus* culture

The following *Cryptococcus* strains were used in this thesis:

- a) *Cryptococcus neoformans* var. *grubii* strain KN99 (KN99 wt)
- b) Transgenic KN99 (KN99 GFP) with a cytoplasmic GFP marker (Gibson *et al.* 2017)
- c) Transgenic KN99 (KN99 mCherry) with a cytoplasmic mCherry marker (Gibson *et al.* 2017)

We chose *C. neoformans* var. *grubii* KN99 strain as it is known to exhibit represent human type virulence in animal models (Morrow *et al.*, 2012).

Cryptococcal strains were stored in Microbank™ beads (Pro-Lab Diagnostics) at -80 °C. Strains were initially revived by culture on YPD agar, before streaking on agar they were stored in inoculated axenic cultures. Cultures for inoculation were grown in YPD broth prior to use in experiments (see below). Cryptococci were grown in yeast peptone dextrose (YPD) medium, as either broth or solid agar media. Yeast peptone dextrose (YPD) broth (Sigma-Aldrich Y1375) contained 20 g/L Bacteriological peptone, 20 g/L Glucose (Dextrose), 10 g/L Yeast extract. 50 g of YPD was dissolved in 1 L of distilled water. Broth was sterilised by autoclaving for 15 minutes at 121°C and stored at room temperature. YPD agar plates were made by adding 2% microbiological agar to YPD broth solution (Oxoid, Agar No. 1). YPD agar solution was sterilised by autoclaving for 15 minutes at 121°C, allowed to cool to ~60°C and poured into 100mm Petri dishes.

2.2.1 Agar plate culture of *Cryptococcus*

Frozen cryptococcal strains were revived by placing a single Microbank™ bead on an YPD agar plates, shaking the bead around the plate to spread the organism and incubated at 28°C for 48 h. Revived strains were checked for uniform growth and morphology. If growth was poor or some areas showed differences in colour or morphology the strain was reisolated from frozen stocks. If growth was good, a sweep of colonies was taken with a 10µl inoculation loop onto a second YPD agar. This stock plate was incubated at 28°C for 48hrs, stored at 4°C for up to one month and used to inoculate axenic broth cultures.

2.2.2 Broth culture of *Cryptococcus*

Cryptococci used in infection experiments or in preparation of samples for rheological measurements were grown in YPD broth for 16-24 h (mid-late log phase growth). A sweep of colonies from a stock plate were taken with a 10µl inoculation loop and used to inoculate 2mls of YPD broth in a 10ml vented culture tube. Broth cultures were rotated at an angle of 30

degrees at 25rpm at 28°C. For rheological measurements cultures of different volumes and growth conditions were used, as described in the rheology section below.

For infection experiments, after growth broth cultures were transferred to a microcentrifuge tube and pelleted in a centrifuge at 6,000g for 1 minute. The supernatant was removed, and the pellet resuspended in 1ml sterile PBS. This washing step was repeated twice more. The concentration of the culture was counted using a haemocytometer and diluted or concentrated as required for infection experiments e.g., to inject 1000 cfu per nl a concentration of 1×10^9 per ml is required.

2.2.3 Large volume, long-term culture for rheological measurements

2ml broth cultures were grown as described above for infection experiments. Two 2ml broth cultures were used to inoculate 200ml YPD broth. For still culture: the 200ml YPD broth was divided equally between four 250ml flat bottomed conical glass flasks and incubated at 37°C. For shaking culture: Two 2ml broth cultures were used to inoculate 200ml YPD broth in a 500ml flat bottomed conical glass flasks and incubated in shaking incubator at 70 rpm, 37°C. After culture, number of cryptococci was measured by haemocytometer or by serial dilution and YPD agar CFU count.

2.3 Infection of zebrafish embryos and larvae.

For infection, zebrafish embryos and larvae were anaesthetised in a 0.168 mg/mL Tricaine in E3. Larvae are ready to be manipulated once no evidence of motility (e.g., no startle reflex) is observed. Cryptococci were suspended in sterile 10% Polyvinylpyrrolidone (PVP), 0.5% phenol red in PBS, at the required concentration for infection. PVP is a polymer which prevents needle blockage in cryptococcal injection (Bojarczuk et al., 2016) and phenol red is an inert dye that allows us to see if the inoculum has been successfully injected.

2.3.1 Preparation of glass microinjection needle for injection

Glass microinjection needles are prepared by pulling glass capillaries 1.0 mm OD glass capillaries (World Precision Instruments) using a pipette puller. Pipette pullers all have different heating elements therefore trial and error are needed to find the settings for your puller that produce needles of the required length and thickness. 5-8µl of *C. neoformans* inoculum was loaded into a microneedle using a gel loading tip. Bevelled needle tips on loaded needles

were made by hand under a stereomicroscope using Dumont #5 forceps. A bevelled break is required because of the larger size of cryptococcal cells requiring a larger diameter needle. Without a bevelled point, the needle is not sharp enough to successfully inject into a blood vessel. Loaded and bevelled needles were inserted into the needle holder of the Pneumatic Pico Pump (PV 830P) and secured in a micromanipulator (Sutter Instrument, MM-33).

2.3.2 Calibration of injection volume

Due to the inherent variability in glass microinjection needle pulling and breaking, pump settings had to be calibrated to each needle. This was achieved using a graticule to measure the diameter of the bolus of liquid expelled from the needle into a layer of mineral oil. The timing and pressure settings were adjusted to achieve a droplet of diameter of ~120 microns for a 2nl bolus.

2.3.3 Injection of zebrafish larvae and embryos

Anaesthetised zebrafish for injection were placed on 2% agarose 98% E3 medium 100mm injection Petri dish plate pre-incubated to 28°C (to help maintain zebrafish optimum temperature during injection). Using a Pasteur pipette zebrafish were added to a tilted injection plate, letting them slide from the top down in order to orient their tails in one direction. Excess E3 was removed from zebrafish until they were lying submerged but not floating on the injection plate. In turn each zebrafish to be injected was brought into focus under a stereomicroscope and the micromanipulator adjusted to position the needle just above and to the right of the injection site. Zebrafish were injected by injection into the hindbrain ventricle at either 1- or 2-days post fertilisation (Figure 3.1) or the Duct of Cuvier at 2-days post fertilisation (Bojarczuk et al., 2016). With one swift motion, the needle was inserted into the injection site, the foot pedal depressed twice (to deliver a total of 4nl) and the needle withdrawn. Successful injection was assessed by the location and spread of the phenol red dye in the injection solution. Injected fish were recovered by pipetting 3ml of E3 medium onto a tilted injection plate from top to bottom over the collection plate. The injected larvae were then collected from bottom side of the injection plate and transferred to a fresh 100mm Petri dish containing E3 medium and at 28°C in an incubator with a 14-10-hour light and dark cycle.

2.3.4 Injecting zebrafish larvae with dextran fluorescent dye

Anaesthetised zebrafish larvae were injected as described in section 2.3.3 with 2MDa FITC dextran in the Duct of Cuvier at 2-days post fertilisation. Larvae injected with *C. neoformans* prior, were left to recover from pathogen inoculation for 5hrs before injecting with dextran.

2.3.5 Quantification of colony forming units in injection inoculum

Confirmation of colony forming units (CFU) injected into zebrafish was performed by injecting into a PBS droplet on a YPD agar plate. A YPD agar plate was prewarmed at 28°C. A 20µl drop of sterile PBS was pipetted onto the plate. As for zebrafish injection, the drop was brought into focus under a stereomicroscope and the micromanipulator adjusted to position the needle just above and to the right. With one swift motion, the needle was inserted into the injection site, the foot pedal depressed twice (to deliver a total of 4nl) and the needle withdrawn. Using a disposable sterile plastic spreader, the drop was spread evenly and the YPD agar plate incubated inverted at 28°C. Colony growth was assessed at 24, 48 and 72 hours, and counted when clear but separate colonies were visible. Three replicate plates were made for each injection needle used for zebrafish infections and the mean number was calculated from the replicates.

2.3.6 Quantification of zebrafish fungal burden colony forming units.

The number of zebrafish fungal burden CFU was measure by plating dissociated zebrafish on YPD agar plates. Infected zebrafish were culled with tricaine overdose until heartbeat ceased. Each larva was added to 98.5µl ice cold PBS in a microcentrifuge tube. 1.5ul of Liberase (Roche, 05401020001 – stock 5mg reconstituted in 2ml PBS and aliquoted, stored at -20°C) was added to each tube (1 in 65 dilution of 2.5mg/ml Liberase). Tubes were incubated at 37°C in a dry heat block for 15 minutes. After incubation, samples were pipetted up and down, first with a 1ml tip followed by 200µl tip – using fresh tips for each sample. Tubes were incubated as before for a further 15 minutes followed by repeated pipetting. Process was repeated for 30-60 minutes until zebrafish tissue was dissociated. Liberase activity was quenched by adding 100ul of FBS. A 10, 100 and 1000 dilution was performed with sterile PBS and 20ul of each sample was plated and counted as described in 2.3.4 and fungal burden calculated.

2.3.7 Drug Treatments of zebrafish larvae

Where larvae were treated with nitric oxide synthase inhibitor or a NO donor, either with or without additional pathogen injection, zebrafish were immersed in E3 medium. The drugs were then added to the E3 to the correct dose concentration (see below) at 28°C for the required length of time. Zebrafish were not anaesthetised for drug treatments by immersion.

Compounds used:

1. N(gamma)-nitro-L-arginine methyl ester (L-NAME) – at a working concentration of 0.5mM
 - a. A non-selective inhibitor of nitric oxide (NO) synthase, which has been used experimentally to **induce hypertension** (NLM, 2023).
2. Sodium nitroprusside dihydrate (SNP) – at a working concentration of 0.1mM (Chhabria et al., 2018).
 - a. NO doner, powerful **inducer of hypotension** in animals and human (Page et al., 1955).

2.3.8 Survival analysis

Larvae which had undergone either injection, drug treatment, both, or were non-injected controls were checked every 24hrs for their survival or mortality. Dead fish were removed, and death recorded. All zebrafish larvae used in experiments were under 5.2 days post fertilisation (dpf) at The University of Sheffield, at which point the zebrafish were disposed through a home office approved method. The Log-Rank Mantel-Cox test was used to assess for differences in probability of survival between different populations.

2.4 Microscopy

2.4.1 Mounting for widefield fluorescence microscopy

Zebrafish were mounted in low melting point agarose (LMPA) (Sigma A9414) for live imaging with widefield fluorescence microscopy. 1% w/v LMPA was dissolved in E3 medium containing 0.168 mg/mL Tricaine. Dissolved LMPA solution was kept in a 38°C to slow its setting. Zebrafish embryos and larvae were anaesthetised in a 0.168 mg/mL Tricaine in E3 medium and transferred in this medium individually to a well of glass bottomed 96-well plate. Excess E3 was removed and 100µl of LMPA solution added. A gel loading tip was used to put Zebrafish in the required position for imaging until LMPA solidified.

2.4.2 Mounting for light sheet microscopy

Zebrafish were mounted in a tube of low melting point agarose (LMPA) (Sigma A9414) for live imaging with light sheet microscopy. 2% w/v LMPA solution was prepared as described above. Zebrafish embryos and larvae were anaesthetised in a 0.168 mg/mL Tricaine in E3 medium. A single anaesthetised zebrafish was placed in an empty Petri dish in a drop of medium. Excess E3 was removed and 200µl of 2% LMPA added on top. Zebrafish was drawn up into a glass capillary tube headfirst (Zeiss glass mounting capillaries with a micro plunger volume 20µl, internal diameter 0.8mm). The tube was slowly rotated to ensure the mounting was parallel to capillary tube.

2.4.3 Widefield fluorescence microscopy

A custom-build wide-field microscope, Nikon Ti-E with a CFI Plan Apochromat λ 10X, N.A.0.45 objective lens, CFI Plan Apochromat λ 20X, N.A.0.75 objective lens, Apo LWD 40x N.A. 1.15 WI λ S and using a custom built 500 µm Piezo Z stage (Mad City Labs, Madison, WI, USA) and using Intensilight fluorescent illumination with ET/sputtered series fluorescent filters 49002 and 49008 (Chroma, Bellow Falls, VT, USA). Images were captured using Neo CMOS camera (Andor). NIS-Elements AR 4.11.01, 64-bit (Nikon) was used for image was used for microscope control and image capture. Microscope was in a temperature-controlled chamber (OKOlabs) maintained at 28°C for zebrafish imaging.

2.4.4 Light sheet microscopy

Light sheet microscopy was performed with Zeiss Z1 Light Sheet Microscope with the following laser lines: 405, 445, 488, 514, 561, 638 nm, Plan-Apochromat 20x/1.0 Corr N.A. 1.38 objective and dual PCO Edge Zeiss sCMOS camera. ZEN black software was used for acquisition and initial image processing. Image acquisition chamber was maintained at 28°C. Lasers were set for dual side illumination with online fusion, using LBF 405/488/561 filter set, and beams split with SBS LP 560 or LP 580 mirror. Two tracks and sequential imaging was for dual reporter imaging (e.g. GFP and mCherry). Image acquisition was set at 0.7x zoom, 16-bit image depth, 1920 x 1920px (approximately 0.33 x 0.33 µm) image size and minimum z-stack interval (approximately 0.5µm). Exposure was adjusted automatically by the software. For high-speed imaging illumination was set to single sided and kept to a single track to reduce acquisition time.

2.5 Image analysis

2.5.1 Fungal burden quantification

Analysis of fluorescent pathogens presence in regions of interest was measured using ImageJ/FIJI (Schindelin et al., 2012). A manual threshold was set to remove background and the number of GFP positive pixels counted using the measure command in FIJI to give a GFP-positive pixel area.

2.5.2 Head size measurement

Dorsal deformation of the zebrafish head was quantified by measuring the size of the cranium (excluding the eyes) in 2D, with the larvae mounted laterally. A region of interest was manually drawn around the areas of the brain (excluding the eye) and the size area was measured using the measure command in FIJI. Attempts were made at partially blinding the analysis by removing the fluorescent channels from stacks and analysing the brightfield channel images across groups, to remove awareness of which larvae are infected and which not. However, it was difficult to not be aware of which groups were being analysed as the brightfield image clearly showed presence of infection.

2.5.3 Quantification of vessel size change in time

Vascular area change was recorded in 2D over time. Converting images in the mCherry channel to binary was done automatically using Otsu thresholding in the thresholding tool of FIJI. Prior to thresholding, the background was subtracted using an automated command in the process panel of ImageJ (Process -> Subtract background) (example of background subtracted images shown in Fig. 4.1B and 4.2B). To reduce noise from widefield imaging the de-speckling command in FIJI was used, which was not necessary when analysing light sheet images. Fill Holes tool in ImageJ (Process -> Binary -> Fill Holes) was used to filled gaps in between vessels. Regions of interest were chosen through observation of vascular areas that were clearly illuminated (for e.g., not behind an eye). In infection vessels groups were chosen to either do or do not have events of cryptococcal cells passing through the vasculature.

2.5.4 Quantification of vascular bed volume in 3D

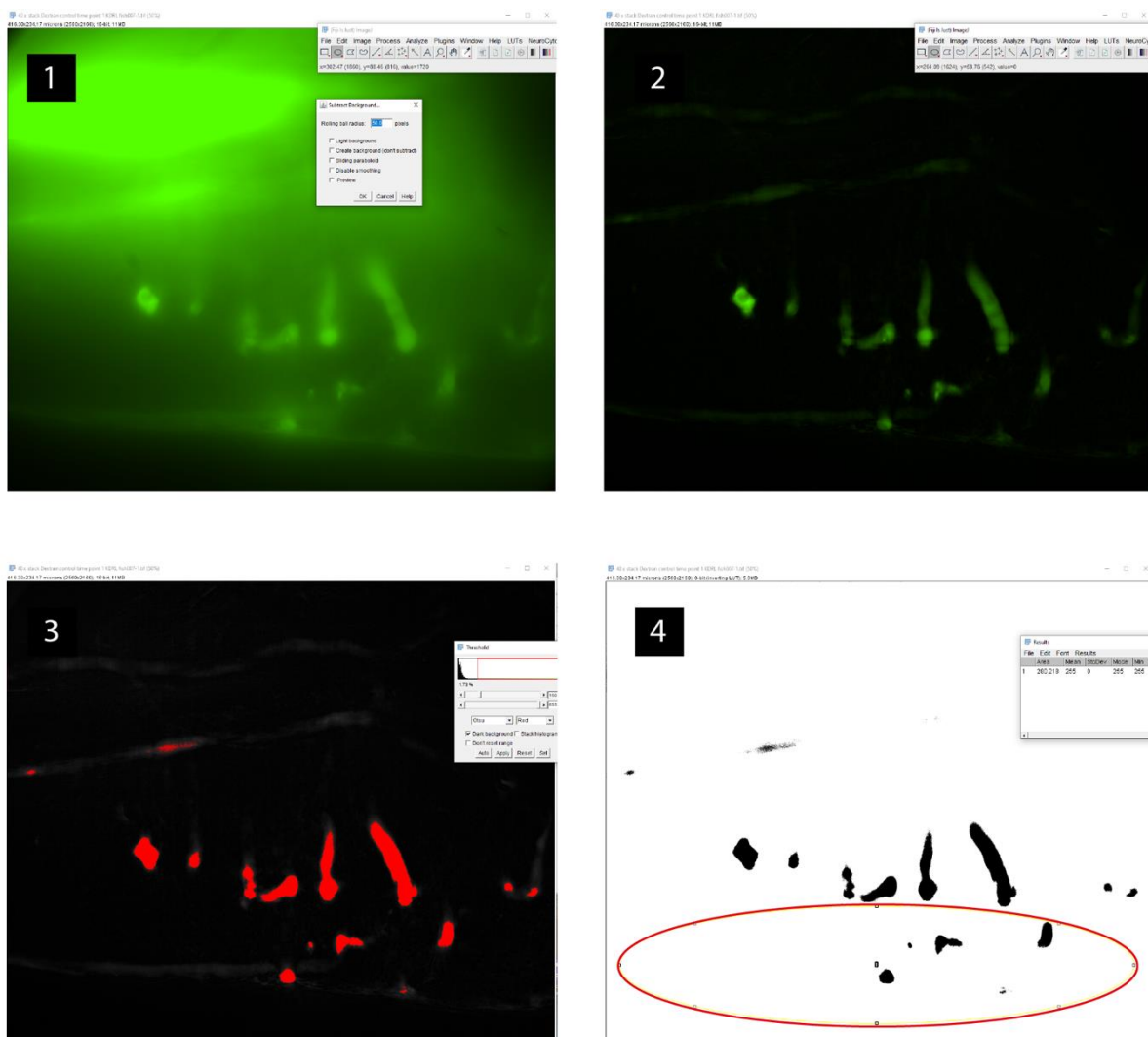
The 3D viewer ImageJ plugin (Schmid *et al.*, 2010) was used to look at the data before and after tubular filtering (Fig. 4.14). Z stacks were globally thresholded using the automated Otsu

thresholding (Otsu 1979) and the volume was calculated using the Segmentation step of the ZVQ tool as seen in Kugler *et al.*, 2022. 3D cranial vascular volume quantification the Z stack data was not enhanced using the Tubeness Plugin.

2.5.6 Dextran fluorescence in brain quantification

Infected and control fish were imaged 2hr post dextran injection and dextran fluorescence in the parenchyma was quantified as shown in Figure 2.1. For dextran experiments, larvae brain was imaged at 40x magnification, the images in Figure 2.1 represent this magnification.

Figure 2. 1 Example analysis process in ImageJ for measuring dextran fluorescence in the brain: analysis of data from figure 4.16



1. Open a single Z panel from a stack* or a single image
2. Subtract background
3. Automatically threshold (Ctrl. + Shift + T; Otsu) -> Convert to Binary
4. Draw a custom ROI around brain above CCtAs -> Measure pixel count (Ctrl. + S)

*Select a Z where CCtAs, brain and ventricles are in focus in 2D

2.6 Rheological measurements

Rheological measurements were made with an Anton Paar MCR502 coaxial cylinder rheometer with a controlled temperature and zero gap set to 10mm. Measurements were taken for 100s with increasing shear rate from 10 to a 100 s⁻¹, at a constant 37°C.

2.7 Purification of *Cryptococcus* polysaccharide capsule

Cryptococcus polysaccharide capsule was purified from culture supernatants by ethanol precipitation. Axenic cultures of *Cryptococcus* were heat killed at 60°C for 2 hours. Yeast cells were pelleted by centrifugation at 6000g, 4°C for 20 minutes. Supernatants were collected carefully, avoiding the cell pellet. Three volumes of ice-cold ethanol were added to culture supernatants and the mixture incubated for 10 minutes on ice. Following incubation on ice precipitated capsule was pelleted by centrifugation at 6000g, 4°C for 20 minutes. Pellets were placed in a level 2 biosafety cabinet to dry. Once dry pellets were weighed and the mass of polysaccharide capsule per volume of culture calculated.

2.8 Statistical analysis

Statistical analysis was completed using GraphPad Prism software (latest version used 9.5.1), tests for homogeneity of variance were performed in SPSS Statistics (version 29) to assess which test to use for true differences between groups (parametric or non-parametric). Graphs representing result from statistical tests and visualising data were done in GraphPad Prism.

2.8.1 Survival analysis

The Log-Rank Mantel-Cox test was used to assess for differences in probability of survival between different populations.

2.8.2 Testing for normality

Data was tested for normal distribution using all tests provided in GraphPad Prism (D'Agostino & Pearson test, Anderson-Darling test, Shapiro-Wilk test, Kolmogorov-Smirnov test). Results from all the tests were assessed for significance and positive vs negative, and the result with majority was accepted to be true. Frequency distributions were plotted to confirm visually the results from the tests.

2.8.3 Analysis of difference between groups, tests used:

2.8.3.1 *Comparison of two groups*

Parametric – unpaired T-test

Non-parametric:

- Mann-Whitney if wanting to compare ranks
- Kolmogorov-Smirnoff if wanting to compare distribution

2.8.3.2 *Comparison of three or more groups*

Parametric – ordinary, one-way, unpaired ANOVA

Non-parametric – unpaired Kruskal-Wallis test

2.8.4 Assessing correlation

Linear regression analysis (line of best fit for data points) was used to test for correlation between measurements of two dependent variables. R^2 (between 0 and 1) value represents the percentage of points which lie on the line, where 1 represents 100% of all points lie on the line.

2.8.5 Power Calculations

Due to time restrictions of the pandemic a lot of the work in this thesis is in the form of a pilot study/preliminary data. Power calculations were done after experiments were complete as no previous data existed to estimate effect size. Calculations of power were done to estimate sample size needed for future experiments in order to achieve 80% power. Power calculations were done in the freely available software G*Power (Faul, Erdfelder, Lang and Buchner, 2007). Descriptive statistics data (mean, standard deviation, 95% CI) were calculated and collected from GraphPad Prism software and input in G*Power to complete sample size calculations. Statistical tests chosen were tests calculating differences between means and more specifically non-parametric t-tests.

Chapter 3: Developing the zebrafish larvae model to study the dispersal of cryptococci in the CNS and the pathophysiology of cryptococcal meningitis.

3.1 Summary

This chapter begins by providing discussion and description of cryptococcal meningitis (CM) as seen in humans, with key features of the pathology are outlined. This provides context for a summary of how animal models have been used to mimic and investigate disease aetiology. I have discussed the strengths and limitations of each animal model. Arguments are presented for the choice to use zebrafish larvae as a disease modelling system.

The main body of the chapter outlines the process in developing new experimental models of cryptococcal meningitis. It discusses how each experimental approach was refined to produce phenotypes of interest and why some models and phenotypes were not considered suitable for further study. The two main experimental models generated are a ventricular infection model and a systemic infection model. Phenotypes arising from the two experimental models were examined for patterns of localisation of *C. neoformans* across the CNS in order to identify possible locations in which the infection may cause pathogenic response that could contribute to pressure increase.

In the ventricular infection model, I did not identify any specific areas of the CNS where cryptococci were localised. However, cryptococci directly introduced into the ventricles could spread to the spinal canal but did not spread to the surrounding brain tissue. This was indicative of an inability by *Cryptococcus* to invade the brain parenchyma. I found that cryptococci could act as a mechanical obstruction in the brain ventricles as dorsal cranial deformation was a common occurrence in ventricular infection. The degree of deformation was linearly related to fungal burden in the ventricles, suggesting increase was due to increase of volume of pathogen. However, the fungal burden in our ventricular infection model is supraphysiological as patients do not exhibit such a high degree of infection burden in the CSF. Therefore, I concluded that further examination of the cranial deformation phenotype may not be suitable for drawing conclusions about the cryptococcal meningitis pathology as seen in humans. In contrast, a systemic infection experimental model demonstrated dissemination into the brain tissue and localisation of the pathogen in cranial vasculature, representative of patient neuroradiological

and post-mortem profiles. Similar to ventricular phenotypes however, there was no obvious pattern of localisation in different stages of infection. As described previously, dissemination events were only captured once and for a single time point in imaging experiments, although dissemination did occur. The systemic infection experimental model appeared to be more representative of the human condition as it allowed for broader distribution of the pathogen, therefore, further observation of the infection development in this model in was used in later chapters.

3.2 Introduction

Summary of gaps in treatments and understanding of human patients CM pathology

More than 50% of HIV positive CM patients have some degree of intracranial hypertension, which is an abnormally increased pressure in the spaces surrounding the brain and the spinal cord (Graybill et al., 2000, Jarvis et al., 2014;). Cryptococcal meningitis treatments prioritise managing fungal burden in the CNS and the arising intracranial hypertension. The latest WHO treatment recommendations for CM antifungals administration are an induction therapy of a single high dose of liposomal amphotericin B (LAmB) with 14 days of 5-flucytosine (WHO Guidelines 2022). Currently, there is a low availability of the substantially more expensive liposomal antifungal agents in developing countries (WHO Guidelines 2022). It is highly likely that there would be an improvement in mortality rates if liposomal antifungals become more accessible in resource limited settings. Currently large efforts in managing the clinical burden of CM are invested in implementing the most effective treatments demonstrated by clinical trials. Nevertheless, even with the better efforts of disease management in clinical trials, evidence shows that there is still a risk of death in 25% of cases (Jarvis et al., 2022). In Western central Europe and North America, where there is generally access to better care for patients with the condition, mortality rates from cryptococcosis were still high in 2020, estimated to be ~50% (Rajansingham et al., 2022). This suggests that maybe access to care and effective antifungal therapy is not sufficient to prevent fatal outcomes, there is still need for improving understanding of the disease in order to fill the gaps in treatment.

When it comes to treatments managing the intracranial hypertension aspect of the pathology, therapeutic lumbar punctures are accepted as the gold standard intervention (WHO Guidelines 2022). WHO guidance suggests an initial lumbar puncture and an early repeat lumbar puncture with measurement of CSF opening pressure to assess for raised intracranial pressure regardless

of the presence of symptoms or signs of raised intracranial pressure (WHO guidelines 2022). Therapeutic LPs are different from initial LP, the former can be as often as daily, and the latter happens only 1-2 times around a week upon diagnosis. Therapeutic LPs are only recommended in the case of initial registration of > 200 mm H₂O OP or if symptoms of IH are present (WHO guidelines 2022). However, recent data from Adjunctive Sertraline for the Treatment of HIV-Associated Cryptococcal Meningitis (ASTRO-CM) suggests that therapeutic LPs are improving 30-day mortality by 50% in a cohort with no symptoms of IH and < 200 mmH₂O OP (Kagimu et al., 2022). It seems that therapeutic LPs could be used in a preventative way to improve survival, access to therapeutic LPs however is limited in developing countries with high prevalence of CM. A more accessible, just as effective, and less invasive alternative to LPs would create a great positive impact on reducing mortality from CM. To find such an alternative we need to investigate how exactly LPs alleviate disease causing mechanisms.

In summary, available antifungal and lumbar puncture therapies are not sufficient or accessible enough to manage the global burden of cryptococcal meningitis. Even with administration of the optimal course of antifungals, there is still significant mortality. Furthermore, LPs, although a very effective treatment with or without IH, are not as accessible as they should be in regions the highest prevalence of disease. It is, therefore, still necessary to work towards more accessible, effective, and specific treatments of cryptococcal meningitis. In my PhD I aimed to improve understanding of the pathophysiology of CM in order to enable the development of such treatments in the future.

The gold standard diagnostic and disease progression monitoring tools are culturing spinal CSF and assessing for the presence and burden of cryptococcal yeast. Higher spinal fungal burden and low rate of clearance are independently associated with increase in mortality at 2-10 weeks post diagnosis (Bicanic et al., 2009). In addition to diagnosis, daily LPs are thought to help alleviate symptoms of IH, potentially due to clearance of cryptococcal cfu from the spinal CSF or reducing the volume of CSF and consequently cranial compression.

The distribution of *C. neoformans* in patient brains tells us that the pathogen is present in all the main components of the CNS, such as parenchyma (white matter lesions), CSF (spinal culture), vasculature (lacunar infarcts), CSF (positive spinal CSF culture) and even dural spaces (leptomeningeal enhancement). There is no specificity to a certain tissue, it appears that the spread is opportunistic and not targeted. However, the information we have on the localisation of *C. neoformans* in infection is mostly from later stages of pathology development, the disease

remains hard to detect in earlier stages. It is unclear if there are niches that favour pathogen survival and act as a source of spread in earlier stages. What is more, how the infection affects each specific tissue is not well characterised.

Our knowledge of localisation of *C. neoformans* in the CNS of cryptococcal meningitis patients comes from post-mortem staining of brain tissue and MRI studies. Post-mortem analysis of parenchymal tissue shows localisation of *C. neoformans* specific to arachnoid granulations (Loyse et al., 2010). Furthermore, common neuroradiological markers for cryptococcal meningitis in patients are:

1. Non-specific white matter lesions often in the form of cryptococcal cysts, more frequently seen in the basal ganglia and brain stem.
2. Dilated perivascular/Virchow-Robin spaces. Presence of this marker is a predictor for poor neurological outcome.
3. Vascular events such as lacunar infarcts
4. Leptomeningeal enhancements

(Lee et al., 2021; Loyse et al. 2015; Charlier et al. 2008; Popovich et al. 1990; Andreula et al. 1993). Post-mortem brain tissue staining, however, involves dehydration and processing of the tissue that may skew information about the presence of cryptococcal yeast cells particularly in fluid filled niches such as the brain ventricles and dural sinuses. Similar limitation is present in MRI studies, it is difficult to assess the components of large fluid filled niches such as the brain ventricles.

When developing an *in vivo* animal model system to mimic the CM pathology as seen in humans, I aimed to generate phenotypes that have a collection of similar CNS dissemination events. Specifically, it is important to see presence of the fungal pathogen in the CSF, brain tissue, and in and around brain parenchyma imbedded vasculature, and to assess how each individual component becomes compromised in disease.

Suitability of the zebrafish animal model for this work (see section 1.3 of Introduction for more detail).

Experimental research in CM aims to shine light on the gaps in our understanding of pathology as seen in humans. Murine models have been a powerful tool for examining immune responses to cryptococcal infection and the model is seen to recapitulate the pathology characteristics in

patients (Mukaremera et al., 2019). However, they do have limitations when it comes to examining CM pathology. They do not allow for:

1. The observation of CSF flow in brain ventricles in vivo, particularly cilia mediated flow.
2. High resolution for observation of host pathogen interactions in vascular structures of the CNS in vivo
3. In vivo observation of deeper cranial structures

Non-mammalian models like *Caenorhabditis elegans* and *Drosophila melanogaster* are highly tractable for live imaging, but they do not provide the opportunity to mimic complex multicellular immune interactions, and critically, anatomical, and physiological aspects of CNS pathology as seen in humans. The zebrafish (*Danio rerio*) is a powerful vertebrate model that has strong parallels with mammalian genetics and anatomy. The simplicity of the system in comparison to murine models makes it easier to focus on individual pathological mechanisms. The zebrafish infection system is now well established for experimentally examining host pathogen interactions in cryptococcosis (Tenor et al., 2015; Davis et al., 2016; Bojarczuk et al., 2016; Evans et al., 2019; Singulani et al., 2021; Gibson et al., 2022). Fluorescent transgenic zebrafish lines are a state-of-the-art model for high resolution in vivo visualisation of small cranial vasculature, brain parenchyma and CNS innate immune cell types (Gibson et al., 2017; van Leeuwen et al., 2018; Hamilton et al., 2020). Due to their transparency, zebrafish allows for non-invasive visualisation of CNS pathology development in real-time. This feature of the model is particularly useful when it comes to observing the pathology in the brain ventricles, something that we have limited visualisation abilities for in other mammalian models and in patients.

To examine how *C. neoformans* infection develops into a CNS pathology we developed two zebrafish larvae models, which differ from one another in the timing of introducing infection, route of inoculation and differences in imaging strategies. In both models the initial aim was to get a phenotype that mimics the disease as seen in humans, primarily by having a distribution of the pathogen across all tissues of the CNS.

3.3 Objectives

9. Generate a zebrafish model of cryptococcal meningitis in which we can observe impact of infection in tissues of the CNS.
 - a. CSF
 - b. Vasculature
 - c. Parenchyma
10. Examine the phenotype of the model in high resolution and measure pathogen localisation.
11. Assess localisation for potential contribution to a pressure pathology.
12. Examine dissemination events of pathogen to assess disruption of CNS tissue homeostasis.

3.4 Localisation of brain ventricles *C. neoformans* KN99 infection and impact on the CNS

There is a particularly large gap in our understanding of the infection phenotype of the brain ventricles in CM. In the beginning of my project, I aimed to assess the phenotype of CSF infection in brain ventricles. My objective was to introduce the pathogen artificially into the brain ventricles and assess pathogen dissemination from the ventricles into the parenchyma, where it localises, and the infection burden introduced into the brain tissue. I aimed to examine if there is observable effect of the infection on brain tissue integrity.

Null Hypothesis: The presence of viable *C. neoformans* culture in the zebrafish larvae brain ventricles does not lead to dissemination into the parenchyma and brain tissue damage.

3.4.1 Injection into the brain ventricle of 2dpf is technically challenging and not suitable for testing the null hypothesis.

Through communication with my supervisor and other members of the lab, I established that previously, when attempting to generate ventricular *C. neoformans* infection, the experimental approach used was as described in Figure 3.1, Experimental set up 1. The zebrafish larval model of cryptococcosis was based on infection at 2dpf because this better recapitulated the innate immune response to cryptococcosis (Bojarczuk et al., 2016). The concentration of the inoculum was chosen based on previous preliminary work in the lab of Simon Johnston that showed promise in visualising CSF flow in infection (Bojarczuk et al. unpublished).

C. neoformans KN99 GFP was the chosen strain to inoculate with as it is a congenic mating pair strain of H99, which in turn was the first strain of *C. neoformans* isolated from a patient and is the most common laboratory strain of the pathogen, therefore, there is a wealth of literature on its biology and behaviour in hosts (Arras *et al.*, 2017). KN99 can reproduce from generating spores, which is a morphological form of the pathogen of interest in host-pathogen interactions and in the Johnston lab, there is a generated library of mutants of interest (eg. a-capsular) that can later be introduced into a developed model system. At the start of my project there was a plan to test patient-derived primary culture strains in the zebrafish model I develop, but unfortunately due to the pandemic that work did not occur.

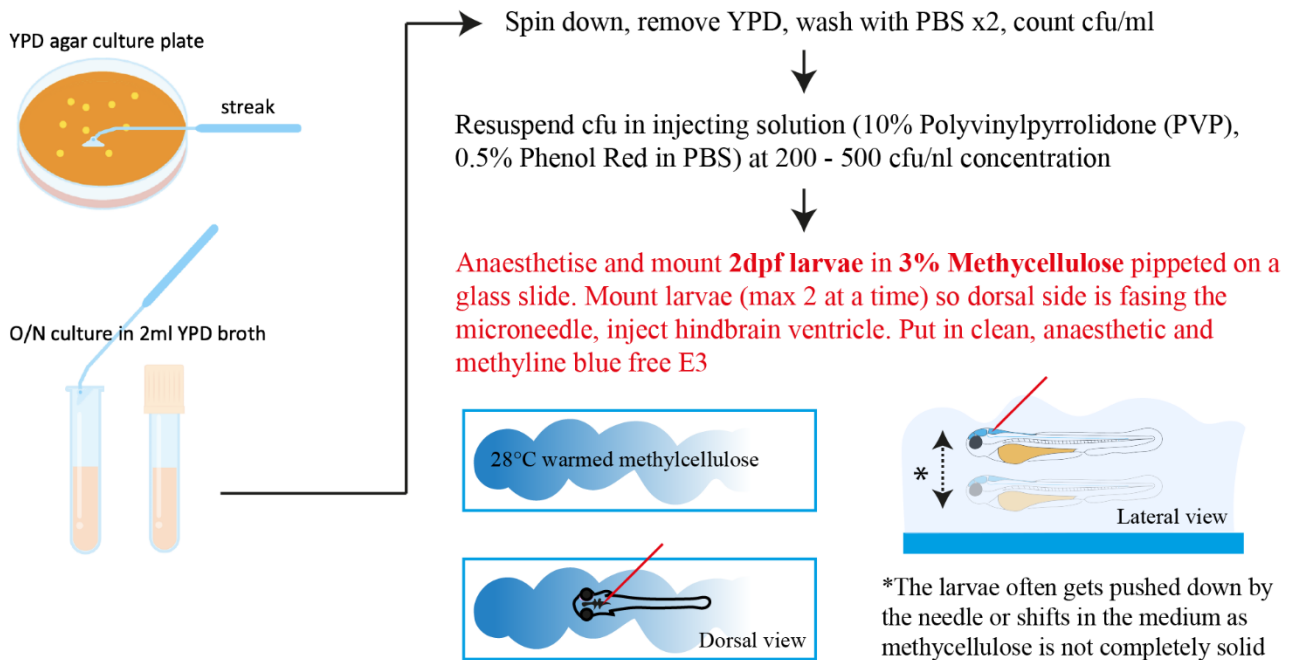
After initial period of protocol testing, I recorded some descriptive data representing the results of the initial experimental set up (Experimental set up 1) (Figure 3.1). Zebrafish larvae were injected at 2dpf, with 200-500cfu/nl of *C. neoformans* KN99 GFP, on a methylcellulose mounting media and with dorsal needle approach. The experimental set up was used in 4 experiments, attempting to inject 30 larvae in each for a total of 120 infections (Figure 3.2). I found that the methylcellulose mounting method was resulting in procedural errors that could be avoided. Larvae were too mobile in the solution which made targeting the desired injection site challenging (Figure 3.1*). It was often unclear if the inoculum was delivered in the ventricle or outside of the cranium, therefore, assumptions of successful inoculation were likely inaccurate as imaging showed a large proportion of larvae (> 50%) lacking any visible infection at 2dpi (Figure 3.2, 1A, E). Some larvae were positive for fluorescence and therefore infection in the brain ventricles (Figure 3.2, 1B), but the numbers were in total below 1/3 of all injected larvae (when discounting mortality of larvae). There was presence of infection in the brain parenchyma (Figure 3.2, 1C, D) but I was not certain that these results were not due to practical error of off-site injection due to methylcellulose mounting and/or the larger size of needle required to inject with cryptococci. Overall, my initial method was technically challenging and yielded a low number of successfully infected fish across all 4 repeats. Low numbers would result in lower power experimental design, therefore, I proceeded to attempt an alteration of the experimental set up and assess if I could improve success rate of inoculation.

Injection of pathogens at 1dpf into the hindbrain ventricle is a well-established procedure in zebrafish studies (Benard *et al.*, 2012) and while injection at 2 dpf is better for studying immune responses to cryptococcal infection it is recognised to be very technically challenging after 1

dpf (Drs Hamilton and Elks, personal communication). Therefore, I proceeded with a second experimental set up (Figure 3.1, 2), where brain ventricle infection was first established at 1dpf. Injecting at 1dpf did not require methylcellulose mounting as the injecting microneedle can approach the ventricles laterally. Larvae were mounted on E3 Agarose plates and injected in the mesencephalic ventricle, which allowed for injection sites further away from the parenchyma than the hindbrain ventricle (Figure 3.1, 2). This approach improved data output (90-100% success in injections), it was significantly more consistent, and all larvae survived the procedure (Figure 3.2, 2C). The survival with experimental method 1 did improve gradually in later repeats (Figure 3.2, 1E) the second approach was better for survival overall as there was almost no mortality (Figure 3.2, 3). In addition, a single trial of 1dpf larvae were injected in methylcellulose media and out of 22 injected, death rate was 36% and alive larvae's tails were all damaged and curved. The effect on the larvae tails is likely because 1dpf larvae are more prone to damage incurred by transfer in and out of methyl cellulose and different containers as they can stick to the plastic of petri dishes and pipettes. Introducing larvae in methylcellulose caused an increase of this tendency and that has been seen in practical work of other colleagues (Drs Noemi Hamilton and Philip Elks). Overall, experimental set up 2 (Figure 3.1, 2) was chosen to generate a brain ventricles infection in zebrafish larvae and to test if the infection affects the brain tissue around the ventricles and how it localises across the CNS.

Figure 3. 1 Experimental approaches tested for zebrafish larvae brain ventricle microinjection.

Experimental set up 1 - Methylcellulose dorsal mount, injecting dorsally in Hindbrain ventricle at 2dpf



Experimental set up 2 - Agar plate lateral mount, injecting in Mesencephalic ventricle at 1dpf

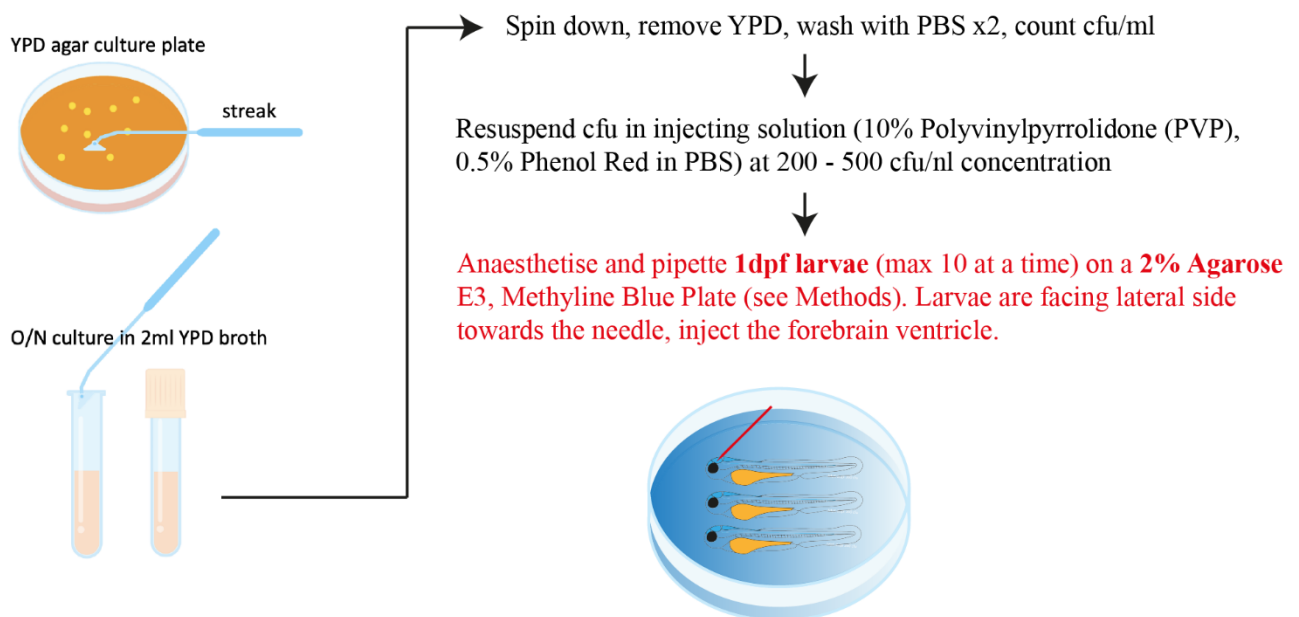


Figure 3.1 Experimental approaches tested for zebrafish larvae brain ventricle microinjection.

Experimental set-up 1 is the initial experimental approach adopted in developing a zebrafish model of cryptococcal meningitis. It involves growing *C. neoformans* KN99 strain in an overnight YPD culture from a streaking plate (see Methods). The inoculum was prepared by washing off the YPD and suspending the cells at 200-500cfu/nl concentration. The larvae were anaesthetised and injected at 2dpf in a methylcellulose mount, in the rhombencephalic/hindbrain ventricle and then returned to clear E3 for recovery from the procedure. After troubleshooting the method and assessing survival and success rate, the procedural approach was altered to be as seen in **Experimental set-up 2**. What was varied was the mounting strategy (agar plate) and the stage of larvae development at which they were injected (1dpf).

Figure 3. 2 In comparison to injection at 1dpf in the mesencephalic ventricle, injection into the hindbrain ventricle of 2dpf is more challenging technically and results in higher mortality.

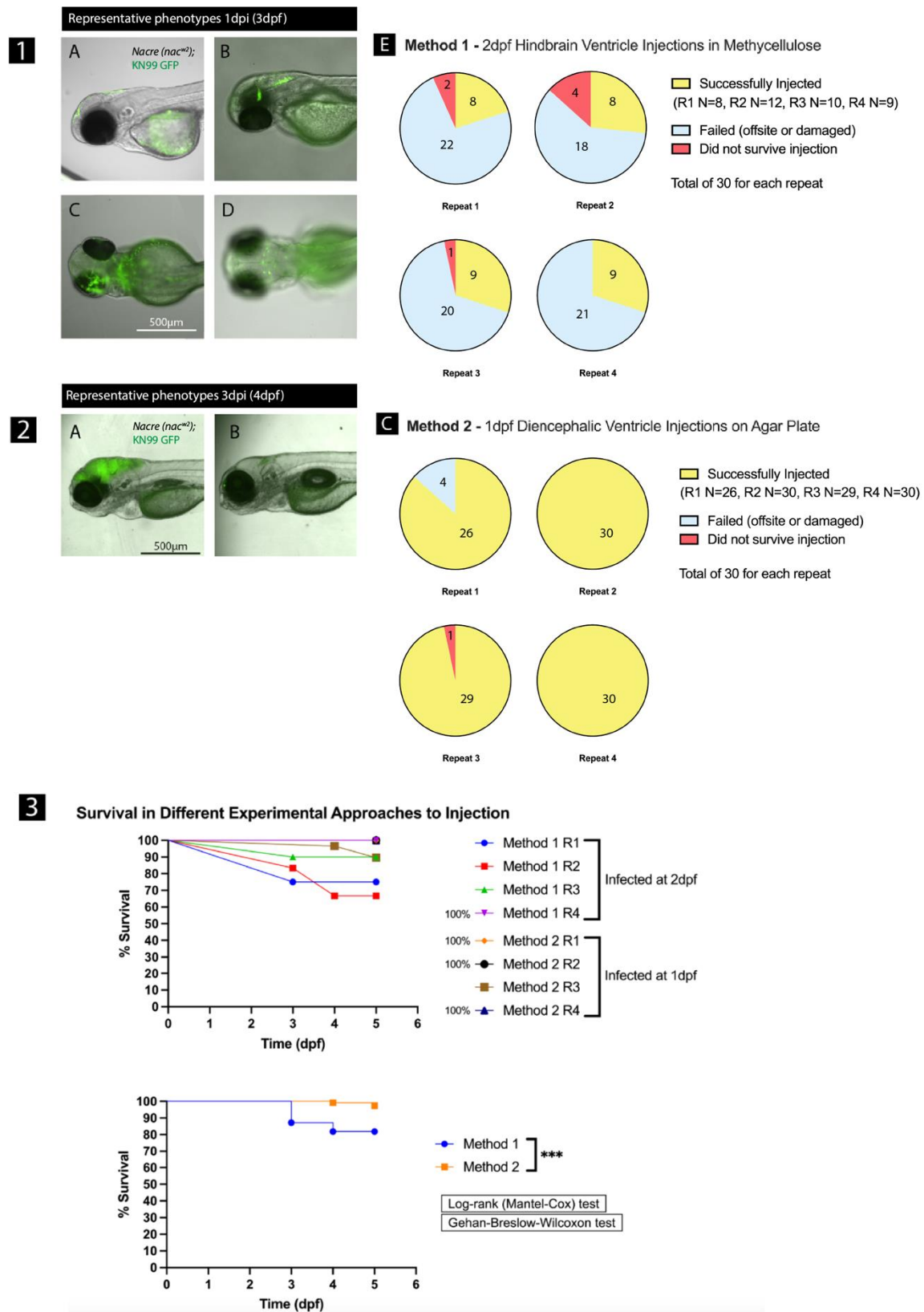


Figure 3.2 In comparison to injection at 1dpf in the mesencephalic ventricle, injection into the hindbrain ventricle of 2dpf is more challenging technically and results in higher mortality.

A methylcellulose mounting method was resulting in procedural errors that could be avoided. Larvae were too mobile in the solution which made targeting the desired injection site challenging. There was a variation of phenotypes. **1A** The majority of attempted injections resulted in no cfu detected in the animal after injection, at imaging. **1B, E** Successful inoculation was achieved in less than 50% of larvae. **1C, D** Nonetheless 4 larvae had infection phenotype that appeared to be as a result of an off-site injection represented in 1C, and successfully infected larvae had very low infection burden detected, contradicting the high cfu concentration (200-500 cfu/ml) of the inoculum (1D). Within the successfully injected groups, there was a degree of mortality at 2dpi that reduced with each experimental repeat (1E). A variation of the experimental method, which included injecting at 1dpf on an E3 agarose plate (Experimental set up/Method 2, see Figure 3.1) produced a much higher success rate in achieving inoculation of the ventricles (90-100%) (**2C**) and the infection appeared much more substantial than in experimental set up/method 1(1B and 2A). Within the successfully injected groups of method 1, there was a degree of mortality at 2dpi that reduced with each experimental repeat, suggesting that mortality may have been as a result of undetected procedural errors while gaining experience with this approach (1E and 3). **3** When comparing survival rate across methods, method 2 showed better chances of survival and the difference was significant ($p = 0.0005$, log-rank Mantel-Cox test and Gehan-Breslow-Wilcoxin test.) Number of animals shown in figure.

3.4.2 Ventricular infection leads to cranial and ventricular deformation but no dissemination to brain tissue.

Zebrafish larvae were injected in the mesencephalic ventricle at 1dpf with 100-200cfu *C. neoformans* KN99 GFP. After 4dpi the infection phenotypes were quantified (Figure 3.3). 62% of infected fish showed a complete colonisation of the cranium with a dorsal cranial deformation (Figure 3.3). Less common phenotypes were infection spread in the ventricular system but with no cranial deformation (14.67%) and complete lack of infection across the whole larva (6%) (Figure 3.3). There was a population of larvae that also showed spread out of the cranium and into the spinal canal, 13.33% out of the total population showed a concentration of the pathogen in the central part of the spinal canal and 4% showed a heavy fungal burden at the caudal end of the spine canal which seemed to spread into the surrounding tissues (Figure 3.3). A Chi-squared test was performed, assessing the hypothesis that population distribution across phenotypes should be even and all phenotypes are equally likely to occur, rejects the null hypothesis ($p < 0.0001$), the observation that the majority of larvae exhibit a cranial deformation phenotype is significant.

At 4dpi it appeared that the growing cryptococcal mass within the ventricles caused enlargement of ventricular spaces, particularly in the lateral arms of the diencephalic ventricle (Figure 3.4, E), and dorsal deformation of the cranium overall (Figure 3.4 A, B). The ventral deformation was measured in 2D from dorsal images and compared to uninjected (control) and mock injected (phenol red). The analysis was partially blinded by only measuring the brightfield channel images of high content data files. The difference in 2D cranial area was significant between infected and control groups (phenol red and no injection = control groups) (Figure 3.4, B). The dorsal deformation measurements when plotted seemed to have a bimodal distribution - symmetric bell curve with two peaks (Figure 3.4, B; Figure 3.5). This means that there are two prevailing cranial sizes within the infected group. Normality tests show that the dorsal deformation measurements population are non-Gaussian with one degree of significance ($\alpha = 0.05$). The histogram of fungal burden just a one tailed distribution but not bimodal-like, it is possible that more than one factor contributes to the deformation of the cranium (Figure 3.5). The most prevalent phenotype of cranial deformation was further assessed in higher magnification imaging in the dorsal orientation (Figure 3.4, C, D, E). Out of 52 larvae imaged dorsally, all of them showed the infection being contained into the brain ventricles with no spread into the parenchyma (Figure 3.4, C, D, E). This accepts the null hypothesis initially set in the beginning of this results section, which is: "The presence of viable *C. neoformans*

culture in the zebrafish larvae brain ventricles does not lead to dissemination into the parenchyma and brain tissue damage”.

Figure 3.3 Phenotypes arising from ventricular injection – cranial deformation in the majority of larvae.

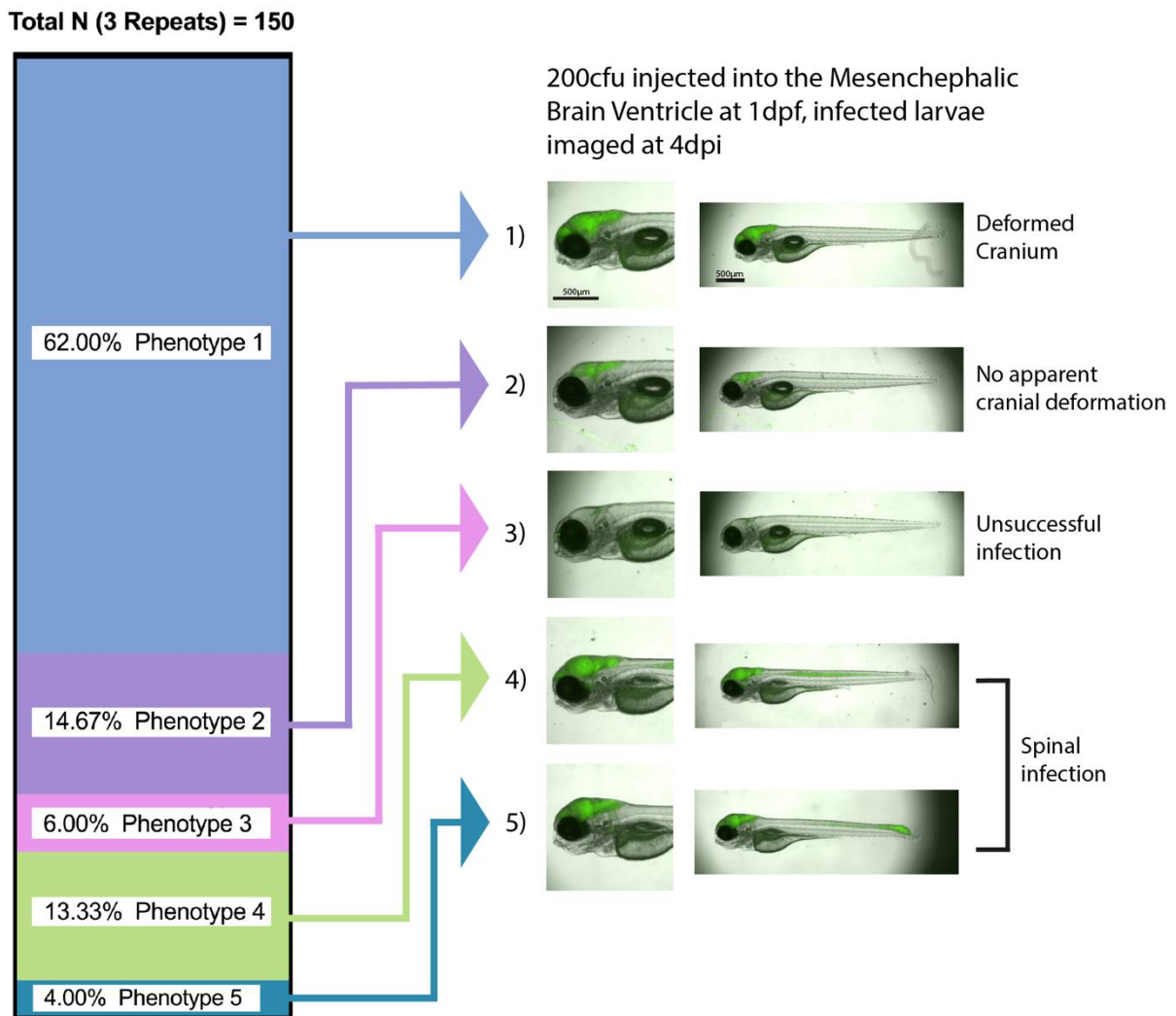


Figure 3.3 Phenotypes arising from ventricular injection – cranial deformation in the majority of larvae.

62% of infection (Experimental approach 2 as seen in Figure 3.1) results in CNS contained infection which appears to cause cranial deformation. Less common phenotypes were infection spread in the ventricular system but with no cranial deformation (14.67%) and complete lack infection across the whole larva (6%). There was a population of larvae that also showed dissemination out the cranium and into the spinal canal, 13.33% out of the total population showed a concentration of the pathogen in the central part of the spinal canal and 4% showed a heavy fungal burden at the caudal end of the spine canal which seemed to spread into the surrounding tissues as well. A Chi-squared test was performed, assessing the hypothesis that all phenotypes are equally likely to occur, rejects the null hypothesis ($p < 0.0001$).

Figure 3. 4 Ventricular infection at 1dpf results in cranial and ventricular deformation. Infection is contained within the ventricular chambers and degree of deformation linearly correlates with fungal burden.

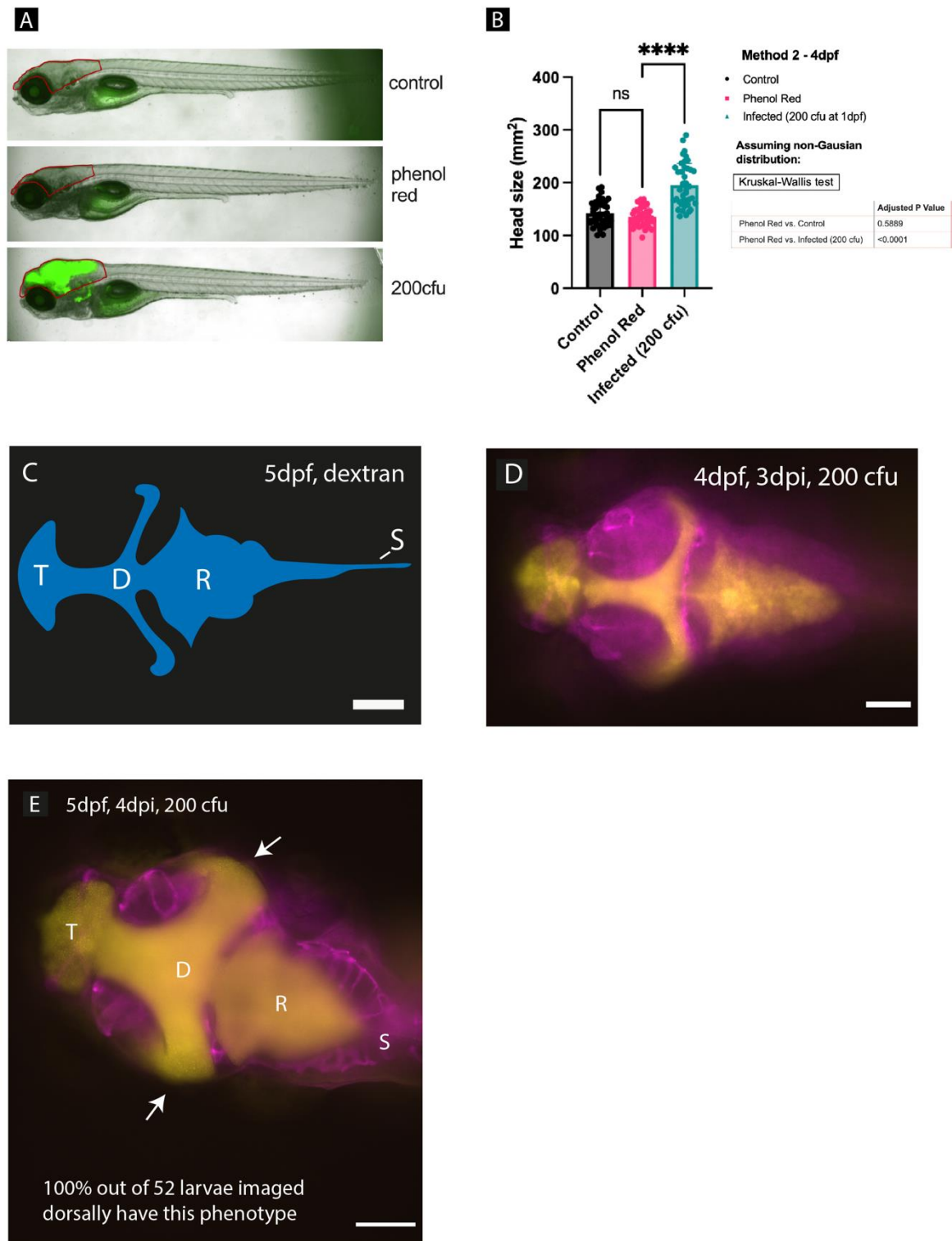


Figure 3.4 Ventricular infection at 1dpf results in cranial and ventricular deformation. Infection is contained within the ventricular chambers and degree of deformation linearly correlates with fungal burden.

A, B Fish were injected 24hpf with phenol red and approximately 200cfu KN99GFP cryptococci (N =30-40 per group) (A); control group was not injected but treated the same way as the other groups (A). Head size was measured in two-dimensions in Fiji software (A, red line indicates head measurement area chosen). **B** Dot plot of head area with mean bar and SD error bars of all three groups. Comparisons were made between control and phenol red and between phenol red and 200cfu injected. Kruskal - Wallis non-parametric test, infected group vs phenol red, $p < 0.0001$. Data in B does not have a normal distribution but what appears to be bimodal distribution (see Figure 3.5) **C** Diagram of healthy zebrafish ventricle area at 5dpf injected with dextran (in blue, Fame *et al.*, 2016) **D,E** Blood vessels (magenta, *Tg(kdrl:mCherry)*^{S916} transgenic zebrafish larvae.) and cryptococci (yellow, KN99GFP **D** Dorsal image of a larva 3 days post infection that was injected at 1dpf with 200cfu injection with *C. neoformans* KN99 GFP in the diencephalic ventricle (3dpi). Ventricular shape is almost the same at 4dpf. **E** Same infection as **D** but 4dpi.

In C-E, T = telencephalic ventricle, D = diencephalic/mesencephalic ventricle, R = rhombencephalic/hindbrain ventricle, S = spine. Scale bar C - 100 μ m, in panel D - 100 μ m, E - 200 μ m.

Figure 3. 5 Frequency distribution of ventricular infection cranial deformation measurements show a bimodal distribution.

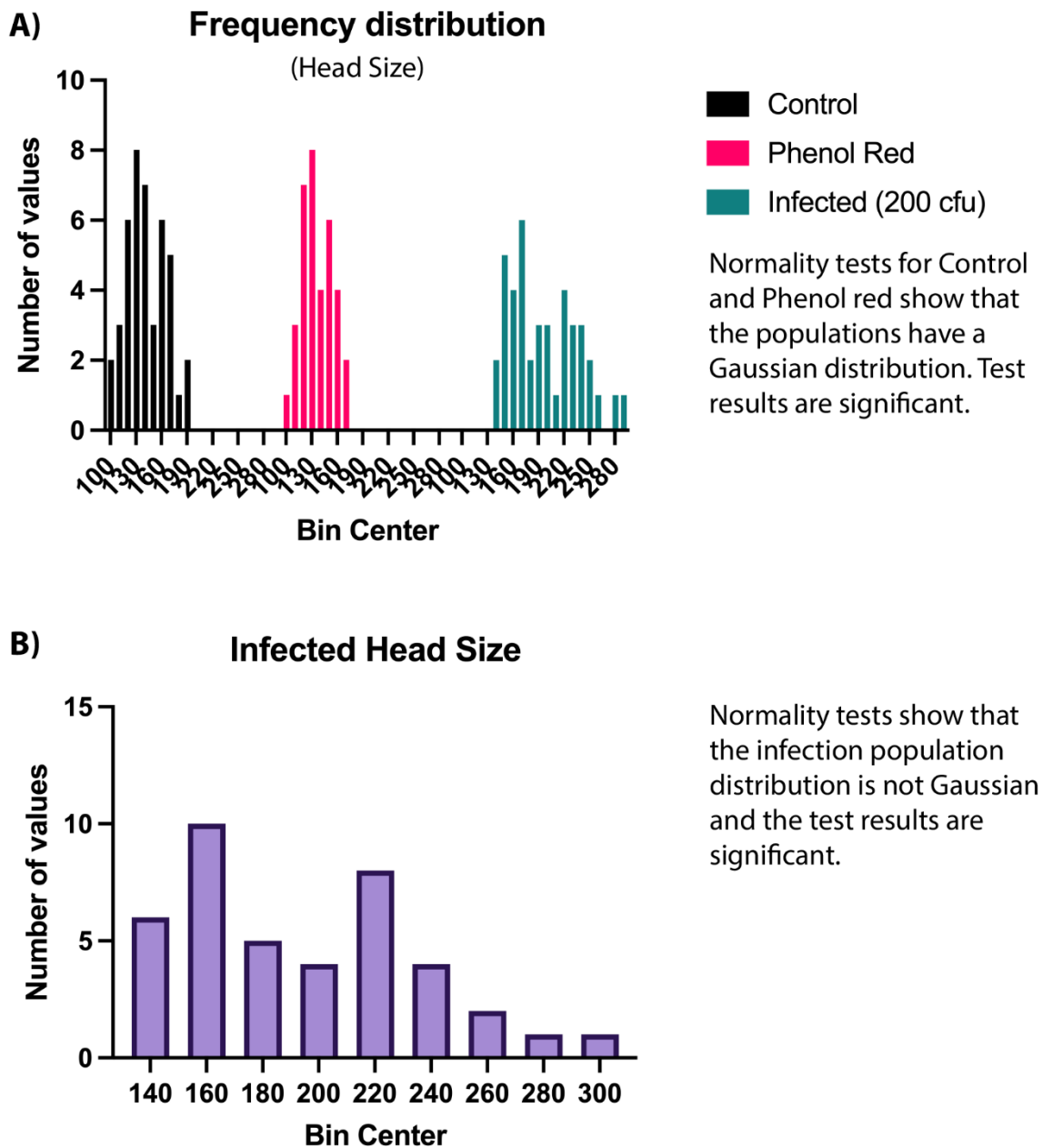


Figure 3.5 Frequency distribution of ventricular infection cranial deformation measurements show a bimodal distribution.

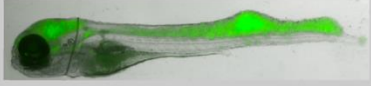
A Frequency histogram of data in Figure 3.4, b. The control and phenol red populations show a normal distribution in the histogram and normality tests are significant for a Gaussian distribution. **B** The infected population histogram shows a bimodal distribution and normality tests confirm that the population is not normally distributed.

3.4.3 Cranial deformation in the zebrafish larvae ventricular infection model is linearly related to fungal burden.

The degree of deformation was linearly correlated with the amount of cryptococci in the ventricles (Figure 3.6, B). The dorsal cranial deformation discussed in the previous section was measured in 2D and compared to infection burden in the cranium (pixel count). Pixel counts measured in this way have been shown to be proportional to cfu (Bojarczuk et al. 2016). As a preliminary confirmation of this relationship, correlative cfu fungal burden was measured 4 days post ventricular infection larvae after imaging (Figure 3.6, A). However, only three correlative measurements were achieved preventing the same analysis used in Figure 3.6 B. The experiment in Figure 3.6, A needs to be repeated with the aim to acquire an N of 30 as a pilot study.

Figure 3. 6 CFU fungal burden in the cranium of larvae with dorsal cranial deformation

A)

Larvae Image	Fungal Burden in Cranium	Fluorescent Pixel count on ImageJ (Total Area of Positive pixels in mm ²)	Size of cranium in mm ² (2D)
	~ 1150 cfu in ventricles	121 (48.4% of total cranial size)	0.250
	~ 600 cfu in ventricles	57 (33% of total cranial size)	0.170
	~ 800 cfu in ventricles	70 (39% of total cranial size)	0.180

B)

“Head size” correlation with “Fungal burden”

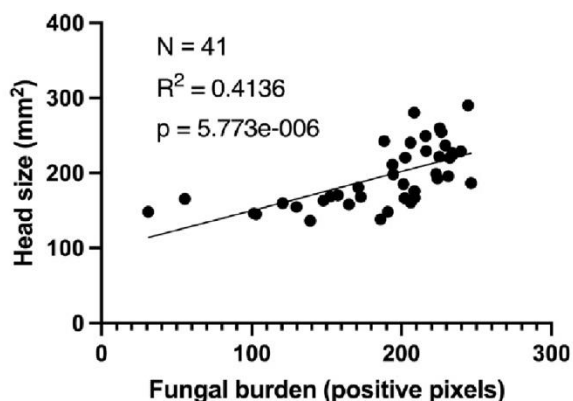


Figure 3.6 CFU fungal burden in the cranium of larvae with dorsal cranial deformation

A Zebrafish larvae were injected at 1dpf with 200 cfu/ml of *C. neoformans* KN99 GFP in the brain ventricles. In column 1 (Larvae image) we can see a composite of larvae at 4dpi, in green is the fluorescence of *C. neoformans*. Larvae crania was lysed and plated for cfu counting. In column 2 (Fungal Burden in Cranium) we can see the fungal burden in each cranium as quantified from cranial homogenate plating. In column 3 (Fluorescent Pixel Count on ImageJ*) we can see values of total fluorescence intensity of cryptococcal masses in the area of the cranium. In column 4 (Size of Cranium in ImageJ**) we can see the area of the cranium in 2D. **B** Scatterplot of fungal burden against head size. Fungal burden was calculated by measuring pixel count in Fiji software (Bojarcz et al., 2016) line is linear regression.

* Fluorescent pixels were measured in the area of the cranium after automatically thresholding the GFP channel with the default setting

**A manual ROI was drawn around the cranium (excluding eyes) and the area in pixels

3.4.4 17% of ventricular infections led to dissemination to the spinal canal.

In 25 out of 150 infections, ventricular infection had spread into the spinal canal (~17% out of 150) (Figure 3.3). Variable distribution of spinal canal infection in humans may also be present. It is important to consider that sampling of patient spinal CSF occurs from the caudal ends of the spinal subarachnoid space, and there might be a different fungal burden concentrated there in comparison to more rostral parts. It is possible that the pathogen colonised the ventricles completely before spread to the spinal canal. Therefore, the hypothesis was formulated that severe infection in the ventricles may promote spread into the spinal canal (Figure 3.7 A, B). However, if this was incorrect it was likely that spinal infection fungal cfu concentration may not be predictive of ventricular infection fungal burden, which is critical when interpreting fungal burden measurements from LP CSF sampling. To test this hypothesis, I quantified cranial burden of the population of larvae with spinal infection compared to zebrafish larvae with no spinal dissemination (Figure 3.7, C and D). There was little difference in cranial burden of larvae with only ventricular (spinal -ve) and larvae with ventricular and spinal infection (spinal +ve) (Figure 3.7, C and D).

Interestingly, in some larvae with spinal infection, parts of the central canal that are linking the spine and the brain ventricles lacked presence of cryptococci, but the larvae still had a prominent fungal burden in the caudal spine (Fig. 3.7, E).

Figure 3. 7 3dpi ventricular infection phenotypes: localisation of infection in the spinal canal

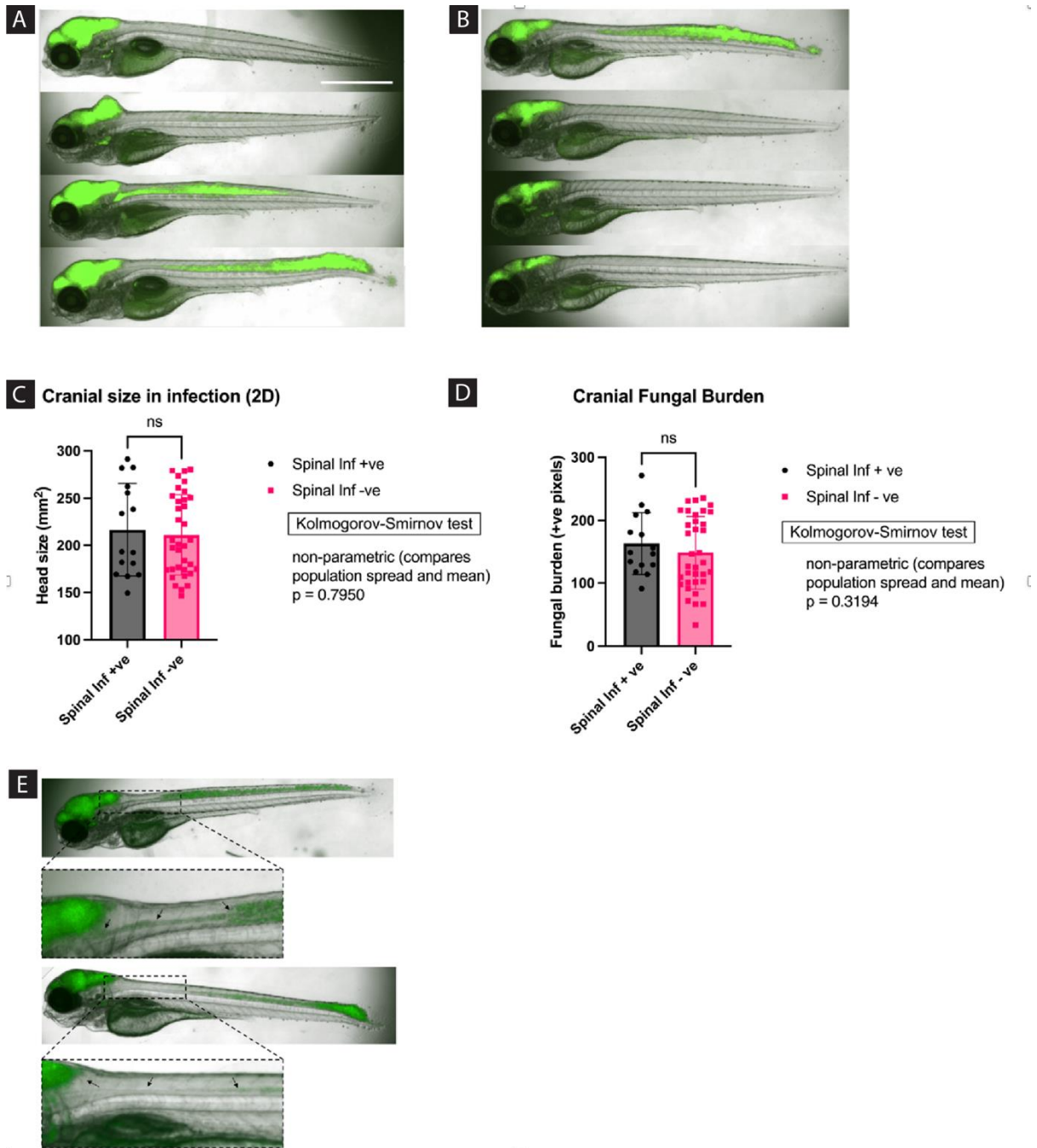


Figure 3.7. 3dpi ventricular infection phenotypes: localisation of infection in the spinal canal

Fish larvae were injected into the forebrain ventricle at 24hpf with approximately 200cfu of *Cryptococcus neoformans* KN99GFP and imaged at 3dpi. (A) Representative images of the most severe phenotypes of ventricular infection (N = 50 injected) (mean fungal burden - 183.6, positive fluorescent pixels in the area of the cranium); bottom two larvae represent phenotypes of dissemination into the spinal cord. (B) Representative images the less severe phenotypes of ventricular infection (mean fungal burden – 136.1, positive fluorescent pixels in the area of the cranium). There was dissemination into the spinal cord present in some animals with lower infection burden (B, top fish). To see if the presence of spinal infection is correlated with higher fungal burden and/or larger cranial size, cranial deformation and cranial fungal burden were compared between populations with and without spinal infection in C and D. All measured fish had a ventricular infection administered at 24hpf. There was only a small mean fungal burden in fish with spinal infection, but the difference was not statistically significant. (E) Dissemination into the spinal cord in some cases (E, top fish) was contiguous with ventricular infection, but in other cases there was an area clear of infection interrupting ventricular and spinal infection positive areas (E, bottom fish). All the larvae represented here were alive when imaged, the infection phenotype was not fatal. Scale bar in all images 780µm.

3.4.5 It was not possible to assess if non-viable *C. neoformans* would cause cranial deformation in ventricular infection.

In order to assess if the mechanisms that cause the observed cranial deformation were due to the growth or virulence factors of viable *C. neoformans*, I decided to inject heat-killed cryptococci into the brain ventricles. The aim was to assess if purely the introduction of a high mass of non-viable cryptococcal cells would result in dorsal cranial deformation similar the progression of infection over time with viable pathogen. After three attempts of injecting heat-killed *C. neoformans*, it was apparent that dead cryptococcal cells were cleared and did not remain in the ventricles long enough to cause a phenotype (Figure 3.8).

Figure 3. 8 Non-viable *C. neoformans* were cleared from brain ventricles.

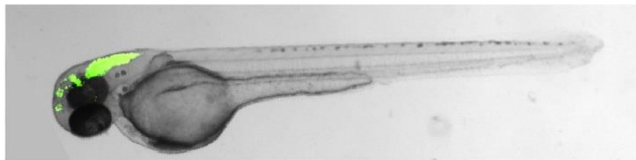
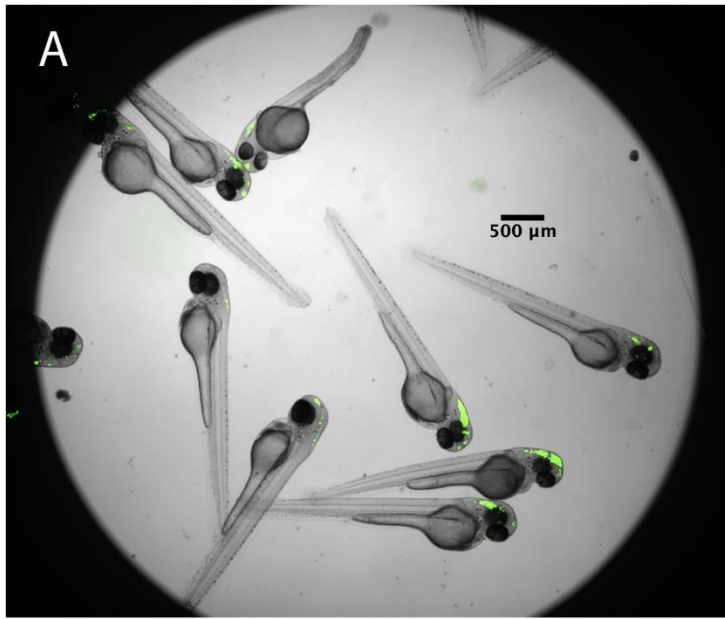
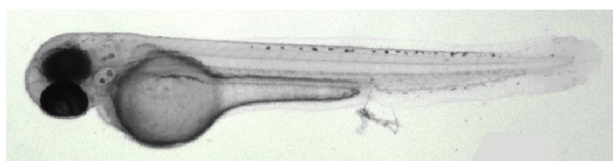
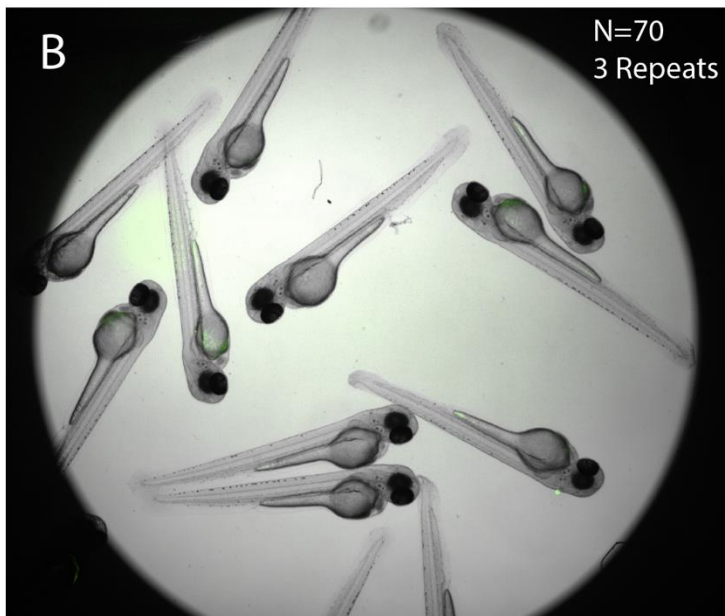


Figure 3.8 – Non-viable *C. neoformans* were cleared from brain ventricles.

A: Larvae injected with 200cfu of viable *C. neoformans* in the D/M ventricle at 1dpf; Imaged 24hpi; Can observe infection presence in the ventricles through registration of fluorescence. **B:** Larvae injected with 700cfu of heat killed (non-viable) *C. neoformans* in the D/M ventricle at 1dpf; Imaged at 24hpi; Cannot observe infection presence in the ventricles through no registration of fluorescence.



3.4.6 Pharmacological manipulation of cranial blood volume did not alter cranial deformation in ventricular infection.

The dorsal part of the zebrafish larvae skull (neurocranium) at 4dpf and 5dpf is not cartilaginous and has a more intramembranous character (Kanter et al., 2019). When measuring correlation of cranial deformation with fungal burden, I saw evidence that there is a positive correlation (Section 3.4.3). With the assumption that cranial deformation occurred as a compensation for the increase of volume within the cranium through the increase of volume of pathogen in the brain ventricles, as *C. neoformans* replicates, I wanted to use cranial deformation as a measurement of intracranial pressure. With this model, I designed an experiment to examine if it was possible to measure impact of cerebral blood volume on intracranial pressure, i.e., to see if the phenomenon of vascular compliance could be observed. In our understanding of human physiology, an initial compensatory mechanism for abnormally raising intracranial pressure is to decrease the volume of the vascular compartment to accommodate new pathological volumes and equalise pressure (See Introduction 1.1.4). In response to pathologically increasing volume in our zebrafish larvae system, the compensation was to increase the cranial volume by dorsal deformation. Therefore, I tested if pharmacological reduction of cranial blood volume would be a sufficient compensatory mechanism to decrease the degree of cranial deformation.

Null Hypothesis: Cranial deformation in ventricular infection of zebrafish larvae would not reduce with pharmacologically induced reduction in cranial blood volume.

I designed an experiment in which I treated zebrafish larvae with a brain ventricular infection with nitric oxide (NO) manipulating agents that induce either hypotension or hypertension to examine if the pharmacological intervention had an influence on cranial deformation. Discussion with experts in cardiovascular research in zebrafish (Timothy Chico, Clare Howarth, Karen Plant) aided in the choice of vasoactive compounds suitable for the developmental stages I was testing. Dr Elisabeth Kugler (at the time a PhD student in the lab of Timothy Chico) was testing effects of those agents on cranial vasculature and assisted in providing the compounds and in suggesting working concentrations and treatments lengths. The compounds chosen for testing were:

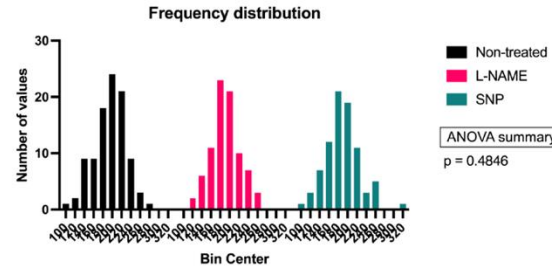
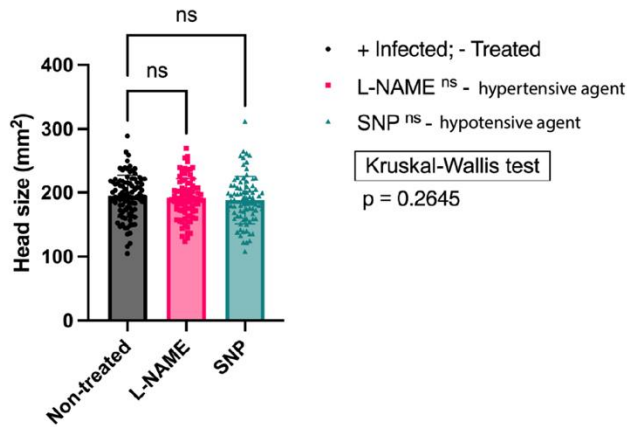
1. N(gamma)-nitro-L-arginine methyl ester (L-NAME) – at a working concentration of 0.5mM

- a. A non-selective inhibitor of nitric oxide synthase, which has been used experimentally to **induce hypertension** (NLM, 2023).
 - b. Shown to reduce vessel diameter -
 - i. At 36hpf in zebrafish larvae (22h of exposure; 10 μ M concentration) (North et al., 2009).
 - ii. In 5-6dpf larvae (injection) (Fritsche, Schwerte, and Pelster 2000).
2. Sodium nitroprusside dihydrate (SNP) – at a working concentration of 0.1mM (Chhabria et al., 2018).
- a. NO doner, powerful **inducer of hypotension** in animals and human (Page et al., 1955).
 - b. It has been shown to increase vessel diameter -
 - i. in 5-6dpf zebrafish larvae (Fritsche, Schwerte, and Pelster 2000).
 - ii. 4 dpf pericyte-covered vessels dilate an average of 6% in response to 1mM concentration for 10min exposure (Bahrami and Childs 2020; after my experiment was conducted)
 - c. SNP has effects on the zebrafish larvae cranial vasculature as seen in studies of neurovascular coupling (Chhabria et al., 2018)

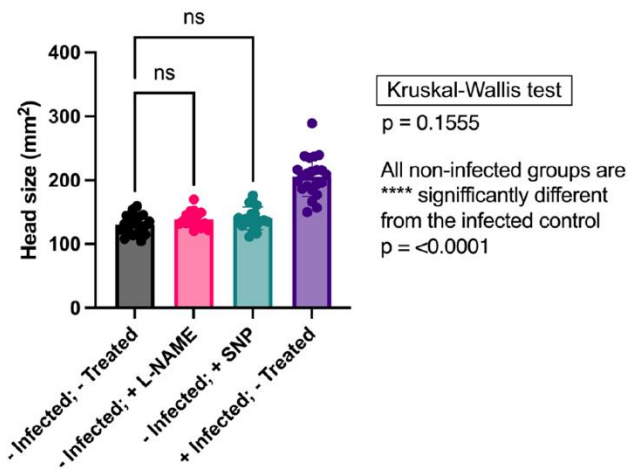
Zebrafish larvae were injected with 200cfu in the diencephalic ventricle at 30hpf (1dpf). The larvae were allowed to recover for 1hr and then groups were treated with L-NAME or SNP until 5dpf. Incubation period was chosen as longer incubation periods (>17hrs) were previously observed by Dr Elisabeth Kugler to have the greatest effect on cranial vasculature. Data from her work on these compounds was not published in context of vessel size. In infected groups, larvae treated with vasoactive compounds did not show any difference in cranial deformation to groups of larvae with no treatment (Figure 3.9, A). In controls, where there was no infection, there was no difference between groups of treated and not-treated larvae (Figure 3.9, B). There were only statistically non-significant differences in survival across the groups (Figure 3.9, C and Figure 3.2). Therefore, based on cranial deformation measurements, the null hypothesis was rejected.

Figure 3. 9 Pharmacological manipulation of cranial blood volume did not change cranial deformation following ventricular infection.

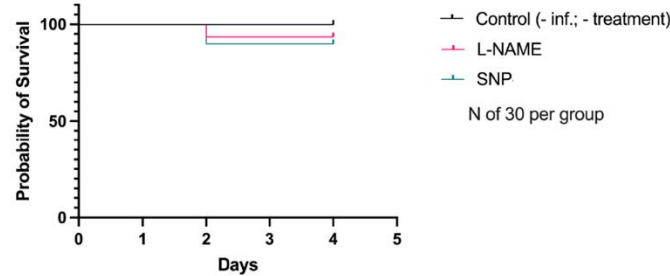
A Repeat 1- 4, populaitons together



B Controls



C Survival with no infection



200 cfu in brain ventricles at 1dpf

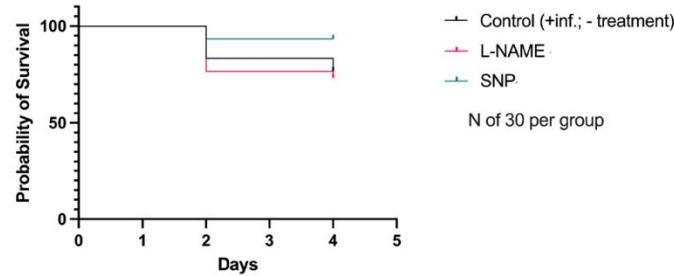


Figure 3.9 Pharmacological manipulation of cranial blood volume did not change cranial deformation following ventricular infection.

A) For each experimental repeat 90-100 larvae were injected with 200cfu in the brain ventricles at 30hpf. The injected larvae were left to recover for 1hr and randomly assigned to treatment groups of 30. Two groups were treated with vasoactive drugs, L-NAME (0.5 mM) and SNP (0.1 mM) until 4dpi (~72hrs of treatment). Cranial size was measured as described above. The experiment was repeated 4 times and all populations combined. The population histograms appeared normal, but normality tests were not significant for Gaussian distributions. Parametric and non-parametric tests show no significant differences in cranial size across groups.

B) Comparison of head size with L-NAME and SNP treatment in the absence of infection. (Groups of 30)

C) Survival analysis of groups without infection but with treatment (top) and with infection and treatment (bottom). The Log-Rank Mantel-Cox test showed no significant difference across groups.

3.5 Dissemination and localisation of systemic *C. neoformans* infection in the CNS from cranial vasculature

A limitation of the ventricular infection model was that it did not mimic how pathology develops in patients, as there was no presence of the pathogen in the brain parenchyma and blood vasculature (Figure 3.4). This is not representative of patient pathology as there is a spread of cryptococcal masses across the whole CNS (See Introduction). Another problem with the ventricular model is that there is a lack of data on cryptococcal culture from brain ventricles. The fungal burden in this experimental model is enough to completely fill the whole brain ventricle system. We have no data to suggest that is the case in human patients. Studies of patients with ventriculoperitoneal shunts (opening and draining of brain ventricle CSF) monitor cryptococcal antigen levels in CSF from lumbar punctures/spine but not the brain ventricles (Cherian et al., 2016; Baddley et al., 2019). Data suggests that in patients with shunts median CSF and serum burden is higher than in patients with no shunts (Cherian et al., 2016; Baddley et al., 2019). Shunts are administered in patients with a particularly severe symptoms of IH, possibly that is due to the higher fungal burden in the CSF. Interpreting data from shunts gives an idea of cfu concentration only in the more severe cases of the pathology. Studies do not specify what the values are particularly for brain ventricles as opposed to spine CSF, therefore, we cannot make any clear conclusions about fungal burden specific to the brain ventricles.

In addition, cryptococcal meningitis arises as a CNS infection by dissemination of yeast from the bloodstream (Stie et al., 2012; Santiago-Tirado et al., 2017; Squizani et al., 2018; Aaron et al., 2018; Gibson et al., 2022). The cranial vasculature plays an important role in sustaining homeostasis of intracranial pressure in health, and it is key to investigate the vascular aspect of intracranial hypertension pathologies (see Introduction). In CM, the infection burden within the CSF would be dependent on how the pathogen disseminates from the bloodstream. We do not know the cfu or absolute (including dead cells) CSF counts in the brain ventricles of patients. Therefore, mimicking how the infection develops as in humans, from the blood circulation, instead of introducing it directly into the ventricles, may give us a more representative phenotype.

Null hypothesis: The presence of viable *C. neoformans* culture in the zebrafish larvae vasculature does not lead to dissemination into the parenchyma.

To investigate CNS infection progression and development from the blood circulation, cryptococci were injected into the main blood stream of zebrafish larvae. Zebrafish were infected at 2 days post fertilisation. The lumen formation and onset of circulation in zebrafish larvae starts around 24hpf (Fouquet *et al.*, 1997). Heartbeat is essential for intra-cerebral vessels development at 32hpf (Kugler *et al.*, 2021). At 48hpf the primary vasculogenesis is complete and CNS vessel networks well established (Isogai *et al.*, 2003; Quiñonez-Silvero *et al.*, 2020). The 2dpf infection point allows for a long enough period of infection development before 5 days post fertilisation where larval tissue thickness limits imaging in the CNS. The Duct of Cuvier (DoC) was chosen as route of introducing infection because this is a common infection route when attempting to achieve a bloodstream infection. DoC was chosen as a preferred injection site to the caudal vein as it is larger, has a higher velocity of flow and it appears to allow for better distribution of pathogens across the whole larva. An inoculum of 700-1000 cfu/nl was chosen as based on previous work in the Johnston Lab done by Dr Josie Gibson, who investigated dissemination of *C. neoformans* KN99 from the vasculature into the brain and myotomes of zebrafish larvae (Gibson *et al.*, 2022). It appears that lower fungal burden injections are not effective in achieving localisation of the pathogen into the cranial vasculature as injections of 200-500 cfu at 2dpf did not result in infection of cranial vasculature at 5dpf.

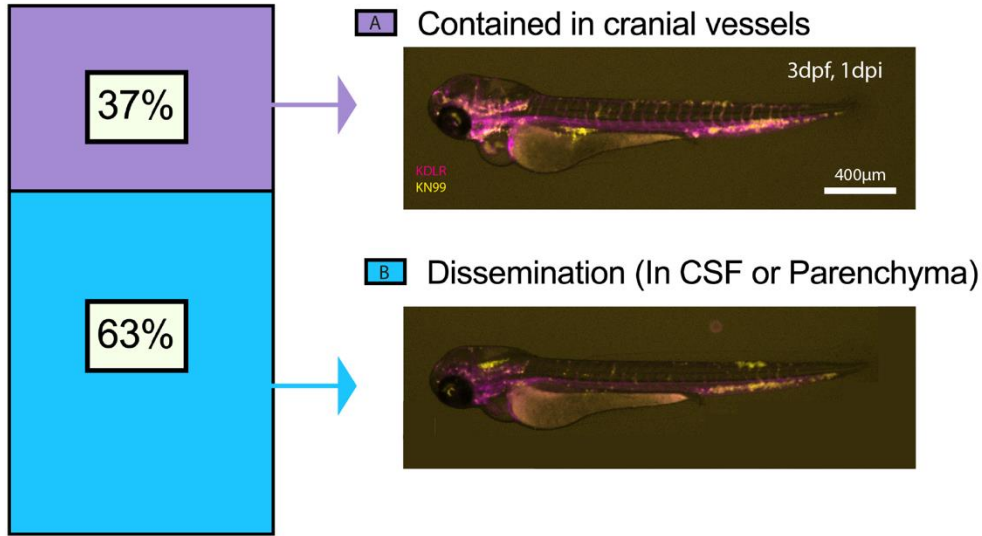
3.5.1 *C. neoformans* systemic infection in zebrafish larvae better represents dissemination as seen in patients but does not lead to persistent cranial deformation as seen in ventricular infection.

Injection of zebrafish larvae in the Duct of Cuvier (DoC) at 2dpf with 700-1000cfu of *C. neoformans* KN99 GFP resulted in dissemination of the pathogen from the blood stream into the CNS (Figure 3.10). At 1dpi cryptococci were present in the brain parenchyma and/or brain ventricles in 63% of cases (Figure 3.10, 1 and 2). The exact point of dissemination was unclear from still images with cryptococci localised in most cranial vessels and distribution of infection varies. Later infection phenotypes (24hpi) can show a seizure in the main blood circulation, as the aorta is colonised and largely obstructed (Figure. 3.10 arrowhead panel 3A). Analysis of this infection time point in later work which interprets vascular pathology (Chapter 4) was excluding larvae in which the pathogen has stopped systemic blood flow. Although the trunk and aorta circulation are completely obstructed by 2.5dpi, there was only 25% mortality within the cohorts of infected larvae with 700cfu (Figure. 3.10 panel 3). There was no statistical

significance in mortality across the groups (Figure 3.10, 3) and no difference in cranial size at 2dpi when compared to larvae injected with phenol red alone (Figure 3.10, panel 4). The clear cranial deformation seen in ventricular infection does not seem to be present in the systemic infection. To assess where dissemination occurs and if dissemination induces disruption of the vascular wall, early infection time points between 3-24hpi were chosen.

Figure 3.10 *C. neoformans* systemic infection in zebrafish larvae results in dissemination to the CNS but does not lead to persistent cranial deformation as seen in ventricular infection.

1 N of 60, 3 Repeats



2

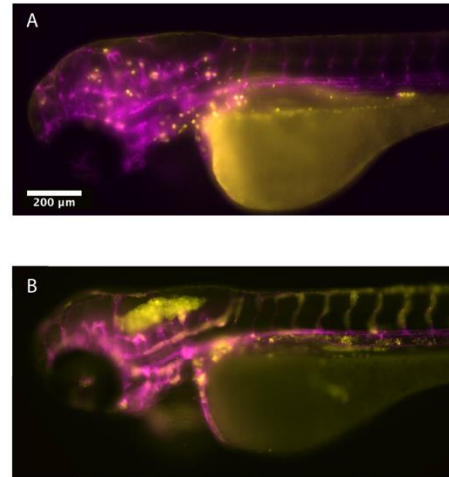


Figure 3.10 *C. neoformans* systemic infection in zebrafish larvae results in dissemination to the CNS but does not lead to persistent cranial deformation as seen in ventricular infection.

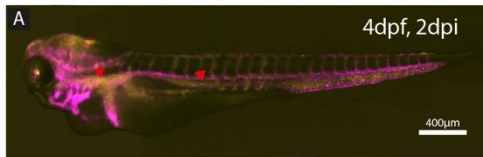
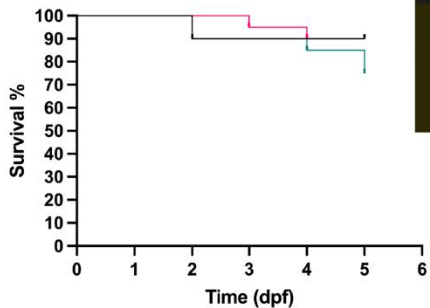
1) Infection at 3 dpf, 1 dpi. Representative of 60 zebrafish larvae injected we see *Tg(kdrl:mCherry)^{S916}* transgenic zebrafish larvae. Blood vessels (magenta) cryptococci (yellow). Zebrafish injected at 2 dpf with 700-1000 cfu/nl with *C. neoformans* KN99 GFP in the DoC. 63% of larvae had dissemination from vasculature into the parenchyma or CSF.

2) Shows representative phenotypes of the populations outlined in 1), in higher magnification. The CSF and parenchyma dissemination in B are clear.

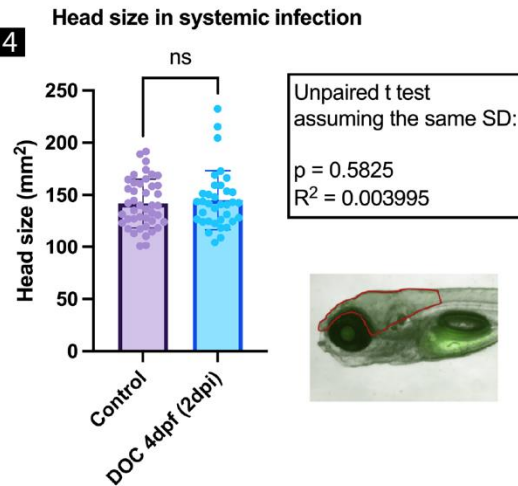
3) Survival of lower infection (200cfu), higher infection (700-1000 cfu) and phenol red control (procedure induced death). 3A, it shows the phenotype of 700-1000cfu infection at 2dpi.

4) Cranial size comparison between control (no infection) and 700-1000cfu infection in the DoC at 2dpi.

3 DOC infection survival



4



3.5.2 The *C. neoformans* dissemination event could not be clearly identified from time lapse images.

Cryptococci were present in the cranial vasculature of all infected larvae, but dissemination from the cranial vasculature into the CNS parenchyma and CSF occurred just in 63% of cases (Figure 3.10.1). In homeostasis, vascular endothelium integrity is essential for the controlled production and secretion of CSF, and disruption of the vascular wall may skew CSF dynamics into facilitating pressure increase (Sweeney et al., 2018; Mestre et al., 2020). Therefore, I proceeded to develop an experimental design that would allow me to capture dissemination events *in vivo* in higher magnification, in order to assess vascular wall integrity. I aimed to capture multiple time points of dissemination events, as it may provide with insight into the mechanics of the process.

Null hypothesis: Dissemination of *C. neoformans* form cranial vasculature into the parenchyma does not disrupt endothelial vascular wall.

In a double fluorescent widefield microscope (see section 2.4) after injection of cryptococci into the blood stream, long observation of 24hrs were done with the aim of identifying dissemination events of *C. neoformans* form the cranial vasculature (secondary fungaemia). 17 infected zebrafish larvae were imaged, with images from two fluorescent channels captured every 5-7 minutes or every 1min. Time-lapses were recorded either 1hpi or 20-24hpi. Dissemination into the cranial vasculature was always seen at 1hpi (N=7). In figure 3.11, secondary fungaemia was clearly present after 6hpi in the forebrain ventricle, but the time-lapse data did not allow for the identification of the vessel from which dissemination occurred (Figure 3.11, E). Observations from 24-48hpi (5 larvae) also showed dissemination into the parenchyma and CSF but it was not possible to determine the vascular endothelium from which the pathogen had crossed and whether crossing required vascular endothelium damage. This occurred possibly due to lack in spatial resolution - in the widefield imaging it was difficult to determine borders in between vessels, and in between vessels and CSF or parenchyma (Figure 3.12, E). In Figure 3.12E a cryptococcal mass is shows to “bud” off a vessel and disrupt the endothelium, the vessel wall appears compressed.

Figure 3. 11 Secondary fungaemia in the CNS captured 6 hours after blood systemic circulation inoculation. Point of dissemination and mechanisms of endothelial cell wall crossing not identified.

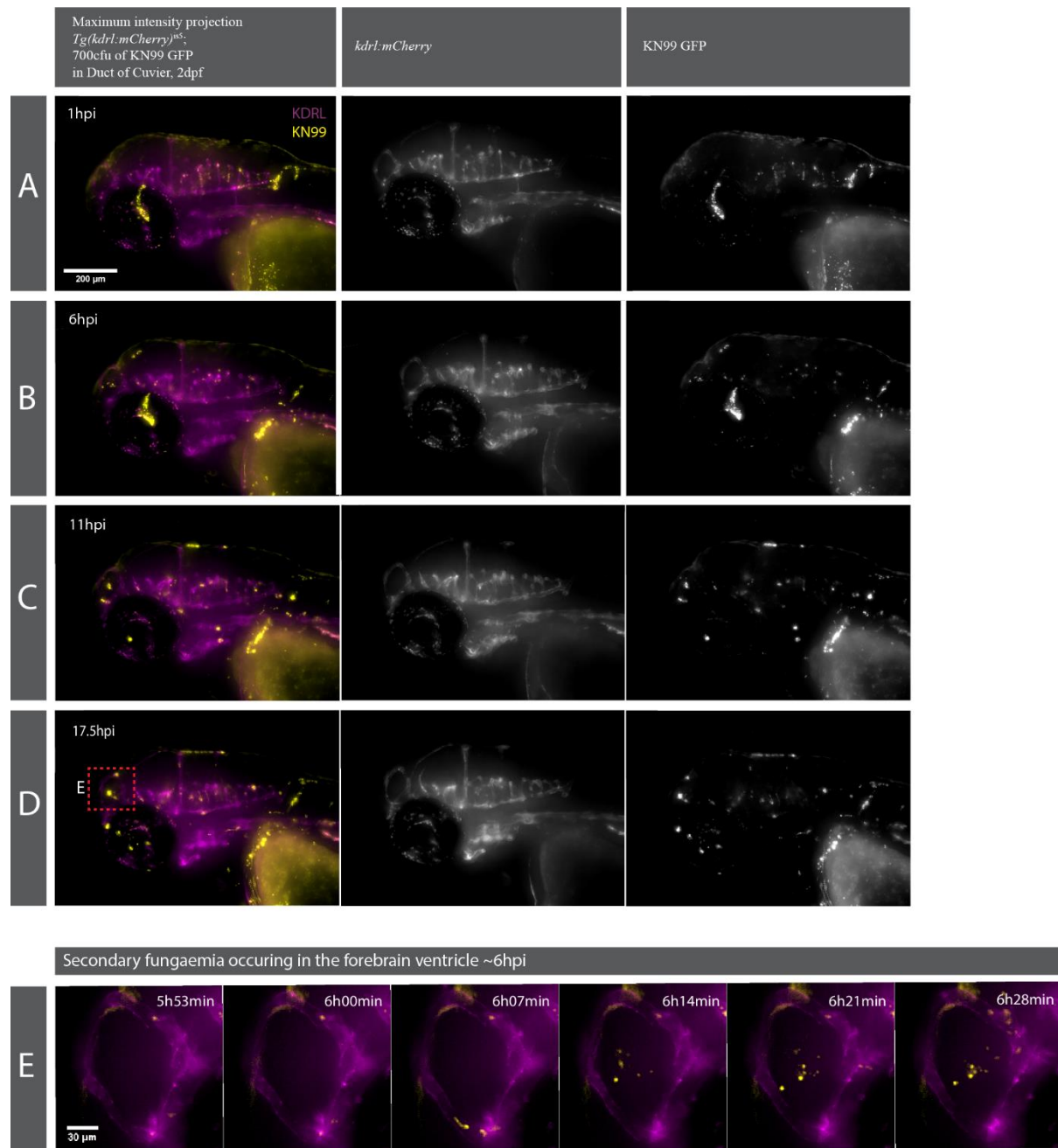


Figure 3.11 Secondary fungaemia in the CNS captured 6 hours after blood systemic circulation inoculation. Point of dissemination and mechanisms of endothelial cell wall crossing not identified.

Tg(kdrl:mcherry)^{is5} zebrafish larvae were injected at 2dpf in the Duct of Cuvier with 700cfu of *C. neoformans* KN99 GFP. 7 larvae were mounted in 1.5% LMPA and imaged for 20hrs in a temperature-controlled chamber with a double-fluorescent widefield Nikon microscope (10x lens and 20x, see 2.4.3). Images were taken every 5-7 minutes from 2 larvae at a time with a Z stack across the whole brain. Panels A-C represent one such a time-lapse imaged at 10x, showing how the infection develops over time. Capture time interval limitation was to do with speed of Z stack collection and the double fluorescence samples. Z stack data was transformed into maximum intensity projections for each time point and each time point was examined to establish points of dissemination (location and time) from the cranial vasculature into the CSF and/or parenchyma (secondary fungaemia into the CNS). Points of dissemination were not identified, in terms of location and the event of crossing the vascular endothelium. In this figure, a representative time-point of dissemination into the CSF is shown in panel E (5h53). Cryptococcal yeast cells are seen in the CSF of the telencephalic ventricle but the vessel that is the source of the infection is not identified.

Figure 3. 12 Pathogen dissemination event from cranial vasculature captured 20hpi to possibly disrupting the vascular endothelium.

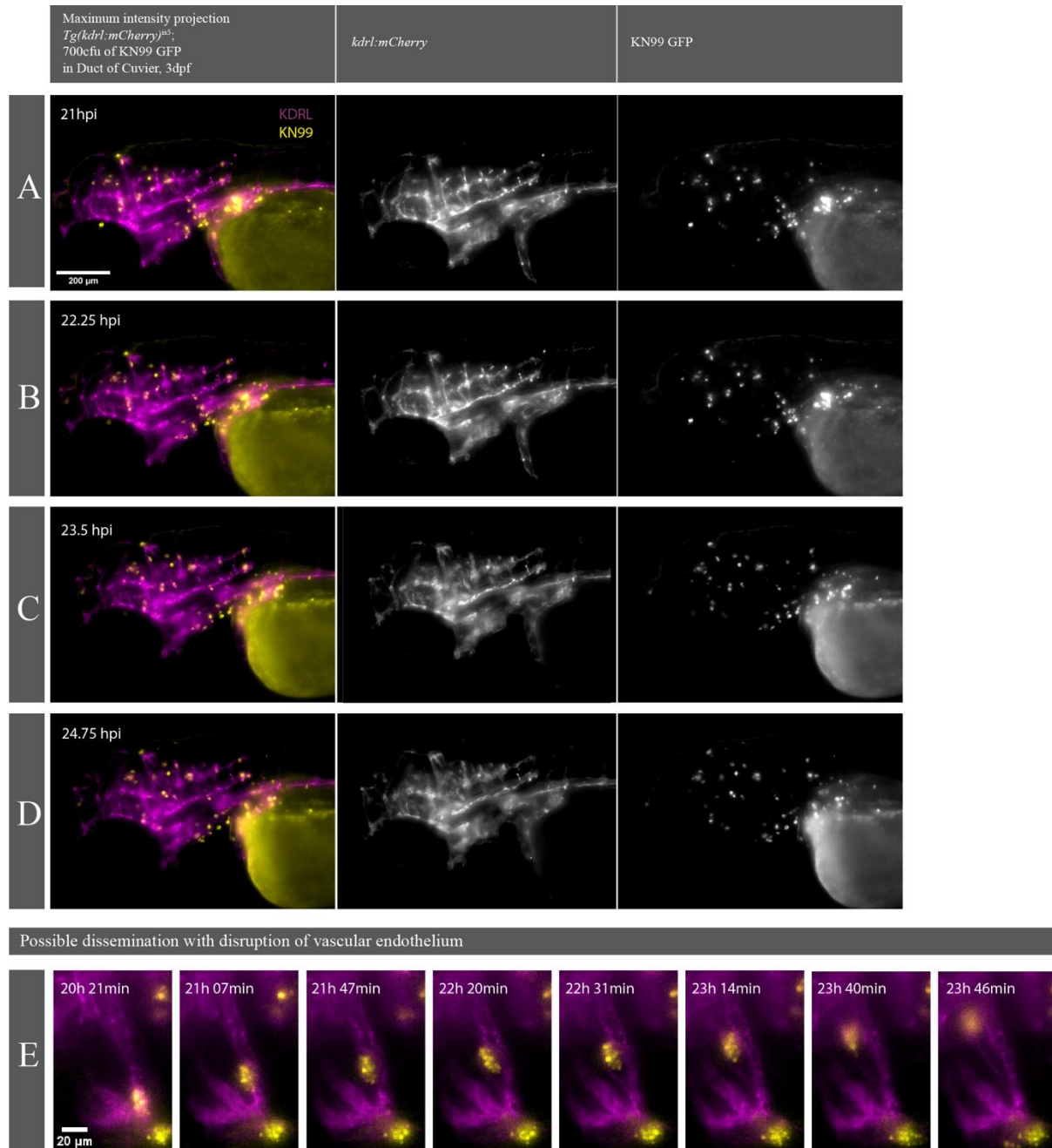


Figure 3.12 Pathogen dissemination event from cranial vasculature captured 20hpi to possibly disrupting the vascular endothelium.

Tg(kdrl:mcherry)^{is5} zebrafish larvae were injected at 2dpf in the Duct of Cuvier with 700cfu of *C. neoformans* KN99 GFP. 5 larvae were left to develop the infection until 20-24hpi, at which point they were mounted in 1.5% LMPA and imaged for 20hrs in a temperature-controlled chamber with a double-fluorescent widefield Nikon microscope (10x and 20x lens, see 2.4.3). Panels A-C represent one such a time-lapse, images were captured every 1 minute from 1 larva at a time with a Z stack across the whole brain. Capture time interval limitation was to do with speed of Z stack collection and the double fluorescence samples. Z stack data was transformed into maximum intensity projections for each time point and each time point was examined to establish points of dissemination (location and time) from the cranial vasculature into the CSF and/or parenchyma (secondary fungaemia into the CNS). In panel E an event of dissemination at 20h21min post infection is captured that is possibly disrupting the vascular endothelium, cryptococcal mass is coming out of one vessel and the endothelial wall appears compressed.

To improve resolution, I chose to utilise the Zeiss Z1 Light sheet Microscope (see 2.4.4), but it was necessary to compromise on the length of time of the observation occurred for, time-lapses only encapsulated 0.5 - 5min of time but with image capture intervals of less than a second. Time-lapses were taken from only 2 larvae. I chose to focus on infection time points around 24hpi, as assumed that further in infection progression I may capture more dissemination events due to a more established systemic fungaemia. I did not manage to capture a dissemination event in the time-lapse data i.e., the process of the pathogen crossing the vascular endothelium, I only captured cryptococcal cells in proximity to some vessels (Figure 3.13, A, B). When observing Z stacks for other experiments however, I observed a cryptococcal cell in the process of crossing the vascular endothelium once (Figure 3.13, C, D). The dissemination event was only noticed as the data was visualised in 3D. From this single data point it is not clear if the vascular endothelium was disrupted from the dissemination event. I did not capture any more dissemination event data points, despite observing 10 larvae Z stacks. For now, conclusions cannot be made about the hypothesis tested. According to what I have found I cannot reject the null hypothesis. Up to this point in my work I have not found evidence that dissemination of *C. neoformans* from cranial vasculature into the parenchyma disrupts endothelial vascular wall.

Figure 3. 13 Pathogen dissemination event from cranial vasculature captured in still images.

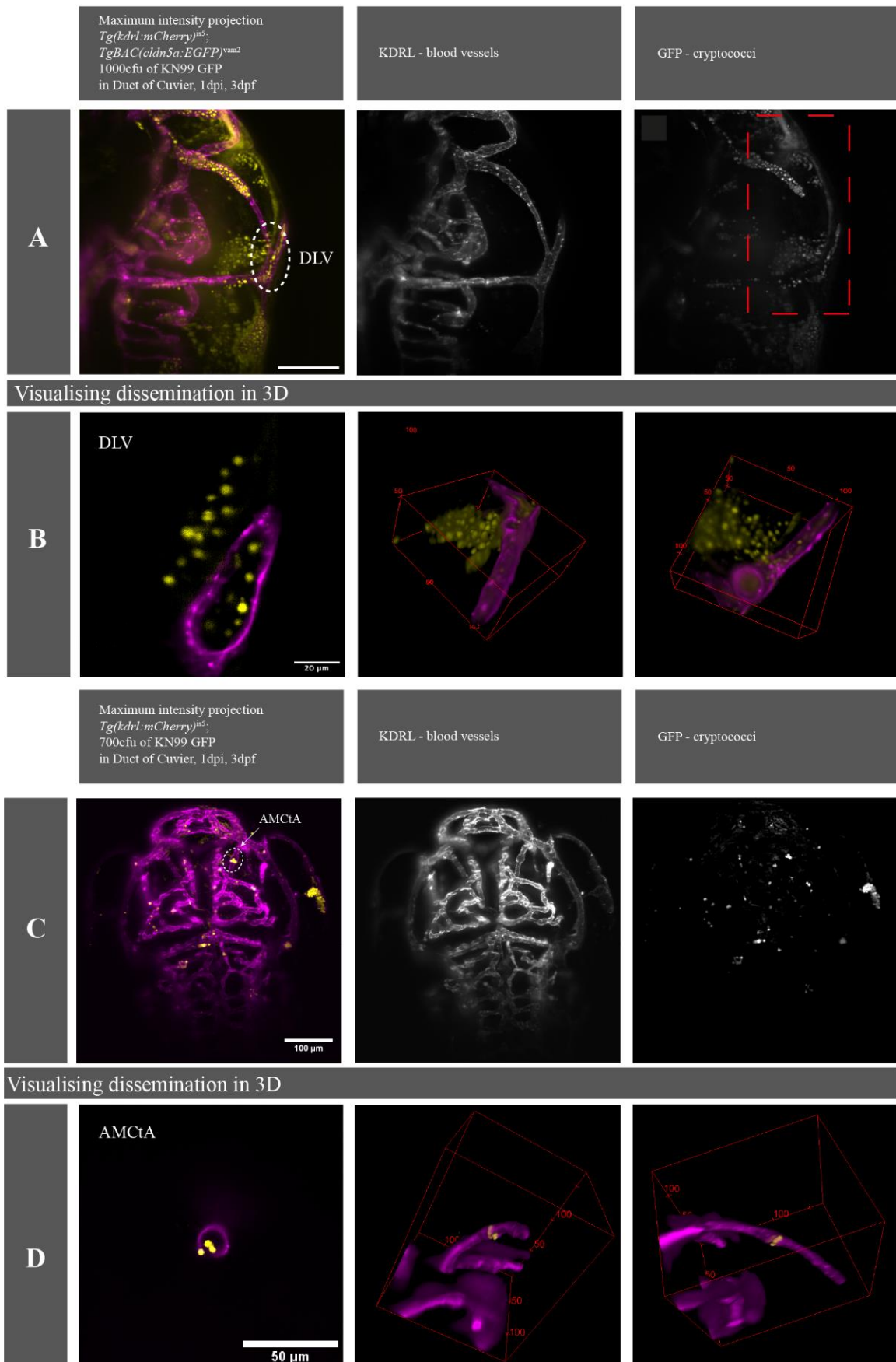


Figure 3.13 Pathogen dissemination event from cranial vasculature captured in still images.

Tg(kdrl:mcherry)^{is5} or *Tg(kdrl:mcherry)^{is5} TgBAC(cldn5a:EGFP)^{vam2}* zebrafish larvae were injected at 2dpf in the DoC with 700-1000cfu of *C. neoformans* KN99 GFP. 12 larvae were left to develop the infection until 24hpi, at which point they were mounted in 1.5% LMPA and imaged with a 20x Zeiss Z1 Light Sheet microscope (see 2.4.4). For 2 larvae, the vasculature was imaged laterally (with tilt) in a single Z, every 0.14 seconds for 0.5-5minutes to attempt to capture a dissemination event, an example time-lapse is shown in Video 3.13, and in A and B panels represent still Z stacks from the same larva. A, B and Supplementary Video 3.13, a cryptococcal mass is shown being dynamic under the DLV and the infection flowing through the DLV, with dissemination event not captured in the time lapse or still images. C, D – time lapse data was recorded for this larva on the level of CCtAs, but dissemination was not captured from that data point (data not shown). In D, when examining the MIP of the same larvae, a cryptococcal cell was captured in the process of crossing the endothelium of an AMcTA, the dissemination was not obvious until the data was visualised in 3D.

MIP maximum intensity projection

DLV dorsal longitudinal vein

AMcTA anterior mesencephalic central artery

3.6 Discussion

3.6.1 Injection into the brain ventricle of 2dpf is technically challenging and not suitable for examining the brain infection.

After assessing the literature on cryptococcal meningitis pathophysiology, it appeared there is a gap in understanding how the pathogen interacts with host tissues on the level of the brain ventricles *in vivo*. It is not possible to perform such observations in mammalian animal models, as ventricles can only be imaged post-mortem. I decided to begin my project with the aim of creating a zebrafish model system that bridges this gap. I tested two experimental methods; I assessed which one is more efficient in producing a stable ventricular infection and better models human CNS infection in CM. The two experimental set ups differed in the developmental time point at which the infection was introduced. Infection at 1dpf as opposed to 2dpf, produced a more stable ventricular fungaemia. It appears that ventricular infection at 1dpf is technically less challenging and allows for generating greater experimental numbers. For future experimental design, ventricular infection was performed at around 32hpf of the zebrafish larvae.

3.6.2 Ventricular infection leads to cranial and ventricular deformation but no dissemination to brain tissues.

Assessing the phenotypes that arise from the established ventricular infection model showed a prevalence of cranial deformation as a result of the infection that was significant in comparison to larvae that were not infected (Figure 3.3; 3.4). The cranial deformation when looked from a dorsal mounting perspective (Figure 3.4e) appeared to be as a result of dilated brain ventricles and increase of volume of pathogen that created pressure on the dorsal side of the cranium and resulted in a dorsal deformation. Cartilage and bone mineralisation stains of 5dpf zebrafish do not stain the dorsal parts of the head (Mork and Crump, 2015). It appears that at this stage of development the dorsal part of the zebrafish skull (neurocranium) is not cartilaginous yet, and it has a more intramembranous character (Kanter et al., 2019). The dorsal deformities in infected fish (Figure 3.4) were likely due to increased elasticity of the cranial vault in this area of the zebrafish cranium at this point in development. When measuring correlation of cranial deformation with fungal burden, I saw evidence that there is a positive correlation between the two factors (Section 3.4.3). This indicated that cranial deformation might occur as a compensation for the increase of volume within the cranium through the increase of volume of pathogen in the brain ventricles, as *C. neoformans* replicates and that cranial deformation might

be a surrogate measurement for increased intracranial pressure and how that could be affected in changes of cerebral blood flow (Section 3.4.6). If we calculated the viscoelastic potential of the tissue surrounding the brain (primordial skull), we could derive a measurement of pressure in the system depending on the degree of cranial deformation (Hochmuth et al., 2000). However, we were unable to identify the viscoelastic potential of the zebrafish primordial skull membrane from the literature or with currently available methods (for example, microrheological measurements would require non-invasive imbedding of micron latex beads in the neurocranium).

There is a lack of data on cryptococcal cfu counts from CM patient brain ventricles. The fungal burden in my model is high enough to completely fill the whole brain ventricle system. We have no data to suggest that is the case in human patients. Studies of patients with ventriculoperitoneal shunts (opening and draining of brain ventricle CSF) monitor cryptococcal antigen levels in CSF from lumbar punctures/spine not the brain ventricles (Cherian et al., 2016; Baddley et al., 2019). Their data suggests that in patients with shunts median CSF and serum cryptococcal antigen levels are higher than in patients with no shunts. Shunts are administered in patients with a particularly severe symptoms of IH. It is possible that is due to the higher fungal burden in the CSF. In Cherian et al., 2016, the antigen values were twice as high in CSF and serum in comparison to patients with no shunts. It is difficult to determine how that relates to the number of cfu and if the difference is significant. Measurement from patients with shunts do not specify what the values are particularly for brain ventricles as opposed to spine CSF (Cherian et al., 2016; Baddley et al., 2019), therefore, we cannot make any clear conclusions about fungal burden specific to the brain ventricles.

However, it is a key observation that high numbers of *C. neoformans* in the brain ventricles was insufficient for dissemination into the parenchyma or vasculature. Larvae survived until the experiment is over with severe ventricular infection and no apparent toxicity to the brain. In future work, it would be interesting to assess if there are any behavioural or functional symptoms to this phenotype. Cryptococcal meningitis can cause confusion or sensitivity to light (Williamson et al., 2016). In the future we could test if similar symptoms are seen in our models using behavioural assays such as testing for preference of light or dark environment in the fish, assays previously used to test photophobia in mice but can be easily translated in fish (Wang et al., 2021).

I found that cryptococci were unable to cross from the brain ventricles into the vasculature despite being able to disseminate in the opposite direction. The lack of dissemination into the blood circulation from ventricular infection may be due to that vessels get compressed by the mass of pathogen around them, possibly the vessel lumen collapses and there is physically no space to cross into the vasculature as a result. This would be difficult to image as the large mass of pathogens in the ventricles prevents light from penetrating to parenchyma impeding vessels. The hypothesis of a collapsed lumen may not be true for vessels sitting on top of the ventricles such as the mesencephalic veins, although in the KDRL transgenic reporter line in figure 3.4e the vessels on the top of the ventricles still cannot be easily seen.

Also, an unexpected observation was that dorsal deformation measurements when plotted seemed to have an almost bimodal distribution - symmetric bell curve with two peaks (Figure 3.5). This suggests that there are two population distributions in the infected group. When the paired to head size fungal burden was plotted, it did not seem to show a bimodal distribution, which indicates that there is not two populations of fungal burden. The distribution may have been due to chance and would form a normal distribution with a larger number of experimental animals. Another explanation is that changes in fungal burden over time may have coincided with different growth stage of the zebrafish cranium that resulted in two different phenotypes.

3.6.3 Cranial deformation in the zebrafish larvae ventricular infection model is linearly related to fungal burden.

When assessing the relationship between fungal burden and degree of cranial deformation, I found a linear correlation with an R^2 of ~ 0.4 suggesting that cranial deformation was due, at least in part, to an increase in volume of the ventricles. Preliminary results from assessing the relationship between cfu count showed that fish with larger infection burden had larger cranium. If zebrafish ventricles are around $6.5\mu\text{l} = 6.5\text{ mm}^3$ in volume at 5dpf (Fame et al., 2016) and if *C. neoformans* KN99 is 7.5 (5 - 10) μm in diameter on average (Okagaki et al., 2010) ($220\text{ }\mu\text{m}^3$ in volume if we assume it is spherical), we can calculate approximately how much pathological volume is added and if it reflects degree of deformation. For example, if the number of cfu in the ventricles is 1150 (Figure 3.6), the total volume of pathogen in the ventricles would be 0.0005 mm^3 (exactly 0.003 but with packing of spheres considered) which is $\sim 1/13,000^{\text{th}}$ of the total volume of brain ventricles. However, this calculation does not consider dead cryptococcal cells, the cryptococcal capsule that will be shed and the

accumulation of fluid. This experiment was only repeated twice, and one was successful but does not have enough data points to make conclusions. However, it highlighted the need of performing a gentler treatment in following repeats to avoid potential loss of viable cryptococcal cells. In my work I repeated this experiment two times, troubleshooting problems arose in the first attempt and the results of the second attempt are shown in Figure 3.6. The dilutions of larvae cranial homogenate needed to be optimised to allow resolution in between colonies on the YPD agar plates. The experiment was unusually time consuming (10hrs to complete procedures not including larvae husbandry prior to experiment) and unfortunately due to time-restraint across my project, more repeats were not conducted. However, the protocol for this experiment is now developed and optimised and this is a good pilot study that can support future experimental design.

3.6.4 Ventricular infection leads to dissemination to the spinal canal which does not have a uniform distribution across the length of the spine

Introducing *C. neoformans* infection into the zebrafish D/M ventricle led to complete colonisation of the ventricular system and occasionally to dissemination into the spinal cord central canal. There was little difference in the population of larvae with spinal infection have an overall more severe cranial infection (bigger cranial deformation and higher fungal burden) than infected zebrafish larvae with no spinal dissemination. Therefore, it is likely that fungal burden does not determine the chances of establishing a spinal infection. It is important to consider posture in fish vs humans which may also contribute to a more heterogeneous distribution of the infection. Also, vasculature around spinal cord allows to separate dissemination routes in the CNS to vasculature in the head, it is unclear if infection entry into the subarachnoid spaces comes solely from cranial vasculature.

An interesting observation was that in some larvae with spinal infection, parts of the central canal that are linking the spine and the brain ventricles lack presence of cryptococci, but the larvae still have a prominent fungal burden in the caudal spine (Figure 3.7e). This may be due to directionality of flow in the spinal cord. Beads in the central canal (CC) in healthy zebrafish larvae have a zero average velocity, but due to the diameter of the structure, the flow is bidirectional (Wyart *et al.*, 2020). If pressure increases enough in the ventricular system, the direction of flow would change to unidirectional, from ventricles to the tail through the CC. This idea is supported by observable distributions of *C. neoformans* in the infected zebrafish

spine, commonly in spinal infection phenotypes there are large cryptococcal masses in the caudal end of the CC and in some phenotypes the CC closer to the ventricles does not show presence of infection, despite the opposite being true of more caudal parts (Figure 3.3, and 3.7c). It is possible that pressure and fluid flow from the ventricles towards the caudal end of the CC causes cryptococcal cells to get pushed towards the tail end and colonise the tissue there. In human physiology CSF flow in the central canal has also been shown to have bidirectional character driven mainly by breathing (Dreha-Kulaczewski *et al.* 2018). Forced inspiration causes a surge of CSF flow volumes from the whole spine towards the brain ventricles, following expiration leads to only lower level spinal CSF (below level of the heart) to change direction towards caudal end of the CC. This bidirectionality could be influenced by the fungal burden and pressure in the cranial ventricles in infection in a similar way to the one suggested for the zebrafish infection, with an increase in pressure in brain ventricles driving dissemination towards the caudal ends of the spine. Lumbar punctures are the primary source of CSF samples from CM patients, samples which are used to measure fungal burden in the whole of the CNS in all CM clinical data collection (Lawrence *et al.*, 2019) with only a few exceptions. In our data we see accumulation of spinal fungal dissemination in the caudal parts of the central canal. Also, CSF in the lumbar portions of the spine has a more caudal fluid flow directionality (Dreha-Kulaczewski *et al.* 2018). It is likely that in infection this type of flow would result in a larger fungal burden accumulation in the lumbar areas of the spine in comparison to other areas of the ventricular system. This would skew data interpretation, potentially making the CNS fungal burden appear larger than it is.

3.6.5 It is not possible to assess if non-viable *C. neoformans* would cause cranial deformation in ventricular infection.

I wanted to test if the physical presence of cryptococcal cells causes cranial deformation or if factors that are only present when the pathogen is viable cause the observed phenotype. I speculate that the pathogenesis of cryptococcal infection is in large due to the mechanical obstruction, rather than factors released by the pathogen. I did not succeed in creating a sustained fungaemia in the brain ventricles using heat-killed *C. neoformans* as an inoculum. Communication with my supervisor revealed that injecting non-viable *C. neoformans* has been previously attempted by him and continuously imaged in the *Tg(mpeg:mCherry-CAAX)^{sh378}* red fluorescent macrophage reporter line. The imaging showed the dead fungal cells getting cleared almost immediately by macrophage phagocytosis. This confirmed that it

may not be possible to execute my experimental design and assess whether non-viable cryptococci would have the same effect on cranial deformation as viable ones. Nonetheless, these observations suggest that living cryptococcal yeast cells may have protective mechanisms against clearance, which allows them to cause a stable infection in cranial niches. It is difficult to assess my mechanical obstruction hypothesis with heat-killed pathogen, for future work the use of inert fluorescently tagged beads may be a better experimental design. The beads need to be in the same concentration as the infection burden that causes cranial deformation, so further assessment of true fungal burden in the cranium needs to be conducted (see 3.4.4 and 3.6.4).

3.6.6 Pharmacological manipulation of cranial blood volume did not influence cranial deformation in infection.

I designed an experiment in which I treated zebrafish larvae with brain ventricle infection with nitric oxide (NO) manipulating agents L-NAME and SNP, that induce either hypertension or hypotension respectively, to examine if blood volume could affect cranial deformation. The experimental design did not include a blinding strategy for data analysis, which needs to be considered and performed in future work. Blinding could be performed by removing labelling on data files by a third party not involved in the experiment, which is to be revealed when data analysis is complete.

The experiment was conducted with the aim of testing if we can observe changes in intracranial pressure (measured by degree of cranial deformation) induced by changes in cerebral blood flow (CBF). The results showed no effect from the tested compounds. There is no definitive evidence in the literature of L-NAME and SNP inducing significant changes in the cranial vasculature of zebrafish larvae between 1-5dpf. A lot of the work showing significant differences in vessel diameter has been done in peripheral vasculature or in later developmental stages (Fritsche, Schwerte, and Pelster 2000; North et al., 2009; Chhabria et al., 2018). It was important to measure the effect on my treatments on vascular diameter or heart rate, to see if the pharmacological manipulation induced significant differences in the cranial vasculature. Also, observing dynamic changes in cerebral blood flow (CBF) would have increased chances in detecting a significant effect from the treatment programme. It is also important to consider that blood pressure in zebrafish larvae being lower than that in mammalian models due to them residing and developing in an aquatic environment and being mostly in a horizontal position (Parker et al., 2013). This maybe reducing the need for pushing blood flow towards the cranium against gravity and reducing blood pressure effects on the cranial vasculature and intracranial

pressure. Those relationships in the zebrafish are still unclear and it is possible that changes in cranial blood volume may not exert any changes in intracranial pressure. A potential improvement in the experimental design may have been to introduce vasoactive compounds after the initiation in heartbeat and blood flow, and generally later in zebrafish development. L-NAME could reduce haematopoiesis when treatment occurred prior to the initiation of the heartbeat (North et al., 2009), this developmental can be circumvented by introducing the treatment after 24hpf and not skewing results. Neurovascular coupling occurs between 6-8dpf, and it influences how non-neuronal cell types regulate cerebral blood flow (Chhabria et al., 2018), it is important to consider this when assessing CBF in my ventricular infection model, as it may not be a good model of vascular compliance at this stage of zebrafish development.

3.6.7 *C. neoformans* systemic infection in zebrafish larvae better represents dissemination as seen in patients but does not lead to persistent cranial deformation as seen in ventricular infection.

Systemic introduction of the *C. neoformans* inoculum results in a dissemination to the CNS first in the cranial blood vessels and second in the brain parenchyma and/or CSF (Figure 3.10). The exact point of dissemination is unclear from still images, cryptococci localise in most cranial vessels and distribution of infection varies. I was not able to identify hot spots for dissemination. Although the trunk and aorta circulation are completely obstructed by 2.5dpi, there is only 25% mortality in the cohorts infected with 700cfu (Figure. 3.10 panel 3). This is due likely to the embryo ability to exchange gas by bulk diffusion via the body surface (Pelster et al. 2010). There is also no observable difference in cranial size 2dpi when compared to larvae injected with phenol red. Nevertheless, such severe obstruction of vasculature is not seen humans or other models, so cranial deformation even if present may not have been a relevant measurement. As noted above, it is important to consider the blood pressure of the zebrafish larvae as well, fish blood pressure control in generally is less critical than in terrestrial animals due to lower gravitational influences in aqueous habitats (Parker et al., 2013). It is possible that blood pressure influence on intracranial pressure is not as prominent as in humans, and that vascular dynamic do not alter cranial volume in the fish.

3.6.8 *C. neoformans* events of dissemination from zebrafish larvae cranial vasculature are highly technically challenging to capture in long-term time-lapse imaging.

The blood stream infection model at 24hpi shows pathology characteristics like the ones seen in immunocompromised CM patients, characteristics such dissemination of *C. neoformans* from the vasculature into the CNS, localisation of the pathogen into the brain parenchyma and CSF (Offiah *et al.* 2015). In my infection model zebrafish were infected with 700-100 cfu which was efficient in producing cranial vasculature dissemination in all infected larvae and secondary fungaemia (dissemination from cranial vasculature into the CNS parenchyma and CSF) in 63% of larvae. Recent reports of work studying secondary fungaemia in zebrafish larvae show a lot lower incidence of dissemination, which is potentially due to the lower fungal burden they administered at initial inoculation (30-70cfu) (Nielson and Davis *et al.*, 2023). The model was different to mine, as they administered infection at day 1 post fertilisation, at the risk of introducing infection before primary vasculogenesis was complete and before heartbeat and blood flow, at the risk of trapping infection in the periphery (Kugler *et al.*, 2021; Isogai *et al.*, 2003; Quiñonez-Silvero *et al.*, 2020).

The work of Nielson and Davis *et al.*, 2023, was published after my experimental work was concluded. Their insights into the difficulty of capturing dissemination events and on cranial vasculature integrity in infection, reflect what I saw in my work. Events of secondary fungaemia into the CNS were rare (~2.6% of 1,635 instances of single cryptococcal cells disseminated to the cranial vasculature) (Nielson and Davis *et al.*, 2023). Most yeast that was seen to cross the BBB were inside macrophages or microglia and crossed either inside the cells or were taken up shortly after crossing by other means. The microglia seemed to prevent other types of dissemination and to sustain the integrity of the vascular endothelium (Nielson and Davis *et al.*, 2023). My work also shows evidence that capturing events of secondary fungaemia in the zebrafish CNS is difficult as such events are rare (Figures 3.11-3.13). I attempted to capture dissemination in time lapse imaging, in high resolution and in high interval imaging but without success. I captured a single event of dissemination in a still data point (Z stack) in Figure 3.13, D. The cryptococcal yeast cell was seen to “bud off” an AMcTA vessel, unclear if it was through transcytosis, Trojan Horse mechanism (intracellular in a microglia) or disrupting the vasculature.

In the work of Nielson and Davis *et al.*, 2023, larger data sets were collected (day 1-4 observation as opposed 1dpi to 2dpi 24hr time lapse observation) from a greater number of

larvae, but they have shown instances of cryptococci crossing the vascular endothelium, and the captured events involved microglia trafficking of the pathogen into the CNS parenchyma. The rarity of these events would make it incredibly difficult for them to be captured in mammalian brains, as mammalian models cannot be observed in such long periods and in such numbers. In Davis et. al., 2023, it was speculated that dissemination occurs so infrequently because macrophages and microglia are so scarcely seen in the blood circulation, and therefore it is rare for them to aid pathogen BBB crossing, which was observed to be the main mechanism for dissemination (Nielson and Davis et al., 2023). From observing video 3.11 and 3.12, what was noticed in the infection progression over time, it seems as cryptococcal yeast cells are clumping together and appearing to be more clustered in later infection. Previous work in the lab of Simon Johnston, done by Dr Bojarczuk, shows that at 24hpi of 2dpf larvae the majority of cryptococcal yeast cells are within macrophages and that their numbers have barely increased (median increase 0.89) (Bojarczuk et al., 2016), suggesting that the cryptococcal masses observed at 24hpi in my time-lapses are likely within macrophages. This hypothesis can be confirmed by injecting and repeating my time-lapse experiments in the *Tg(mpeg1:mCherryCAAX)sh378* mCherry tagged macrophage reporter line (Renshaw et al., 2016), to count intracellular vs extracellular *C. neoformans* and to confirm previous observations. This work is important as the pathophysiology of cryptococcal meningitis could be looked in a new way if we imagine the majority of the pathogen remains intracellular and the impact on host tissues is not through direct physical interaction with the pathogen cell wall. It is also unclear how CNS tissue resident microglia are behaving, whether they leave the brain to clear the infection, whether they can clear the infection or if they die with cryptococcal cells within them, or if they remain alive for a prolonged period, hiding pathogen within themselves. *C. neoformans* KN99 GFP expresses GFP in the cytosol (Gibson et al. 2017), it is possible that the interactions of the pathogenic yeast cell with the endothelial wall are not clearly seen as the capsule is not visible on the in fluorescent imaging and difficult to visualise for deeper structures in brightfield imaging.

As dissemination events were not detected, I moved on to testing for endothelial disruption more indirectly (Chapter 4). During my investigation of data for secondary fungaemia, I noticed that there may be a difference in the dynamics of the cranial vascular bed in infection, which was also further explored in Chapter 4. I moved on from attempting to capture dissemination events to aiming to characterise the impact of the infection of vascular wall dynamics and permeability.

Chapter 4: *C. neoformans* systemic infection affects cranial vasculature dynamics, size, and blood brain barrier permeability.

4.1 Summary

In Chapter 3 I described the development of a zebrafish bloodstream infection model that mimics features of the human pathology such as dissemination into the parenchyma and CSF. Patients with such patterns of dissemination already exhibit severe symptoms of IH, with advanced pathology and poor prognosis (Charlier et al 2008; Offiah et al. 2015). One gap in our understanding of CM comes from the lack of information on the development and aetiology of pathology prior to the severe presentation commonly present in CM patients. There is need for examining disease progression in early stages of infection, as it could help identify new mechanisms of pathophysiology and identify new targets for development of disease altering treatments.

As described in my introductory chapter, cranial vasculature homeostasis directly impacts CSF secretion and flow (Introduction 1.1). In chapter 4 I aimed to examine the impact of *C. neoformans* infection on cranial vessels dynamics and architecture, in order to identify mechanisms of pathology development that would influence the CSF compartment and contribute to intracranial hypertension. The main objective was to explore infection progression from initial stages to late stages and characterise changes in the cranial vasculature *in vivo* that might alter CSF secretion and flow.

My work identified that in comparison to healthy vasculature (no infection), infected vasculature has a more prominent baseline pulse and undergoes acute, periodic, vascular contractions and dilations I termed “pulsations”. I found that the passage of cryptococcal microcolonies through a cranial vessel result in vessel dilation, redirected flow and was the likely cause of pulsations. The cerebral vascular bed pulsations mostly had a general homogenous rhythm across cranial vessels. The cerebral vascular bed had an overall increase in volume that I argue maybe physiologically significant. I also found that cranial vasculature had an increased permeability during cryptococcal infection that was independent of infection burden.

4.2 Introduction

The metabolic demand of the brain makes for approximately 20% out of the basal oxygen consumption of the body, the brain is a highly vascularised structure and neurons are incredibly vulnerable to oxygen deprivation (Meng et al., 2015). When investigating pathologies of the CNS the cranial vasculature is almost always a major player in disease development, and this is the case for intracranial pressure pathologies. The vascular component has several roles in sustaining ICP homeostasis. The cranium has a fixed volume, introducing an abnormal mass such as a haemorrhage or tumour or pathogens requires a displacement of some of the components of the CNS such as blood and CSF. The capacity of the brain for displacing volume (before pathology) is made mostly through drainage of venous sinuses (Madhok et al., 2018). Arterial pulsations or cranial vasculature is what drives CSF flow in perivascular spaces around the brain (Mestre et al., 2018). CSF is produced through the filtration of blood from vessels at the choroid plexus and BBB, the integrity of vasculature, BP and HR affect CSF production. Reabsorption of CSF also occurs at venules in the glymphatic system, blocking CSF drainage at this level is a possible mechanism for AD pathophysiology (Mestre et al., 2020). Considering the significance of the cranial vasculature in ICP it is an important component of CNS to investigate when examining IH in CM.

Some of the most common neuroradiological features of CM are dilated perivascular spaces and lacunar infarcts (see Introduction 1.2.2). The most common cerebrovascular pathology is lacunar infarcts, and they can present as multiple infarcts (Mishra et al., 2018). Post-mortem work in mice has shown cryptococcal masses blocking small brain vasculature, altering small vessel wall architecture and formation of cryptococcal cysts around capillaries and venules (Olszewski et al., 2004). *In vivo* real-time imaging of *C. neoformans* H99 interactions with the cranial vasculature in mice shows cryptococcal masses getting trapped in small vessels and cryptococci disseminating into the parenchyma from the microvasculature (Shi et al., 2010). Cryptococcal yeast cells are seen to be trapped in locations of vessel narrowing and they are shown to not slow down before trapping, indicating this is a mechanical not a receptor mediated mechanism, such as with lymphocytes (Shi et al., 2010). Murine model studies, however, are limited in assessing changes in the whole system, *in vivo* access to cranial vasculature is limited to pial and superficial vessels. The mechanics of vasculature imbedded into deeper brain structures may differ and there are benefits in looking into the changes in the whole vascular bed in infection, rather than isolated structures, particularly when trying to understand IH.

Furthermore, it has been rare to capture dissemination from the vasculature into the parenchyma in mouse models (1-2% of cranial vessel cryptococcal cells) (Shi et al., 2010) as in general BBB crossing events seem rare. This has limited our understanding of possible pathogenic mechanisms that may arise due to dissemination and what triggers such events. The zebrafish model has potential to bridge this gap as it can provide much larger timespan of observation of infection progression *in vivo* and data can be collected from a larger number of animals before higher severity procedures are required. The larval zebrafish infection model allows imaging of the whole vascular compartment of the cranium at high temporal and spatial resolution. Furthermore, the BBB and BCSF in the zebrafish larvae mimic mammalian structures, by having the same cell type composition in the neurovascular unit (Jeong et al., 2008). Choroid plexus tight junction protein claudin 5a, which is an ortholog of the human claudin 5, is found in the cerebral vessels of zebrafish as early as 3dpf and is in almost all cranial vasculature by day 5 (van Leeuwen *et al.*, 2018). Alongside of composition, in functionality, the cranial vasculature shows restricted permeability as early as 3dpf, by excluding large molecules such as 2000-kDa dextran (Jeong et al., 2008). These similarities in physiology show that pathology of the cranial vasculature in the zebrafish animal models are relevant to the human condition.

In our lab we have used the zebrafish infection model to look at the infection development within intersegmental vessels. What was seen is that single or a very small number of cryptococcal yeast cells get trapped in a blood vessel and develop into cryptococcomas (Gibson et al., 2020). Dissemination of the pathogen can be accompanied by vessel rupture, but this is not necessary. However, data for Dr Gibson's work was collected almost entirely from peripheral vasculature and not cranial vessels, in my project we decided to investigate the cardiovascular pathology in the zebrafish CM model in more detail. Previous work examining the cranial vasculature in the zebrafish cryptococcal infection model, shows that dissemination into the CNS parenchyma occurs mostly by cryptococcal cells crossing the BBB within microglia carriers (Davis et al., 2023). 80% cryptococci in the cranial vasculature on the other hand remained extracellular. Events of parenchymal dissemination from vasculature (secondary fungaemia) were rare, (~2.6% of 1,635 instances of single cryptococcal cells disseminated to the cranial vasculature) (Davis et al., 2023). The microglia seemed to prevent other types of dissemination and to sustain the integrity of the vascular endothelium (Davis et al., 2023). Dextran dye angiogram-like experiments show some instances where the cranial

vasculature was leakier due to infection. However, as in the periphery, vascular disruption was not necessary for dissemination events to occur (Davis et al., 2023).

In chapter 3.5.2, I attempted to capture events of dissemination into the parenchyma in real-time. It captured events of dissemination, but they did not appear to damage the vascular endothelium, i.e., the dissemination did not occur due to disruption of the endothelial wall. In this chapter I aimed to examine further if there is in fact no disruption in the cranial vascular wall integrity. Endothelium integrity in homeostasis is essential for the controlled production and secretion of CSF, and disruption of the vascular wall may skew CSF dynamics into facilitating pressure increase. I also observed a possible difference in the dynamics of cranial vasculature in infection, and in this chapter, I aimed to explore this further by examining in detail vascular wall dynamics in infection in real-time and in high resolution. This work is key for understanding how *C. neoformans* may impact cerebral vasculature pulsability and compliance, factors which greatly influence CSF flow and pressure gradients in the cranium.

4.3 Objectives

1. Examine cranial vessels from early infection and identify any changes in vascular wall dynamics.
2. Examine if there is a change in overall vascular volume of the cranial vascular bed.
3. Examine if there is a change in permeability of cranial vasculature in infection.
4. Test if the effects of the infection are purely mechanical by injecting beads with the same procedure as pathogen was introduced into the blood stream of the zebrafish larvae.

4.4 Results

4.4.1 “Pulsations” - acute cranial vascular volume fluctuations observed during cryptococcal infection.

I sought to examine the development and aetiology of cryptococcal meningitis pathology by using fluorescently labelled blood vessel transgenic zebrafish larvae (*Tg(kdrl:mCherry)*^{S916}) injected with 700-1000cfu of *C. neoformans* KN99 GFP in the Duct of Cuvier (DoC) at 52hpf. Infected larvae were mounted and screened for dissemination of cryptococcal cells into the cranial vasculature. Larvae with infection present in the cranial vessels and controls (uninfected larvae) were imaged from the lateral side. 20hr time lapses were recorded of the mounted larvae

from 1-2hpi, as this was the earliest time point mounting and screening could be completed (Supplementary Video 3.1, 3.2, 4.1, 4.2). Time lapses were examined to identify events of fungal dissemination from vasculature, structural obstruction or other mechanisms of pathology progression that could be of interest. Individual events of dissemination of cryptococci from the cranial vasculature into the brain were never clearly identified. However, there was obvious progression of the infection from the vessels into the parenchyma and CSF over the course of the experiment.

In the examination of the data what came to my attention was the dynamic nature of the cranial vasculature in infection. The central cerebral arteries (CCtAs) in particular were undergoing rapid expansion and shrinking, and at times they appeared to develop cystic-like structures (potentially *kugeln* (Kugler *et al.*, 2019)), but eventually recovered their architecture (Supplementary Video 4.1) (Figure. 4.1). In uninfected larvae (Figure. 4.2) CCtAs showed small pulses only in occasion during the 20hr time lapses, in contrast to infection where the CCtAs were constantly undergoing severe expansions and constrictions (Supplementary Video 4.1 and 4.2). The volume fluctuations seemed to happen simultaneously in several vessels at a time or in just a single vessel, and it was not necessary of vasculature to contain cryptococcal cells to show this phenotype (Supplementary Video 4.1). The CCtAs in control larvae appeared to be elongating with time, the CCtAs in infection were mostly widening with time (Supplementary Video 4.1 and 4.2). Dynamic vasculature volume fluctuation in infection was only observed in the head, other tissue embedded vessels such as intersegmental arteries did not show the same phenomenon (Supplementary Video 4.3). In initial observations of long-time lapses with 5min capture interval, all infected larvae (N=10) showed this rapid expansion and shrinking of vasculature. I termed this phenomenon “pulsations”.

Figure 4. 1 Acute vascular volume fluctuations are seen in infected cranial vasculature.

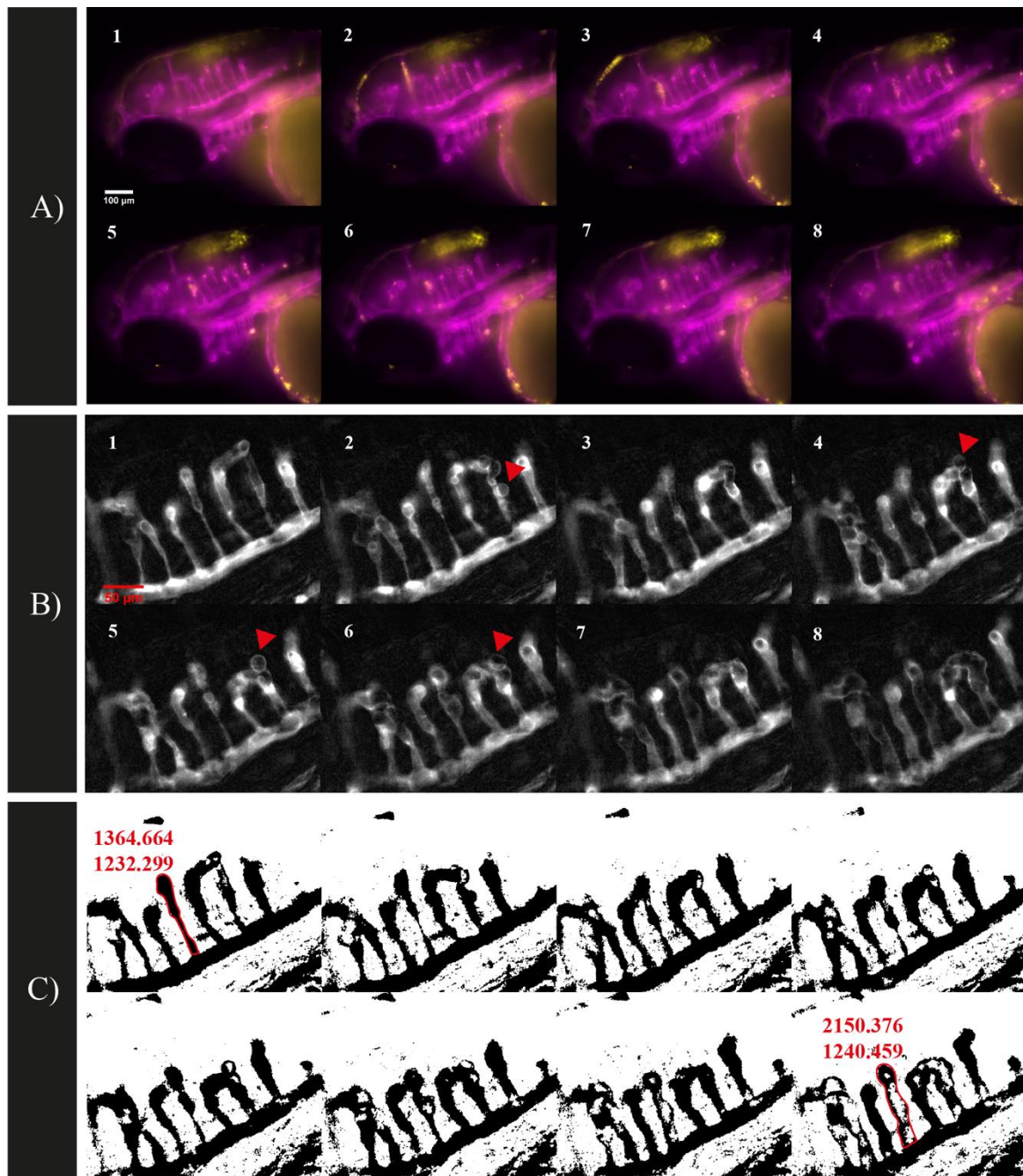


Figure 4.1 Acute vascular volume fluctuations are seen in infected cranial vasculature in 5min image capture interval time-lapses.

This figure is showing a representation (N=10) of a 20hr time-lapse (~60-80 or 80-100hpf) imaging the lateral side of the cranial vasculature of a *Tg(kdrl:mCherry)^{S916}* transgenic zebrafish larvae, 1-2hpi or 20-24hpi in the DoC with *C. neoformans* KN99 GFP (on shown composite images - GFP is yellow; mCherry is magenta). Images in the time lapse represented here (60-80hpf, 1-2hpi) were collected every 5 minutes, the whole time-lapse can be seen in Supplementary Video 4.1. Panel A shows composites of time points 100 minutes apart. Panel B shows a focus on the CCtAs from the same time points shown in panel A, red arrows point to the development of possibly *kugeln* like structures. Panel C shows the binary processed version of images in panel B. For the first and last image the true area of the vessel in red (top number) and the area above threshold (bottom number) are shown in red.

CCtA - central cerebral artery

Figure 4. 2 Acute vascular volume fluctuations are not observed in zebrafish larvae without infection.

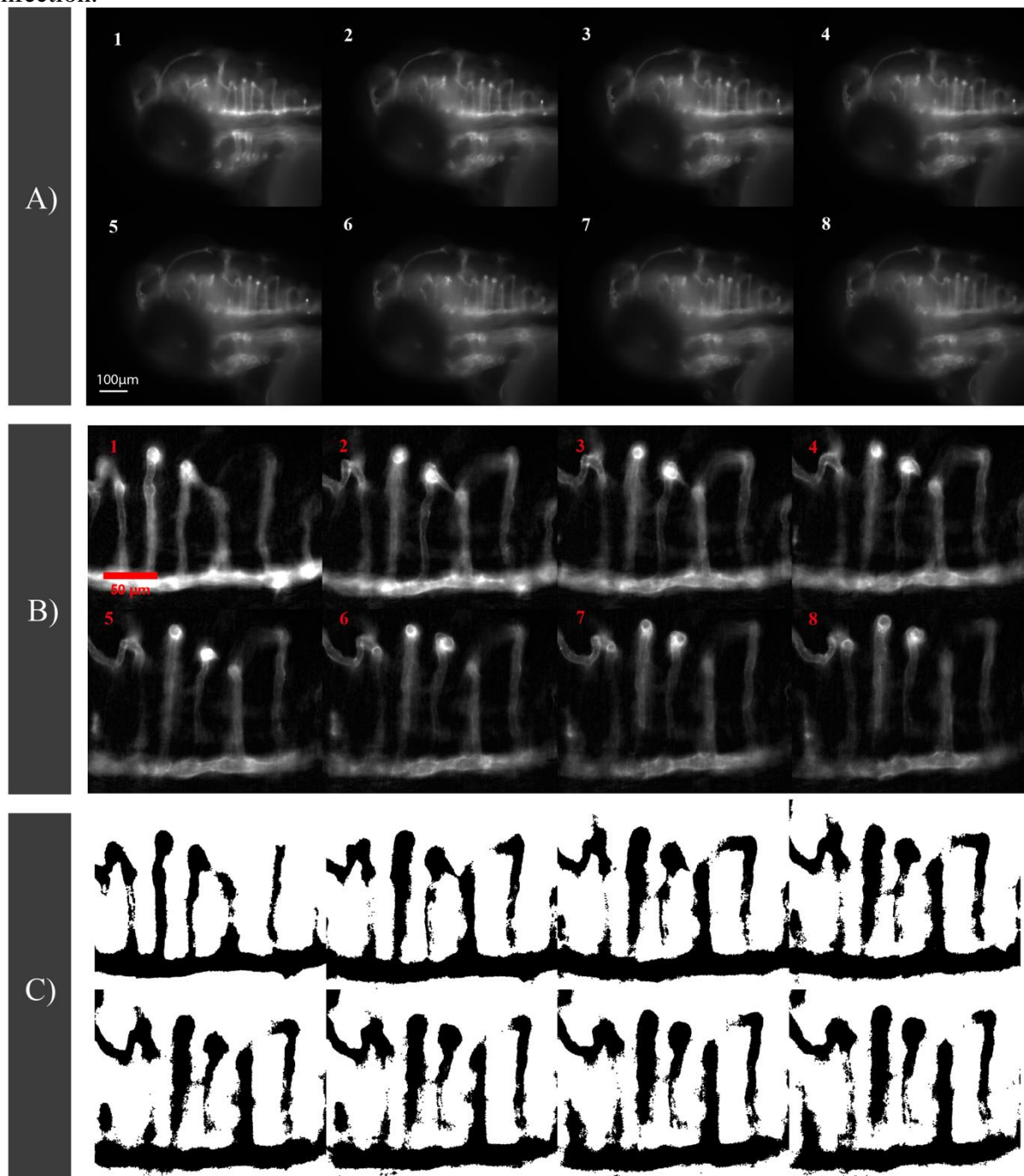


Figure 4.2 Acute vascular volume fluctuations are not observed in zebrafish larvae with no infection in 5min image capture interval time-lapses.

This figure is showing a representation of a 20hr time-lapse (~60-80hpf) imaging the lateral side of the cranial vasculature of a *Tg(kdrl:mCherry)^{S916}* transgenic zebrafish larvae (N=4). Images in the time lapse were collected every 5 minutes, the whole time-lapse can be seen in Supplementary Video 4.2. Panel A shows the mCherry channel with images of time points 100 minutes apart. Panel B shows a focus on the CCtAs from the same time points shown in panel A. Panel C shows the binary processed version of images in panel B. CCtA - central cerebral artery

4.4.2 Intensity and frequency of “pulsations” at higher temporal resolution.

The time lapses represented in Figure 4.1 (Sup. Video 4.1) and 4.3 (Sup. Video 4.3) show the same beginning time point following infection but temporal resolution. The initial strategy of imaging had a larger interval in between image capturing but a longer time span. Initial time lapses had an interval of imaging of every 5 minutes for 20-24hrs (Sup. Video 4.1). Shorter intervals in between image capturing (1-2s) imaging (higher temporal resolution) revealed that the intensity and frequency of vascular area fluctuations were less. Each constriction followed by contraction (pulsation) occurred much more gradually than it appeared in 5min/image time-lapses (Supplementary video 4.3). In time lapses with higher temporal resolution “pulsations” were captured in 6 larvae out of 10 imaged despite the much shorter imaging time frame. The classification of presence of pulsations is not automatically determined but assessed by eye, the prevalence in higher temporal resolution data cannot be yet assessed. A method for an automated quantification needs to be created in order to do that.

4.4.3 Quantification and automated analysis of vessel pulsations from wide-field fluorescence time lapse was not possible.

To quantify the phenomenon of pulsations I required measurement of how the area of the cranial vasculature changed over time. For time lapses (Fig. 4.1, 4.2, 4.4) the analysis involved extracting a time series for a single Z image slice (marking KDRL expressing vascular endothelium) and converting images to binary, so only the area of the vasculature is measured (Fig 4.1C). As the measurements of vascular size were done for a single Z, the data generated was in the form of the vascular area change in 2D over time (lateral view) (Fig. 4.4). Converting images to binary was done automatically using the thresholding tool in ImageJ with background subtraction (example of background subtracted images shown in Fig. 4.1B and 4.2B). In the control group (CNR of mCherry channel images ~ 47; 26 after background subtraction) thresholding of images was specific for the vascular fluorescence (Fig.4.2 and 4.4. Panel 1), but imaging in 2D sometimes meant that the whole vessel was not visible which resulted in image segmentation errors (Fig. 4.1 B and C). In time lapses of infected larvae (CNR of mCherry channel images ~ 62;) even after background subtraction (CNR reduced to 20) and noise de-speckling, the thresholding was unspecific to the vasculature in some areas and showed as noise around vessels (Fig.4.1C and 4.4. Panel 2). A greater problem in the processing of infected larvae time series, was that in an event of vascular dilation, the lumen of the vessels had an absence fluorescence (the fluorescent mCherry marker is expressed in

vascular walls), which meant that the increase in vascular area could not be detected and instead measurements show a decrease in vascular area in 2D (single Z area analysis) (Fig. 4.1C). For example, in Fig 4.1C for the first and last panel, a manual ROIs were drawn around the same vessel for different time points. Measurements of true vessel area and area limited to threshold are shown in red (Fig. 4.1C). The data of dilation is lost following thresholding - in the first time point true vessel area is 1364 px, in the last time point where the vessel appears obviously dilated and the true vessel area is 2150 px but the area limited to threshold for both time points is ~1200 px (Fig. 4.1C). To correct for this, I tested two image processing corrections: Thresholding images of dilated vessels resulted in artefactual holes, therefore I attempted to correct this issue using the Fill Holes tool in ImageJ (Process -> Binary -> Fill Holes) but the tool filled gaps in between vessel instead of within vessels. Secondly, data enhancement was performed using the Tubeness filter in ImageJ but could not produce representative images of the original data.

Data from automated area measurements of time-lapses is shown in Fig. 4.4. Representative panels of threshold images are shown in 1B) and 1C). The infection time lapse measured in Fig. 4.4. 1A) showed relatively good specificity in thresholding but some vessels still had gaps in them after dilation. The control time lapse (no infection) showed good specificity in thresholding. In interpreting the data in Fig.4.4 the aforementioned artefacts of analysis need to be taken into consideration. The measurements of uninfected time lapses (Supplementary Video 4.2) in Fig. 4.4 show an interesting pattern of intervals of sudden volume increase followed by a gradual decrease and then repeat of the same events but in a longer interval (Fig. 4.4. 1C). Volume fluctuation intervals (from expansion to constriction) were between 3-10mins long. Data from the time lapse of an infected larva showed regular volume fluctuation intervals (pulsation-like) with length of each pulse less than 10min (Fig.4.4 2D). In the infection time-lapse, fungal burden in time was also measured (Fig.4.4 2D and 2E). At some point the vasculature rapidly increases in volume after which the volume starts to gradually decrease (Fig 4.4 2D). During the rapid vascular volume increase the fungal burden dips (Fig.4.4 2D). At the point where the vascular volume starts to gradually decrease there is a rapid increase in fungal burden (Fig.4.4 2D and 2E). The vascular data becomes less noisy around the 500th minute of the time lapse, the same is true for the fungal burden data (Fig.4.4 2D and 2E). After that the two values go in the opposite direction with time, fungal burden increases, and overall vascular area decreases (Fig.4.4 2D and 2E). In the control time lapse, there is a general decrease in vascular volume with time as well (Fig. 4.4. 1C).

Automated analysis was trialled on a 5-minute time lapse with an increased temporal resolution (1.7s/capture vs 5min/capture) (Supplementary Video 4.3) (Fig. 4.3). The same issues arose as before, with holes appearing in dilated (Fig. 4.3. – 3B, vessels not in red area). Two adjacent and coupled vessels did not have gaps in them across the time lapse (Fig. 4.3. – 3B, area in red). The automated measurement of volume fluctuations accurately quantified pulsations (Fig. 4.3 – 2, data points outlined in red). The first vessel pulsation (Fig. 4.3 – 2) lasts around 20s, with rapid volume expansion lasting 10 seconds, followed by 10 seconds of rapid volume reduction.

Figure 4. 3 Acute vascular volume fluctuations are seen in infected cranial vasculature in 2s image capture interval time-lapses.

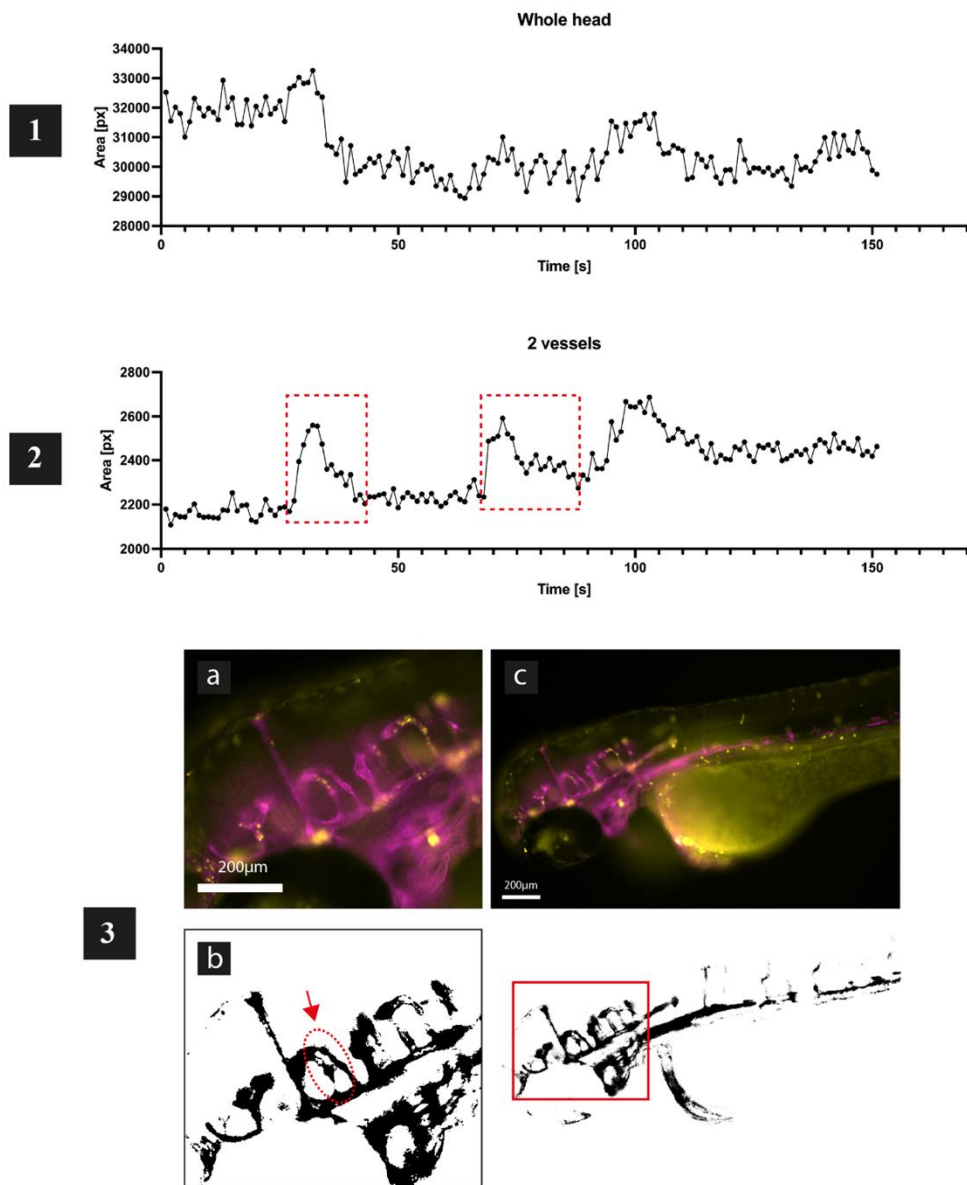


Figure 4.3. Acute vascular volume fluctuations are seen in infected cranial vasculature in 2s image capture interval time-lapses. Intensity of “pulsation” phenomenon does not seem as severe as in 5min image capture intervals.

This figure is showing a representation of a 5-minute time-lapse (N=6) (~60hpf) imaging the lateral side of the cranial vasculature of a *Tg(kdrl:mCherry)^{S916}* transgenic zebrafish larvae, 2hpi in the DoC with *C. neoformans* KN99 GFP (on shown composite images - GFP is yellow; mCherry is magenta). Images in the time lapse were collected every 2 seconds, the whole time-lapse can be seen in Supplementary Video 4.3. Panel 1 shows an automated analysis of the area fluctuations of the whole cranial vasculature (2D) with time. The area quantified is outlined in panel 3a and b. Panel 3b shows a binary image of the mCherry channel (vasculature) of the image represented in panels 3a and c. The area of the vessels outlined in red in panel 3b were quantified in time and the data is shown in panel 2. Data outlined in panel is where a “pulsation” event occurs.

Figure 4. 4 Results from initial attempts of “pulsations” quantification (widefield, 5min/image for 20hrs). Failure at automated vessel area measurements

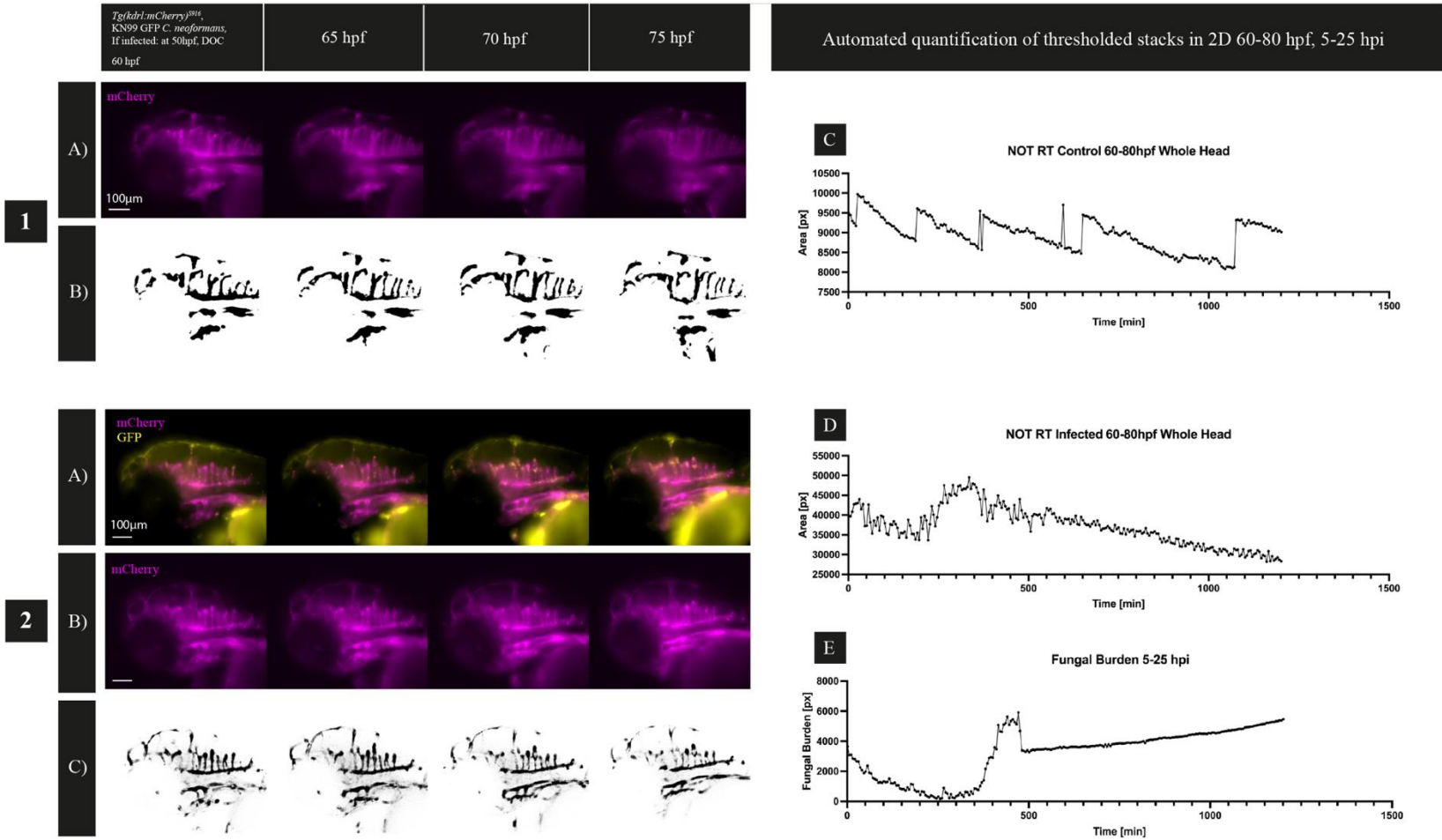


Figure 4.4 Results from initial attempts of “pulsations” quantification (widefield, 5min/image for 20hrs). Failure at automated vessel area measurements.

This figure is showing a representation of a 20hr time-lapses (~60-80hpf) imaging the lateral side of the cranial vasculature of a *Tg(kdrl:mCherry)^{S916}* transgenic zebrafish larvae with no infection in panel 1 and in panel 2 - 3hpi in the DoC with *C. neoformans* KN99 GFP. Images in the time lapse were collected every 5 minutes, the whole time-lapse can be seen in Supplementary Video 4.2 (control) and Supplementary Video 4.4 (infection). Panel 1 and 2 A) show representative images of time points 5hrs apart. Panel 1B and 2C shows the binary processed version of images in panels 1A) and 2B) respectively. Panel 1C and 1D show data from automated quantification of changes in the area of cranial vasculature in time. Panel 2E shows a quantification of the GFP positive pixels in each time point (fungal burden in time).

4.4.4 Implementation of light sheet imaging and high time resolution (<1s) allows for accurate automated quantification of vessel volume fluctuations.

Given the problem with automated analysis, several attempts were made at developing different widefield imaging and analysis (even with high temporal resolution). In most cases images did not lend themselves to accurate thresholding. Thresholding of this data set was accurate with significantly less noise than in other data, but there was still some noise that skewed measurements (Supplementary Video 4.5a and 4.5b). In quantification the data looked like it had a base pulse but when looking at the original time lapse, that base pulse was not visible, the vessels appeared completely static (Fig. 4.5, Supplementary Video 4.5a and 4.5b). The pattern of overall decrease in vessel size was still there, as also seen in Fig. 4.4. Therefore, to perform automated analysis of vessel changes I required images with reduced noise.

With the aim to generate data with less noise, I decided to move to imaging using selective plan illumination or light sheet microscopy. Supplementary Video 4.6 shows a light sheet real time (0.5s/capture) time lapse of a 2dpf *Tg(kdrl:mCherry)^{S916}* transgenic larva 5hpi with 700-1000cfu of *C. neoformans* KN99 GFP in the Duct of Cuvier (DoC) at 52hpf. The baseline pulse of vessels was as a result of the heartbeat and acute volume fluctuations (pulsations) occurred at a larger scale than the baseline pulse (Fig. 4.6 and Supplementary Video 4.6). There was no noise in thresholding of images from light sheet time lapses, in vessel dilatation there were still gaps generated but the Fill Holes tool was able to accurately fill them. The automated quantification accurately represented the baseline pulse and acute pulsations” (Fig. 4.6, Supplementary Video 4.6). Therefore, light sheet imaging was from then used for collecting data on vascular “pulsations”.

Light sheet time lapse imaging demonstrated a clear baseline pulse in all cranial vessels and pulsations occurred as a sudden significant expansion and constriction of vessels. Supplementary Video 4.7 shows a light sheet real time (0.5s/capture) time lapse of a 2dpf *Tg(kdrl:mCherry)^{S916}* transgenic larva without an infection. The focus of both Video 4.6 and 4.7 is a single Z in the larva head showing groups of central cerebral arteries (CCtAs). I performed an automated quantification of CCtAs area fluctuation with time (in 2D) for vessel groups in infection and control (Fig. 4.7). The quantification demonstrated that in both control and infection there is a baseline vessel pulse, but in infection the vasculature is more dynamic with acute and significant fluctuations in volume (pulsations) (Fig. 4.7). In addition, it appeared

that the baseline pulse itself was more visible in the infection, with volume fluctuations even without a pulsation being larger (Fig. 4.7; Supplementary video 4.6, 4.7).

Light sheet imaging of pulsations was recorded from only 2 larvae without infection and 2 with (control). More biological repeats are necessary to set exclusion range (range of volume fluctuation) for automatically identifying pulsation positive and negative larvae. From the time lapses acquired in light sheet imaging, I attempted to characterise singular pulses more closely, I picked criteria such as interval length and synchronicity across vascular tree.

Figure 4. 5 “Pulsations” quantification in widefield microscopy at high resolution and 2s/image – resolution improves automated vessel area measurements.

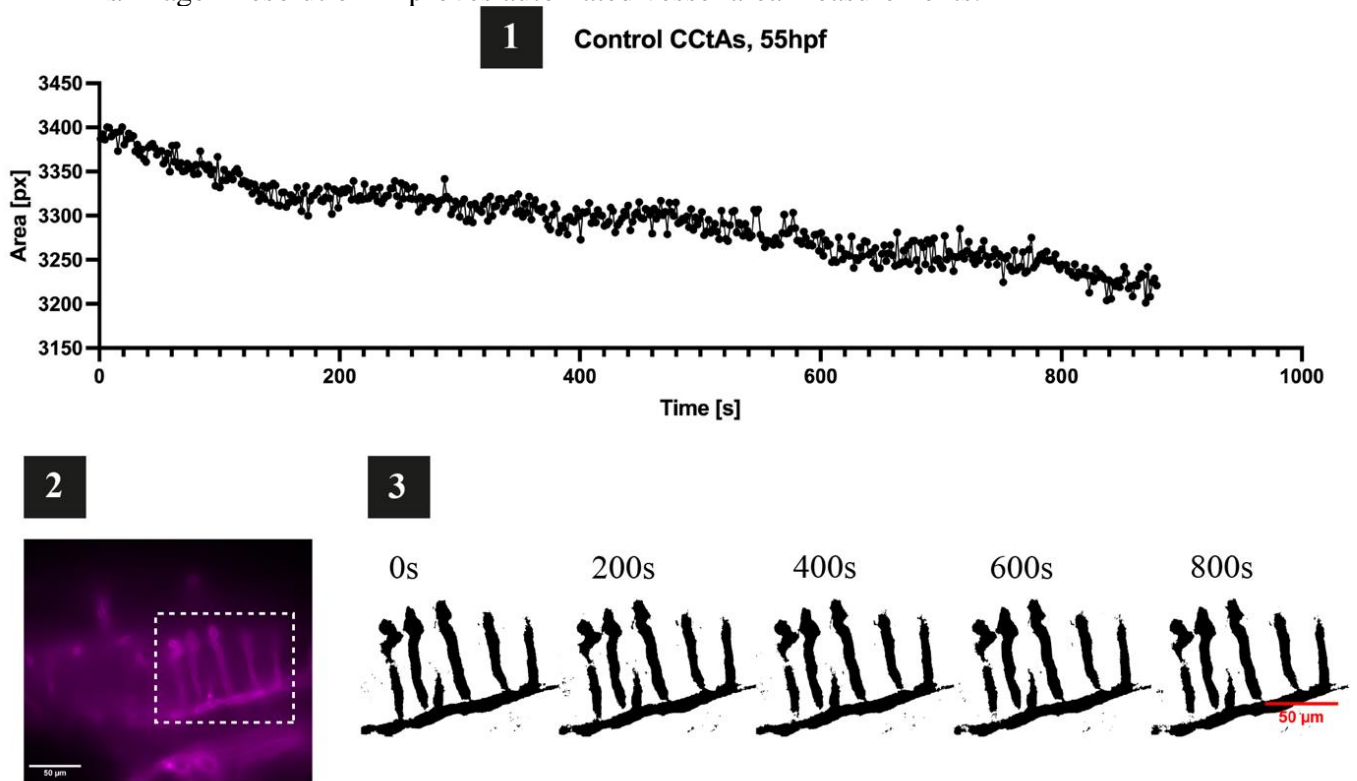


Figure 4.5 “Pulsations” quantification in widefield microscopy at high resolution and 2s/image – resolution improves automated vessel area measurements.

This figure is showing a representation of a 15min time-lapse at 40x magnification, imaging the lateral side of the cranial vasculature of a *Tg(kdrl:mCherry)^{S916}* transgenic zebrafish larvae with no infection. Images in the time lapse were collected every 2 seconds, the whole time-lapse can be seen in Supplementary Video 4.5a. (mCherry) and Supplementary Video 4.5b (binary). Panel 2 shows a representative image of the mCherry fluorescent channel. Panel 3 shows binary processed images of the mCherry channel with focus on CCtAs in different time points. Panel 1 shows automated quantification of changes in the area of cranial vasculature in time.

Figure 4.6 “Pulsations” quantification in light sheet imaging allows for accurate automated measurements of vessel area.

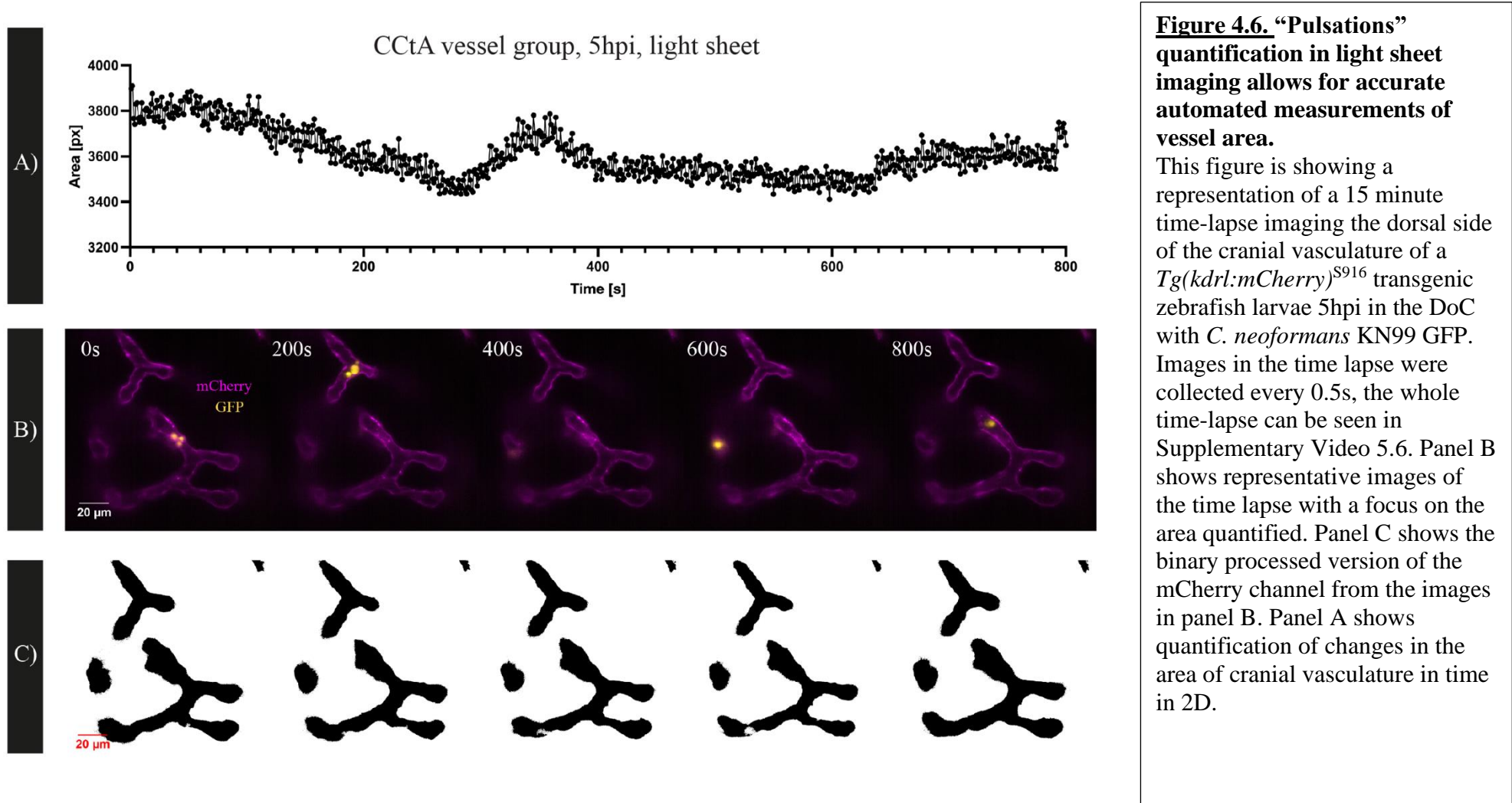


Figure 4. 7 Successful quantification of differences in vascular dynamics in infection and control through automated vascular area quantification in time

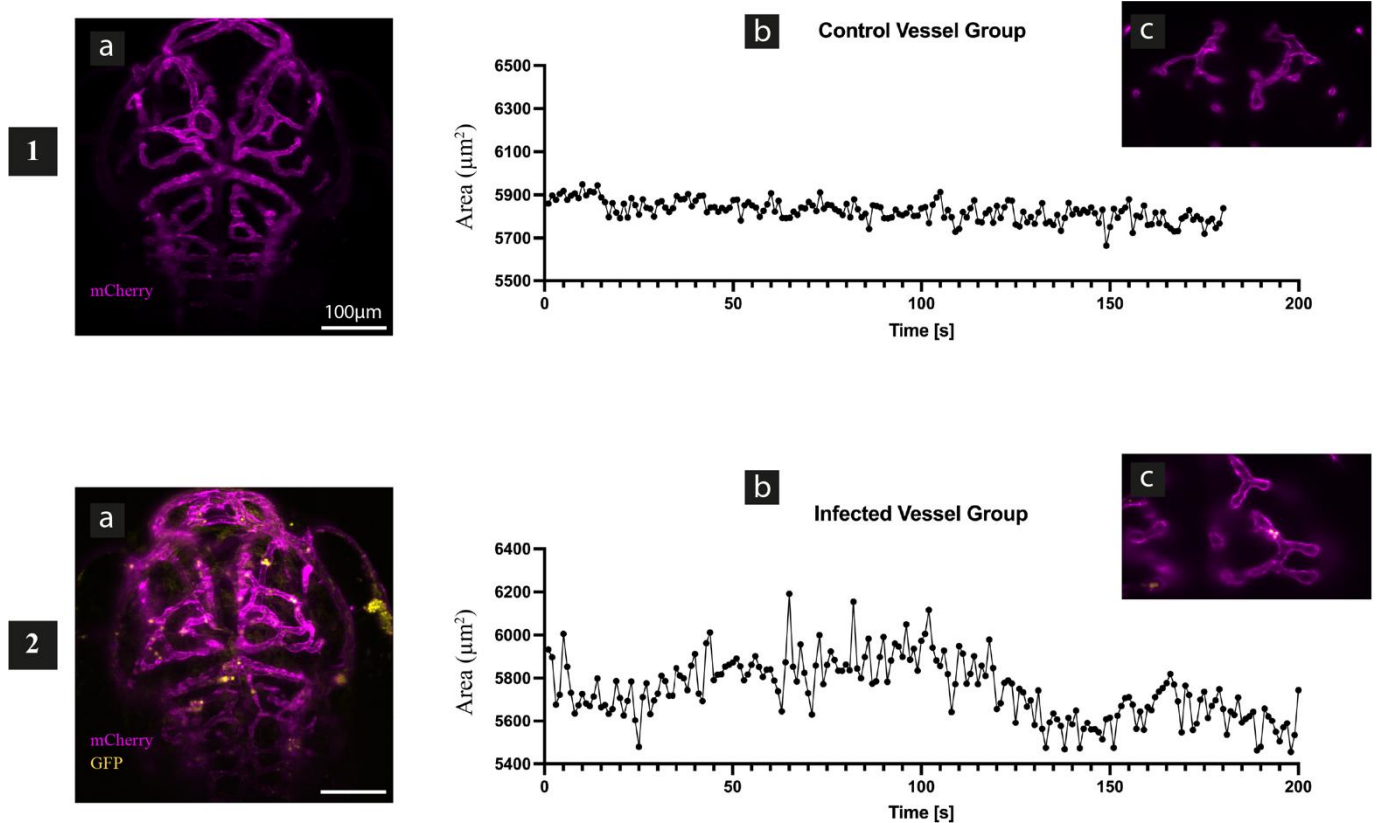


Figure 4.7 Successful quantification of differences in vascular dynamics in infection and control through automated vascular area quantification in time

This figure is showing a representation of a 3 minute time-lapse imaging the dorsal side of the cranial vasculature of a *Tg(kdrl:mCherry)^{S916}* transgenic zebrafish larvae, in control and in 5hpi in the DoC with *C. neoformans* KN99 GFP. Images in the time lapse were collected every 0.5s, the whole time-lapses can be seen in Supplementary Video 4.7 (control) and Supplementary Video 4.6. (infection). Panels 1a and 2a show a maximum intensity projection of the larvae whole cranial vasculature. Panel 1b and 2b show a quantification of changes in vascular area in 2D (a single Z) with time for CCTAs in the areas shown in panels 1c and 2c. Light sheet imaging of pulsations was recorded from only 2 larvae without infection and 2 with (control).

4.4.5 Characterisation of pulsation intervals and synchronicity across vascular tree

I characterised the nature of pulsations in infection by measuring the changes in two different vessel groups in the same infected larva (Supplementary Video 4.6; Fig. 4.8). It appeared that the two vessel groups had a similar profile and rhythm of volume fluctuation, with the exception of one more acute dip in vascular area in vessel group 2 (Fig. 4.8). Vessel group 1 had 8 events of cryptococcal masses passing through, vessel group 2 had one event. Event of fungal cells passing through in vessel group 1 were short, the cryptococci passed through in a couple of seconds (Fig. 4.8 - 1). The single event of passing in vessel group 2, however, lasted about 2 minutes, that was in the middle of a gradual volume reduction part of a pulsation. Immediately before the cryptococcal cells leave the vessel there is sudden increase in vessel volume, it looks like an inflow of blood pushes on the blockage and expels it (Fig. 4.8 - 2). Volume fluctuations during event M1 in vessel group 2 were reflected in vessel group 1, demonstrating how a transient blockage in one vessel group could possibly be affecting the dynamics of another, although it is not a direct proof of a relationship.

From the vessel groups in Figure 4.8, a single pulsation within each group was examined closely. For vessel group 1, pulsation 1 was characterised in Fig. 4.9. The pulsation lasted 3.3 minutes, with 2.2 minutes of vessel area decline and less than a minute (0.78s) of vessel area increase (Fig. 4.9). From the smallest vessel area to the largest, there is a 1.1 mm^2 difference (Fig. 4.9). For vessel group 2, pulsation 2 were characterised in Fig. 4.10. The pulsation also lasted for 3 minutes, with 1.4 minutes of vessel area decline, 15s of stable volume and 44s of vessel area increase (Fig. 4.10). From the smallest vessel area to the largest, there is a $15 \text{ }\mu\text{m}^2$ difference. For both pulsations the decline in vessel area lasted about double the time it took for the vessel to increase its area back to baseline, or about the time during which vessels abnormally constrict with the area of a vessel group fluctuates with about 10-15%.

Figure 4. 8 Area fluctuation of separate vessel groups in the same infected larva – Evidence of synchronicity across pulsations

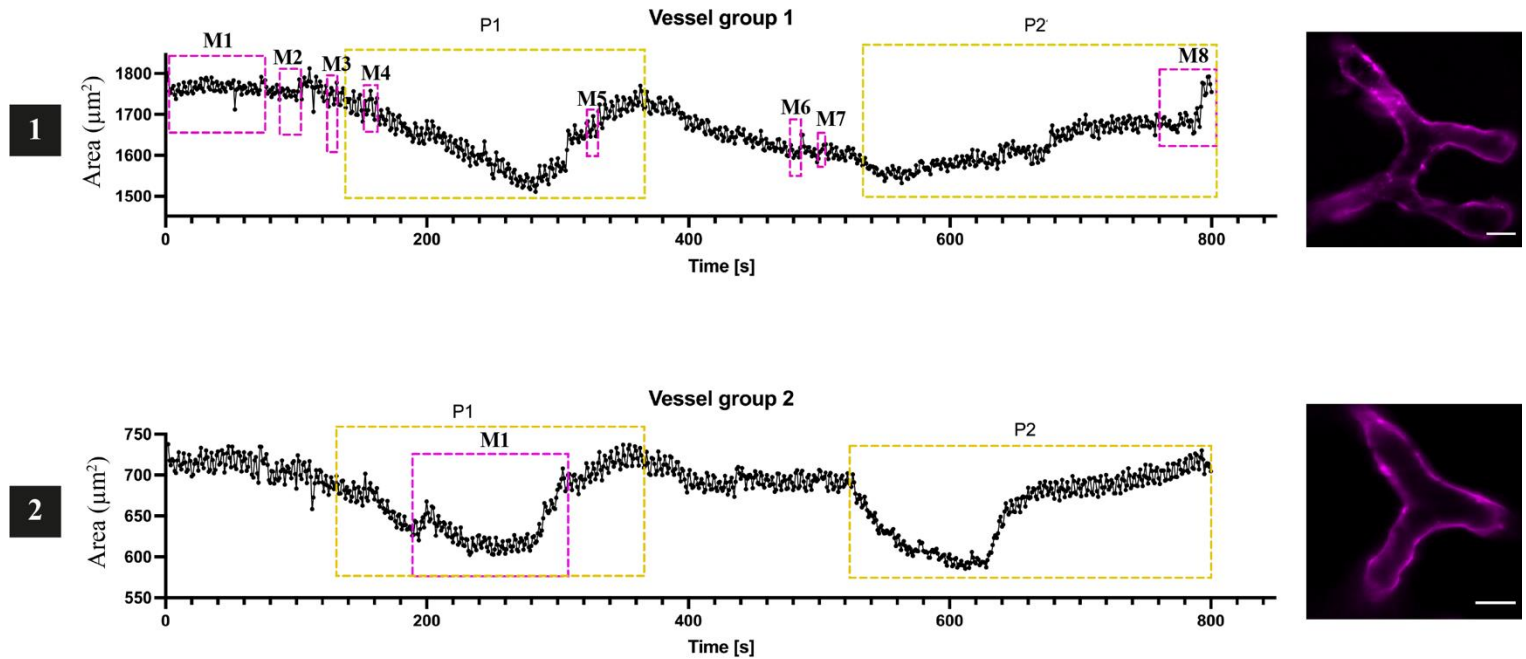


Figure 4.8 Area fluctuation of separate vessel groups in the same infected larva – Evidence of synchronicity across pulsations

CcTA vessels in measured are from the head of a dorsal plane imaged *Tg(kdrl:mCherry)^{S916}* zebrafish larvae 52hpf, 5hpi with *C. neoformans* KN99 GFP (Supplementary Video 4.6). This figure shows data from vessel group 1 and 2, which are both in the same fish and imaged at the same time. Each panel represents the fluctuation in area of a whole vessel group. The purple boxes over certain data points delineate an event of a *C. neoformans* mass passing through the vessel in question (M1= mass 1, etc.). The yellow boxes delineate an event of acute area change with no presence of *C. neoformans* within the vessel group (P1 = pulsation 1). Panel 1 visualises measurements from a vessel from group 1. This vessel has 8 events of *C. neoformans* mass passage. Panel 2 visualises measurements from a vessel from group 2. This vessel has 1 event of *C. neoformans* mass passage and one obvious event of a pulsation (acute area fluctuation).

Figure 4.9 Time interval of a single pulsation event and range of volume fluctuation – vessel group 1

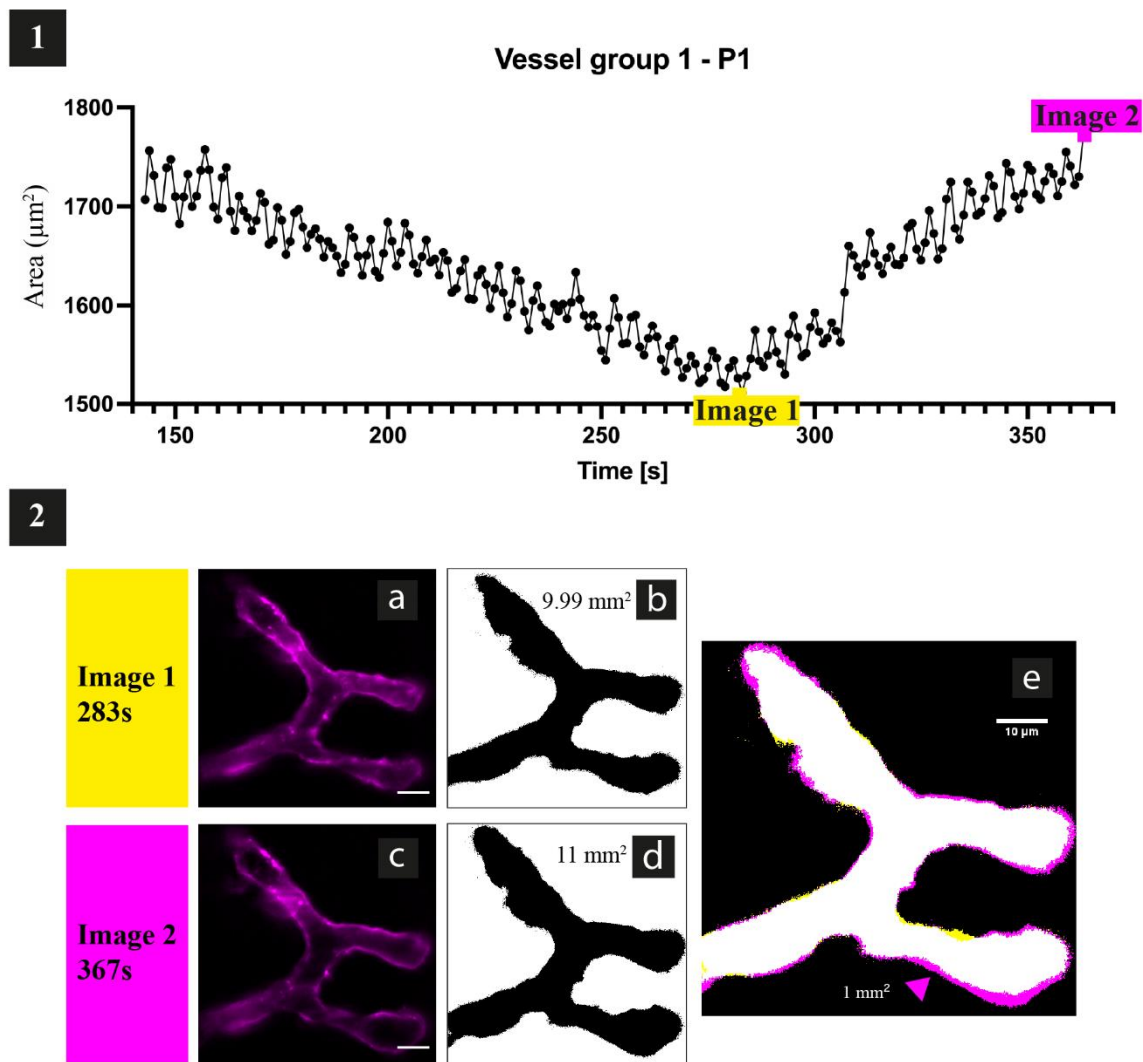


Figure 4.9 Time interval of a single pulsation event and range of volume fluctuation – vessel group 1

The CCtA vessels in focus are from the head of a dorsal plane imaged *Tg(kdrl:mCherry)^{S916}* zebrafish larvae 52hpf, 5hpi with *C. neoformans* KN99 GFP (Supplementary Video 4.6). This figure focuses on a part of the time lapse where the vessel group undergoes an acute volume change in less than one minute. The vessel area fluctuation happens while two blockages are passing through the vessel group (Fig.4.8). Panel 1 shows the area fluctuation of the vessel group for every second over 200s. The time period in panel 1 is 1/4th of the whole time-lapse in Supplementary Video 4.6. From around 150s to 283s into the panel 1 section, the area of the vessel group is on a decline until it drops to 9.99 mm² (panel 2a and 2b). The area of the vessel group then it very rapidly goes back up to 11 mm² (panel 2c and 2d). In panel e masks of image 1 and image 2 are merged to show visually the difference between the two states of constriction (panel 2a, b) and expansion (panel 2c, d). In panel e, the magenta colour shows the difference in the size of the two states, it is about 1 mm². The scales in panel 2 are 10 µm in width and 5 px in height.

Figure 4.10 Time interval of a single pulsation event and range of volume fluctuation – vessel group 2

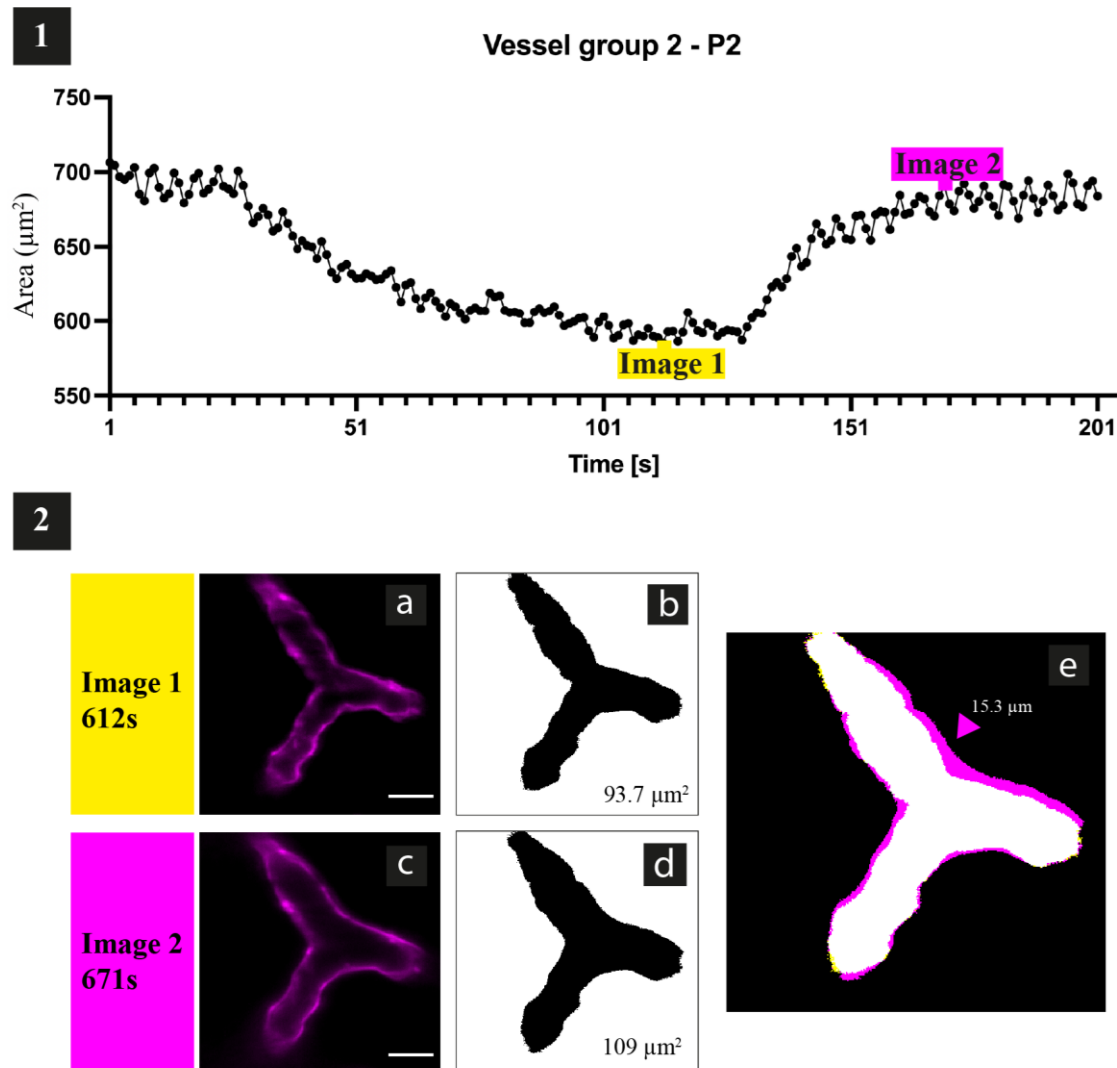


Figure 4.10 Time interval of a single pulsation event and range of volume fluctuation – vessel group 2

The CCtA vessels in focus are from the head of a dorsal plane imaged *Tg(kdrl:mCherry)^{S916}* zebrafish larvae 52hpf, 5hpi with *C. neoformans* KN99 GFP (Supplementary Video 4.6). This figure focuses on a part of the time lapse where the vessel group undergoes an acute volume change in less than one minute. The vessel volume fluctuation does not happen while any blockages are present in the vessel group. Panel 1 shows the volume fluctuation of the vessel group for every second over 200s. The time period in panel 1 is 1/4th of the whole time-lapse in Supplementary Video 4.6. From around 15s to 112s into the panel 1 section, the volume of the vessel group is on a decline until it drops to 93.7 μm^2 (panel 2a and 2b). The volume of the vessel group stabilises for about 15s until it very rapidly goes back up to 109 μm^2 (panel 2c and 2d). In panel e masks of image 1 and image 2 are merged to show visually the difference between the two states of constriction (panel 2a, b) and expansion (panel 2c, d). In panel e, the magenta colour shows the difference in the size of the two states, it is about 15 μm^2 . The scales in panel 2 are 10 μm in width and 4 px in height.

4.4.6 Vascular wall shape is disrupted in infection to apparently accommodate passing of *C. neoformans* masses.

After exploring the dynamic volumes of the cranial vasculature in infection, we wanted to observe the physical interactions of the pathogen with the vessel endothelium. Cryptococcal cells passing through vessels caused deformation of the vessel wall (Fig. 4.11. a2). Once the cells left the vessel, there was remaining disruption of the vessel wall shape (Fig. 4.11. a3 and b4). This suggested that vessel endothelial wall may have degree of plasticity. In support of this hypothesis, I determined how deformation remained after it was formed. This was complicated by multiple fungal cells passing through the same vessel (Fig. 4.12). The second event of passage (89s after event 1) expanded the vessel wall further at the same point (Fig. 4.12. a2). Between event 1 and 2 the vessel wall begins to retract back (Fig. 4.12 b, 0-89s). The following events of cryptococcal cell passage did not stretch the wall further at the point of the first dip (Fig. 4.12). Overall, the vessel wall gradually retracted back but the deformation was still visible, until a pulsation occurs at 763s and expands the whole vessel, and the deformation become less prominent (Fig. 4.12). It seems that before the pulsation the deformation remains visible for over 10 minutes.

Vessel group 2 had only one event of cryptococcal cell passage (Fig. 4.8 and 4.13). Between 0 and 200s of the time lapse the vessel area was between 175-200px, around 200s there was large increase in vessel volume from cryptococcal cells entering the vessel (Fig. 4.13). While the yeast cells remain the vessel volume stabilised, after which the cells appear to push on the vascular wall, cause deformation and before completing their passage through the vessel (Fig. 4.13 A4, A5). The deformation was most apparent at the points of vessel branching (Fig. 4.13 D5). After the yeast cells pass through the area of the vessel increases overall to between 200-225px, for around 3 minutes until there was a pulsation starting at 520s (Fig. 4.13 graph). Even during the pulsation, the stretch at the base of the vessel remains (Fig. 4.13 6A, 6D) and the vessel expansion after the pulsation causes a further increase in vessel area (Fig. 4.13 7D) i.e., the passage of cryptococcal cells appeared to make the vessel more prone to dilation. In addition, while the cryptococcal cell passed through the vessel, there was a widening in the connected vessel, possibly due to redirection of blood volume (Fig. 4.13. C3,4)

Figure 4. 11 Vessel architecture disruption in infection – vessel 1, single event

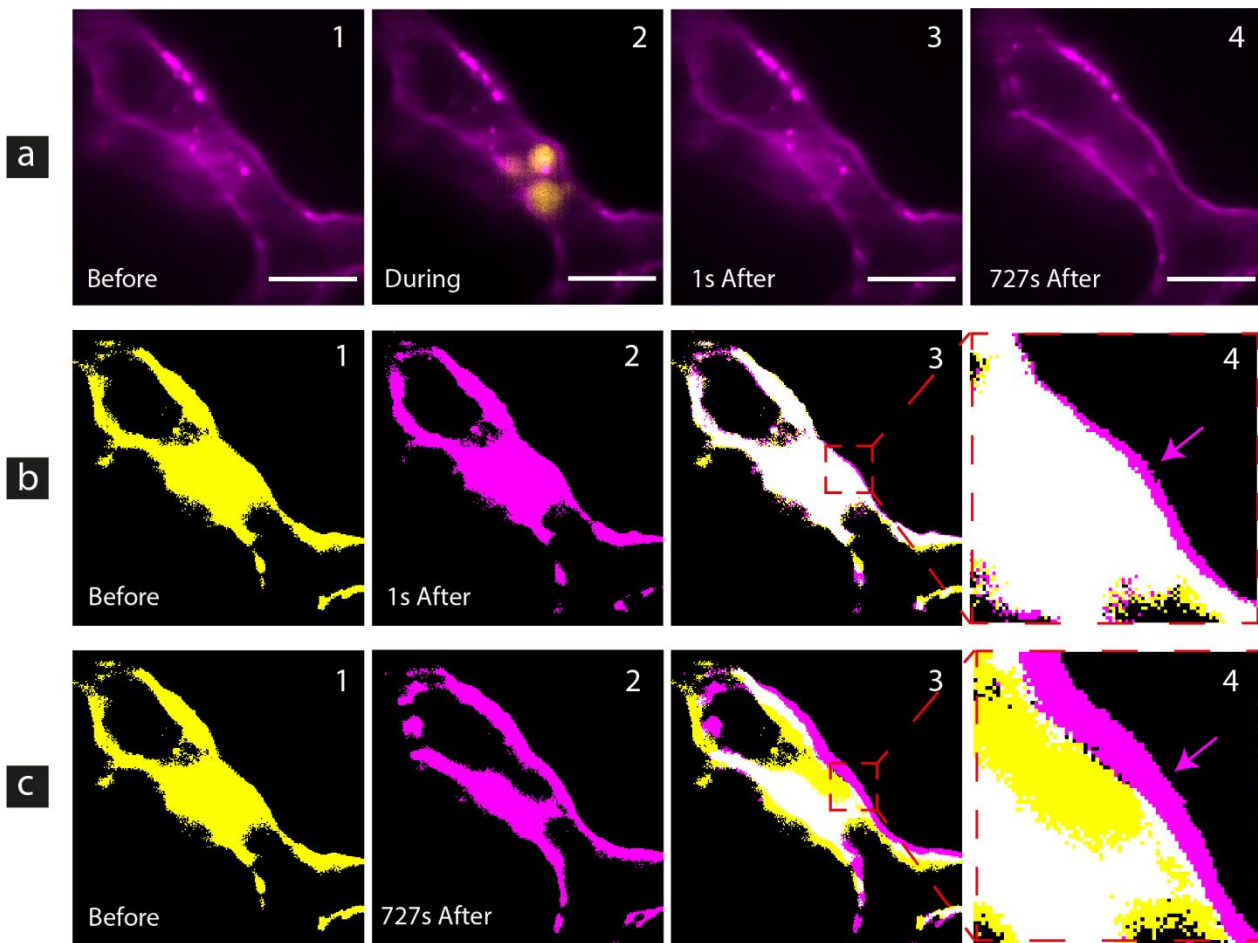


Figure 4.11 Vessel architecture disruption in infection – vessel 1, single event

The CCtA vessel in focus is from the head of a dorsal plane imaged zebrafish larvae 52hpf, 5hpi with *C. neoformans* KN99 GFP (Fig. 4.8, Fig. 4.9, Supplementary Video 4.6). In panel a1 we can see the vessel in focus devoid of any cryptococcal yeast. Panel a2, represents a time point after panel a1 where the vessel becomes obstructed by a clump of 3 stuck together cryptococcal yeast. The clump pushes on the vascular wall and stretches it out (panel a2). In panel b2 we can see a thresholded mask*of the image in panel a3, seconds after the clump passes through the vessel. Observe panel b4, when overlayed with the mask of the vessel before the clump passes through (panel b1), it seems that in panels a3 and b2, the vessel wall is slightly wider around the point where the clump of *C. neoformans* previously applied pressure. The difference between panel b1 and b2 is shown in magenta in panel b4. Following the passage of the yeast clump, the vessel retains structural changes and does not revert to its original architecture (panel b4). Panel a4 shows the vessel in focus 727 seconds after the clump of yeast passes through it. In panel c4 we can see that the shape of the vessel has changed considerably (c4, magenta area). This change is not directly a result of the clump passage in a4 (See Fig. 4.12). It is not just the size and shape of the vessel that changes but also its position in the tissue (panel c4). The scales in panel are 12um in width and 4px in height.

*Images in panels b and c were thresholded with the same range (1309/65535). Following thresholding the images were converted to mask and added artificial colour. For panel b4 and c4 overlays mask images were turned into a composite.

Figure 4. 12 Vessel architecture disruption in infection – vessel 1, 8 events

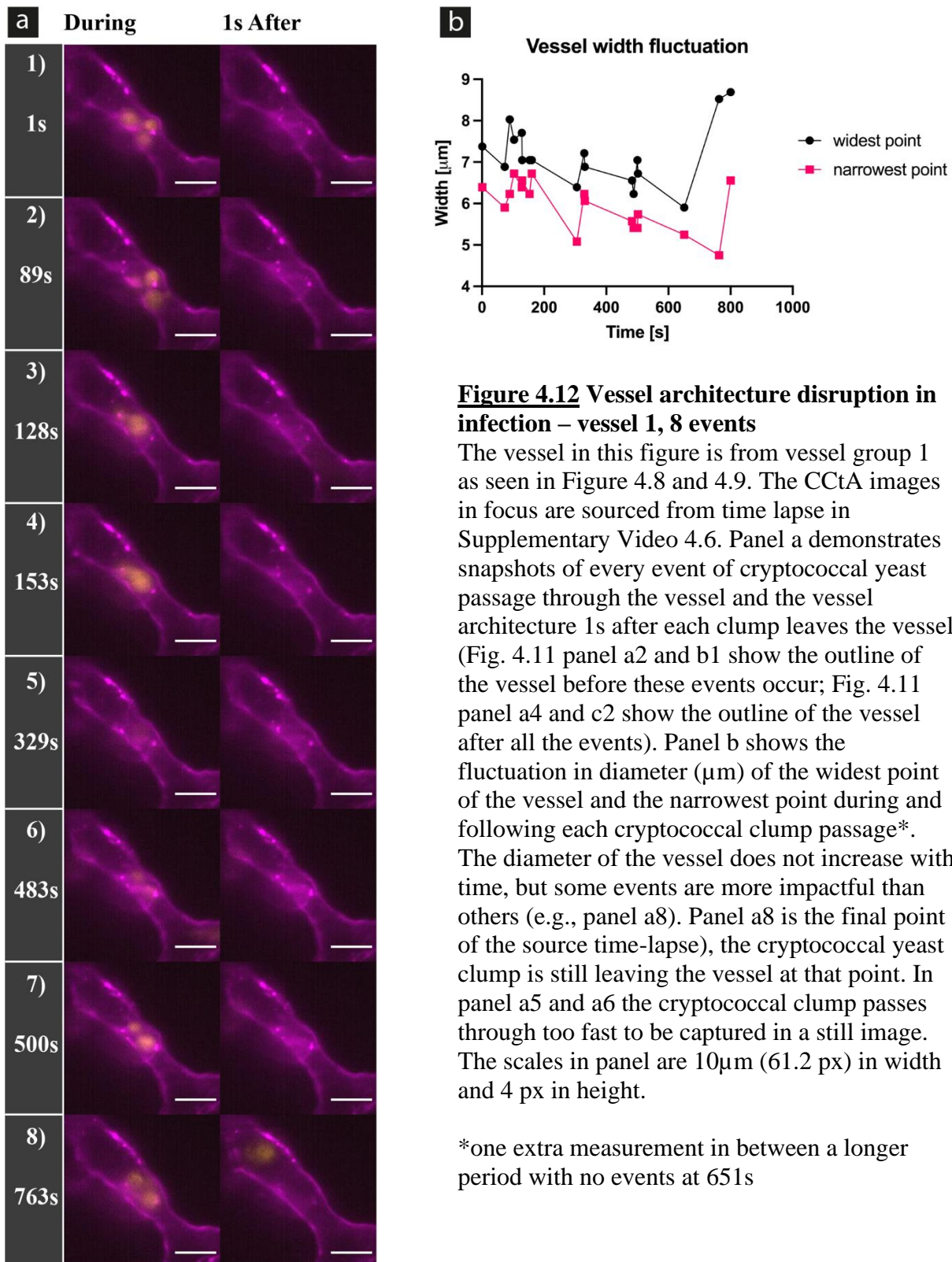


Figure 4.13 Vessel architecture disruption in infection – vessel 2, single event

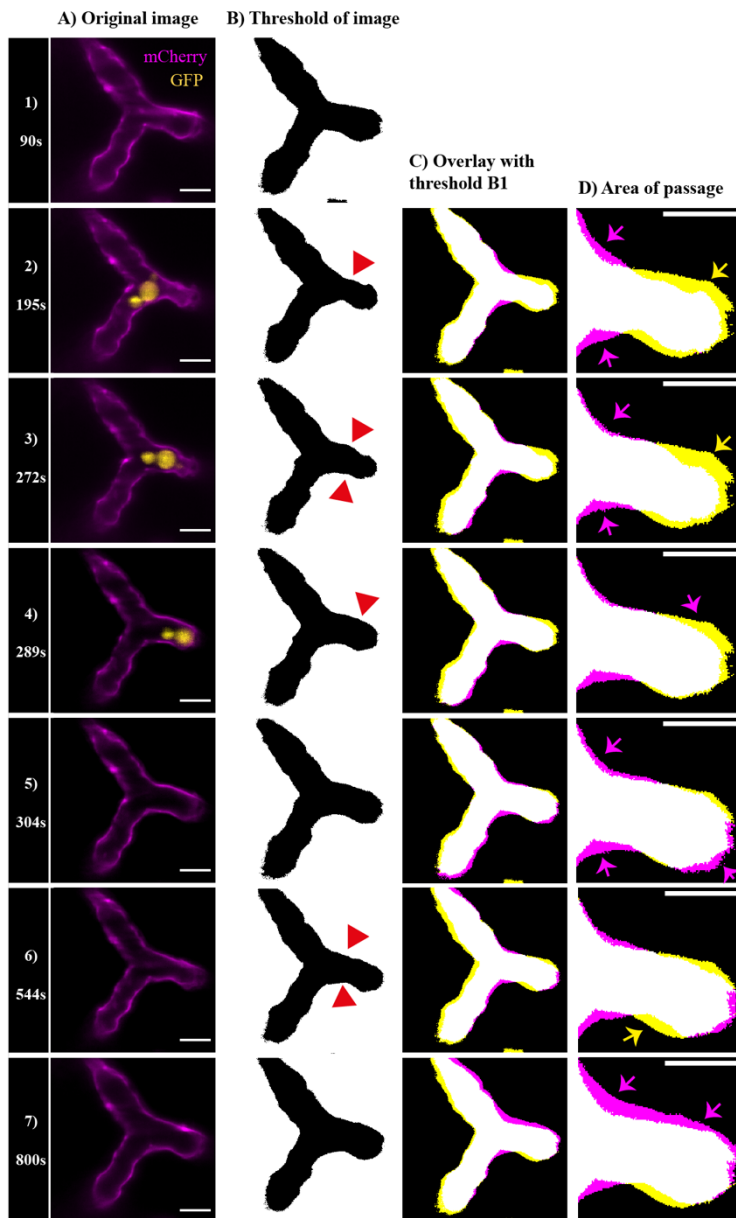
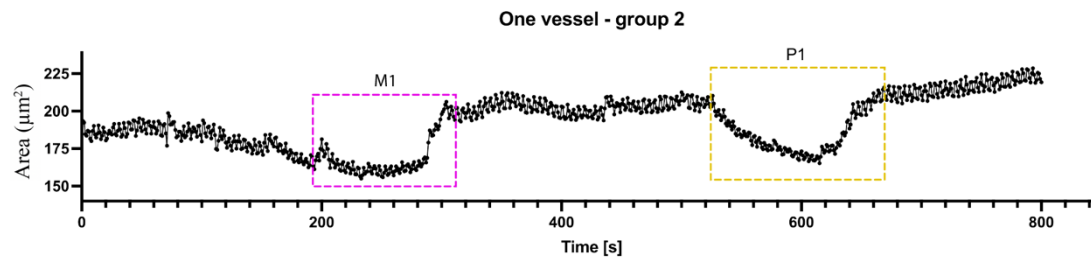


Figure 4.13 Vessel architecture disruption in infection – vessel 2, single event

The CCtA vessels in focus are from the head of a dorsal plane imaged *Tg(kdrl:mCherry)^{S916}* zebrafish larvae 52hpf, 5hpi with *C. neoformans* KN99 GFP (Supplementary Video 4.6). The graph represents a quantification of the area of a single vessel represented in column D. B1 is a cryptococcal mass of cells passing through the vessel and P1 is a pulsation. Column A shows the original images of the vessels in focus. Column B is the thresholded image of the KDRL channel (vessels only). Columns C and D represent an overlay of panel B1 (time point 1) with the thresholded image of a following time point, in magenta we see the areas where the vessel has widened in different time points (Yellow = time before any cryptococcal yeast pass through vessel; Magenta = all time points after). Column D is more specifically focused on the vessel that the *C. neoformans* clump passes through (Yellow arrow = new narrowing; Magenta arrow = new widening). Throughout the whole time-lapse only one *C. neoformans* clump passes through a vessel in focus (panel A2-4). In column B the red arrows point to the shape of the vessel being altered as the clump passes through or as a result of a “pulsation”.

4.4.7 Volume of cranial vasculature is increased by cryptococcal infection

During cryptococcal infection I observed that the baseline pulse of cranial vessels became more pronounced, there were acute volume fluctuations as vessels dilated and cryptococcal cells passed, and they become more susceptible to stretch in pulsations. Therefore, I hypothesised that the strain on the vascular endothelium would result in widening or increased in the total volume of the cranial vascular bed.

To quantify cranial vascular volume, I used a previously developed tool for 3D vascular voxel-based volume quantification (Kugler *et al.*, 2019). This tool used the ImageJ Tubeness Plugin to enhance vascular registration, based on Sato (Sato *et al.*, 1997), and implemented by Mark Longair, Stephan Preibisch and Johannes Schindelin (Schindelin *et al.*, 2012). The 3D viewer ImageJ plugin (Schmid *et al.*, 2010) was used to look at the data before and after tubular filtering (Fig. 4.14). In the enhancement some of the data of vessel volume seemed to be lost. Wider vessels were getting registered as 2 different structures and vasculature seemed a lot thinner overall, that was particularly visible in the 3D rendering of the data (Fig. 4.14). Adjusting the enhancement parameters did not seem to improve registration of the vascular width. Therefore, 3D cranial vascular volume quantification the Z stack data was not enhanced using the Tubeness Plugin. Z stacks were globally thresholded using the automated Otsu thresholding (Otsu 1979) and the volume was calculated using the Segmentation step of the ZVQ tool as seen in Kugler *et al.*, 2022. Results can be seen in Fig. 4.15.

Overall cranial vasculature volume was higher in infection than in control larvae, but with a p-value of 0.39 (Fig. 4.15). The power of this experiment was estimated based on the sample size, statistical test chosen (Mann-Whitney) and the effect size, and my calculations showed 40% power. Standard requirements for experimental power in research in 80-90% power (Jones, Carley, and Harrison, 2003). In future experimental plans, a sample size of 30/group would allow for 80% power to be achieved.

Fungal volume was quantified in the same way vascular volume and a linear regression was analysis was performed, the goodness of fit R^2 is 0.63, which means that 63% of vascular volume variation could be accounted for by fungal burden. Therefore, it is demonstrated so evidence of a relationship between the two variables (Fig. 4.15).

Figure 4.14 Cranial vasculature volume quantification in 3D – before and after tubular enhancement

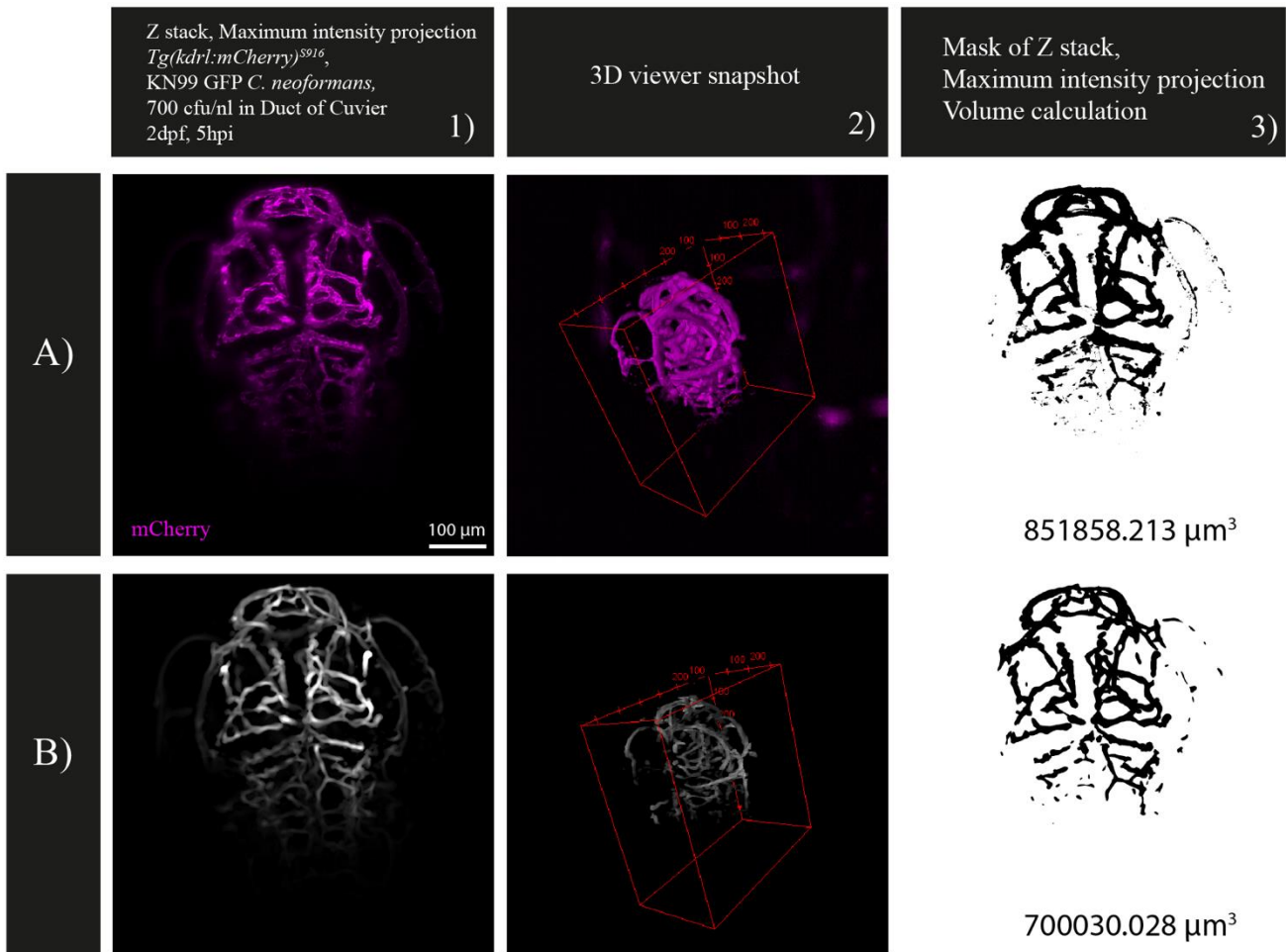
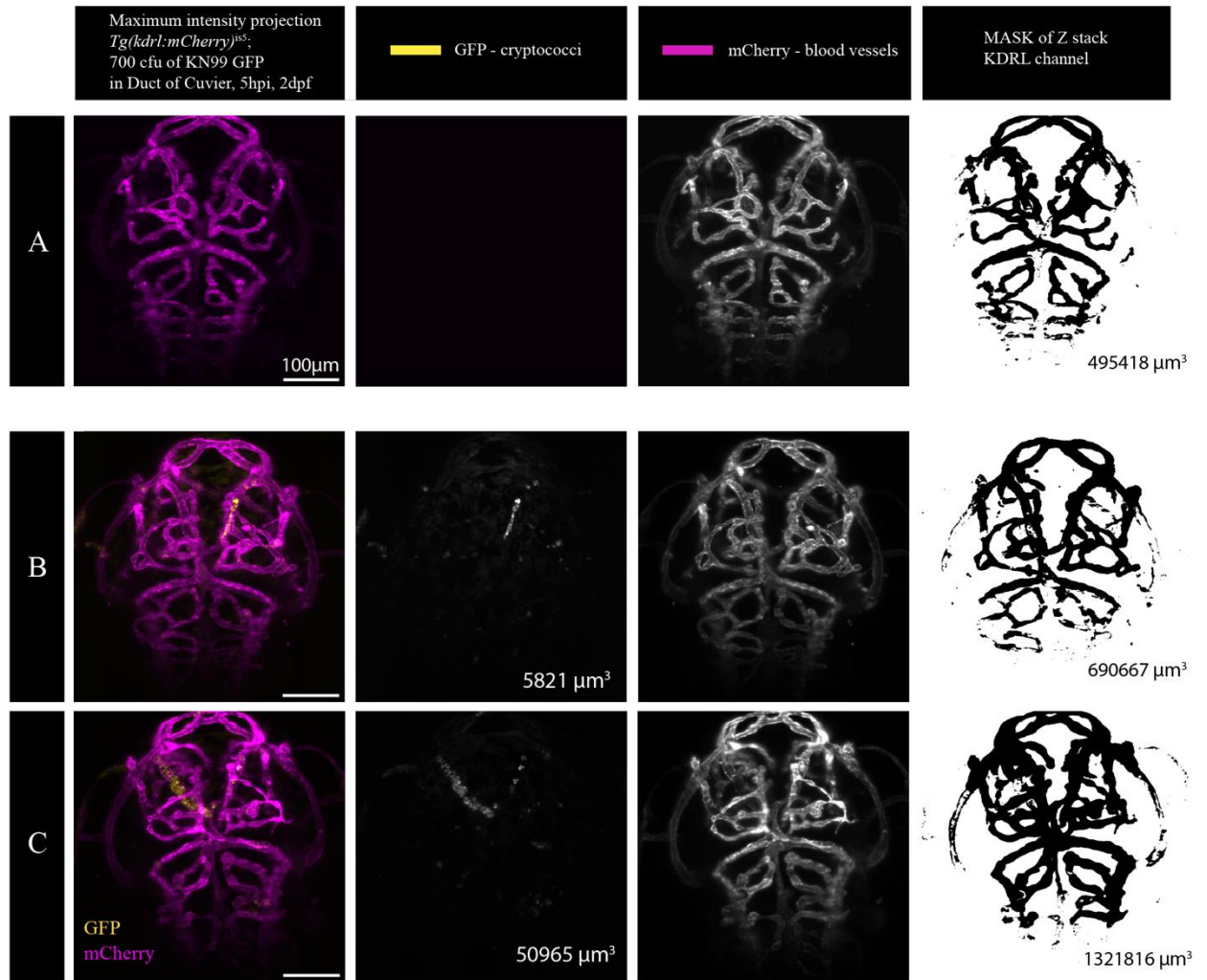


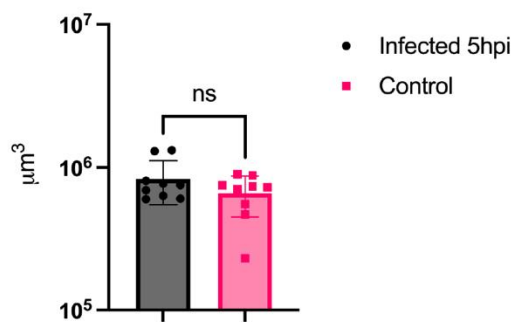
Figure 4.14 Cranial vasculature volume quantification in 3D – before and after tubular enhancement

This figure shows a representation of Z stacks data collected from imaging the dorsal side of the cranial vasculature of a *Tg(kdrl:mCherry)^{S916}* transgenic zebrafish larvae 5hpi in the DoC with *C. neoformans* KN99 GFP. Data was collected using a Zeiss Z1 Lightsheet Microscope as described in Section 2.4. The Z stack data was visualised in 3D using the 3D viewer plugin in ImageJ (Schmid *et al.*, 2010) and shown in column 2. In panel B), raw data Z stack (panel A) was enhanced using the Tubeness plugin in ImageJ (Sato *et al.*, 1997; Schmid *et al.*, 2010). In column 3, the raw data and enhanced were thresholded using global Otsu thresholding (Otsu 1979) and volume was calculated as seen in Kugler *et al.*, 2019. The volume values are shown in numbers over the thresholded Z stacks in column 3.

Figure 4. 15 Cranial vasculature in volume quantification in 3D – volume of vasculature in bigger in infection and is not correlated to infection burden



D Total Volume of Cranial Vasculature



Mann-Whitney test for panel D;
 two tailed p; $p=0.39$

E

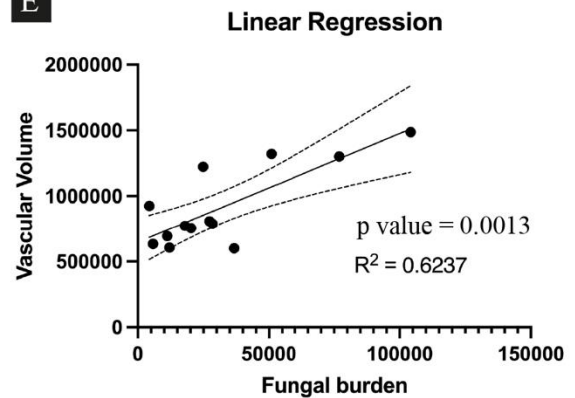


Figure 4.15. Cranial vasculature in volume quantification in 3D – volume of vasculature in bigger in infection and is not correlated to infection burden

This figure shows a representation of Z stacks data collected from imaging the dorsal side of the cranial vasculature of a *Tg(kdrl:mCherry)^{S916}* transgenic zebrafish larvae 5hpi in the DoC with *C. neoformans* KN99 GFP. Data was collected using a Zeiss Z1 Light sheet Microscope as described in Section 2.4 of Methods. In column 1 MIPs of raw data can be seen, with the GFP channel and mCherry channel represented in column 2 and 3 respectively. In the GFP channel column numbers are showing the volume of cryptococcal cells within the respective stack. In column 4, the raw data was thresholded using global Otsu thresholding (Otsu 1979) and volume was calculated as seen in Kugler *et al.*, 2019. The volume values are shown in numbers over the thresholded Z stacks in column 4. Panel D shows a comparison between volumes of infected and control larvae in the whole cohort measured (N = 9 for each group). In panel E a linear regression analysis was performed for vascular and fungal volume values to test if there is a relationship between the variables, 63% of vascular volume variation can be accounted for by fungal burden. MICP- maximum intensity projection

4.4.8 Cranial vasculature permeability increases in cryptococcal infection

The pulsations and vessel architecture disruptions observed in the previous sections of this chapter, led us to question if the integrity of the vessel wall endothelium could be compromised in infection. Therefore, I used a fluorophore conjugated dextran to create an angiogram-like analysis of the cerebral vasculature integrity in the zebrafish larvae. If the cranial vasculature is more permeable that would impact the production of CSF particularly in the glymphatic system, where CSF flow within the interstitium is dependent on passive diffusion through AQP4 channels (see Introduction). Increase in diffusion would potentially lead to increase in flow velocity and fluid pressure and impact brain tissue through local pressure differences.

Tg(kdrl:mCherry)^{S916} transgenic zebrafish larvae were infected with 700-1000cfu of *C. neoformans* KN99 GFP in the Duct of Cuvier (DoC) at 52hpf. 5 hours post infection images were taken of the infection burden without mounting or anaesthetising the larvae. At 5hpi infected and control fish (57hpf) were injected in the DoC with 1nl of 2 MDa FITC dextran. The high molecular weight of 2 MDa dextran has been shown to be retained within the brain vasculature of 2 and 2.5dpf zebrafish larvae and not to penetrate the brain parenchyma (Jeong *et al.*, 2008; Wenke 2013; Quiñonez-Silvero *et al.*, 2020). The same size ROI was used for all images. The GFP fluorescence emitted from *C. neoformans* did not skew measurements of dextran fluorescence as the exposure settings for imaging dextran did not pick up the GFP signal coming from fungal cells (Fig. 4.17). The data showed that dextran was leaking in the brain parenchyma of infected fish in significantly larger quantities than in control larvae ($p = 0.0012$) (Fig. 4.16). Minor leaks and some autofluorescence was detected in controls (Fig. 4.16). A linear regression analysis was performed for the variables of cranial fungal burden and size of dextran leak, there appeared to be no relationship between the two (Fig. 4.16, H). Therefore, it appears that *C. neoformans* blood stream infection may compromise the integrity of the cranial vasculature and fungal burden is not a variable that is seen to influence that.

Figure 4.16 Permeability of cerebral vasculature is increased in infection

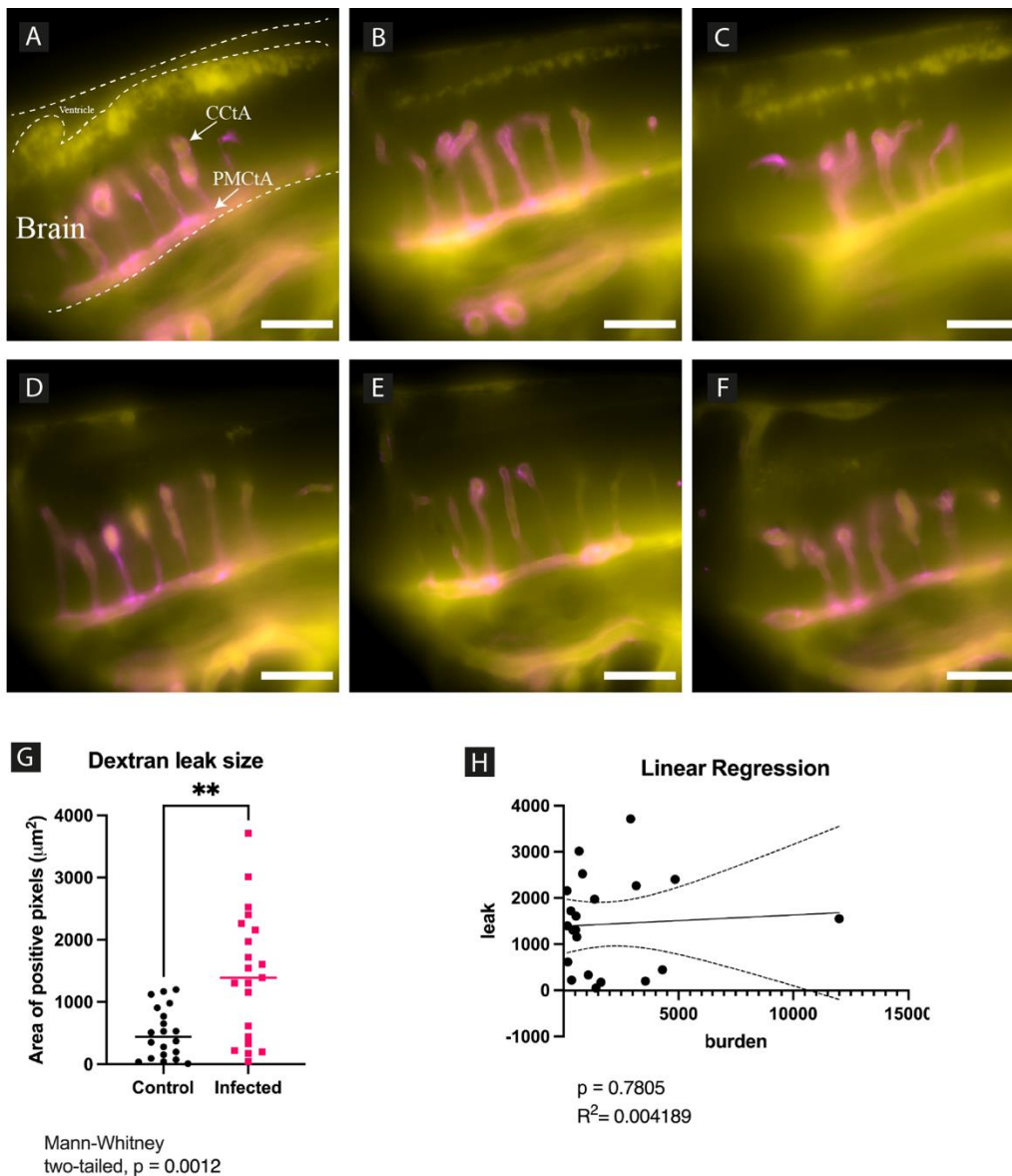


Figure 4.16 Permeability of cerebral vasculature is increased in infection

Panels A-F: Images are taken from the lateral side of *Tg(kdrl:mCherry)^{S916}* zebrafish larvae hindbrain at 3dpf, 2hrs after systemic dextran fluorescent dye injection. In view are the hindbrain embedded central cerebral arteries (CCtA) and posterior mesencephalic central artery (PMcTA). Above the brain parenchyma is the ventricular compartment. The yellow fluorescence is 2MDa FITC dextran dye injected into the bloodstream, in magenta is the mCherry fluorescent tag on the KDRL blood vessels endothelium protein. Panels A-C are showing images of larvae 5 hours after introduction of a 700-1000 cfu of *C. neoformans* systemic infection. Panels D-F are showing images of the brains of uninfected controls. Significant deposits of dextran can be observed in the brain parenchyma above CCtAs of infected fish but not controls. Panel G shows a quantification of fluorescence within the parenchyma above CCtAs in both infected and control cohorts (See Method Fig 2.1) A two-tailed t-test was performed on the data, showing a significant difference between the groups (P value = 0.0012). Panel H shows a linear regression analysis assessing the relationship between head fungal burden (positive pixels) and dextran deposit in infected fish. The test shows no significant relationship between the two variables ($R^2 = 0.0041$, P value = 0.78). Panel a-f scale bar: 50 μm , 50 px height.

Figure 4. 17 Pathogen fluorescence does not skew data shown in Fig. 4.16

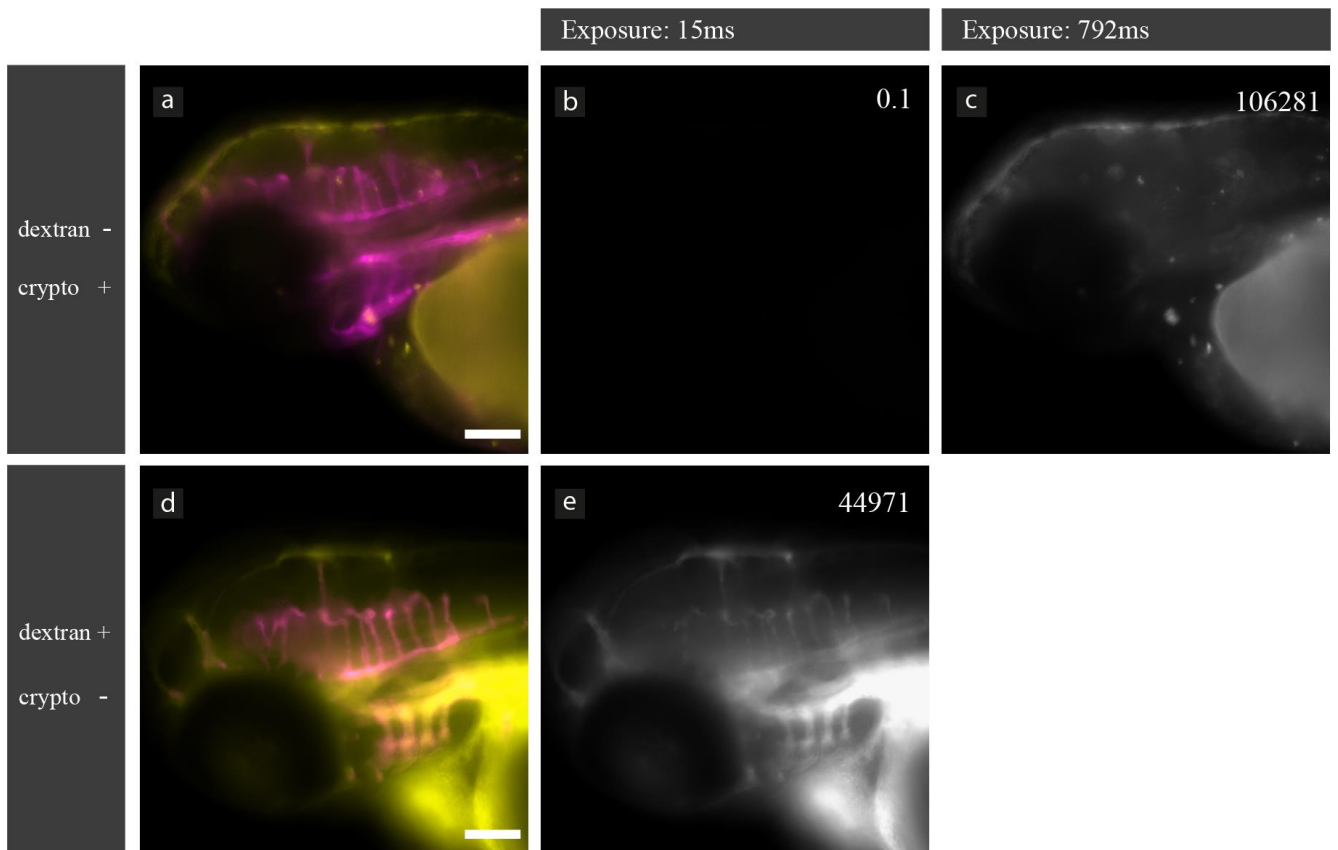


Figure 4.17 Pathogen fluorescence does not skew data shown in Fig. 4.16

This figure is supplementary to Fig.4.16. It shows microscope settings for imaging GFP conjugated dextran and GFP expressing *C. neoformans* KN99. Panel a-c: a 2dpf *Tg(kdrl:mCherry)^{S916}* larva with a GFP expressing KN99 systemic infection, 5hpi. Panel d-e: no infection control larva systemically injected with 2MDa FITC dextran. Panel a and d show a *kdrl:mCherry* and GFP channel overlay. In panel b and e, the image of the GFP channel is taken with exposure of 15ms, the settings for imaging GFP dextran injected larvae. Panel b shows that at 15ms the fluorescence of *C. neoformans* is not visible. In ImageJ the panel b image was thresholded and measured using the same settings for the image in panel e, the programme picks up 0.1 positive pixels for panel b and 44971 positive pixels for panel e. In panel c the image of the GFP channel is taken with exposure of 792ms, 777ms higher exposure than the settings for imaging fluorescent dextran. After processing in ImageJ (same path as images in panel b and e, see Method Figure 2.1, the image in panel c showed 106281 positive pixels. Higher exposure for imaging fluorescent dextran bleaches the image and does not allow for accessing regional distribution of the dye. The fluorescence of GFP KN99 is too weak to be picked up by an exposure of 15ms. The scale on panel a and d is 100µm and 50px in height. All images are taken on a Nikon custom widefield microscope (see section 2.4) with settings of no binning and Gain 4. Images were processed with the path demonstrated in Figure 2.1 but with no ROI (measurement of pixel count for the whole image).

4.5 Discussion

4.5.1 Implementation of light sheet imaging and shorter imaging intervals allows for accurate automated quantification of vessel volume fluctuations

In my work I explored different approaches to imaging, data analysis and automation in quantification of a dynamic vascular area. Shorter intervals in between image capturing (1-2s) imaging (higher temporal resolution) revealed that the intensity and frequency of vascular area fluctuations was less than first observed. In time lapses with higher temporal resolution “pulsations” were still captured in 6 larvae out of 10 imaged. In lower temporal resolution all 10 larvae imaged showed a pulsation phenotype. It seems that for the accurate assessment of vascular dynamics, the time lapse data needed to be with shorter intervals between imaging, as it allowed for more accurate characterisation of changes in vascular volume in time. The use of a widefield imaging proved inefficient when it comes to achieving the resolution necessary for automated identification of vascular area in the processing stages. Vessel area was not being registered accurately from in quantification strategies, the vessel area measurements from the widefield time lapse data cannot be interpreted to any conclusion because it is likely they represent imaging artifacts and not actual changes. In widefield imaging the presence of “pulsations” was determined through observation, as quantification was not successfully developed.

Acquisition of data using light sheet microscopy instead of widefield allowed for an automated quantification strategy that works reproducibly across different imaging samples. This was done at the cost of length of time-lapses acquired, instead it was chosen to do shorter observation spans with smaller time intervals between images. After assessing that the accurate and automated quantification of light sheet data is possible and optimising the data analysis pipeline, the data was processed and examined in detail. It was intended to collect a larger data set in order to better assess the prevalence in the pulsation phenomenon, nonetheless, time constrains did not allow for this. To create an automatic way to detect the presence of a pulsation, time lapses from more larvae need to be collected from both infected and control groups. Regions of interest would have been set to random locations in the vasculature but in the same size and range of vascular volume fluctuation measured. That will allow to compare ranges and set a range of volume fluctuation in infection and not. Setting the range will allow for creating an exclusion criterion for pulsation positive and negative larvae.

4.5.2 Characterisation of pulsation intervals and synchronicity across vascular tree

It appeared that the two vessel groups in the same larvae had a similar profile and rhythm of volume fluctuation. A transient blockage in one vessel group seemed to be affecting the dynamics of another. These relationships were only measured in two vessel groups, and the sample size must be expanded to confirm observations. For both vessel groups “pulsations” the decline in vessel area lasted about twice the time it took for the vessel to increase its area back to baseline, or about the time during which vessels abnormally constrict with the area of a vessel group fluctuates with about 10-15%. It is unclear on why the vascular dynamic in infection exhibit such characteristics. Assessing cerebral blood flow and heart rate in infected larvae alongside characterisation of pulsation could possibly provide more detail on the vascular phenotype. To do that, the *gata1:dsRed* line could be used to estimate velocity and volume of blood reaching cranial vessels of infected larvae. Some imaging was done to attempt this analysis, but this requires a lot of optimisations in terms of approach of data analysis and reproducible acquisition.

I propose that pulsations arise due to obstruction of part of the vasculature, which results in a decreased overall vessel area in the cranial bed. The same volume of blood (m) passes through a smaller area (a) and the pressure that the fluid creates (F) overcomes vascular resistance (SVR) causing vascular dilation, this is followed by a constriction when the force of pressure is not enough to overcome vascular resistance.

$$SVR = \frac{MVP}{CO}$$

SVR = systemic vascular resistance

MVP = mean vascular pressure (assuming there is no difference in venous and arterial wall physiology in the larvae at this stage of development)

CO = cardiac output

Cardiac output does not change but the area that receives the volume reduces.

$$F = m * a$$

F = force of pressure that the blood exerts on the vascular wall

m = the mass of blood on an area of vascular wall

a = area of vascular wall (accepting as a constant before dilation)

$$\uparrow m = \uparrow F$$

If we say that cardiac output is a measurement of the force blood puts on the area of vasculature

$$F = CO$$

$$\uparrow CO = \downarrow SVR = \textit{dilation}$$

Peripheral resistance is also increased but possibly the blood volume/area of vascular wall increase is greater, the force overcomes resistance and leads to dilation, and an increase in stretch and tension on the vascular endothelium. Pulsations occur sporadically possibly due to cryptococcal cells being stuck and being pushed out. Another mechanism that is potentially in play is that as cells get stuck, blood builds up at the area of the blockage, widening connected vessels and eventually collecting bulk volume enough to generate the force necessary to push out the mass clump. Once the vessel obstruction is removed, there is a sudden increase in blood volume causing vessel dilation. When the build-up blood passes through, and the vessel returns to normal (in a simple system of a single vessel system, in reality with multiple vessels there is communication of forces across the system).

4.5.3 Vascular wall shape is disrupted in infection to apparently accommodate passing of *C. neoformans*.

Cryptococcal cells passing through vessels appeared to cause deformation of the vessel wall. Once the cells leave the vessel, there is a remaining disruption of the vessel wall shape, which suggests for a degree of plasticity of the endothelial vessel wall. CCtAs in the zebrafish larvae only have one vessels wall layer – the endothelium cell wall layer. The properties of the vessel depend on endothelial cells and the junctions between them (Quiñonez-Silvero, Hübner and Herzog 2020). It is known that the smaller vasculature the less elastin and therefore elastic potential it has, in humans and adult zebrafish (Hoareau et al., 2022). The properties of the intima, or the endothelial cell layer, in terms of elastic potential have not been studied, it is just assumed they are much less elastic due to the lack of elastin, but they would still have elastic potential.

To measure if we are indeed observing the vessel wall to exhibit plasticity, it is necessary to see how long this deformation remains and if the vessel wall eventually regains its original shape (shape before cryptococcal mass passes through). Measuring the degree of deformation after a long period that is caused by a single cryptococcal mass passing through the vessel proved difficult as multiple masses pass through. In between masses passing through, there appeared to be some recoil into the original vessel wall width/shape. Nonetheless, things are further complicated by the arrival of a “pulsation”, which appears to stretch the vascular wall for a more than a minute per event. It could be possible to assess the elastic potential of CCTAs by introducing larger beads in the circulation in smaller quantities in the attempt to see if passing through the vasculature permanently widens it or if there is a recoil. This is similar to what was attempted with the pathogen in my experiments, but it would be a control in which blockages are more likely to happen, but beads are passing through each vessel less frequently to allow for time to assess the recoil period. Direct measurements of vessel tension/stretch need to accompany this work in order to confirm increase in shear strain on vascular wall (described in the next section).

4.5.4 Volume of cranial vasculature is increased by cryptococcal infection

There is evidence for overall global vasodilation and increase in peripheral resistance in intersegmental vasculature of zebrafish larvae (Gibson et al., 2022). This supports what was observed in my work (overall cranial vasculature volume in infection was higher in infection than in uninfected larvae) but my experiment was not sufficiently powered to achieve statistical significance. Power analysis, considering my work as a pilot study, suggests 30 larvae per group to achieve 80% power in experimental design. To completely exclude the possibility of significant vascular volume increase in infection, it would be important to test a larger sample size and possibly different timepoints of infection progression, as infection strain on vasculature for longer periods of time may produce a different phenotype.

Pathogen mass in the cranial vasculature may directly contribute to the increase of the cranial vascular volume in infection, voxel volume analysis was done on the GFP positive (cryptococcal mass indicating) pixels, similarly to vascular volume. Pathogen volume in the cranial vasculature across the head was calculated and in a scatter plot with overall cranial vascular volume to perform a linear regression analysis of the two variables. From the R^2 , it

was deduced that 63% of cranial vascular volume increase can be accounted for by fungal burden. There, is a strong relationship between the two variables, but there seems to be other variables that could be influencing the cranial vasculature increase, like for example fluctuations in peripheral resistance in infection due to blockages in the vascular tree. Blockages in some of the vessels in the cranial vasculature would decrease the surface area of the vascular tree and increase wall shear stress on the endothelium and general resistance in the vasculature. If the forces of pressure from the blood flowing into the cranial vasculature remain the same but the surface area reduces, cranial vasculature that remains unblocked and receives those forces may be more prone to distend. This is the same explanation proposed for the occurrence of pulsations.

It would be interesting to couple analysis of volume difference in infection with analysis for the presence of pulsations, in order to test for possible correlation between the two factors. An important analysis would be to directly test if there is an increase in tension (stretch) in the cranial vascular wall. This could be done by attempting to replicate the experiments of Gibson et al. 2022 but for cranial vessels, using the FRET reporter, the zebrafish transgenic line *TgBAC(ve-cad:ve-cadTS)^{uq11bh}* that allows for the visualisation of intra-molecular tension at cell-cell junctions between vascular endothelial. This work can be done in context of the “pulsation” phenomenon characterisation, observing if FRET signal reduction occurs at vessel dilation and *vice versa* in vessel constriction. Vascular volume increase did not appear to be correlated with fungal burden in larvae head, which suggests that volume increase is not as a result of the volume of pathogen but possibly due to other mechanisms, such as the pulsations and/or cryptococcal masses causing stretch in the vascular wall.

4.5.5 Cranial vasculature permeability was increased by infection.

Cryptococcal masses passing through the cranial vessels seems to cause a disruption of the vascular wall shape, which appears as the wall stretched to accommodate the size of the mass. Pulsations maybe caused by a larger than normal volume of blood causing pressure on a smaller area and possibly introducing strain on the vascular wall. Strain from cryptococcal masses and pulsations are likely to induce weakening of the vascular wall in the form of damage or loss of cell-cell junctions in the endothelium and may explain the increase in permeability of brain parenchyma embedded vasculature as seen in my work (Figure 4.16).

Previous work in our lab has supported this hypothesis. When examining the peripheral vasculature in *C. neoformans* infection, it appears that there is an increased tension in the vessels during cryptococcal infection, in vessels with and without cryptococcal cells (Gibson et al., 2022). In the periphery there was a lot of vessel rupture observed in infection, but dissemination was also seen around intact vasculature. It is important in future work to test why the increased permeability of the cranial vasculature occurs and if it does come as a result of damaging vascular endothelium cell-cell junctions.

In my work I did not observe vessel rupture in the brain although there was dissemination from the vasculature into the parenchyma and CSF. I did not examine the intersegmental vasculature closely, but from preliminary observations I have seen the pathogen to trap and establish infection. It would be interesting to see if infection establishes and expands easier and sooner in intersegmental vessels, this will contribute to the differences in impact of the infection on different vasculature. I speculate that speed of trapping in different vasculature would have to do with blood flow velocity, branching of the vascular tree and size of the vessels.

Although, I did not examine intersegmental vasculature, this work was already previously conducted by Dr Gibson in our lab, and she observed increase in endothelial wall rupture in the intersegmental vessels in infection (Gibson et al., 2020). When vascular elasticity is inhibited/peripheral resistance was increased, vessel rupture was seen to increase as well (Gibson et al., 2020). That suggests that the elastic potential of vasculature would influence its susceptibility for rupture, and the elastic potential of the vasculature in the cranium as opposed to the trunk may be different. Dissemination events from the brain vasculature observed in mouse models are not accompanied by vessel rupture either (Shi et al., 2010). Haemorrhages are not common in patients with CM (Mishra et al., 2018), and it seems it is possible that the dissemination of cryptococcal yeast into the brain parenchyma and CSF occurs without vessel rupture, but it is mediated by mechanisms such as macrophages acting as a Trojan Horse or transcytosis (Charlier et al., 2009; Strickland and Shi 2021). Previous work examining the cranial vasculature in the zebrafish cryptococcal infection model, shows that dissemination into the CNS parenchyma occurs mostly by cryptococcal cells crossing the BBB within microglia carriers (Davis et al., 2023). Dextran dye angiogram like experiments show some instances where the cranial vasculature was leakier due to infection. However, as in the periphery, vascular disruption was not necessary for dissemination events to occur (Davis et al., 2023). In

future work attempts to assess vascular rupture in infection in the cranium could be done with light sheet imaging and 3D analysis of vessel integrity.

4.5.6 Experimental set up for injecting inert beads into the zebrafish larvae bloodstream is an important control that needs development and validation.

The vascular pathology that has been observed in my experiments could be due mechanical interactions of the pathogen with the vascular wall, as opposed to receptor-dependent biological ones, such as in the case of lymphocytes. I need further evidence in support of this hypothesis, I aim to do that in future experiments by introduction inert beads into the circulations of zebrafish larvae and examining for the presence of similar effects on the vasculature as seen in infection. Beads injection experiments have been previously done in mice and show that the inert beads present with similar dissemination patterns and vascular obstruction in cranial capillary beds as cryptococcal yeast cells (Shi *et al.*, 2010). Experiments with 4.2 μm inert beads (similar size as the average cryptococcal yeast cell) in the zebrafish larvae however, showed no trapping in smaller vasculature but a slight increase in vascular width (Gibson *et al.*, 2022). I aimed to expand on this work by optimising beads injections and imaging dissemination patterns and vascular dynamic in the cranium with high temporal and spatial resolution. I began developing these experiments but time constraints due to the pandemic prevented me from completing them. What needs to be done is assess the true fungal burden (cfu counting from plating of larvae homogenates) of zebrafish larvae with systemic infection 5hpi (when pulsations and dextran permeability were imaged) and introduce beads with the same concentration into the blood stream (because the cryptococcal cell can increase in number with time and beads cannot). Initial attempts of beads infections showed that beads are prone to clumping and a strategy to prevent that needs to be developed in order to allow a better spread of the beads across the cardiovascular system. I initially injected 500 beads (4.2; GFP tagged) per larvae, which showed clumping at the site of injection (Duct of Cuvier), but some disseminate to intersegmental vessels and cranial vessels, concluded from still images, and needs to be confirmed in time-lapse imaging. Beads may require e.g., sonification in order to prevent clumping and arrest of spread when injected. Unfortunately, due to time constrains this work could not be continued further.

4.5.7 Summary

Cranial vasculature wall dynamics is different in infection, the vasculature undergoes rapid expansion and shrinking termed “pulsations”, with no apparent rhythm, but vessel groups within the same CNS show signs of being synchronous in their pulsations. I speculate that pulsations occur due to masses of infection transiently trapping in the cranial vessels and temporarily decreasing surface area of the cranial vascular tree, which generates more force of shear stress from blood flow and overcoming surface tension of the endothelial wall. The periodic distending of the vascular wall may be impacting the integrity of the endothelium, I saw an increase in cranial vasculature permeability in infection that could be related to pulsations and increase of shear stress.

Chapter 5: Impact of cryptococcal infection on CSF properties and optimisation of the zebrafish model to study CSF flow in infection

5.1 Summary

This chapter introduction provides a summary of our understanding of CSF flow in human physiology. It outlines the importance of examining viscosity and flow profile properties of the CSF as a fluid. A summary is provided of our current understanding of CSF physiology in the zebrafish larvae animal model. My results demonstrate that the viscosity of fluids containing growing cryptococci increases and that this increase is correlated with the concentration of cryptococci, but the increase in viscosity is small and the fungal concentration of solution supraphysiological. In the second part of the results the CSF flow directionality and velocity in infection is visualised *in vivo* in the zebrafish ventricular system. Some preliminary data is shown on measuring the velocity of CSF in blood stream ventricular infection models. It appears that directionality of flow in ventricles driven by cilia beating is retained in infection.

5.2 Introduction

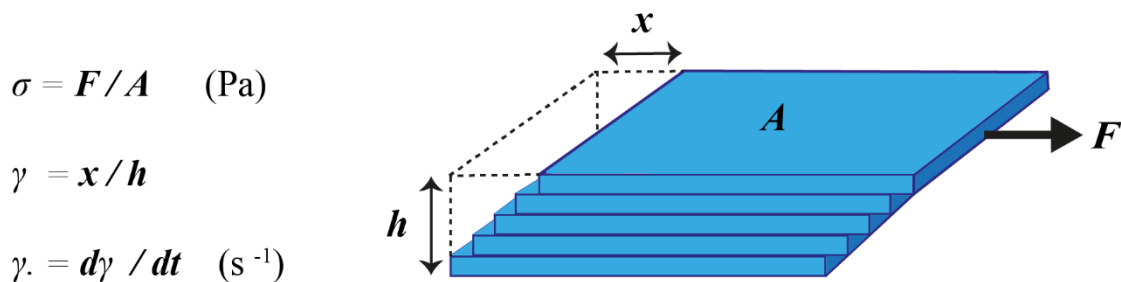
CSF flow in human physiology

In humans, 80% of CSF is secreted by the choroid plexus epithelium and 20% is thought to be secreted on the level of the BBB in the perivascular spaces or parenchyma imbedded capillaries (Kimelberg *et al.*, 2004; Orešković *et al.*, 2010; Redzic *et al.*, 2011; Brinker *et al.* 2014). CSF flows through the brain ventricles, subarachnoid space of brain and spine, and brain interstitium (Bothwell *et al.*, 2019). Reabsorption of CSF happens at the level of arachnoid granulations and venous perivascular spaces (Mestre *et al.*, 2020). CSF flow is driven by ependymal cilia beating, arterial pulsations, hydrostatic pressure, and the action of breathing (see section 1.1.2.3 of Introduction). CSF rate of secretion is dependent the integrity of the BCSFB and BBB (Mestre *et al.*, 2020; MacAulay *et al.*, 2022). Those barriers are seen to be compromised in infections which present with an IH pathology (Schwerk *et al.*, 2014;). In CM the most common neuroradiological feature in patients is choroid plexitis (high infection burden at the CP) and dilated perivascular spaces (Charlier *et al.*, 2008; Loyse *et al.*, 2015; Xia *et al.*, 2016; Lee *et al.*, 2021) both of which are sites of CSF secretion. This suggests that impairment of IH in CM may be as a result of impairment of CSF secretion homeostasis.

Viscosity of CSF in health and cryptococcal infection

Rheology is the study of the flow and deformation of matter which describes the interrelation between force, deformation, and time. Rheometry is an experimental technique which allows us to determine the viscoelastic and flow properties of matter (Barnes *et al.*, 2000). Shear flow can be depicted as layers of fluid sliding over one another with each layer moving faster than the one beneath it (Fig. 4.1). **Shear flow** is a flow of a fluid under forces of deformation termed **shear stress** (σ). Shear stress is defined by a force (F) acting on a unit of area (A). A fluid under shear stress has a displacement gradient, the upper layer will move a distance (x), while the bottom layer will remain stationary. The displacement gradient (x/h) is termed shear strain (γ). For fluids the shear strain continues to increase over a period during which shear stress is applied, this created a velocity gradient termed **shear rate** ($\dot{\gamma}$). The shear rate represents the strain over time (dy/dt), which is a velocity gradient.

Figure 5. 1 Shear flow and quantification of shear rate and shear stress



The coefficient of proportionality between the shear stress and shear rate is defined as the shear **viscosity** (η). Shear viscosity is a measure of internal fluid friction and associated with damping or loss of kinetic energy in the system. **Newtonian fluids** are fluids in which the shear stress is linearly related to the shear rate and hence the **viscosity is invariable with shear rate or shear stress** (Barnes *et al.*, 2000).

$$\eta = \sigma / \dot{\gamma}. \quad (\text{Pa}\cdot\text{s})$$

There are two more types of fluid apart from Newtonian: shear-thinning and shear-thickening. Newtonian fluids do not change viscosity when shear forces are applied, shear-thinning (blood)

and shear-thickening (corn starch in water) fluids respectively become less or more viscous when shear forces are applied. Polymers suspended in a fluid can change its flow profile. When polymers are in a resting state they tangle up and increase the viscosity of the fluid. When shear force is applied to a polymer suspension, the polymers tend to straighten up and reduce the viscosity of a fluid. Therefore, polymer suspensions tend to have a shear-thinning flow profile.

Cryptococcus neoformans yeast cells have a polysaccharide capsule, which is attached the cell wall but is also shed as free polysaccharide (Cherniak and Sundstrom, 1994). On its own the capsule has a large molecular weight and is polymeric in nature (McFadden *et al.*, 2006). When introduced into a Newtonian solution, polymers change viscoelastic properties of the fluid (Barnes *et al.*, 2000.). CSF is a Newtonian fluid; its viscoelastic properties are like water i.e., it does not change its viscosity when subjected to deformation forces (Barnes *et al.*, 2000.). It is possible that the introduction of *C. neoformans* in the brain forms polymers that change the viscoelastic properties of CSF, which in turn alters the velocity of flow (Rohn 1995). Furthermore, the production of CSF is dependent on osmotic pressure across capillaries, the net charge of the capsule polymer may influence the charge of the CSF, alter the osmotic pressure gradient and therefore net CSF production. The cryptococcal polysaccharide capsule has been previously shown to change the viscosity of a solution (McFadden *et al.*, 2006). *In vitro*, a correlation was demonstrated between the increased capsule size in strains of cryptococci from patients with higher ICP during cryptococcal meningitis (Robertson *et al.*, 2014). Therefore, it appears that when examining the CM pathophysiology, both the influence of cryptococcal cells and the polysaccharide capsule on CSF properties need to be considered.

I hypothesised that the introduction of capsule shedding *C. neoformans* into the CSF would change its properties to make it more resistant to flow. Experiments were conducted to find out whether the introduction of *C. neoformans* in a fluid with the same flow profile as CSF, would change the behaviour of that fluid when it was subjected to forces of deformation. Shear rate/velocity was quantified in different time points when applying the same amount of shear stress, the flow profile visualised and the dynamic viscosity of the fluid determined (Mezger *et al.*, 2014).

An experimental method to test this hypothesis was created in collaboration with Dr Oleksandr Mykhaylyk in the Department of Chemistry at the University of Sheffield. We discussed what available set ups would be suitable for determining the viscosity and flow profile (function of

shear-stress and shear rate) of suspensions of *C. neoformans* and their shed polysaccharides. The method chosen used a coaxial cylinder cell because it is a suitable system for measuring information on how molecular structure affects flow in less concentrated suspensions as it is more sensitive (Macosko CW 1994). This set up requires larger sample size (~ 10ml), therefore it was necessary to grow larger “batch” cultures, which allowed volumes left over for procedures of measuring different time points of growth, repeats of measurement, agar plating and cfu/counts. Batch cultures grown for rheology experiments were of 50 - 200ml in volume.

High mortality from cryptococcal meningitis has been attributed to delay in care and diagnosis in a lot of studies, patients are given clinical attention in later stages of the pathology and a lot of what is understood about pathophysiology in humans is relevant to late disease (Link et al., 2022). Cryptococcal antigen presence is detectable in systemic blood weeks to months before onset of meningitis symptoms (Liechty et al., 2007; Rajasingham et al., 2017 and 2019). Therefore, it is unclear how long from initial infection to dissemination into CNS to diagnosis it takes in patients. It is possible cryptococcal growth in CM patient brains could be occurring over months before clinical intervention and getting a report on fungal burden in the CNS. *In vitro*, in a prolonged period of growth factors such as capsule shedding, rate of doubling and amount of dead yeast cells would be very different to short term, 1–2-day old culture. This could change the properties of the fluid the culture is suspended in; assuming the pathogen is in the CNS for longer than a week before it causes symptoms, I decided to measure samples came from cultures that had more than 7 days incubation, to attempt to replicate conditions of longer growth.

It should be noted that fluid viscosity is both pressure and temperature dependent, with viscosity generally increasing with increased pressure and decreasing temperature. The set-up we used did not allow us to control pressure, but it allowed for control of temperature, samples were measured and grown (to mimic growing conditions in the human body) at 37°C. Also, in cranial niches where cryptococcal yeast are found in CM (perivascular space, ventricles, interstitial spaces), there is fluid exchange and low shear flow (Trumbore, 2016). Such forces of shear introduced during cryptococcal growth could potentially change the viscoelastic properties of the CSF, as opposed to growth in an environment with no shear flow. Therefore, samples consisted of cryptococcal culture grown in two different conditions – termed shaken and still. *C. neoformans* cultures were grown in YPD broth as our initial growth media and media for measuring viscosity. The alternative and theoretically more pathology mimicking

media, would have been CSF. There is no clear understanding of how *C. neoformans* grows in CSF, cryptococcal pathogen has been reported to reduce in growth in *ex vivo* CSF (Sabiiti et al., 2014), but it is unclear how growth related to death rate and if it all had anything to do with physiological environments of growth providing more nutrients. Artificial CSF (ACSF) has also been used as a media for conditioning - an already grown *C. neoformans* culture, with suprphysiological concentrations, was introduced to ACSF medium for 72hrs and (Rathmore, Raman and Ramakrishnan 2016), the work did not report growth rate in ACSF media. One other group used ACSF as a conditioning media, to assess changes in gene expression, but again growth rate and survival was not assessed, the pathogen was introduced in ACSF at suprphysiological concentrations for 24hrs only (Yu et al., 2021). In future experiments, the literature available can help settle on recipes for artificial CSF in which we could attempt to grow *C. neoformans* and examine the viscosity and capsule content in different suspensions.

YPD broth and water have the same Newtonian flow profile (linear relationship between shear-stress and shear rate) as CSF. Also, the viscosity of healthy CSF is 0.7 to 1 mPa/s, in comparison the viscosity of YPD is 0.89 mPa/s and the viscosity of water at 37°C is 0.7 mPa/s. The use of YPD as an alternative to CSF would not skew rheology measurements, and it was chosen for null hypothesis testing as the growth of the pathogen in YPD broth is well documented and better understood, unlike artificial CSF.

- Null hypothesis 1: *C. neoformans* not have any role in fluid flow profile change.
- Null hypothesis 2: *C. neoformans* not have any role in fluid viscosity change.

CSF flow in zebrafish larvae

The zebrafish larvae used in this chapter are between 2-4dpf. The CSF system in these stages consists of a telencephalic (TV), diencephalic/mesencephalic (D/M), rhombencephalic (RV) brain ventricles and the central canal (CC) of the spinal cord (Fig. 4.2) (Lowery *et al.*, 2005; Fame *et al.*, 2016; Olstad *et al.*, 2019;).

In humans, a large portion of CSF is known to be produced by the choroid plexus (CP). The CP is a continuous epithelial sheet with tight junctions which surrounds a subset of the cranial microvasculature (Lun *et al.*, 2015). Like higher vertebrates, the zebrafish CP possesses brain barrier properties such as tight junction and transporter activities (Henson *et al.*, 2014; van

Leeuwen *et al.*, 2018). The claudin proteins are important tight junction proteins in mammalian brain endothelial cells, and therefore key structures for the regulation of permeability of brain barriers (Greene and Campbell *et al.*, 2016). Claudin 5 is the most strongly expressed in mammalian brain micro vessels (Greene *et al.*, 2019). The zebrafish claudin 5 orthologues, claudin5a, is shown to associate with almost all cerebral vasculature in the zebrafish larvae by 5dpf and to associate with CP like epithelial sheets surrounding cranial vessels (van Leeuwen *et al.*, 2018). Claudin5a is seen to be expressed in ependymal cells which protrude cilia into the zebrafish brain ventricles as early as 2dpf (van Leeuwen *et al.* 2018). Ependymal cells are known to both secrete CSF and drive CSF flow in the brain ventricles particularly in early development (Kramer-Zucker *et al.*, 2005; Del Bigio *et al.*, 2010). It appears that the directionality CSF flow in the zebrafish larvae ventricles is influenced by three factors: cilia motility, heartbeat, and body movement (Olstad *et al.*, 2019) (Fig. 4.2). Motile cilia on ependymal cells protrude into the zebrafish ventricles and direct a circular type of flow within the TV and D/M ventricles (Olstad *et al.*, 2019) (Fig. 4.2). Heartbeat causes pressure changes that are seen to influence flow across different ventricular compartments of the zebrafish system (Olstad *et al.*, 2019) (Fig. 4.2). Body motility in zebrafish causes fluid movement from caudal to rostral end in the ventricular system (RV to TV) (Olstad *et al.*, 2019). The direction of movement across the TV and DV ventricle changes in different stages of larvae development. 27-30hpf CSF moves from TV to D/M, 51-54hpf CSF moves from D/M to TV (Fame *et al.*, 2016). That could potentially be as a result as sheer volume of the ventricular cavities unevenly changing or differences in developmental progression of CP structures across the ventricular system (Garcia-Lecea *et al.*, 2008). Movement between the D/M to the RV in all stages of larvae development is seen to be always in a caudal direction (Fame *et al.*, 2016). CSF flow in the central canal is bidirectional around 30hpf, with cilia on the ventral wall of the canal generating local flow and the average flow rate to be generally null (Wyart *et al.*, 2020). Thus, the properties of the choroid plexus (CP) in zebrafish are complex and mimic the human physiology (Henson *et al.* 2014).

I aimed to develop the zebrafish ventricular infection models further to examine how *C. neoformans* pathogen distributes in the CSF system and make observations on how it may impact fluid flow. I visualised the directionality of flow that yeast cells exhibit in the ventricles and attempted to measure velocity of flow in infection to later compare to bead controls. I hypothesised that flow would be physically obstructed and slowed down during infection. The

work in this chapter suggests of impact of infection on CSF flow but more work needs to be conducted.

- Null Hypothesis 1: *C. neoformans* presence in the zebrafish ventricles physically obstructs CSF flow.
- Null Hypothesis 2: *C. neoformans* presence in the zebrafish ventricles slows down CSF flow.

Figure 5. 2 Diagram of directionality of CSF flow in a healthy zebrafish larva

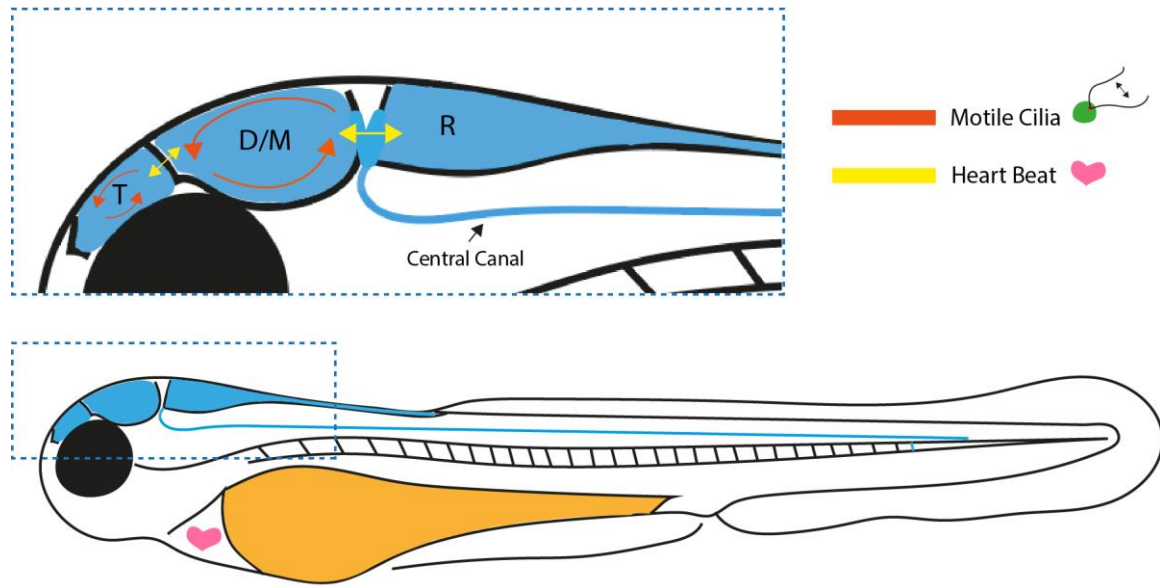


Figure 5.2 Diagram of directionality of CSF flow in a healthy zebrafish larva

This figure is inspired by the graphical abstract in Olstad *et al.* 2019, where they show that the directionality of CSF movement in the zebrafish ventricles is dependent on several factors such as: motile cilia of ependymal cells, pressure changes due to heartbeat and the bodily movement of zebrafish (not represented in this diagram). The compartments where CSF is present in the zebrafish larvae anatomy are coloured in blue. The ventricular system shape and anatomical structures are representative of 2-4 dpf developmental stages. Orange arrows show the direction of CSF movement that motile cilia on ependymal cells initiate, yellow arrows show the direction of movement caused by the heartbeat. The central canal of the spinal cord comes out of the rhombencephalic ventricle.

T telencephalic ventricle, D/M diencephalic and mesencephalic ventricle, R rhombencephalic ventricle.

5.3 Objectives

1. To measure the changes in fluid properties in the presence of *C. neoformans* and its capsule using rheology
2. To develop the zebrafish infection model for the study of the impact of the *C. neoformans* pathogen on CSF fluid flow in the brain ventricles

5.4 Results Section 1: CSF properties in infection

5.4.1 The presence of *C. neoformans* does not alter the shear flow profile but increases fluid viscosity.

I hypothesised that the presence of encapsulated *C. neoformans* in the CSF would change its fluid profile from Newtonian to shear-thinning because the polysaccharide capsule of *C. neoformans* has been seen to form polymer-like structures, which could make infected CSF behave like a polymer suspension. To test this prediction, the shear viscosity of *C. neoformans* cultures was measured under applied shear stress. Each sample was introduced to shear stress at a constant rate, and the shear rate was measured at 100 time points (Fig. 5.3). Data of viscosity was deduced by from the relationship between shear rate and shear stress. Viscosity of each sample was compared against two control Newtonian fluids: deionised water and YPD broth. YPD broth has a 0.1 mPa/s higher viscosity than water (Fig. 5.3). Samples consisted of cryptococcal culture grown in two different conditions – termed shaken and still. Shaken culture was grown at 37°C in a shaking incubator at 70 rpm, still culture was grown at 37°C in a still incubator (*see section 2.6 of Methods*). The rate of shear flow induced by 70 rpm is not representative of shear flow seen in cranial niches but the shaken culture condition as a proof of concept for showing whether any rate of flow would alter the fluid properties induced cryptococcal capsule (e.g., increased capsule sheading).

The presence of *C. neoformans* in a Newtonian fluid did not change its shear flow fluid profile (Figure 5.3). This was irrespective of introducing forces of shear flow during the growth period when compared to a static culture growth condition (Figure 5.3). After a 4-week incubation period, the static cultures had a cfu of 2×10^8 cfu/ml and the shaken culture - 0.6×10^8 cfu/ml. Dilutions of the still culture were made to compare the flow profile and viscosity of the two conditions (shaken and still) with almost the same cfu (Fig. 5.3). The 25% still culture dilution (0.5×10^8 cfu/ml) has a similar viscosity to the shaken culture (0.6×10^8 cfu/ml) (Fig. 5.3). The shear flow profile of all measured samples was Newtonian, the same as water and YPD, with

no difference between the shaken and still culture (Fig. 5.3). The viscosity of fungal culture was higher than that of YPD and water. Patients with most severe disease have $\sim 0.2 \times 10^7$ cfu/ml of cryptococci in their CSF (Bicanic *et al.*, 2005; Bicanic *et al.*, 2007; Bicanic *et al.*, 2009). The closest to that concentration is the 25% dilution of the 4-weeks old still culture in Fig. 5.3. The viscosity of the 25% dilution at 100 1/s is 1 mPa/s, 1.12 times more viscous than clear YPD broth alone (suspension fluid).

Figure 5. 3 Flow profile of shaken and still *C. neoformans* liquid culture showed no difference in flow profile across growth conditions.

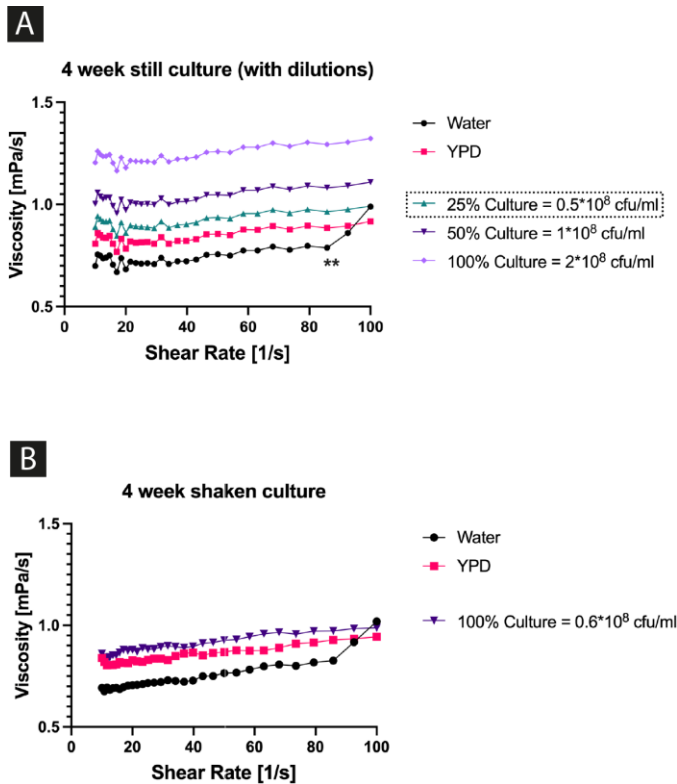


Figure 5.3 Flow profile of shaken and still *C. neoformans* liquid culture show no difference in flow profile across growth conditions

Flow profile of fluid *C. neoformans* culture (See *In vitro* Rheology: Methods for details on growth conditions). 1) fungal culture grown still in culture flasks or 2) culture continuously shaken at 70rpm in a beaker. a) the flow profile of a 4-week-old still culture in different dilutions (25, 50 and 100%/stock). All dilutions have the same flow profile as water (Newtonian). The 25% dilution has the similar cfu/ml as the CSF cfu/ml of cryptococcal meningitis patients with severe disease. The viscosity of the 25% dilution at 100 1/s is 1 mPa/s, 1.12 times more viscous than clear YPD (0.89 mPa/s). Panel b) shows the flow profile of a 4-week-old shaken culture. The flow profile of the culture is again the same as water (Newtonian). The cfu/ml of 4-week-old shaken culture (0.6×10^8) is close to the 25% of the 4-week-old still culture in panel a) (0.5×10^8). The viscosity of the 25% still culture at 100 1/s is 0.99238 mPa/s, the viscosity of the shaken culture at 100 1/s is 0.98679 mPa/s.

** An artefact in all measurements from our rheometer is an exponential increase in the viscosity of water above 80 1/s, this is due to faults in the machinery, and it is not a part of data interpretation

5.4.2 Viscosity of YPD increases with increased concentration of cryptococcal yeast.

Still growth cultures continued to double over the 40 days of culture (Figure 5.3A). However, the shaken culture concentration was stationary (Figure 5.3A). Similarly, there was increase in viscosity of still cultures over time, which this had positive linear relationship with cfu concentration, but not seen in shaken culture (Fig. 5.4B, C). After 4 weeks of incubation the shaken culture was in stationary phase and even declined in population; therefore, correlations of fungal burden increase, and viscosity increase was only done for still culture (Fig. 5.4C and 5.4D following). Dilutions of 4-week-old still culture had a different viscosity, there appears to be an increase of viscosity with an increase in stock (100% culture) concentration (Fig. 5.3A). Plotting the viscosity of dilutions of a range of still cultures with different lengths of growth period gave the fold increase in viscosity between from a 50% solution to 100% solution (4-week-old culture) as 1.2-fold, when the change in cfu/ml is 2-fold (Fig. 5.4D). For 1 and 2-week-old cultures, which had much lower growth than 4-week-old cultures, differences in viscosity from a 50% solution to 100% solution were equivalent (Fig. 5.4D).

Figure 5. 4 There is a positive linear correlation of *C. neoformans* YPD liquid culture viscosity and cfu/n

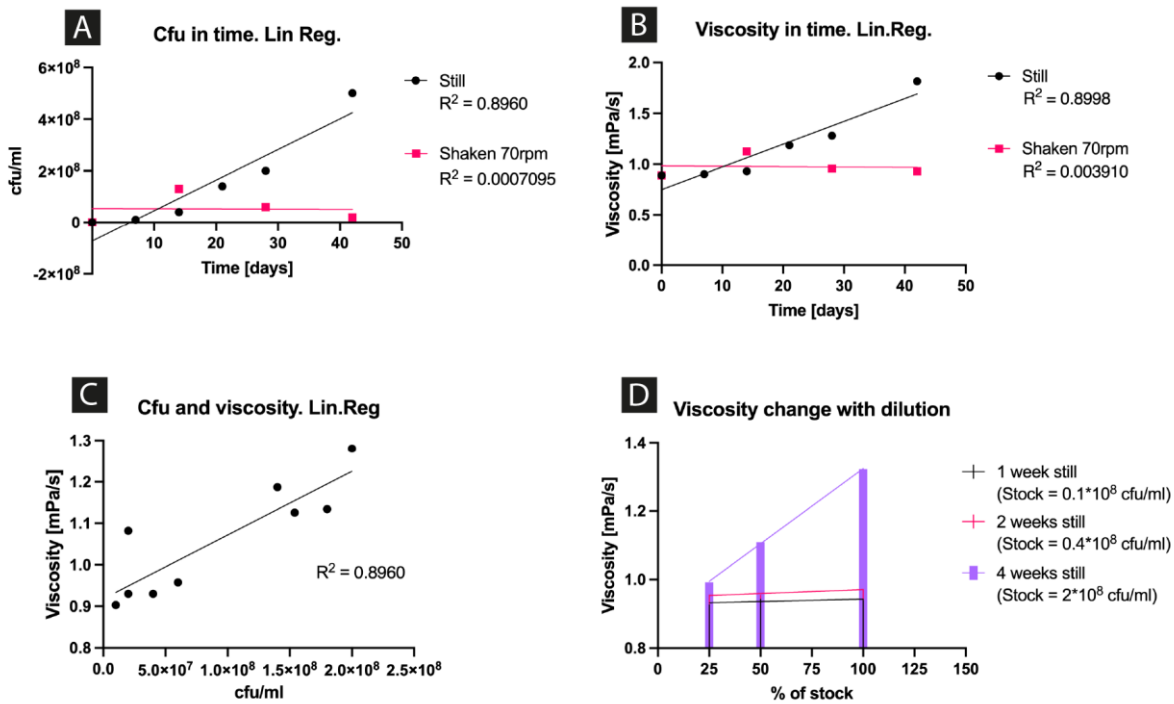


Figure 5.4 There is a positive linear correlation of *C. neoformans* YPD liquid culture viscosity and cfu

Long-term *C. neoformans* cultures (from 7 to 40 days of growth). See section 2.6 of *Methods* for details on growth conditions. The two growing conditions represented on this graph are: 1) fungal culture grown still in culture flasks or 2) culture continuously shaken at 70rpm in a beaker. A) The rate of growth of long-term cultures in both conditions. Still culture grows with doubling time of 9.53 days. B) Measurements of viscosity from the same set of cultures as in A) with linear regression analysis. C) Linear regression analysis of the two variables measured (cfu/ml and viscosity). These measurements plotted in panel c are from both shaken and still culture. There is a strong positive relationship between the variables of cfu/ml and viscosity of cultures ($R^2 = 0.8998$). Viscosity of dilutions of a single culture show that with increase in culture concentration the viscosity also increases. In panel D) the increase in viscosity from a 50% solution to 100% solution (4-week-old culture) is 1.2-fold, whether change in cfu/ml would be 2-fold. For 1 and 2-week-old cultures, differences in viscosity from a 50% solution to 100% solution are a 1.02-fold.

5.5 Results Section 2: Zebrafish larvae as a tractable model for the assessment of velocity and directionality of flow of cryptococci in brain ventricles

5.5.1 Observations show circular flow of *C. neoformans* in the D/M ventricle in zebrafish ventricular infection

Tg(kdrl:mCherry)^{S916} transgenic zebrafish larvae were injected with 200 cfu of *C. neoformans* KN99 GFP at 1dpf in the rhombencephalic brain ventricle. Larvae 24hpi were recorded in 1–2-minute time lapses, imaging the zebrafish head every 4 seconds. Using the TrackMate plugin in ImageJ (Tinevez *et al.*, 2017) the directionality of movement measured (Fig. 5.5). Patterns of circular flow of yeast cells could be seen in diencephalic/mesencephalic (D/M) ventricle, with an average velocity of $\sim 1.25 \mu\text{m/s}$ (Figure 5.5). Flow in between D/M and rhombencephalic, and between D/M and the telencephalic ventricle was not observed.

Figure 5.5 Observations show circular flow of *C. neoformans* in the D/M ventricle in zebrafish ventricular infection

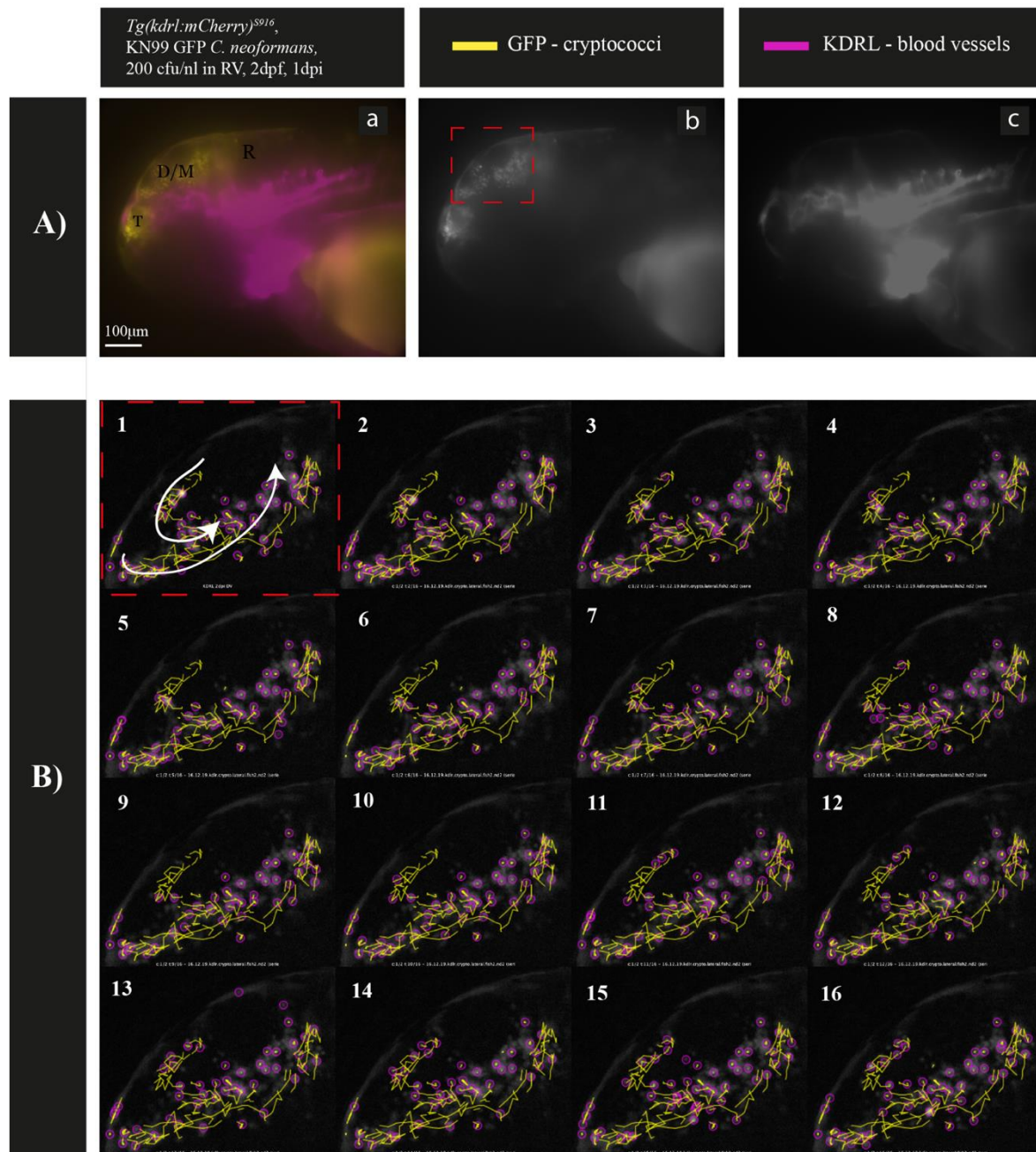


Figure 5.5 Observations show circular flow of *C. neoformans* in the D/M ventricle in zebrafish ventricular infection.

This figure is showing a representation of a time-lapse imaging the movement of *C. neoformans* yeast cells within the dienchecephalic/mesenchecephalic (D/M) ventricular space of the larvae cranium (Supplementary Video Fig.5.5). In panel A) we can see images of the whole larvae cranium from a single time point. In panel B) we can see images of all time points (3.98s Interval) with a focus on the D/M ventricle. In panel B), yellow lines show the whole tracks of individual cryptococcal yeast cells, the magenta circles are individual yeast cells. In panel B1, the white arrows show the general directionality of movement of all yeast cells, this is easier to see in Supplementary Video Fig. 5.5.

5.5.2 Dissemination from cranial vasculature into the CSF allows for examination of CSF flow in the zebrafish vascular infection model.

Light sheet imaging of *Tg(kdrl:mCherry)^{is5};TgBAC(cldn5a:EGFP)^{vam2}* transgenic zebrafish larvae were injected with 1000 cfu of *C. neoformans* KN99 GFP at 2dpf in the Duct of Cuvier demonstrated dissemination from cranial vasculature into the brain ventricles. The larva had a large fungal burden in the cranial vasculature, and it was possible to observe blood flow from the fluorescence of the cryptococcal yeast. Therefore, this unique phenotype allowed for observation of infected blood flow and the motion of *C. neoformans* yeast cells in the brain ventricles. A time-lapse (0.15 s/capture) was recorded of a single Z (Fig. 5.6) focusing on the D/M ventricle (Supplementary Video 5.6). I observed the dorsal longitudinal vein (DLV) (References to vascular anatomy - Isogai *et al.*, 2001) and around it some expression of the *claudin5a: GFP* reporter (Fig. 5.6). *Claudin5a: GFP* reporter is expressed in ciliated ependymal cells which become incorporated into the choroid plexus vasculature endothelium of zebrafish (van Leeuwen *et al.*, 2018).

There was dissemination into the D/M ventricle, with a single mass of cryptococcal cells located under the DLV (Fig.5.6 h) and smaller masses located away from any vasculature but ventral to *claudin5a: GFP* marker positive cells (Fig.5.6 g, b, c). Although there were masses within the CSF surrounding the vasculature, in high speed/interval imaging, disseminations events are not clearly observed (Supplementary Video 5.6a). The DLV seems to have blood flowing through at a high velocity (Supplementary Video 5.6a) with a heavy fungal burden (Fig. 5.6). One of the mesencephalic veins (MsV) (Fig.5.6 a and b), is almost completely obstructed by cryptococcal yeast and does not show signs of blood flowing through it. Dissemination around the MsV with a blockage was not observed (Fig.5.6 MsVa).

The velocities ($\mu\text{m/s}$) of yeast cells within each location type (bellow DLV; not bellow DLV) were measured (Fig.5.6 g, h) from the time lapse shown in Supplementary Video 4.6b (analysed using the TrackMate plugin in ImageJ (Tinevez *et al.*, 2017) Supplementary Video 5.6c). Cryptococcal yeast located under the DLV had maximum velocities with 39.27 $\mu\text{m/s}$. Cryptococci that were not located under the DLV had a maximum velocity of 8.5 $\mu\text{m/s}$. Cryptococci within the DLV can be seen to move with blood flow at an average speed of 12 $\mu\text{m/s}$, which is ~ 10 times faster than the yeast cells in the ventricles. However, there were many cryptococcal cells entering into and out of the imaging frame which skews track registration in the TrackMate software and registers tracks where there is no movement (Supplementary

Video 5.6 b and c). Looking at the original time lapse in the Supplementary Video 5.6a, it seemed that the cryptococcal cell cluster underneath the DLV was moving in a circular motion. Two cells under the *claudin5a: GFP*, away from the DLV marker expression, seem to be spinning in one spot (Supplementary video 5.6b and d; Fig. 5.6g). A manual cell tracking measurement was performed on the cells of the cluster in Fig. 5.6 g (not under DLV; under *claudin5a*), the track looked the same and the velocities were similar as the analysis in TrackMate (1.5 $\mu\text{m/s}$ mean; 7-10 $\mu\text{m/s}$ max). Manual measurements of single cell in frame under the DLV showed velocities of 0 $\mu\text{m/s}$ (Supplementary Video 5.6d). For cells that were moving in and out of the Z plane, motion could not be measured accurately in the manual measurement.

Figure 5. 6 Flow velocity of *C. neoformans* in the brain ventricles can be examined in the systemic infection model.

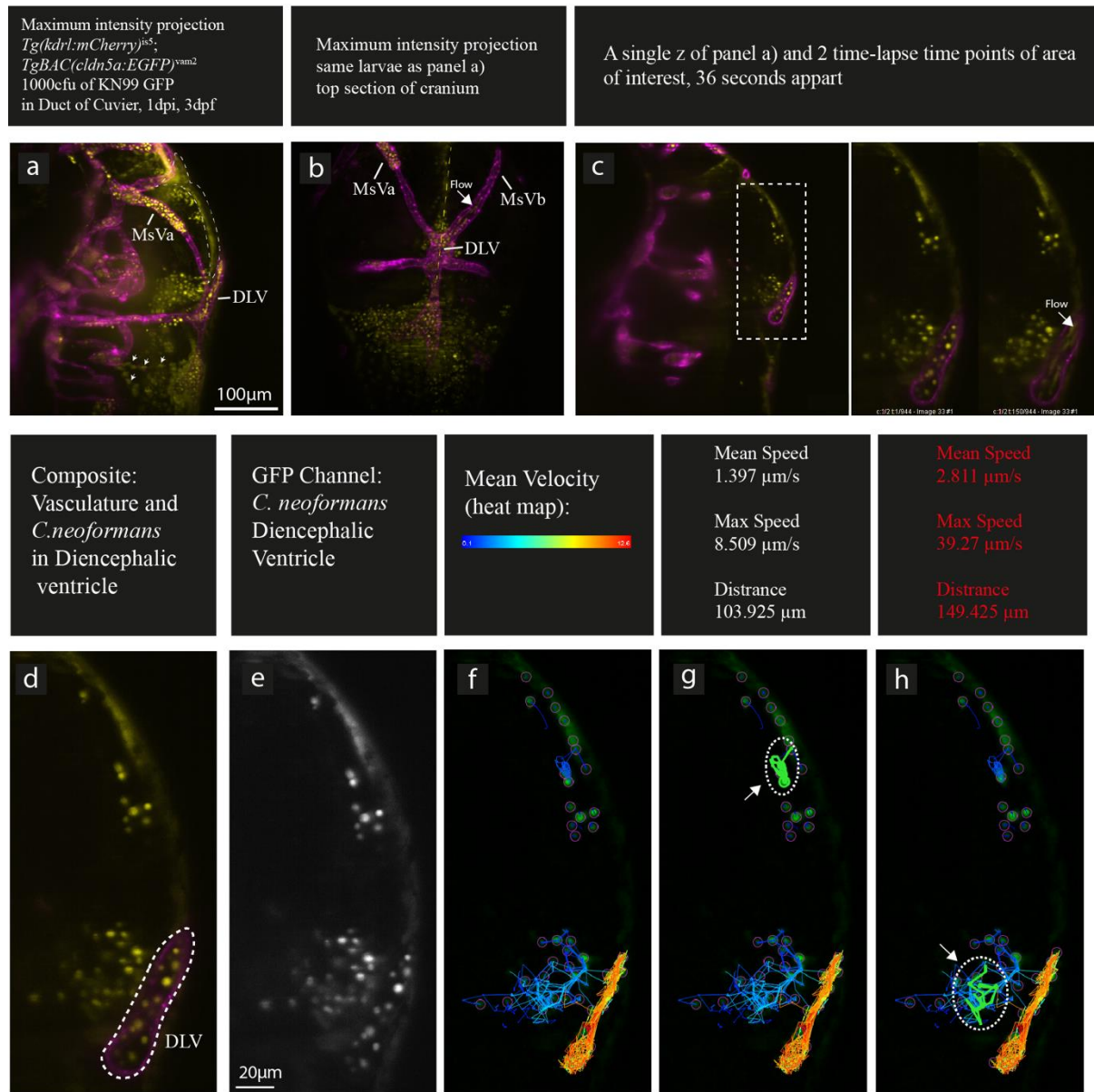


Figure 5.6 Flow velocity of *C. neoformans* in the brain ventricles can be examined in the systemic infection model.

Analysis and representative images from Supplementary Video 4.6 a. The video shows a time lapse of an infected zebrafish larvae in a single Z, at 0.15s/image capture, with a focus on the D/M ventricle. In panel a) we can see the MICP of a Z stack of the whole head imaged from a lateral perspective with a slight tilt. White arrows and the area outlined with a dashed line is where we see some expression of the *claudin5a:GFP* reporter. In panel b) we can see a MICP of a Z stack imaged from a dorsal point of view, yellow dashed line shows the location of the Z in panel c. In panel c) we can see whole size imaged of the single Z and an outline of the area of interest measured in the velocity analysis. Panels d-h represent the Track Mate analysis done on time lapse in the area of interest in panel c. In panel g and h we can see two tracks of focus, one away from the DLV (g) and one under the DLV (h)*. For the two tracks particle velocities/speeds are outlined. The cryptococcal yeast cells did not flow with a uniform velocity, mean, and max velocity in each area is given. MsV mesencephalic vein; DLV dorsal longitudinal vein; D/M diencephalic/mesencephalic ventricle; MICP maximum intensity projection.

*see issues with automated analysis in results;

5.6 Discussion

5.6.1 Viscosity increase observed *in vitro* could be physiologically relevant, despite large differences with spinal fungal burden in patients.

I hypothesised that the presence of encapsulated *C. neoformans* in the CSF can change its fluid profile from Newtonian to shear-thinning. However, I have found that the fluid profile of *C. neoformans* batch cultures were Newtonian, and it did not change under shear stress but there was an increase in shear viscosity. Patients with most severe disease have $\sim 0.2 \times 10^7$ cfu/ml of cryptococci in their CSF (Bicanic *et al.*, 2005; Bicanic *et al.*, 2007; Bicanic *et al.*, 2009). The closest to that concentration is the 25% dilution of the 4-weeks old still culture. The viscosity of the 25% dilution at 100 1/s is 1 mPa/s, 1.12 times more viscous than clear YPD broth alone (suspension fluid). The concentration of 0.2×10^7 is however the very high end of spinal CSF fungal burden in patients with intracranial hypertension (Bicanic *et al.*, 2009). Mean baseline fungal burden from all patients (+/- intracranial hypertension) is $\sim 10^5$, with is 3 decimal places less concentrated than the lowest fungal burden measured in my viscosity experiments (25% solution in 4-week-old still culture), which is 1.12 more viscous than water. The concentrations in my measurements appear to be supraphysiological for spinal CSF samples. However, we do not have information on fungal burden in niches in the cranium such as perivascular spaces, and dilated perivascular spaces are a good predictor for poor cognitive outcome or decline in cryptococcal meningitis (poor neurological outcomes in CM (Lee *et al.* 2021). High fungal burden and slower CSF flow may be a pathology of these cranial niches. There is no evidence that zebrafish larvae have perivascular spaces with the same anatomical functions for CSF flow into interstitium as in humans. Zebrafish larvae may not be currently the best model to study VR spaces, experimental design may require mammalian models, particularly mice, as VR spaces in the brain are extensively studied in murine animals (Sweeney *et al.*, 2018; Mestre *et al.*, 2020). Tracking of fluid flow velocity in VR spaces *in vivo* in mouse brain has been done before, and is possible to be used in a systemic infection to assess if there are viscosity changes in those niches contributing to pathology in CM.

In a system with a constant overall volume such as the cranium, increase in CSF viscosity would not directly lead to changes in pressure (Barnes *et al.*, 1989), but it would just lead to a slower fluid turn over. At the level of VR spaces this could mean slower transfer of CSF from perivascular to interstitial and/or slower reabsorption at the level of the venous vasculature in the glymphatic system of flow (Mestre *et al.*, 2020). In terms of pressure, dilation of VR spaces

due to retention may exert compression forces on the parenchyma and the vasculature imbedded in perivascular spaces. The pressure on the vasculature may induce compliance compensation in vascular constriction, which however is finite, and after a while pressure may build up due to global retention of CSF. If the CSF viscosity is increased, more force would be necessary to generate shear strain and flow. In CM, this may result in less circulation of CSF (i.e., CSF may spend more time in one area). This could lead to an abnormal accumulation of proteins and molecules in the ventricular space. If CSF secretion is dependent on an osmotic gradient, build-up of ions in the ventricular system would result in an initial increase in net CSF production (Bothwell *et al.*, 2019; Boron and Boulpaep 2017). However, there is some evidence of the choroid plexus robustly producing CSF during isotonic conditions and, and especially when faced an oppositely directed osmotic gradient (MacAulay *et al.*, 2021). It is still not well understood how the choroidal epithelium works to overcome or is influenced by osmotic gradients; it is therefore difficult to speculate how an increased osmolality in the CSF ventricles would influence CSF production. CSF viscosity influences the shear stress that the fluid will exert on tissues it passes through, which could cause damage to those tissues. In neurodegeneration models, reduced velocity of CSF within the narrow spaces of the brain interstitium has been suggested to alter protein composition and form toxic oligomers (Trumbore, 2016). If the presence of *C. neoformans* in fluids increases their viscosity, fungal presence would potentially allow for increase in toxic aggregates within the brain parenchyma. Cases of CM patients have been previously reported to present with symptoms of vascular dementia (Chishimba *et al* 2022; Ala *et al.* 2004; Aharon-Peretz *et al.* 2004; Steiner *et al.*,1984). It is possible that the link between the CM and dementia pathologies is altered velocities of fluid flow in the CNS, which makes research in understanding the CSF flow during infection relevant to other conditions.

5.6.2 Zebrafish larvae as a tractable model for the assessment of velocity and directionality of flow of cryptococci in brain ventricles

The aim of the second portion of this results chapter was to examine the potential of the zebrafish infection models described in Chapter 3, for measuring changes in ventricular CSF flow in infection *in vivo*. This is not possible in mammalian models, as the ventricles are not accessible for imaging in mammalian brains while the animals are alive. I hypothesised that the zebrafish infection model can fill this gap in available experimental systems. The observations in this chapter come from singular biological repeats and there is some

improvement in the imaging strategy that needs to be developed, but the work does show that zebrafish are a tractable model for the study of ventricular CSF flow in infection *in vivo*.

I examined *C. neoformans* yeast cells velocity and directionality of flow in mounted zebrafish larvae. In Olstad *et al.*, 2019, it was suggested that CSF flow is influenced by heartbeat, motile cilia, and bodily motion (Fig. 4.1). As the larvae are mounted, any type of flow observed in the data in this chapter is likely to be because of the influence of the heartbeat or cilia beating. Motile cilia beating in zebrafish brain ventricles facilitates circular flow in within each individual ventricular chamber around the whole chamber (Olstad *et al.*, 2019). At 2dpf, in a ventricular infection model 1dpi, cryptococcal yeast cells in the D/M ventricle were moving in a circular flow pattern around the whole ventricle. At 3dpf, in lower fungal burden in the D/M ventricles cryptococcal cells can be seen spinning in one spot and circulating under an area with *claudin5a: GFP* marker expression. Claudin5a expression is seen in ependymal cells which protrude into the D/M ventricle as early as 2dpf (van Leeuwen *et al.*, 2018; Olstad *et al.*, 2019).

At 2dpf cilia directed flow in the D/M has been shown to have a mean velocity of $\sim 3.5 \mu\text{m/s}$, and maximum velocity of $\sim 6 \mu\text{m/s}$ (Olstad *et al.*, 2019). At 4dpf those values change to $\sim 0.6 \mu\text{m/s}$ mean and $\sim 1.4 \mu\text{m/s}$ max. In a blood stream infection system, 3dpf ($\sim 90\text{hpf}$), 1dpi velocities of cryptococcal yeast in the D/M ventricle appear quite high for that developmental stage ($1.5 \mu\text{m/s}$ mean; $7-10 \mu\text{m/s}$ max). Motion of cryptococcal yeast as shown in Supplementary videos 4.6 (a, b, c, d) could be influenced by complicated factors that are not present in a healthy, uninfected, system. The infection would influence the distribution of blood flow across cranial vasculature. As some vessels (MsV) were completely occluded by infection (Fig. 4.6a, b) a larger volume of blood would go to vessels with no occlusions, such as the DLV. This may change the rate of fluid diffusion across brain barriers and increase the velocity of CSF flow in the DM.

Therefore, it is important to consider two factors when thinking about the influence of *C. neoformans* on CSF flow: 1) The influence of fungal cells on the CSF velocity of flow inside the ventricles; 2) The influence of fungal cells on structures involved in the production of CSF outside the ventricles.

The phenotypes observed in this chapter suggest cryptococcal yeast cells following a flow pattern that is directed by motion of ciliated ependymal cells. The data also shows the potential of the model for tracking velocity of CSF in infection. This work suggests that zebrafish is a powerful model for studying changes of CSF flow in infection, but there is a lot of optimisations to be done before any conclusions on emerging pathological mechanisms can be drawn. The intervals of imaging in the first data set are too long to accurately track cryptococcal yeast and assess velocity. Also, important controls are missing such as measuring flow of inert beads the size of cryptococci yeast into the ventricles. Using inert beads as a control would help determine if the impact of infection is mechanical or if it includes biological factors and cellular interactions. A variation of the experiment would be to attempt to stop the larvae heart, mount them and specifically investigate flow as a result of cilia beating. Another good control would be introducing an infection of acapsular *C. neoformans* mutant, which would provide insight into how the capsule contributes to flow patterns in infection. However, acapsular mutants, similar to heat killed *C. neoformans*, have been shown to be avirulent in murine models (Chang, Y. C., and K. J. Kwon-Chung et al., 1994,1998,1999; Chang, Y. C., L. A. Penoyer, and K. J. Kwon-Chung 1996), the pathogen was seen to accumulate in the abdomen in large granuloma like structures which consist of intact dead yeast, dissemination was not seen in the brain (Fromtling R A, Shadomy H J, Jacobson E S, 1982). Furthermore, a nuclear fluorescent strain of acapsular mutants has not been yet created, which would make particle tracking difficult to optimise. Lastly, an interesting set up would be to acquire a ependymal cilia reporter line such as the *T2BGSZ10 (foxj1b:gfp)* (Olstad et al., 2019) and in it observe the interactions of cilia with the cryptococcal cells or beads controls.

Chapter 6: Final Discussion

6.1 Introduction

This thesis aimed to develop and use *in vitro* and *in vivo* models to investigate how the CSF and cranial vasculature systems develop pathology in *C. neoformans* infection. In my introductory Chapter 1, I described the anatomy and physiology underpinning our knowledge of intracranial pressure and the pathological intracranial hypertension associated with cryptococcal meningitis. From my analysis of the existing knowledge, I identified that our lack of knowledge of the physical interaction of the pathogen with the different tissues (blood vessels, brain parenchyma and ventricles) as cryptococcal meningitis develops was a major barrier in our understanding on the pathophysiology of cryptococcal meningitis associated intracranial hypertension. In order to fill this gap in knowledge, I first surveyed and described the existing experimental models used. As described in my thesis aims and objectives, I concluded that there is a need for a suitable *in vivo* animal model that would allow me to examine the interactions of the *C. neoformans* pathogen with the brain ventricles and parenchyma, and within and around capillary sized vessels imbedded within the brain parenchyma. I explained the utility of infection models in the zebrafish larvae system and outlined my objectives. In addition, I concluded that to make measurements of the biophysical properties of how CSF containing cryptococci might behave, I acquired *in vitro* rheological measurements. Chapter 2 provided the materials and methods for the thesis and Appendix 1 is a published methods chapter on 'Zebrafish larvae as an experimental model of cryptococcal meningitis'. In my three results chapters I demonstrated how I addressed each of my objectives: In Chapter 3, I developed and validated a zebrafish model of cryptococcal meningitis in which we can observe impact of infection in all main tissues of the CNS. I tracked and examined the location of the pathogen as CM developed and showed that there was no dissemination from the brain ventricles into the brain tissues, that dissemination from the blood stream did result in infection of brain blood vessels, parenchyma, and ventricles. Injection of the cryptococci directly into the brain ventricles resulted in an increased cranial volume. While this volume change was linearly related to fungal burden, these burdens exceeded what has been measured from CM patients (Bicanic *et al.*, 2005; Bicanic *et al.*, 2007; Bicanic *et al.*, 2009). Increased cranial volume did not occur when cranial infection occurred via dissemination from the bloodstream. Comparison of cryptococcal infections to injections of heat-killed cryptococci was not possible due to their efficient clearance from the bloodstream. In Chapter 4, I developed methodology to measure the dynamic changes to cranial blood vessels during

development of CM. Using my methodology, I could demonstrate there was measurable change in the total vascular volume and there was an increase in the permeability of the brain to high molecular weight dextran. In addition, I presented preliminary findings regarding morphology and pulsations of infected cranial vessels. In Chapter 5, I described the physical underpinning to potential changes in the CSF flow in CM and how a fluid containing cryptococci increased in viscosity following still culture over a period of weeks, but without changing to its Newtonian properties. Finally, I demonstrated how my zebrafish model of CM could be used to measure the changes in CSF *in vivo*. Here, in my final discussion, Chapter 6, I will discuss my findings, their implications, limitations, and possible directions for future research projects.

6.1.1 High fungal burden and low toxicity of ventricular infection zebrafish model of cryptococcal meningitis

A ventricular infection zebrafish model was created with the aim to improve understanding of how the pathogen interacts with cranial tissues, and how these interactions lead to the pathologies associated with cryptococcal meningitis. *C. neoformans* was introduced into the brain ventricles at 1dpf. It appeared to just grow contained within the ventricles and even after 4dpi, there was no sign of dissemination into the parenchyma or vasculature. The result was a complete colonisation of the brain ventricular space with very little mortality. The fungal burden achieved proportionately far exceeded that which has been measured in patients. Therefore, it is hard to argue its direct relevance to the human condition and if any pathogenic pressure observed in this phenotype could have been translated to our knowledge of human disease. However, what was observed was a low toxicity to the brain induced by the pathogen, as there was very little mortality and no evidence of tissue degradation around the ventricles. This should be further assessed by examining the larvae for signs of apoptotic or necrotic cell death in the parenchyma or for increase in inflammation in the parenchyma, all of which could be tested using TUNEL or other *in situ* techniques (Yang et al., 2023). In cell culture work *C. neoformans* is well known as a pathogen that does not cause major cytotoxicity in mammalian cells and in animal models, it does not lead to tissue necrosis that is seen with other fungal pathogens (Luo et al., 2008; Casadevall, Coelho and Alanio 2018). However, it has been shown that *C. neoformans* does release some cytotoxic factors such as tissue degrading enzymes (e.g., protease, urease) and upon being phagocytosed it is detrimental to the homeostasis of monocytes such as macrophages (Casadevall, Coelho and Alanio 2018). Therefore, it is

important to examine what molecular and cellular impact the pathogen may have on brain tissue, that is not visible in my microscopy observations. Also, in future work, it would be interesting to test for any behavioural symptoms to this phenotype. Masked physiological impairment may be revealed through the presence of behavioural phenotypes. Animals could be tested for cognitive impairment, although complex cognition is observed in later stages of development, memory formation and habituation are exhibited in larval stages from 4dpf (Best et al., 2007; Reemst et al., 2023). These could be good candidate traits to test for impairment in infection, assays such as the reflex modification pre-pulse inhibition would be suitable to test for issues in simple cognition changes (Koch 1999).

The lack of toxicity of *C. neoformans* towards surrounding tissues is an important finding to validate as it helps us understand how much of the pathogenic impact of *C. neoformans* is purely due to mechanical obstruction. In mice, it has been shown that the pathogen traps in locations of vessel narrowing and cryptococcal yeast do not slow down before trapping, suggesting a mechanically induced trapping rather than a receptor binding such as leukocyte extravasation by rolling adhesion (Shi *et al.*, 2010). On the other hand, in zebrafish, 4.2µm beads injections into the systemic circulation do not show any trapping in the cranial vasculature, unlike *C. neoformans* inoculation (Gibson et al., 2022). It is possible trapping is induced by properties of the polysaccharide capsule which are not replicated by the surface of inert beads. HIV associated CM is also generally known for its scarcity of inflammation, the lack of immune control is generally a problem preventing containment of the infection (Stie et al., 2012; Santiago-Tirado et al., 2017). The lack of adaptive immune system in the larvae may prevent tissue toxicity coming from adaptive immune cells invasion.

6.1.2 Is brain ventricle dissemination unidirectional?

Another interesting observation coming from the ventricular infection model was that there was no dissemination into the vasculature. As there is dissemination from cranial vasculature into surrounding tissue, it was intriguing that opposite appeared not to occur in my model. In the ventricular infection model, the vasculature did not reabsorb the pathogen into the blood stream which means that it is possible that for cryptococcal yeast cells getting inside the CNS is easier than leaving it. It is rare to capture a dissemination event from cranial vasculature into the parenchyma in zebrafish larvae (Nielson and Davis et al., 2023), but in all of my ventricular infection experiments I did not see any larvae that showed dissemination from the ventricles

into the blood circulation (N=300), in contrast to dissemination from vasculature to CSF and or parenchyma which was seen in 63% of larvae 24hpi (N=150). In Nielson et al., 2023, 80% of disseminated cryptococcal yeast were intracellular, engulfed in microglia, possibly microglia do not traffic pathogens in the opposite direction (from CSF/parenchyma to vessels). Another reason for lack of dissemination into the blood circulation in my model may be that vessels get compressed by the mass of pathogen around them and that blood flow is restricted to infected areas. Zebrafish larvae can survive without blood circulation as they can absorb oxygen by diffusion, lack of blood delivery to the brain would not cause mortality (Gut et al., 2016, Lawson and Weinstein 2002).

It was interesting to see that in ventricular infection the *C. neoformans* does not cross into the vasculature and into the systemic blood stream but in systemic infection the pathogen does disseminate from the blood stream into the CNS i.e., there is a directionality in crossing barriers. However, studies of dissemination have only looked at one direction, from vasculature into the brain and not the other way. It is important to aim observations at testing if there is any host mediated transport **out** of the CNS, which would be with the purpose of clearance. Whether this is specific to the CNS and not to other organ system would require further testing by infecting other organ systems such as the liver tissue and assessing whether the infection progresses into the bloodstream. These experiments can reveal causes of the vulnerability of the CNS to cryptococcal infection. From my examination of the literature, I hypothesise that observing closely the involvement of the native immune system and tissue resident monocytes would shine a light on possible causes for system specific vulnerability (Charlier et al., 2009; Sorrell, T. C., et al. 2016; Santiago-Tirado et al., 2017; Gilbert et al., 2017; Strickland and Shi 2021; Nielson and Davis et al., 2023). If there is no host mediated transport out of the CNS, that would advocate for testing the hypothesis that therapeutic lumbar punctures do not alleviate symptoms only due to compensating for pathologically increased volume in the CNS but also it may be that they aid the removal of active pathogen in the CNS, something which may not be otherwise mediated in the host response. It is possible that the pathogen does not cross into the blood stream in my zebrafish larvae models due to the lack of adaptive immune response at this point of development of the zebrafish immune system. In normal immunity there is evidence that adaptive immunity mediated macrophage response leads to clearance of infected lung tissue, but in disseminated infection with compromised immunity it is not completely clear what the role of the missing adaptive immunity is (Mukaremera and Nielsen, 2017).

It is also possible that the digestion of the pathogen and clearance occurs within the infected tissue, and it never actually crosses back into the systemic infection once it is in the brain. The directionality of movement across tissues may be also a feature specific to the CNS, in pulmonary cryptococcosis the *C. neoformans* moves from infected alveolae into the blood stream (Denham and Brown et al., 2018), so the directionality is organ system to systemic blood flow and the infected tissue gets cleared by infection, something that does not seem to happen in my observations of CNS infection. This tissue specific directionality possibly depends on the properties of cell junctions in the apical and basal membranes of blood vessels or endothelium cell walls. Also, the pressure differences across two tissues the pathogen is crossing from and into may affect if the pathogen can physically go in a given direction across tissues. Finally, there may be just a preference to establishing niches in the brain due to availability of certain nutrients favoured by the pathogen and only present in the CNS. This may be causing a certain tissue retention that is specific to the CNS as the pathogen would be better at proliferating and infection not easily controlled by local phagocytes. The brain has the highest energy demand out of all organ systems and the steady-state brain tissue glucose concentration is about 20% of that in arterial plasma (Simpson, et al 2007). *Cryptococcus neoformans* can utilise glucose as a nutrient resource and it has been seen the presence of the pathogen leads to a reduces glucose concentration in the CSF (Zhang, Tan, Tien 2020).

6.1.3 Colonisation of brain tissues by cryptococci

Cranial deformities were observed in the larvae, and they were linearly correlated to fungal burden. This, and the lack of visible toxicity to surrounding tissues, suggests that the cryptococcal yeast are expanding in volume and mechanically compressing the top of the cranium to cause deformation. It is possible similar mechanism occurs in niches in the human brain, dissemination from the cranial vasculature could allow for pathogen trapping in perivascular spaces, where the fungal cells can establish colonies that grow in volume and compress surrounding tissues.

In my work I show that high concentrations of cfu in fluids cause an increase in fluid viscosity. Although these concentrations exceed commonly seen values of cfu from spinal CSF of patients, it is unclear if those fungal burden estimates represent the whole of the CNS. Dilated perivascular spaces are one of the most common neuroradiological markers of CM (Loyse *et*

al. 2015; Charlier *et al.* 2008;). Therefore, it is possible dilation is caused by cryptococcal colonies expanding in volume and slowing down CSF flow, leading to some retention of CSF in those niches and further compression of surrounding tissues and my data supports this. Colonies establishing in perivascular niches could lead to increase in viscosity of CSF in those areas. Zebrafish larvae may not be currently the best model to study VR spaces as anatomically similar niches have not been examined yet in zebrafish. Experimental design may require mammalian models, particularly mice, as VR spaces in the brain are extensively studied in murine animals (Sweeney *et al.*, 2018; Mestre *et al.*, 2020). Tracking of fluid flow velocity in VR spaces *in vivo* in mouse brain has been done before, and is possible to be used in a systemic infection to assess if there is viscosity changes and pathogen trapping in those niches contributing to pathology in CM.

In contrast to the ventricular infection model, systemic infection produced dissemination and pathogen presence in the vasculature and parenchyma as well as the CSF. Inoculation with pathogen was done through the duct of Cuvier at 2dpf, and the developmental stage was chosen as at 48hpf the primary vasculogenesis is complete and CNS vessel networks well established (Isogai *et al.*, 2003; Quiñonez-Silvero *et al.*, 2020). This recapitulates the involvement of those tissues in human patient phenotypes. Cryptococcal yeast cells were seen to establish in the cranial vasculature as soon as 1hpi but could potentially be even sooner if observations were made as the pathogen was injected into the bloodstream, which was unfortunately practically unfeasible at the time of experiments. I aimed to capture dissemination events in order to assess if endothelial cell wall crossing is mediated by disruption of the tissue's integrity. Dissemination in the CNS and parenchyma was common (63% 24hpi), but the event of pathogen crossing through the cranial vasculature endothelium into parenchyma or CSF was rarely captured (2/19 imaged larvae, 17 of which imaged for 20hrs or more) in dynamic imaging, despite extensive observation of infection development. This is reflective of recent studies of *C. neoformans* dissemination into the CNS in the zebrafish larvae, where events of endothelial cell wall crossing were detected but the event itself could not be visualised (Nielson and Davis *et al.*, 2023). One or two instances are visually represented of where vessel permeability has increased next to cryptococcal cells disseminated in the parenchyma, it was concluded that dissemination can be but is rarely disruptive to BBB integrity (Nielson and Davis *et al.*, 2023) and only 3 images presented an assessed increased cranial vasculature permeability in infection (Nielson and Davis *et al.*, 2023). In my work I examined this further, I assessed the deposition of dextran in the parenchyma from all the CCtAs in groups of 20

larvae and I showed that permeability of cranial vasculature in infection appears to be increased and there is a significant difference from larvae with no infection. Fungal burden in the parenchyma and CSF was not correlated to permeability increase, and dextran deposits in the parenchyma were not colocalised with specific vessels, so disruption of the vascular endothelium integrity was never morphologically detected. Functional increase in permeability was not necessarily due to dissemination, but rather the presence of *C. neoformans* in the vasculature. Factors secreted by the pathogen may influence the properties of the BBB, it has been previously shown in an *in vitro* BBB model that *C. neoformans* secretes metalloprotease (Mpr1) that appear to be required for brain vascular endothelium crossing (Vu et al., 2014). Validating this work in my zebrafish model could be done in the future by inoculating with Mpr1 lacking *C. neoformans* mutants and assessing the integrity of the BBB in systemic infection with the mutant.

Chemical factors secreted from the pathogen are one explanation as to why vascular infection may cause increase in BBB permeability/leakiness. Another explanation is mechanical obstruction of the pathogen that triggers mechanisms inducing shear stress and physical strain on the vascular wall. This has been previously shown using fluorescence resonance energy transfer (FRET) in transgenic zebrafish lines that report for tension in between cell-cell junctions in the vascular wall (Gibson et al., 2022). The work showed that in zebrafish with systemic *C. neoformans* KN99 infection, in vessels with and without cryptococcal trapping and colonisation, tension in the vascular wall is increased as distance between cell-cell junctions is also increased (Gibson et al., 2022). It seems that what is occurring is a system wide increase in shear stress on the vasculature. In the examination of dissemination progression time lapses what came to my attention was the incredibly dynamic nature of the cranial vasculature in infection. In comparison to larvae without infection, cranial vessels, particularly the CCTAs, showed a phenotype of rapid expansion and shrinking. I termed this phenotype/phenomenon “pulsations”. I created a method to quantitatively represent the characteristics of each pulsation, allowing for comparison of the pulsation profile with infection and without. More high-resolution data points are needed to create exclusion intervals for automated classification of pulsation +ve or -ve larvae. The presence of the phenomenon was determined through observation in 15 out of 18 larvae imaged. These numbers cannot be used for accurately assessing prevalence but are confirmation that the phenotype exists, and it is likely commonly found. Preliminary data on characterising pulsations suggested that they can be observed synchronously across vessel group in the head of the same larvae, which is indicative of triggers

that elicit a system wide response. I proposed that blockages may decrease the vessel area accessible to the cerebral blood volume inflow from the heart i.e., the force coming from the heart is the same, but it is applied on a smaller area, which overcomes resistance in the vessel wall and distends/ dilates it. Pulsations intensity could potentially be used as a measure of peripheral resistance increase in the cranial vasculature, and it could be tested if the amount of cryptococcal mass blockages present in the cranial vasculature correlates with intensity of pulsations/peripheral resistance increase.

6.2 A summary theoretical model of cranial pressure in the presence of C. neoformans

6.2.1 Existing knowledge base and assumptions of summary model

To understand my findings in the context of pressure we need to consider how the components of the CNS such as the CSF, vasculature, and brain tissue, influence one another to propagate pressure or create it. In my introduction I discuss this topic at length, and I provide references to variable theories of intracranial pressure mechanics and work that supports it (see section 1.1.4). My summary model (Fig. 6.1) makes assumptions based on evidence presented in the introduction. The assumptions are:

1. Assume the cranium is a closed system with an equalised hydrostatic pressure, with flow and pressure described with consideration of Pascal's principles.
2. The skull is a rigid container of fixed volume.
3. The CSF compartment is a closed system with incompressible fluid in it.
4. The total volume of CSF is fixed (apart from small variations in production that will be ignored here)
5. The cerebral vasculature surrounds the brain and is embedded in it.
6. Blood is also an incompressible fluid and for our purposes can be considered as of fixed volume across the whole body.
7. The cranial vasculature is a closed system of flow but, in contrast to the CSF, with a pump, which in terms of its physics can be considered a piston.
8. The CSF is in contact with the vascular system, which expands and contracts. Within the closed volume of the cranium the force generated by the expansion and contraction of the vasculature will propagate into the CSF system

9. Expansion and contraction would generate a push, pull like CSF displacement, with volumes of CSF moving caudally or rostrally depending on whether vessels in the brain are expanding or contracting.
10. The larger blood vessels in the cranium around the cortex (grey matter), the subarachnoid space and skull restrict outward expansion – most of the blood volume in the outward blood vessels have a net inward push on the parenchyma towards the ventricles.

Considering those assumptions, I created a simplified infographic (Fig. 6.1) that may present the cranium as dynamic pressure system, in which forces of pressure come from the vascular compartment. The anatomy of the cranium is represented by the different tissues within it, their compressibility, and their compartments. The tissues are:

1. Skull – incompressible rigid box
2. Dura – impermeable and incompressible collagen membrane
3. Dural CSF – incompressible fluid filled sinuses.
4. CSF – ventricular and subarachnoid (surrounding the brain)
5. Neuronal tissue (parenchyma) – for now we do not make assumptions of compressibility.
6. Vascular – blood filled vessels; the blood is incompressible, and the vessels have capacity to distend; as per assumption 9, the vessels with capacity to distend are mostly around and not within the brain so I have represented them as a mass that pushes on top and around the brain.

The different compartments in my infographic model are:

1. Vascular
2. CSF in ventricles and around the brain (and in and around the spine)
3. Dural – representing sinuses.

Borders in between these compartments are impermeable such as the dura and the skull, and permeable, which is represented in orange and encapsulate arachnoid granulations, choroid plexus, and venous reabsorption of CSF at the spine (Fig. 6.1). The permeability of the vascular compartment as a whole is not yet considered. At the end of the vascular compartment is the heart which is represented by a piston that applies or relieves pressure. Pressure in this model is measured from an opening at the level of the spine and by measuring the height of column

of CSF that comes out. The higher the column the bigger the pressure. In this infographic we first assume a state of rest, where there is yet no forces of pressure coming from the heart. The CSF is present around the brain and in the Dural sinuses at a state of rest (no flow) and the pressure is normal. Pressure measurements at rest are measuring hydrostatic pressure.

In a state of systole, the heart/piston introduces a pressure gradient in the vasculature. Added blood volume and flow into the cranium causes vasculature that distends to expand and push (propagate force) on the brain, which contracts inward (in this model also downward). The brain pushes on ventricular CSF towards the spine, around the brain, into the dura and out of the brain. Vascular compartment expansion causes the system to have a temporary pressure gradient that generates CSF flow. During systole, the opening pressure measurement would increase as CSF is pushed towards the spine and the volume in the cranium is increased as the blood enters the system. The measured pressure is hydrostatic pressure plus the pressure from the heart.

So how is pathological increase in volume and pressure possible if there is no room in the skull to introduce more volume as it is a rigid structure, and the vasculature has a generally fixed volume across the body? To increase pressure in such a system, density of matter must increase, as volume cannot. Therefore, for this model to work, we must assume that the parenchyma is compressible, as it is the one tissue that could be compressible. It is important to know whether brain tissue is incompressible and if the forces of pressure from the vascular compartment will increase its density or only displace volume. If density of the tissue does increase, then we would have an increase in the hydrostatic pressure the tissue exerts on the container i.e., the skull. Classically, the brain is accepted to be incompressible and to behave as a fluid when forces of deformation are applied (Klarica et al., 2013), but recent reports claim the brain contains sufficient soft compressible material to be compressible (Hosseini-Farid et al., 2019). Brain density has been previously assessed using computer tomography (CT) and is defined by CT Hounsfield Units (CTHU). Using this method, patients with extra-axial haematoma with brain deformation, overall density was seen to increase (Nguyen et al., 2016). Therefore, I will consider the neuronal tissue as compressible, but this will likely cause damage to the patient if it is compressed beyond a certain tolerance.

Figure 6. 1 A simplified model of the dynamics of intracranial pressure

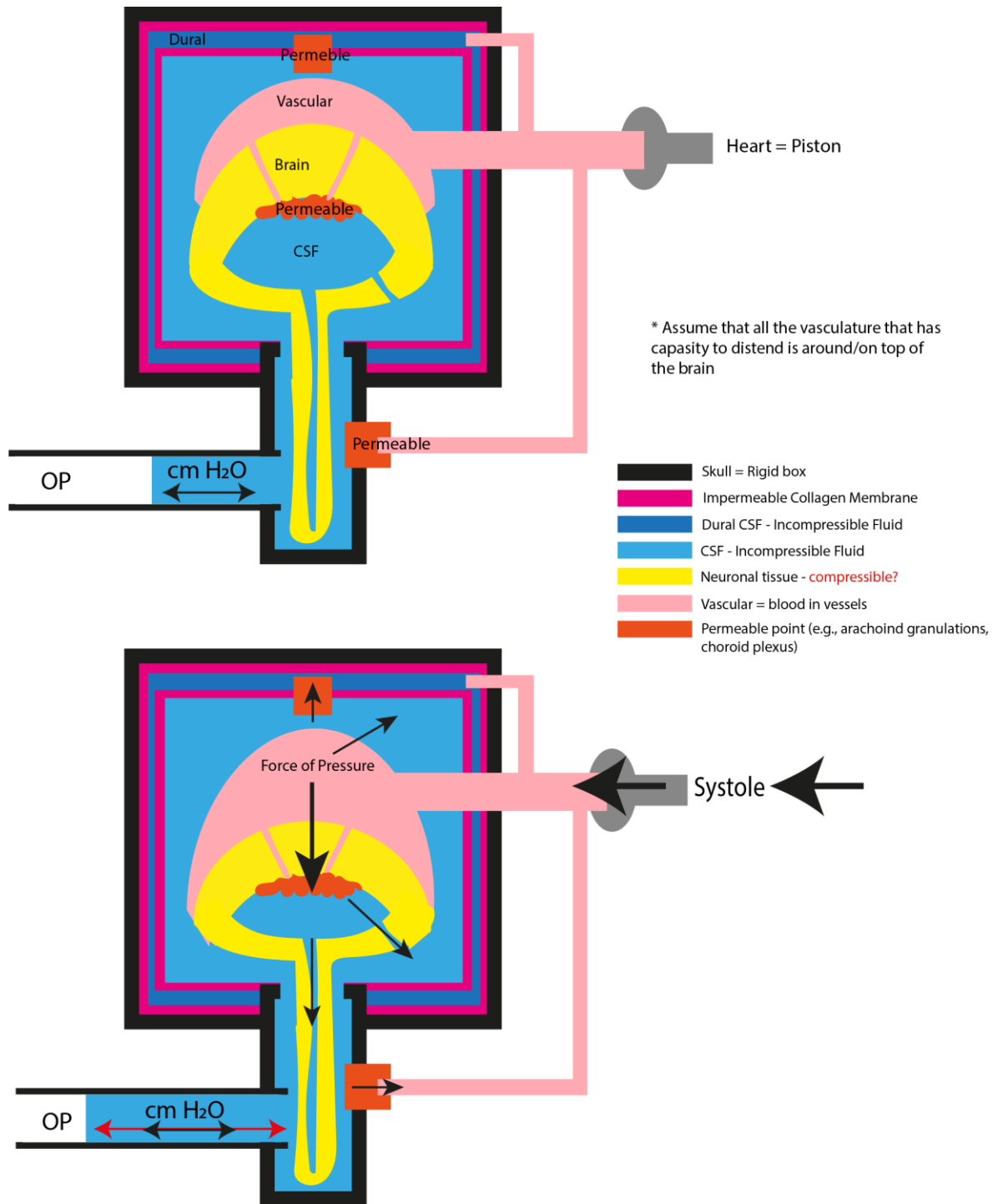


Figure 6.1 A simplified model of the dynamics of intracranial pressure

A simplified infographic that may present the cranium as dynamic pressure system, in which forces of pressure come from the vascular compartment. The anatomy of the cranium is represented by the different tissues within it, their compressibility, and their compartments. The tissues are: Skull – incompressible rigid box; Dura – impermeable and incompressible collagen membrane; Dural CSF – incompressible fluid filled sinuses; CSF – ventricular and subarachnoid (surrounding the brain); Neuronal tissue (parenchyma) – for now we do not make assumptions of compressibility; Vascular – blood filled vessels; the blood is incompressible, and the vessels have capacity to distend; the vessels with capacity to distend are mostly around and not within the brain so they are represented them as a mass that pushes on top and around the brain. The different compartments in my infographic model are: Vascular; CSF in ventricles and around the brain (and in and around the spine); Dural – representing sinuses. One direction arrows are directions from high pressure to low. Double ended arrows are movement of fluid, red double ended arrow is change in range of movement. OP = opening pressure at the lumbar spine subarachnoid space.

For detail description of the model this infographic represents please refer to section 6.2.1 of the Final Discussion.

6.2.2 *C. neoformans* pathogenic presence in the context of theoretical model of pressure

Degree of parenchyma and venous compression related to pathogen volume in the CNS.

Pathogen masses are present in the CNS in the form of brain tissue cysts or colonies in niches (Lee *et al.* 2021; section 3.5.1). A foreign volume would cause some existing volume to leave, likely through vascular compliance i.e., in the form of venous blood outflow. The venous compartment has the most potential to distend and during heart rate BP changes the venous compartment normally would greatly contribute to forces of pressure on the brain tissue, which would contract inward as a result. If those dynamic forces of pressure are reduced, as they are CSF outflow drivers, it is possible that this would make it more difficult to expel CSF through the arachnoid villi or through reabsorption by venules in the glymphatic system. Post-mortem work showing pathogen trapping in arachnoid villi, reducing villi permeability, is likely going to contribute to increase in CSF in the subarachnoid and ventricular compartment possibly similarly to communicating hydrocephalus (Loyse *et al.*, 2010; Koleva and De Jesus 2020). In some patients, hydrocephalus or dilated perivascular spaces could be as a result of a higher CSF content in the CNS. As we accept that the volume of the cranium is constant and pressure equalises in the system, pressure in the case of CSF retention will increase if the density of brain increases due to compression from dilated spaces that contain the excess of CSF. However, how big the volume of pathogen is in the brain is unclear during the course of the disease, therefore it would be difficult to predict the degree of its influence on compliance and venous compression.

Venous sinus stenosis is an MRI and a magnetic resonance venography (MRV) marker of dural sinus compression seen in idiopathic intracranial hypertension (Zhao *et al.*, 2022). It would be useful to assess the prevalence of this in cryptococcal meningitis, to do larger scale quantification and of the degree of stenosis in different stages of infection/different CSF fungal burden, with the aim of examining if compression of cranial structures may be related to spinal CSF cfu concentration.

Also, if CSF retention occurs in infection, it may be possible to test that in the zebrafish larvae infection model, by introducing nanoparticles in the ventricles of systemically infected fish and compare clearance from the ventricles into the circulation between infected and control non-infected larvae.

Arterial pulsations could increase influx of CSF into parenchyma and/or mediate CNS compression in selected regions.

If the pathogen does enter the CNS through cranial vasculature, which is what dissemination studies suggest, and it also has a tendency of mechanical trapping in smaller vessels, shown in mouse and zebrafish studies, it is likely it will end in spaces around smaller vessels or remain trapped in smaller vessels. Trapping in small vessels would manifest in small infarctions at first, and indeed lacunar infarcts are commonly seen in patient neuroradiological profile assessments (Mishra et al., 2018). As the capillary bed contains a large amount of the surface area of the cranial vasculature (Smith et al., 2019), the decrease in area would increase resistance for blood inflow. I am seeing that this may result in increase of vascular distending, which looks like pulsations, it could possibly mean that pressure coming from the heart in systole in some areas is greater, and arterial pulsations which drive CSF flow may be more pronounced. Arterial pulsations are the main contributor of CSF influx into perivascular spaces (Mestre et al., 2018). Coupled with possibly compliance occurring in infection and veins constricting, driving CSF into dural sinuses may be dampened, but driving CSF into perivascular spaces may be increased. This would explain the fact that dilated perivascular spaces are the most commonly identified neurological marker in CM patients (Lee et al., 2021; Loyse et al. 2015; Charlier et al. 2008;). Perivascular spaces are surrounding the brain, it is likely an increase in influx of CSF in those spaces causes a compression of brain tissue around and increase in pressure due to increase in brain density.

Perivascular spaces are not yet identified in the zebrafish brain, neither in larvae nor adults. The dynamics of flow in perivascular spaces have been extensively studied in murine models, through cranial window approaches (Mestre *et al.*, 2018). Murine cranial window models have been used to study initial infection vascular pathology (Shi et al., 2010; Kauffman-Francis et al., 2018; Coelho et al., 2019), those models can be adapted to examine pressure and how perivascular spaces flow dynamics relate in a more established infection. For example, to avoid disturbing ICP homeostasis, opening pressure could be measured in several time points in rat models before doing invasive investigation of the pathology by creating a cranial window and imaging flow around perivascular spaces. Coupled with that, processing of true fungal burden in the brain could be done by plating homogenate on antibiotic plates and relating fungal volume to the makeup of the pathology as seen in cranial window microscopy and pressure measurements.

CSF retention in perivascular spaces may be exacerbated by increase in CSF viscosity due to high concentrations of *C. neoformans* in those niches.

The increase in arterial pulsations and influx of CSF into the perivascular spaces would be even more exacerbated when there is pathogen present in those spaces. We know that in humans *C. neoformans* causes lacunar infarcts and in animal models it gets trapped and can form colonies in smaller vasculature. It is unclear in both human and animals if this is happening in human sized arteries and veins, and perivascular spaces are mostly around those vessels in human brains. We know however, that there is a presence of the pathogen in the CSF, from lumbar punctures, dissemination from the smaller vasculature into the CSF may occur where the vasculature is in contact with the CSF and not with the brain parenchyma. Such a site is the choroid plexus, which is a hub of small vessels directly suspended in the ventricles. What could be occurring is that the pathogen is disseminating through those structures into the CSF and through pathogenic flow dynamics favouring CSF influx into perivascular spaces, cryptococcal masses may establish in those spaces. If there is indeed a presence of *C. neoformans* colonies in VR spaces, the local concentration of pathogen may increase viscosity of the CSF as seen in my *in vitro* experiments. Viscosity increase of CSF in the VR spaces niches can further exacerbate CSF build up in those niches and the compression on the brain tissue. AQP channels would allow for some influx of CSF into the brain parenchyma, an influx rate that would increase if there were a build-up of fluid. This may sustain a good mental cognition due to clearance of neuronal metabolism by-products through the glymphatic system. However, the rate of influx into the interstitium may not be fast enough to prevent that build-up of CSF in the VR spaces, overtime leading to larger and larger compression of the brain tissue. Particle tracking fluid dynamics experiments in perivascular spaces of murine models (Mestre et al., 2018), as suggested in the previous paragraph, can also help assess if the presence of *C. neoformans* in these spaces causes a decrease in flow velocity and possibly increase in viscosity.

6.2.3 *C. neoformans* presence in the CNS resulting in pathological influence that may not be due to intracranial pressure increase.

Cryptococcal meningitis also has a history of being misdiagnosed as vascular dementia or AD pathology (Steiner et al., 1984; Aharon-Peretz et al., 2004; Alla, Doss, and Sullivan 2004; Hoffmann et al., 2009; Chishimba et al., 2022). In a study that analysed serial brain MRI findings of 76 patients, periventricular lesion extension has been found in more than half of the

cohort (Lee et al., 2021). Those lesions look like a cloud surrounding the ventricles on T2 fluid attenuated inversion recovery (FLAIR) images and are a factor that is strongly associated with poor neurological outcomes (Lee et al., 2021). Small vessel disease is associated with such a neuroradiological presentation, alongside recent small subcortical infarcts and lacunes, which are also seen in CM (Wardlow et al., 2013). In my work I have seen evidence of increase in permeability of the brain vasculature in infection, increase in vascular permeability suggests for compromised vascular integrity. Periventricular lesions could also be a presentation of this compromised vascular integrity due to infection, possibly a build-up of permeability which is leading to brain tissue toxicity from exposure to compounds that are not normally present in brain tissue. It may be that occlusions of small vasculature happens commonly enough in infection to present as a vascular dementia-like pathology.

6.3 Final conclusion

The causes of intracranial hypertension in cryptococcal meningitis are still unknown. In this thesis I have shown how zebrafish larvae can be used to study this question, and its strengths and weaknesses. In addition, I have analysed the published evidence for the possible mechanisms of intracranial hypertension using a theoretical physics approach. In this final discussion chapter, I have further discussed the analysis of the literature in the context of my PhD studies. I have considered all my observations, from mine and previously published work, and I have reviewed how the presence of cryptococcal yeast would induce pathogenic changes in a theoretical model of pressure. Experimentally, I have shown that there is low toxicity of high fungal burden in the ventricles, and that brain parenchyma and blood vessels are not colonised from the ventricles, suggesting the possibility of unidirectional dissemination. I made preliminary characterisation of a new phenomenon in the pulsation of cranial blood vessels during zebrafish cryptococcal infection. Significant further work is needed to understand the underlying cause for this phenomenon and its possible biological significance. Finally, I have discussed how *C. neoformans* presence in the CNS resulting in pathological influence that may not be due to intracranial pressure increase. In conclusion, while the central question of my PhD remains, I have contributed theoretical and experimental methods and data that will be of benefit to future research.

Supplementary Videos: Legends and Links

Supplementary video titles correspond with the number of the figure they are represented and described in.

1. Video 3.11

Tg(kdrl:mcherry)^{is5} zebrafish larvae injected at 2dpf in the Duct of Cuvier with 700cfu of *C. neoformans* KN99 GFP, mounted in 1.5% LMPA and imaged for 20hrs, starting at 1hpi, in a temperature-controlled chamber with a double-fluorescent widefield Nikon microscope, with a 10x lens (see section 2.4.3 of thesis). Images were captured every 7 minutes for two channels (mCherry and GFP fluorescence). The white arrow on video represents a dissemination event.

Video 3.11 link: https://drive.google.com/file/d/1LlOuzTo8o4vYsanXj1-laqzkb-SqosjU/view?usp=share_link

2. Video 3.12

Tg(kdrl:mcherry)^{is5} zebrafish larvae injected at 2dpf in the Duct of Cuvier with 700cfu of *C. neoformans* KN99 GFP, infection was left to develop for 20hrs. Larvae was mounted in 1.5% LMPA and imaged for 20hrs in a temperature-controlled chamber with a double-fluorescent widefield Nikon microscope, with a 10x lens (see section 2.4.3 of thesis). Images were captured every 1 minute for two channels (mCherry and GFP fluorescence). The white arrow on video represents a dissemination event.

Video 3.12 link: https://drive.google.com/file/d/1izBhHKSc1TQOoc-5wK13KGFDDHQwoSIP/view?usp=share_link

3. Video 3.13

Tg(kdrl:mcherry)^{is5} TgBAC(cldn5a:EGFP)^{vam2} zebrafish larva was injected at 2dpf in the DoC with 700-1000cfu of *C. neoformans* KN99 GFP. Larva was left to develop the infection until 24hpi, at which point they were mounted in 1.5% LMPA and imaged with a 20x Zeiss Z1 Light Sheet microscope (see 2.4.4). The vasculature was imaged in a single Z, every 0.14 seconds for 0.5-5minutes to attempt to capture a dissemination event. A cryptococcal mass is shown to

be dynamic under the DLV and the infection flowing through the DLV, with dissemination event not captured in the time lapse or still images.

Video 3.13 link:

https://drive.google.com/file/d/1NPeVwkdqtU7qLTYNZ2dlehfkRztbdhwH/view?usp=share_link

4. Video 4.1

A 20hr time-lapse (~60-80) imaging the lateral side of the cranial vasculature of a *Tg(kdrl:mCherry)^{S916}* transgenic zebrafish larvae, 1-2hpi in the DoC with *C. neoformans* KN99 GFP (on shown composite images - GFP is yellow; mCherry is magenta). Images in the time lapse represented here were collected every 5 minutes.

Video 4.1 link:

https://drive.google.com/file/d/1TXsDPI3BAIhFmO8Fe4ArNj0306EwxPDL/view?usp=share_link

5. Video 4.2

A 20hr time-lapse (~60-80hpf) imaging the lateral side of the cranial vasculature of a *Tg(kdrl:mCherry)^{S916}* transgenic zebrafish larvae. Images in the time lapse were collected every 5 minutes. (GFP is yellow; mCherry is magenta).

Video 4.2 link:

https://drive.google.com/file/d/12j7jeExG0qF71YEgQSrekXLU2E8NuU0_/view?usp=share_link

6. Video 4.3

A 5-minute time-lapse (~60hpf) imaging the lateral side of the cranial vasculature of a *Tg(kdrl:mCherry)^{S916}* transgenic zebrafish larvae, 2hpi in the DoC with *C. neoformans* KN99 GFP (GFP is yellow; mCherry is magenta). Images in the time lapse were collected every 2 seconds.

Video 4.3 link: https://drive.google.com/file/d/1DPJDhJigYt0331zd5UW9HaaOcpbR-wL3/view?usp=share_link

7. Video 4.4

A 20hr time-lapses (~60-80hpf) imaging the lateral side of the cranial vasculature of a *Tg(kdrl:mCherry)^{S916}* transgenic zebrafish larvae 3hpi in the DoC with *C. neoformans* KN99 GFP. Images in the time lapse were collected every 5 minutes. (GFP is green; mCherry is magenta).

Video 4.4 link:

https://drive.google.com/file/d/1YsBcsWaddf9kAhCSPTaaREvXoVdVD3BB/view?usp=share_link

8. Video 4.5a, b

15min time-lapse at 40x magnification, imaging the lateral side of the cranial vasculature of a *Tg(kdrl:mCherry)^{S916}* transgenic zebrafish larvae with no infection. Images in the time lapse were collected every 2 seconds, the whole time-lapse can be seen in original mCherry in 4.5a and binary converted mCherry channel in Video 4.5b.

Video 4.5a link: https://drive.google.com/file/d/1nTKN0b-hqTWy1U0eyjhF46PF11znl_ik/view?usp=share_link

Video 4.5b link:

https://drive.google.com/file/d/1Fj_s0M7LAbG_R2WBf3UraGMJJAbUf18x/view?usp=share_link

9. Video 4.6

A 15 minute time-lapse imaging the dorsal side of the cranial vasculature of a *Tg(kdrl:mCherry)^{S916}* transgenic zebrafish larvae 5hpi in the DoC with *C. neoformans* KN99 GFP. Images in the time lapse were collected every 0.5s (GFP is yellow; mCherry is magenta).

Video 4.6 link: https://drive.google.com/file/d/1J48r3vAuJDIM-Sn2LCIPViwuh931Oatx/view?usp=share_link

10. Video 4.7

A 3 minute time-lapse imaging the dorsal side of the cranial vasculature of a *Tg(kdrl:mCherry)^{S916}* transgenic zebrafish larvae, in control larva (no infection). Images in the time lapse were collected every 0.5s. mCherry channel is artificially colored magenta.

Video 4.7 link:

https://drive.google.com/file/d/1wiQHi_O9Xryo_P6Fk26aKjMHJBYPjTDj/view?usp=share_link

11. Video 5.5

A time-lapse imaging the movement of *C. neoformans* yeast cells within the diencephalic/mesencephalic (D/M) ventricular space of the larvae cranium with imaging interval 3.98s with a focus on the D/M ventricle.

Video 5.5 link:

https://drive.google.com/file/d/1InHB7Ekxfkmfsymfac042MXgys8bbM_j/view?usp=share_link

12. Video 5.6a, b, c, d

Video 5.6a shows a time lapse of an infected *Tg(kdrl:mcherry)^{is5} TgBAC(cldn5a:EGFP)^{vam2}* reporter zebrafish larvae in a single Z, at 0.15s/image capture, with a focus on the D/M ventricle. Videos b, c and d show the Track Mate analysis done on time lapse of the area of interest in (shown in video b). The cryptococcal yeast cells did not flow with a uniform velocity, mean, and max velocity in different areas.

Video 5.6a link: https://drive.google.com/file/d/1_1mAfGBTijumrCIQ3-Mwm6Xit1-JfLM7/view?usp=share_link

Video 5.6b link: https://drive.google.com/file/d/1oOnO-Yd7MECyLh7C0VFeG-da0THXTORZ/view?usp=share_link

Video 5.6c link: https://drive.google.com/file/d/1g-MyKXCJdh04AFgBy05hcCuptr3Bf07E/view?usp=share_link

Video 5.6d link: https://drive.google.com/file/d/1fJYcSWxouDUb6lOCGwrZiXJOrHCE-MEb/view?usp=share_link

Appendix 1

*Formatting issues are to do with converting chapter from published format into Microsoft Word format. Please also refer to Appendix 1 as a supplementary attachment file.

Metadata of the chapter as visualized online

Chapter Title	Zebrafish Larvae as an Experimental Model of Cryptococcal Meningitis
Copyright Year	2023
Copyright Holder	The Author(s), under exclusive license to Springer Science+Business Media, LLC, part of Springer Nature
Author	Family Name Chalakova Particle Given Name Z. P. Suffix Organization University of Sheffield, Firth Court Address Western Bank, UK Email zchalakova1@sheffield.ac.uk
Corresponding Author	Family Name Johnston Particle Given Name S. A. Suffix Organization University of Sheffield, Firth Court Address Western Bank, UK Email s.a.johnston@sheffield.ac.uk
Abstract	This chapter provides guidance for introducing <i>Cryptococcus neoformans</i> into the zebrafish larvae model system to establish a CNS infection phenotype that mimics cryptococcal meningitis as seen in humans. The method outlines techniques for visualizing different stages of pathology development, from initial to severe infection profiles. The chapter provides tips for real time visualization of the interactions between the pathogen and different aspects of the CNS anatomy and immune system.
Keywords (separated by '-')	<i>Cryptococcus neoformans</i> - Cryptococcal meningitis - Fungal meningitis - Host-pathogen interactions - Zebrafish - Live imaging - Time lapse microscopy

Zebrafish Larvae as an Experimental Model of Cryptococcal Meningitis 2 3

Z. P. Chalakova and S. A. Johnston 4

Abstract 5

This chapter provides guidance for introducing *Cryptococcus neoformans* into the zebrafish larvae model 6 system to establish a CNS infection phenotype that mimics cryptococcal meningitis as seen in humans. The 7 method outlines techniques for visualizing different stages of pathology development, from initial to severe 8 infection profiles. The chapter provides tips for real time visualization of the interactions between the 9 pathogen and different aspects of the CNS anatomy and immune system. 10

Key words *Cryptococcus neoformans*, Cryptococcal meningitis, Fungal meningitis, Host–pathogen 11 interactions, Zebrafish, Live imaging, Time lapse microscopy 12

1 Introduction 13

Cryptococcal meningitis (CM) is an opportunistic fungal infection 14 of the central nervous system (CNS) caused by members of the 15 genus *Cryptococcus*. Annual cases of CM were last estimated to be 16 223,100 globally, and despite the presence of antifungal pharma- 17 ceuticals, AIDS-related CM mortality is very high with CM 18 accounting for 15% of all AIDS-related deaths worldwide [1]. 19

At the point of diagnosis of CM, symptoms are already severe, 20 and the pathology is in its late stage of development [2, 3]. There- 21 fore, human clinical studies rarely provide information about early 22 processes that lead to severe pathology, which masks potential 23 targets for treatment. MRI imaging is the best tool we have for 24 observation of CNS pathology in living patients, but MRI imaging 25 has a lot of limitations in resolution, and it does not allow for 26 visualization of smaller scale interactions on the levels of capillary 27 vessels and immune cell behavior in the CNS [4]. 28

Experimental research in CM aims to shine light on the gaps in 29 our understanding of pathology as seen in humans. Murine models 30 have been a powerful tool for examining immune responses to 31

cryptococcal infection, and the model is seen to recapitulate the pathology characteristics in patients [5]. Nonetheless, mouse models (and other mammalian animal models) are limited as they do not allow for observation of host pathogen interactions in real time in vivo. Nonmammalian models like *Caenorhabditis elegans* and *Drosophila melanogaster* are highly tractable for live imaging, but they do not provide the opportunity to mimic complex multicellular immune interactions, and critically, anatomical and physiological aspects of CNS pathology as seen in humans.

The zebrafish (*Danio rerio*) is a powerful vertebrate model that has strong parallels with mammalian genetics and anatomy. The simplicity of the system in comparison to murine models makes it easier to focus on individual pathological mechanisms. The zebrafish infection system is now well established for experimentally examining host pathogen interactions in cryptococcosis [6-10]. Fluorescent transgenic zebrafish lines are a state-of-the-art model for high resolution in vivo visualization of small cranial vasculature, brain parenchyma, and CNS innate immune cell types [11-13]. Due to their transparency, zebrafish allows for noninvasive visualization of CNS pathology development in real time.

In this method chapter, we outline procedures that enable the utilization of the zebrafish infection system to study host pathogen interactions of *C. neoformans* in the CNS in real time. Major procedures in the method include preparing cryptococcal culture for microinjection, introducing pathogens into the bloodstream or brain ventricles of zebrafish larvae, procedures on immobilizing zebrafish for imaging, and tips on high content imaging of living infected larvae. In this chapter, we outline variations of the main method, each more suitable for studying a particular aspect of the pathophysiology of CM (see Note 21).

2 Materials

Solutions should be prepared using distilled water. Solutions should be stored according to instructions given below.

2.1 Preparing Striking Plate and Pathogen Culture

1. *Cryptococcus neoformans* var. *grubii* KN99 (see Note 1). Strains (select according to fluorescent reporters in chosen transgenic):
 - (a) KN99 GFP [11].
 - (b) KN99 mCherry [11].
2. Yeast peptone dextrose (YPD) broth: 20 g/L Bacteriological peptone, 20 g/L Glucose, 10 g/L Yeast extract. Suspend 50 g in 1 L of distilled water. Autoclave for 15 min at 121 °C.
3. 90 mM Petri Dishes for making YPD agar plates.

4. YPD agar plates: YPD broth solution with 2% Oxoid Agar 74 Bacteriological (Agar No. 1). Autoclave for 15 min at 121 °C before pouring (see Note 2). 75 76
5. Incubator set at 28 °C with a Blood tube rotator. 77
6. Inoculation loops. 78
7. 1% Virkon solution or other suitable sterilizing solution active against *Cryptococcus*. 79 80
8. 70% Industrial methylated spirit (IMS or denatured ethanol): used for disinfection of working space. 81 82
9. Simport tubes with clip on caps. 83
10. Laminar flow hood or other suitable safe lab site for handling fungal pathogens. 84 85
11. Filtered tips. 86
12. Phosphate buffered Saline (PBS): In tablet form. One tablet dissolved in 200 mL of deionized water to yield 0.01 M phosphate buffer, 0.0027 M potassium chloride and 0.137 M sodium chloride, pH 7.4, at 25 °C. 87 88 89 90
13. 6000 g Benchtop centrifuge. 91
14. 10% Polyvinylpyrrolidone (PVP), 0.5% Phenol Red in PBS (see Note 3): Autoclaved before use. 92 93
15. Hemocytometer. 94

2.2 Zebrafish Husbandry, Sorting, and Dechorinating

1. Lines: 95
 - (a) *Tg(kdrl:mCherry)^{sh916}* – *mCherry* marker of endothelial vascular cells [21]. 96 97
 - (b) *Tg(kdrl:mCherry)^{is5}; TgBAC(cldn5a:EGFP)^{vam2}* – GFP *claudin5a* tight junction protein marker expressed on the zebrafish choroid plexus ependymal cells; *mCherry* marker of endothelial vascular cells [12]. 98 99 100 101
 - (c) *Tg(mpeg:mCherry-CAAX)^{sh378}* – *mCherry* reporter of macrophages and macroglia. Origin – Johnston lab [8]. 102 103
2. Breeding trap for marbling or any standard zebrafish husbandry material for obtaining embryos [14]. 104 105
3. 90 mM Petri Dishes for transport and collection of embryos. 106
4. Plastic tea strainer for collecting embryos from adult fish tank. 107
5. Fire-polished wide-bore Pasteur pipet: Used to transfer larvae between containers. 108 109
6. E3 with methylene blue: 10× stock of E3 (NaCl 5 mM, KCl 170 μM, CaCl₂ 330 μM, MgSO₄ 330 μM). Dilute to 1× and add methylene blue (0.000025%). Store at 28 °C. 110 111 112
7. Dissecting stereomicroscope: For observing and manipulating embryos. 113 114

	8. 1% Virkon solution: Used to cull zebrafish embryos that will not be raised.	115 116
	9. Dumont #5 forceps: Used for removing the chorion around larvae.	117 118
2.3 Zebrafish Injection with C. neoformans, Plating Inoculum and Mounting		
	1. Injecting equipment set up (Fig. 1):	119
	(a) Pneumatic Pico Pump (PV 830P): for creating pump pressure for injecting.	120 121
	(b) Micromanipulator (Sutter Instrument, MM-33): for adjusting the needle position.	122 123
	(c) Dissecting stereomicroscope: For observing and manipulating embryos.	124 125
	2. Tricaine methanesulfonate (MS222): 0.168 mg/mL solution in E3.	126
	3. Gel loading pipette tips.	127
	4. Graticule slide 100 × 0.05 = 5 mM scale (Fig. 2b).	128
	5. Microneedle: Injection needles are needed for injecting pathogens into the bloodstream or brain ventricles of the larvae. Injection needles are prepared by pulling glass capillaries	129 130 131
	1.0 mM OD glass capillary (World Precision Instruments) using a pipette puller. Pipette pullers all have different heating elements; therefore, trial and error are needed to find the settings for your puller that produce needles as shown in Fig. 2a.	132 133 134 135
	6. E3 agarose injection plates: 2% Agarose (Molecular Biology Grade Agarose) solution in E3 with methylene blue.	136 137
	7. Cell spreader.	138
	8. Heat block/Digital dry bath at 38 °C: keeping LMPA from solidifying.	139
	9. Low melting point agarose (LMPA) mounting solution: Transparent mounting solution used to immobilize live zebrafish embryos during imaging. In a 15 mL falcon, add 9.6 mL of E3, 420 µL tricaine (4%), and 0.1 g LMPA powder (1%) to make 1% LMPA mounting solution (see Note 21).	140 141 142 143 144
	10. Corning® high content imaging plate; 96 well: High resolution imaging is not possible using plastic well plates due to the thickness of the material. Acquire glass bottom imaging plates specific for high resolution imaging.	145 146 147
	11. Glass mounting capillaries with a micro plunger (provided by Zeiss for Light sheet microscopy): volume 20 µL, internal diameter 0.8 mM, Pk 100, color code black.	148 149 150
	12. Imaging equipment.	151
	(a) <i>Nikon custom widefield</i> : A custom-build widefield microscope, Nikon Ti-E with a CFI Plan APOCHROMAT λ 10×, N.	152 153 154
		155
		156

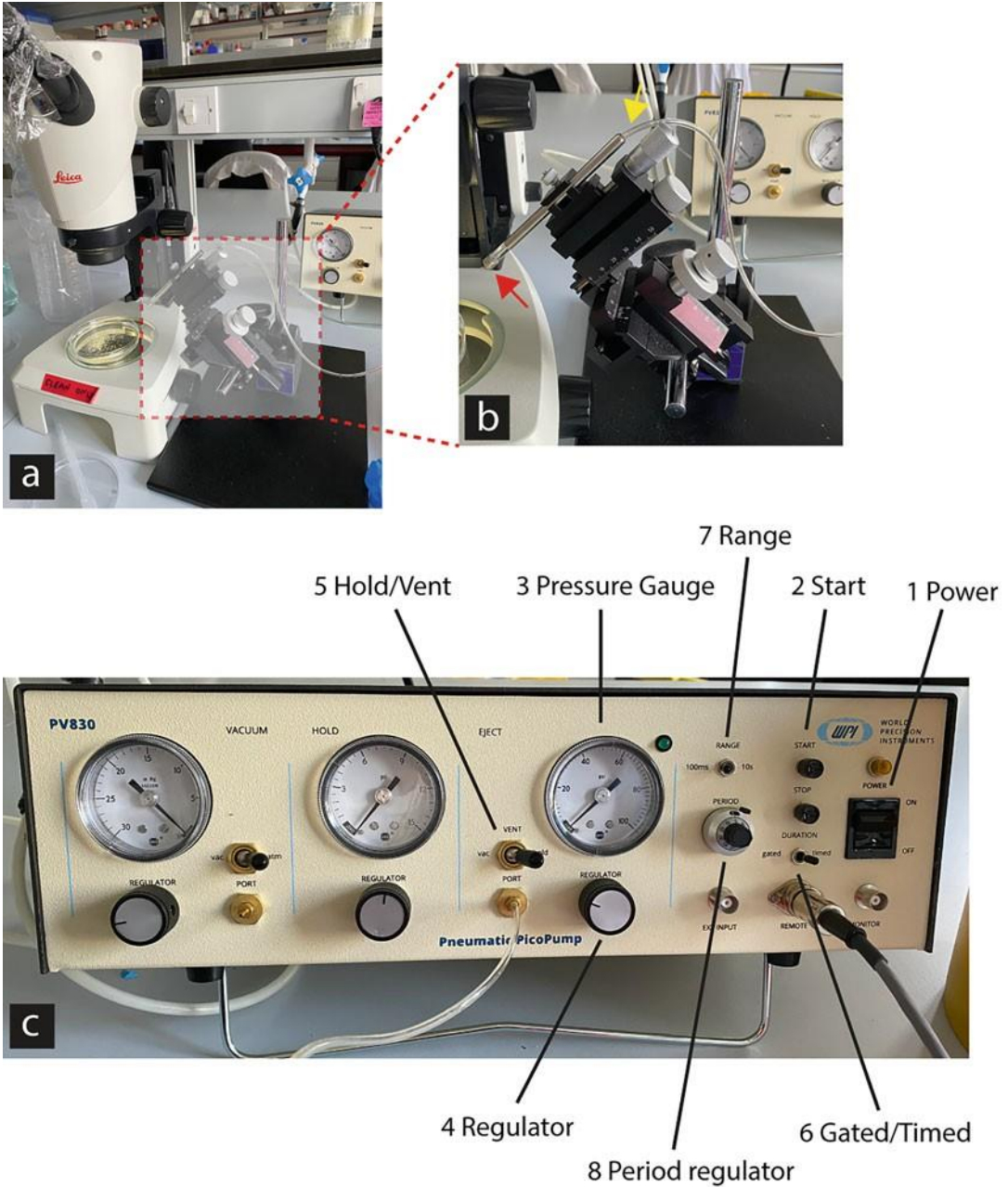


Fig. 1 Injecting equipment set up: panel (a) shows a dissecting stereomicroscope with a micromanipulator (b) next to it and a Pico Pump (c) behind. In panel (b) the red arrowhead points to a microneedle gets inserted, the yellow arrowhead points to the tube connecting the Pico Pump and the micromanipulator. The silver nodules on the micromanipulator control the position of the needle in 3D space. In panel (c) we can see the controls of a Pico Pump clearly. Labels are pointing to controls adjusted during the injection procedure in the method

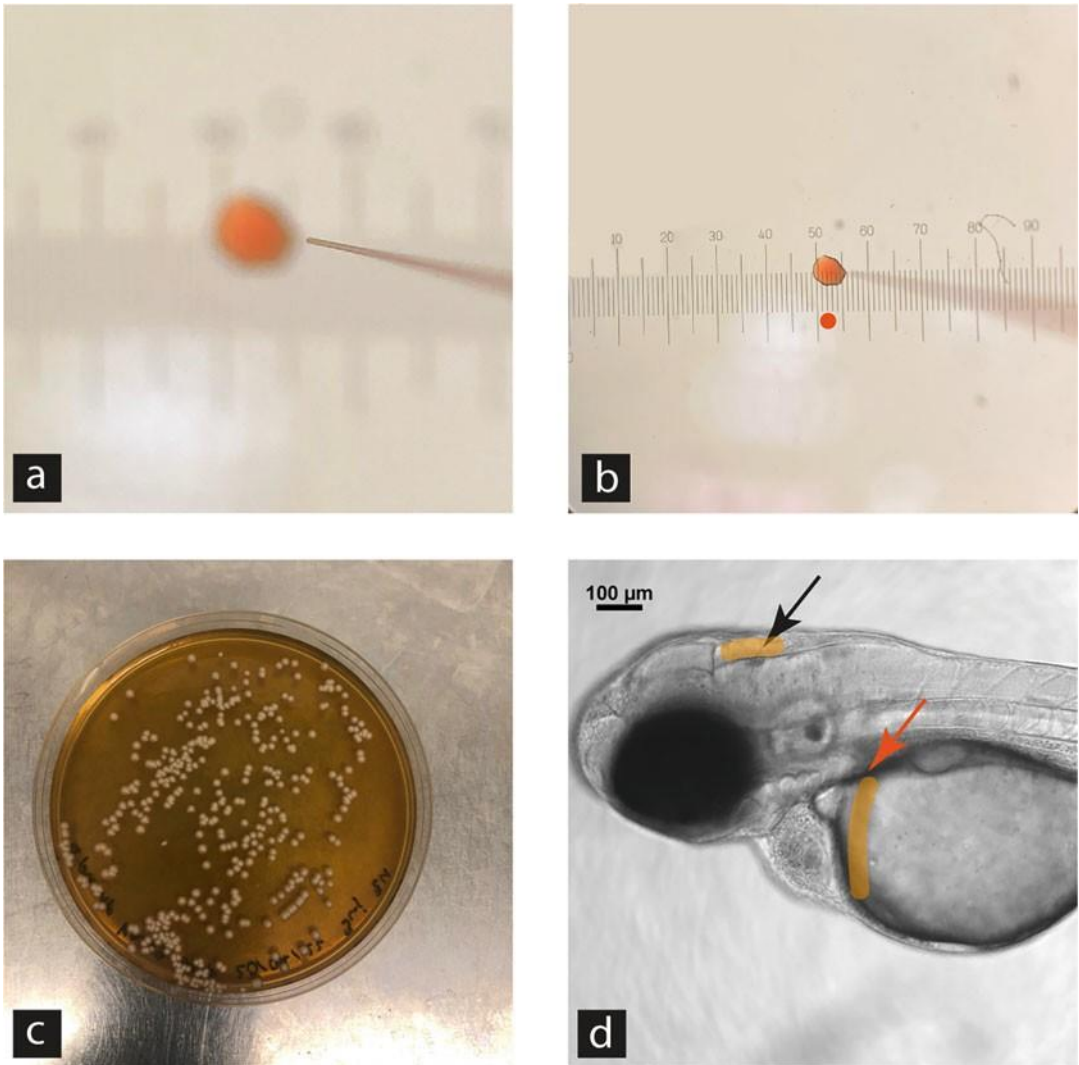


Fig. 2 Injecting and plating inoculum: Panel (a) shows an example of a needle for injection. The needle is above a droplet spread on a 5 mm graticule. The needle is broken and the size of the needle tip and shape are optimised for injecting 1 and 2 dpf larvae. Panel (b) shows the inoculum coming out of the needle from one pump, and the graticule in focus. An orange circle indicates what the inoculum looks like in droplet form as it floats in the mineral oil above the scale. The size of the droplet is approximately 0.12 mm in diameter (2 nL). Panel (c) shows a plated 2 nL of 700 cfu/nL inoculum that came out of an injection needle. The plate was incubated at 28 °C for 48 h. The colonies on this plate are ~400. In our method we inject 4 nL of 700 cfu/nL inoculum per larva to account for discrepancies between concentration estimation in a haemocytometer count and concentration in a micro needle droplet. Panel (d) shows sites of injecting on a 2 dpf larva. The orange arrow points to the duct of Cuvier, a site of injection for bloodstream infection. The black arrow points to the hindbrain ventricle, a site of injection for CSF infection. It is important to note that hindbrain ventricle injections are typically done in 30 hpf larvae. The orange areas on the fish are where the inoculum will travel immediately after injection into respective injection sites

- A.0.45 objective lens, a custom built 500 μ m Piezo Zstage (Mad City Labs, Madison, WI, USA) and using Intensilight fluorescent illumination with ET/sputtered series fluorescent filters 49,002 and 49,008 (Chroma, Bellow Falls, VT, USA). NIS software for acquisition.
- (b) *Zeiss Z1 Lightsheet Microscope*: Lightsheet.Z1. Laser lines: 405, 445, 488, 514, 561, 638 nm. Plan-Apochromat 20 \times /1.0 Corr nd = 1.38 objective and a scientific complementary metal-oxide semiconductor (sCMOS) detection unit. ZEN black software for acquisition.
13. Data analysis software: ImageJ, System software.

3 Methods

- 3.1 *Zebrafish Microinjections with C. neoformans*
- 3.1.1 *Making a Streaking Plate*
- 3.1.2 *Day 1: Zebrafish Husbandry and Marbling*
- 3.1.3 *Day 2: Obtaining Embryos and Sorting*
- Streak an YPD agar plate with the desired *C. neoformans* strain from suitable frozen stocks (e.g., Microbank beads) and incubate at 28 °C for 48 h. Check plate for good and uniform growth. If growth is poor or some areas show differences in color or morphology reisolate from frozen stocks, otherwise restreak onto a second YPD agar plate being careful to take a sweep across the plate. Incubate restreaked plate at 28 °C for 48 h and dispose of original plate. Restreaked plate should be sealed with parafilm and can be stored at 4 °C for up to 1 month. For experimental cultures, an inoculation loop sweep is taken from stock plate and used to inoculate 2 mL of YPD broth as 24 h cultures which are used to prepare zebrafish infection inoculum (see Subheading 3.1.4).
- Adult zebrafish should be kept in aquarium facilities that meet ethical and local legal requirements. They should be maintained on a 14- to 10-h light and dark cycle at 28 °C.
 - Zebrafish embryos can be generated by “marbling” (or other suitable breeding trap) or by pair mating. “Marble” a selected tank after 6 h prior to dark period to allow adult fish to adjust to their new environment prior to light cycle transitioning into dark.
 - Obtain embryos from breeding trap within 4 h following light cycle initiation. If pair mated zebrafish are divided prior to mating, then dividers should be removed as soon as possible after light cycle initiation and embryos collected within 4 h following light cycle initiation. To collect the embryos, pour the contents of the bottom container of the breeding trap through a tea strainer. Using a wash bottle filled with E3 medium, rinse the eggs from the tea strainer into a 90 mM petri dish.

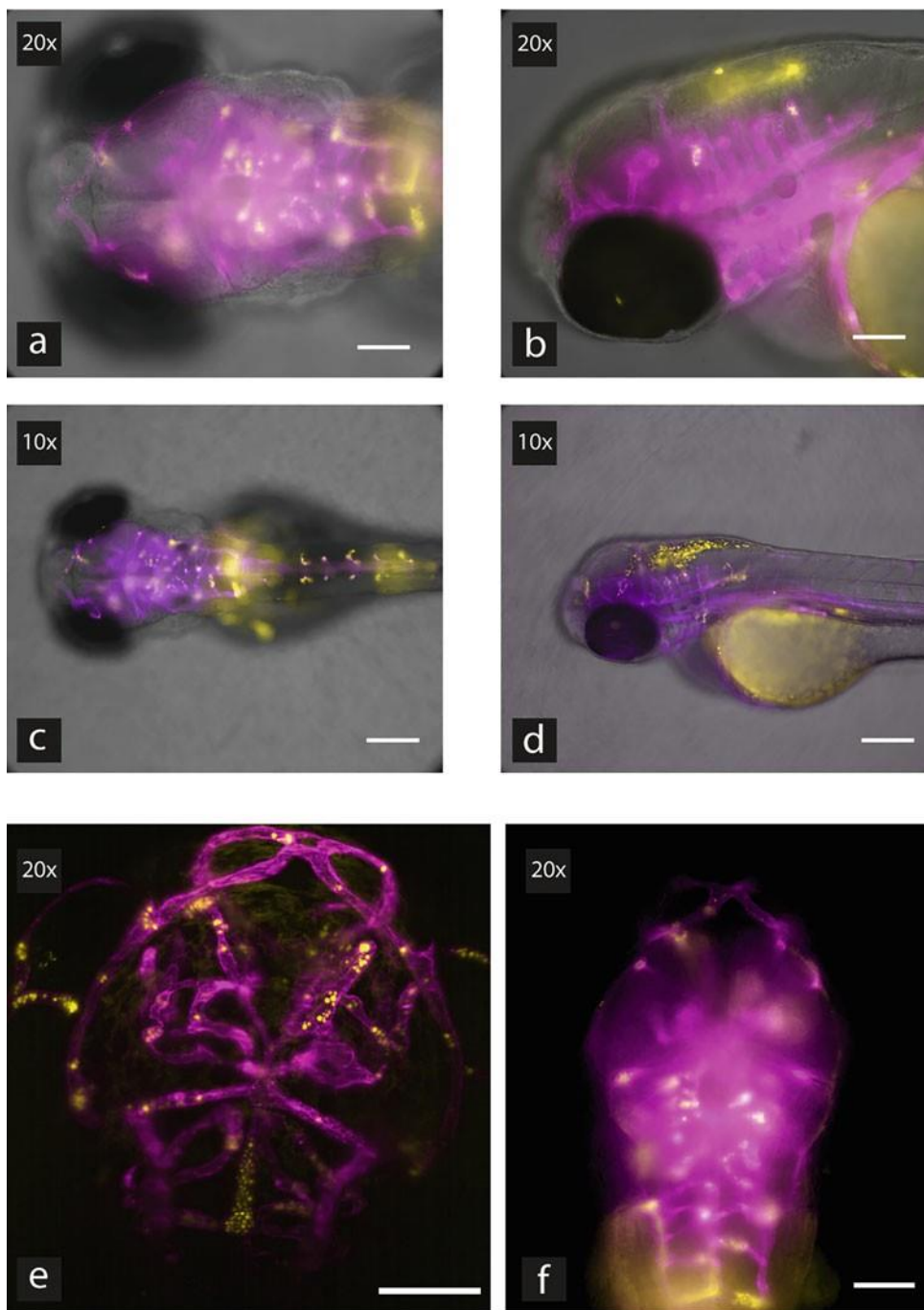
2. Under a stereo dissecting microscope, observe the petri dish with collected eggs. Developmentally stage zebrafish embryos. Depending on the time of sorting, the embryos selected should be around 4 h postfertilization (hpf), mostly in their high or oblong stage of development. Select healthy embryos that have been fertilized at 8 am the same day (see Note 4).
 3. Transfer selected embryos into a 90 mM petri dish approximately $\frac{3}{4}$ full with E3 methylene blue media (see Note 4). Maximum number of embryos per dish is 80 (see Note 4).
 4. Discard embryos that were not selected in 1% Virkon solution or other suitable disinfectant.
 5. Store embryos in a 28 °C incubator with a 14- to 10-h light and dark cycle.
 6. 8-10 h postfertilization, observe embryos under a light microscope. Discard all dead or damaged embryos in 1% Virkon solution (see Note 4).
- 3.1.4 Day 3:
Dechorinating and
Preparing Pathogen Culture
1. Dechorinating: At 30hpf (see Note 5) using two sets of Dumont #5 forceps (it is critical for the forceps to be sharp), remove the chorion around the larvae. This can be done by using both forceps, one to hold the embryo in one place and the other to pinch and pull. Dechorinating can also be done using one forceps by poking a small hole in the chorion as the forceps ends are touching and then releasing the forceps to open the chorion. It is essential to keep the larvae in the same plate in which they were dechorinated (see Note 5).
 2. Preparing zebrafish infection inoculum: From a *C. neoformans* KN99 GFP streaking plate, take a sweep using an inoculation loop and use it to inoculate 2 mL YPD broth. Rotate horizontally at 20 rpm at 28 °C for 16-24 h.
 3. At the end of the working day, check plates with larvae to again remove dead or damaged specimens.
- 3.1.5 Day 4: Preparing
Injection Inoculum
1. Put E3 agarose plate and 3 YPD agar plates stored at 4-28 °C incubator to warm up (see Note 6).
 2. *Cryptococcus neoformans* inoculum preparation.
 3. Wash cryptococcus culture with PBS: collect KN99 GFP overnight culture; add 1 mL of culture to a 1.5 mL microcentrifuge tube; pellet 1 mL culture at 6000 g, RT for 1 min; remove supernatant and resuspend pellet in 1 mL of PBS.
 4. Second PBS wash: Pellet 1 mL resuspended pellet (Step 3) at 6000 g, RT for 1 min; remove supernatant and resuspend pellet in 1 mL of PBS; use this as washed culture suspension.
 5. Make a 20× dilution of washed culture suspension: take 5 µL from 1 mL washed culture suspension and dilute with 95 µL of

	fresh PBS. Add 10 μ L of diluted culture to a hemocytometer slide under a coverslip.	245 246
	6. Count 20 \times dilution: Count colony forming units (cfu) (<i>see</i> Note 7) using an upright light microscope. Calculate the number of cfu in the diluted and therefore 1 mL washed culture suspension according to the hemocytometer manufacturer's instructions.	247 248 249 250
	7. Resuspend washed culture suspension in 10% PVP phenol red PBS: Pellet 1 mL culture at 6000 g, RT for 1 min; Remove supernatant; Resuspend culture in 10% PVP in phenol red PBS to achieve a desired cfu/nL. For our experiments we use 1000 cfu/nL or 700 cfu/nL (<i>see</i> Note 7).	251 252 253 254 255
	8. Clean all areas that have come into contact with pathogens with 70% IMS or other suitable disinfectant. Suspend all contaminated consumables into 1% Virkon solution or other suitable disinfectant.	256 257 258 259
	1. Setting up Pneumatic Pico Pump (Fig. 1c).	260
	(a) Open air supply to Pneumatic Pico pump.	261
	(b) Switch on pump (1 Power).	262
	(c) Check for air (2 Start).	263
	(d) Check pressure (3 Pressure gauge)—should be approx. 40 psi for injecting 1000 cfu—alter using the regulator (4).	264 265
	(e) Select “Vent” (5 Hold/Vent).	266
	(f) Select “Timed” (6 Gated/Timed).	267
	(g) Select 100 ms (7 Range).	268
	2. Anesthetize a plate of zebrafish larvae (~50hpf) in a 0.168 mg/mL Tricaine in E3. Larvae are ready to be manipulated once no evidence of motility (e.g., no startle reflex) is observed.	269 270 271
	3. Add 5–8 μ L of <i>C. neoformans</i> inoculum into a microneedle using a gel loading tip (<i>see</i> Note 8).	272 273
	4. Unscrew the end of the micromanipulator needle holder, attach the needle, and tighten.	274 275
	5. Under dissecting stereo microscope, place a graticule slide onto an upturned petri dish, add a drop of mineral oil, and focus on the scale bar.	276 277
	6. Bring the needle tip into view and break the tip at an angle using Dumont #5 forceps resulting in a beveled point (<i>see</i> Note 9) (Fig. 2a).	278 279
	7. Using the micromanipulator move the tip of the needle so that it enters the oil on the slide and depress the foot peddle once (you will need to withdraw the needle quickly to prevent reuptake of droplet unless microinjector has balanced pressure capability).	280 281 282 283
		284 285 286 287 288
3.1.6 Day 4: Setting Up Needle and Anesthetizing Fish		

	8. Measure the size of the droplet produced—3 small divisions on the illustrated graticule for 2 nL inoculation volume with each foot pedal depression (Fig. 2b; see Note 9).	289 290 291 292
3.1.7 Day 4: Injecting Zebrafish Larvae	(Duct of Cuvier, bloodstream infection, see Notes on method variation; Fig. 2d)	293 294
	1. Prepare a fresh plate (collection plate) with clear E3 (no methylene blue) for containing injected fish (see Note 3).	295 296
	2. Take a prewarmed E3 agarose plate (injection plate) from the incubator.	297
	3. Dip a gloved finger into the E3 medium containing anesthetized fish to be injected and wet the surface of the E3 agarose.	298 299
	4. Take a Pasteur pipette. With a circular motion, swirl the E3 and tricaine media in the Petri dish filled with anesthetized larvae; this allows larvae to collect in the middle of the plate.	300 301 302
	5. Pipette 15 larvae with using Pasteur pipette.	303
	6. Pipette the larvae onto tilted injection plate letting them slide from the top down, this way the tails will orient in one direction.	304 305
	7. Remove excess E3 until larvae are not floating but sit submerged on injection plate.	306 307
	8. Place the infection plate under dissecting stereo microscope and bring the left most larva into focus.	308 309
	9. With the naked eye, adjust the micromanipulator apparatus so the needle is above the fish in focus.	310 311
	10. Under the microscope, focus on the needle and adjust the micromanipulator to hover the needle above the duct of Cuvier (Fig. 2d).	312 313 314
	11. With one swift motion, inject the needle into the duct of Cuvier, depress the foot pedal twice (2 pumps), and pull out the needle. If the injection is successful, you will see a red liquid going over the yolk and into the heart (Fig. 2d, see Note 10).	315 316 317 318
	12. Repeat for all fish on the plate.	319
	13. Take 3 mL of clear E3 from collection plate.	320
	14. Tilt the injection plate and pipette clear E3 from top to bottom over the collection plate. The injected larvae will collect in the bottom corner of the injection plate and spill into the collection plate. Keep pipetting clear E3 until all larvae are in the collection plate.	321 322 323 324
	15. Repeat the injection and collection process until you reach the desired number of infected larvae, leaving a desired number of fish for control groups (see Note 11).	325 326 327 328 329 330

	16. Once a desired number of larvae are injected, a collection container with infected fish needs to be returned into the incubator for 2 h for the fish to recover. Separate containers with control fish in clear E3 should also be left in the incubator for 2 h.	331 332 333 334 335
3.1.8 Day 4: Plating Inoculum	Plating the injection inoculum is a secondary method of estimating how many cfu are being injected into the zebrafish larvae (see Note 12). Once the desired number of larvae is injected, plate some of the inoculum using the same injection needle and inoculum used to inject larvae.	336 337 338 339 340
	1. Prepare a cell spreader next to the injector scope.	341
	2. Collect a warmed YPD agar plate from the incubator.	342
	3. Fill a pipette with 20 μ L of PBS.	343
	4. With one hand hold the pipette under the injector scope, with the other, adjust the micromanipulator to get the needle in front of the opening of the pipette tip. Pipette lightly so a droplet holds on the tip of the pipette tip. Lower the needle into the droplet and inject 1 pump (2 nL) into the droplet. Suck the droplet back into the pipette tip so it mixes in. Pipette the 20 μ L in the center of the YPD agar plate. Spread the liquid evenly around the plate and place the lid on.	344 345 346 347 348 349 350
	5. Repeat with another plate.	351
	6. Perform 2 repeats with 2 pumps (4 nL) of inoculum.	352
	7. Incubate inoculated YPD agar plates at 28 $^{\circ}$ C.	353
	8. Check if colonies are visible after 24 h, 48 h, and 72 h.	354
	9. Once visible (Fig. 2c), count the number of colony forming units on each plate. Take the mean number between replicate plates and adjust depending on injection volume.	355 356 357
	10. Clearing up working area: Dispose of all contaminated materials into suitable waste streams and clean equipment with disinfectant such as 1% Virkon.	358 359
	1. Preheat block to 38 $^{\circ}$ C.	360 361
	2. Low melting point agarose (LMPA) mounting solution prep.	362
	(a) Prepare low melting point agarose mounting solution at desired percentage (see Note 21).	363 364
3.2 Mounting for Widefield Fluorescence Microscopy	(b) Heat with low temperature until solution reaches boiling point. Repeat several times until the powder is dissolved and the solution is clear and homogeneous. Aliquot 500 μ L of clear solution per microcentrifuge tube and keep it in a 38 $^{\circ}$ C heat block prevents setting before use. You will need approx. 100 μ L/larvae to mount. Prepare the desired amount of LMPA accordingly.	365 366 367 368 369 370 371 372 373 374

	3. Collect plates with recovered injected and control larvae. Anesthetize plates. Distribute larvae in a high content imaging 96-well plate, with one larva per well and enough clear tricaine E3 to just cover larva. Keep the 2 groups of fish (control and injected) in separate rows and handle each group with its own pipettes to avoid cross contamination. Always keep the rows around the edges of the plate empty, short working distance (e.g., most high magnification) lenses do not allow focusing on the edges of the plate.	375 376 377 378 379 380 381 382 383
	4. Pipette 100 μ L LMPA per well for 5 larvae. Return LMPA to heat block to prevent it solidifying.	384 385
	5. Use a gel loading tip to position larvae in LMPA to the bottom of their wells.	386 387
	6. Use the tip to manipulate the orientation of the larvae (lateral side or dorsal side downward) (see Note 21). Do this until the LMPA solidifies.	388 389 390
	7. Repeat steps 4, 5, and 6 until all larvae are mounted.	391
	8. If doing time lapse imaging allow for the anesthesia of the larvae to subside after mounting for at least 20 min to stabilize heart rate.	392 393 394
3.3 Screening and Mounting for Light Sheet Microscopy (see Note 13)		
3.3.1 Screening	1. Collect plates with recovered injected and control larvae. Anesthetize plates. Distribute larvae in a high content imaging 96 well plate, with one larva per well and enough clear tricaine E3 to just cover larvae. Keep the 2 groups of fish (control and injected) in separate rows and handle each group with its own pipettes to avoid cross contamination. Always keep the rows around the edges of the plate empty, short working distance (e.g., most high magnification) lenses do not allow focusing on the edges of the plate.	395 396 397 398 399 400 401 402 403
	2. Using a gel loading tip carefully manipulate fish to go to the bottom of their wells and on their side (lateral view) (see Note 14).	404 405 406
	3. Carefully transport plate to widefield fluorescence microscope.	407
	4. Place the 96-well plate in a widefield microscope sample holder.	408
	5. Locate and image each larva with appropriate settings to identify desired reporter fluorescence and dissemination into the CNS (examples of infection burden in CNS Fig. 3).	409 410 411
	6. Add 50-100 μ L E3 to wells to prevent them from drying out before mounting.	412 413 414
3.3.2 Mounting	1. Preheat block to 38 °C.	415
	2. Put 500 μ L aliquots of 2% LMPA in heat block.	416
	3. In one of the marked wells of the 96-well plate, add 1 μ L of tricaine and mix E3.	417 418



— KDRL - blood vessels
— GFP - cryptococci

Fig. 3 Different mounting orientation and microscopy: All larvae shown on this figure are 2dpf in development and imaged in real time. Panel (a) and (c) show dorsal mounting in 20 \times (a) and 10 \times (c) magnification. Similarly, panel (b) and (d) show lateral mounting in different magnifications. The images in (a–d) are taken with a fluorescent widefield microscope. Panel (e) and (f) show the difference in the spatial resolution between blood vessels that light sheet imaging can provide (e) as opposed to widefield fluorescence imaging (f). Scales on 20 \times images are 100 μ m and on 10 \times images are 200 μ m

4. Pick an embryo from the marked well along with the tricaine E3 in a Pasteur pipette.	419 420
5. Pipette onto suitable flat surface, for example, lid of a Petri dish squeeze so the medium remains as a droplet around the larva.	421 422
6. Collect media around the larva until it is just covered. Pipette 200 μ L 2% LMPA on top of the fish.	423 424
7. Using glass capillary tube pipette larva headfirst.	425
8. Slowly rotate the capillary tube so the fish mounts straight in the tube.	426
9. Place the capillary in the light sheet imaging chamber for imaging.	427
10. If doing time lapse imaging allow for the anesthesia of the larvae to subside after mounting for at least 20 minutes to stabilize heart rate.	428 429
1. General set up (the same in all imaging): Humidified temperature controlled at 28 $^{\circ}$ C.	430 431 432
2. Real-time imaging (focus on acute change in blood vessels size and shape; <i>see</i> Note 15 and 16): Suggested 20 \times and 40 \times objective lens with 0.7–1.1NA. Wavelength for 555 nM for mCherry (KDRL reporter line; <i>See Materials</i>). Exposure between 20 and 300 ms for mCherry reporter. Capture 1fps for mCherry channel.	433 434 435 436 437
3. High speed imaging (<i>see</i> Note 15 and 17): Suggested Lenses 20 \times and 40 \times objective lens with 0.7–1.1NA. Wavelength for 555 nM for dsRed (<i>gata1</i> reporter line; <i>See Materials</i>), 470 nM for GFP (reporter in KN99 GFP strain or silicon beads; <i>see Materials</i>). Exposure max 20 ms. Achieve using increased gain and/or illumination. Capture at least 30fps for chosen reporter (<i>see</i> Note 17).	438 439 440 441 442 443
4. 24 h time lapse imaging (focus on dissemination progression; <i>see</i> Note 18): Consider using lower magnification lens, if possible, to reduce problems related to photo toxicity Wavelength for 555 nm for mCherry (KDRL reporter line; <i>see Materials</i>), 470 nM for GFP (reporter in KN99 GFP strain; <i>see Materials</i>). Reduce exposure where possible but longer exposure is preferred to increased illumination. Capture 1 frame every 5 min.	444 445 446 447 448 449 450
5. One time point Z stack imaging (focus on pathogen distribution; <i>see</i> Note 19): The acquisition time for a whole group of fish should be as short as possible, set up a list of coordinates from each larva in a group and allow for automated acquisition (<i>see</i> Note 19). Consider using lower magnification lens, if possible, to reduce problems related to photo toxicity Wavelength for 555 nM for mCherry (KDRL reporter line; <i>see Materials</i>), 470 nM for GFP (reporter in KN99 GFP strain;	451 452 453 454 455 456 457 458 459 460 461 462 463

3.4 Imaging

3.4.1 Widefield Set-Up Variations

	see Materials). Laser power and exposure can be varied	464
	depending on what produces the best quality images, but the	465
	settings need to be the same for each channel across all larvae	466
	images for measurements. Suggested Z stack interval 3 μM (the	467
	size of smaller cryptococcal cells).	468
		469
3.4.2 Light Sheet Set-Up	1. General set-up and 1 time point Z stack imaging: Image acqui-	470
Variations (see Note 20)	sition chamber incubation at 28 $^{\circ}\text{C}$. Lasers should be set up for	471
	dual side illumination with online fusion, turn on lasers	472
	488 nM (for GFP) and 561 nM (for mCherry). LBF	473
	405/488/561 filter set, and beams split with SBS LP 560 or	474
	LP 580 mirror. Two tracks and sequential imaging to be used	475
	for imaging of two reporters (e.g., one track for GFP and	476
	another for mCherry). Lens to be at 0.7 \times zoom, 16-bit	477
	image depth, 1920 \times 1920px (approximately	478
	0.33 \times 0.33 μM) image size and minimum z-stack interval	479
	(approximately 0.5 μM). Exposure automatically adjusted.	480
	2. Real-time lapse imaging: adjust illumination to be one side	481
	illumination and keep to a single track to reduce acquisition	482
	time. Manipulate the exposure to allow for 1fps capture time.	483
		484
3.5 Processing Data	We suggest using automated Otsu thresholding in ImageJ.	485
	1. Real-time data: Select frames of interest to represent events	486
	observed and analyze and extract from a time lapse file using	487
	ImageJ.	488
	2. Slow motion imaging: For particle tracking software use the	489
	free Track Mate plugin in ImageJ.	490
	3. 24 h time lapse imaging: Can be challenging with ImageJ due	491
	to Java memory usage implementation. In this case, software	492
	from acquisition system might be preferable.	493
	4. Light sheet Z stack processing: Utilize ImageJ plugins for	494
	tubular, volume and branching analysis of vascular bed	495
	architecture.	496

4 Notes

497

1. We chose *C. neoformans* var. *grubii* KN99 strain as it is known to exhibit 498
represent human type virulence in animal models [15]. 499
General handling of pathogen: 500
- (a) Long-term storage cultures for use in experimental pro- cedures are 501
kept in Microbank (Pro-lab Diagnostics, UK) stock vials at -80°C . 502
See *Methods* for information on handling the pathogen. 503

504

505

(b) <i>Cryptococcus neoformans</i> var. <i>grubii</i> is a Hazard 2 class pathogen and it should be handled in a Containment Level 2 infection facility.	506 507 508
(c) Consumables and containers that have come into contact with the pathogen should be disposed of in sealed containers or inactivated with 1% Virkon solution for 30 minutes or other suitable disinfectant. Inactivated or sealed waste should be disposed of in an appropriate waste stream.	509 510 511 512 513
(d) All pathogens that need to be transported between rooms (e.g., from tissue culture to microscopy rooms) should be in a sealed container such as a securely closed microcentrifuge tube or well-plate. Distance of travel between rooms should be reduced as much as possible.	514 515 516 517 518
(e) Zebrafish larvae and fungi are both grown at 28 °C. This is the temperature of the natural environment of zebrafish; the fungi are grown in the same temperature to condition the pathogen to favor the host's environment.	519 520 521 522
2. To prevent bacterial contaminants from growing on YPD agar plates, plates should be poured in sterile conditions (in a laminar flow hood or under a Bunsen burner flame). An additional precaution can be taken by adding antibiotics (e.g., penicillin and gentamicin) to YPD agar before pouring.	523 524 525 526
3. Cryptococcal cultures are to be re-suspended in PVP in phenol red, where PVP is a polymer which prevents needle blockage in cryptococcal injection and Phenol Red is an inert dye that allows us to see if the inoculum has been successfully injected.	527 528 529 530
4. Sorting and husbandry tips:	531
(a) Discard unfertilized eggs.	532
(b) The health of zebrafish embryos can be determined by the lack of dark spots in their tissue. Darker tissue usually indicates dying cells.	533 534
(c) All zebrafish embryos used in experiments should be in the same stage of development to avoid any variability in physiology that can create data outliers and skew results.	535 536 537
(d) Methylene blue is an antimicrobial agent that prevents unwanted growth of pathogens in the growth environment. However, it has been seen that overuse of E3 methylene blue can cause autofluorescence in imaging and can activate autophagy in host and pathogen cells. When preparing methylene blue E3, the solution should be pale blue in color (approx. 0.000025% methylene blue). After infecting larvae with <i>C. neoformans</i> , keep them in E3 without methylene blue.	538 539 540 541 542 543 544 545 546 547 548 549

(e) Increased numbers of embryos (over 80) in a single petri dish can create an environment with low nutrient and oxygen availability, which would lead to developmental and health issues that are not due to the infection procedure [14].	550 551 552 553
(f) The presence of dead embryos in the environment of growth is bad husbandry practice [14] and factors released from the decay of tissue can be damaging to living embryos.	554 555 556
5. Zebrafish larvae under 24 hpf are fragile and easily damaged. In our work, we have found that dechorinating around 30 hpf produces the best results (less to no damage). We have also seen that 1dpf larvae can adhere to plastic consumables. Adherence also seems to occur more frequently when larvae are transferred to a fresh plate. To avoid damage from sticking to a Pasteur pipette or a new Petri dish, larvae are left in the same Petri dish they have been dechorinated in for at least 2–5 h recovery period prior to injecting. If the method is varied for injections to be done in 1 dpf larvae, dechorination can be done earlier in the day to allow for the larvae to recover in time prior to injecting.	557 558 559 560 561 562 563 564 565 566
6. E3 agarose injection plates are warmed up to the body temperature of zebrafish larvae, to allow less stress and damage to occur during the injection procedures.	567 568 569
7. The cfu/nl suggested in the methods (1000 or 700) works best in bloodstream larvae infection; it is the amount of cfu required to see dissemination into the cranial vasculature at the desired imaging time points. For infection of brain ventricles, we suggest 200 cfu/nL. That prevents excessive growth and allows for better resolution between cryptococci during imaging. Brain ventricles injections are also done at 1dpf developmental stage of larvae. If that is a more desired procedure, vary the method accordingly.	570 571 572 573 574 575 576
8. Extreme care should be taken when handling injection needles containing pathogens. Needles should be loaded, used, and disposed of in the same location, under no circumstances should they be transported. To protect from needle stick injury, a fingerguard can be worn on the hand that is handling the needle. Should injury still occur encourage bleeding, thoroughly wash the area with water and seek medical attention.	577 578 579 580 581 582
9. When breaking the injection needle, the aim is to get the tip as small as possible so it allows for less damage to occur when injecting the larvae. The needle tip needs to be also big enough to let inoculum escape when 40 psi pump pressure is applied. However, cryptococci are very prone to clumping, especially when injecting 700–1000 cfu/nL. This means the needle tip	583 584 585 586 587 588 589 590 591 592 593 594 595

needs to be broken with a relatively bigger opening and that the pump period regulator (Fig. 1c, see Note 8) needs to be on the higher end values ~2.5-3. The period regulator on the Pico Pump alters the length of period in which air is pushed into the needle—it should be somewhere between 1 and 3.

10. To avoid any differences in infection burden across larvae, aim to inject all larvae with the same needle. Unfortunately, that is sometimes not possible as injection needles (especially with high cfu content) tend to clog at their tip. Once the needle is clogged, it needs to be discarded, a new needle and volume of inoculum is used, which may cause variation in needle tip size and cfu injected. Tips on avoiding needle clogging or unclogging the needle:
 - (a) Prior to pipetting inoculum, each time vortex 3 times for 10 s. This is done to prevent clumps of the pathogen forming and clogging the injection needle. This also favors a more even distribution of cfu across the volume of the inoculum.
 - (b) If the needle clogs, you can try injecting several times into the E3 agar.
 - (c) Try breaking the needle slightly larger, but not too big to avoid bleeding following injection.
 - (d) Try diluting inoculum further, reducing the droplet size and pumping more than 2 times when injecting. Count what comes out of the needle and estimate how many pumps are necessary for 700–1000 cfu. Make sure you maintain the same pump number across all injections and plate the inoculum afterwards to get a quantification of how many cfu have been injected.
11. Two different control groups can be used. One group of fish that have been treated the same way as injected cohort (dechlorinated, anesthetized the same number of times). This group allows to account for differences in physiology due to tricaine treatment or dechlorinating. Another group can be an injection procedure control; this cohort can be injected with 2 nL of just 10% PVP phenol red, to account for any physiological changes that might occur due to the injection procedure.
12. When preparing the *C. neoformans* inoculum, the cfu concentration is determined by a hemocytometer count. That cfu estimate, however, does not account for several factors during the injecting procedure. Cryptococci are not completely homogeneously distributed in the inoculum, when transporting it via pipetting a different amount of cfu would be picked up each time, despite it being in the same volume of inoculum. The cryptococci in the inoculum would also replicate during

the time of the injection procedure. Also, the inoculum dis- 642
tributes unevenly into the injection needle, which would yield 643
different concentrations at the tip of the needle as opposed to 644
the top (due to the 80° angle of the needle when injecting). 645
The closest and most accurate estimation of infection burden at 646
the time of injection is by counting what comes out of the 647
injection needle. The method of plating the inoculum that 648
comes out of the needle seems the most representative of the 649
infection burden we see during imaging. The hemocytometer 650
count is still done to get a rough estimate of how much 651
dilution the culture needs before injecting. 652

13. Many light sheet microscopes only allow imaging of one sam- 653
ple at a time. Mounting and processing each specimen takes up to 1 h. Therefore, it is 654
important that samples are carefully screened on another microscope 655
prior to imaging with the light sheet microscope. 656
14. When screening fish to image in the light sheet, they cannot be mounted. 657
Taking as much media out of the 96 wells as possible will keep the fish from 658
floating away from the bottom of the wells. If adjustments are made, the larvae 659
can also keep lying on their side without much disruption of their orientation to 660
ease the process of screening. It is easier to examine overall infection burden 661
and health of each larva if they are in a lateral orienta- 662
tion, instead of dorsal or ventral for example. 663
15. An important advantage of this method is that it provides options for 664
observation of host pathogen interactions in differ- 665
ent time scales: slow- 666
motion, real-time, 24 h time frame, and one time-point. 667
16. Real-time imaging is attempting to take a time lapse where the whole process 668
of acquisition takes place within maximum 1 s (illuminating sample, opening 669
and closing camera shutter, col- 670
lecting information from camera matrix). 671
Time lapses cannot be of two reporters because acquisition time cannot be 672
within 1 s, that is, imaging GFP reporter and mCherry at the same time is 673
not possible in real-time imaging. Real-time imaging is usually done for a 674
short time range (2-10 min) to decrease file size and make data processing 675
less cumbersome. In our work, we use real-time imaging to observe acute 676
changes in vascular size and shape in infection. We have found important 677
patterns which are imperceivable in longer intervals of acquisition 678
(imaging that is not representative of real time changes). 679
17. High speed imaging is reducing acquisition time even further than real time 680
imaging. We can reduce acquisition time further from 1fps to 30fps. The 681
biggest factor changed in this type of imaging is reducing the field of 682
view significantly and so shortening the time necessary for information 683
transfer between camera and computer. 684

685
686
687
688

18. Longer time-lapses do not necessarily require short exposure and data collection times. Adjusting the acquisition settings is done in favor of clearer, higher quality images. Intervals of capturing should be a minimum of 5 min (or longer) to prevent data loss in large files and make data processing less cumbersome. In our work, we use 24 h time lapses for exploratory purposes or to show dissemination progression over time.
19. Single time point Z stacks are used to show in detail cryptococcal yeast distribution across tissues at a particular point in the infection progression. Can be used to show infection burden and distribution, for example, with or without treatment with pharmaceuticals of interest. When collecting information for several groups, it is important that the time of imaging between groups (or single fish) is as short as possible. This is because between 2 infected groups a larger time interval will allow for the infection to progress and 1 group might be more infected than the other because of procedural issues not actual differences. Also, a larger time interval between imaging an infected and control groups, for example, can show differences due to imaging in different developmental stages.
20. Light sheet imaging can be used to get higher resolution real-time or single point imaging. You should choose light sheet microscopy if, for example,
- (a) In real time: you want to observe changes in interconnected vascular structures in a smaller illumination plane.
 - (b) In a single time, point: you want to observe the spatial distribution of infection in 3D or the morphology of the vascular bed in infection.
21. *Notes on method variation.*
- For observing dissemination in the parenchyma, blood vessel morphology and damage*
- (a) *Developmental stage of zebrafish: 2dpf.* Dissemination route in human patients with cryptococcal meningitis is from lung infection to blood circulation to CNS. To mimic the pathology as seen in humans, replicate the infection route from blood vessels to brain tissue/parenchyma.
 - (b) 2dpf as opposed to 1dps is a good point for introducing a systemic infection into the larvae. The lumen formation and onset of circulation in zebrafish larvae start around 24hpf [16]. Heartbeat is essential for intra-cerebral vessels development at 32hpf [17]. At 48hpf, the primary vasculogenesis is complete and CNS vessel networks well established [18, 19]. The 2dpf infection point allows for a long enough period of infection development before 5 days postfertilization, after which it becomes much more unethical to use the animal model for infection work.

(c)	<i>Choice of infection route: Duct of Cuvier.</i> This is a common infection route when attempting to achieve a bloodstream infection. We prefer this injection site to the Caudal vein as it is larger, has a higher velocity of flow, and appears to allow for better distribution of pathogens across the whole larva. This is important especially when attempting to achieve CNS dissemination.	736 737 738 739 740 741
(d)	<i>Choice of cfu content in inoculum: 700–1000 cfu;</i> it is enough to disseminate into the CNS, smaller infection burden rarely produces CNS dissemination within 24 h of infection, and severe infection profile after 2 days.	742 743 744 745
(e)	<i>Choice of time point of imaging:</i>	746
	1. For a severe infection profile: 2 days postinfection.	747
	2. For tracking infection progression: between 4 h and 24 h postinfection.	748 749
(f)	<i>Choice of LMPA concentration:</i> The percentage of LMPA can be varied depending on the imaging technique used or the time that the larvae are to be kept immobilized. The higher the percentage, the quicker the solution will solidify and the less stretch it will provide for an organism to grow within it. In the imaging acquisition, a single larva lasts more than 1 h, choose a low percentage (0.3–0.5%). For light-sheet imaging, fast solidifying is the most important to get the orientation of the larvae right, choose high percentage (1–2%).	750 751 752 753 754 755 756 757
(g)	<i>Choice of mounting orientation and imaging:</i> Dependent on what is imaged.	758 759
	<i>For dissemination</i> into the parenchyma and ventricles, it is good to visualize with a widefield fluorescent microscope in a lateral view (Fig. 3b, d). The widefield allows for image collection from a larger cohort in comparison to the light sheet.	760 761 762 763 764
	<i>For blood vessel</i> morphology and dynamics have data both in dorsal and lateral orientation of the larvae. Light sheet microscopy and dorsal orientation will provide a better resolution when attempting to represent the vascular bed in 3D at a single time point (Fig. 3e, f).	765 766 767 768 769
	<i>For 24 h time lapse imaging,</i> use the widefield microscope to avoid large data files. Real-time time lapses can be done in the Light Sheet as well and widefield fluorescence like systems.	770 771 772 773 774 775 776
	<i>For observing flow of infected CSF in vivo</i>	777
(a)	<i>Developmental stage of zebrafish: 1dpf.</i> Injections into the CNS after 40 hpf becomes harder to achieve and is more likely to cause damage. The tissue around the brain ventricles is more	778 779 780

difficult penetrate as bone cell progenitors are already localizing and adopting fate, although ossification occurs later [20].

(b) *Choice of infection route: Hindbrain ventricle.* Allows to immediately monitor CNS infection. Dissemination from blood-stream infection is a relatively rare event.

(c) *Choice of cfu content in inoculum: 100 cfu.*

(d) *Choice of time point of imaging: 2 h after injection.*

(e) *Choice of LMPA concentration: 0.3–0.5%.*

(f) *Choice of mounting orientation and imaging: lateral orientation and widefield imaging.* There are several types of flow within the ventricular system; it is easier to see them in a lateral orientation of the larvae. In this case, it is more efficient to select a 2D imaging model and observe a simplified version of the system overall. Widefield microscopy is a good tool to do exactly that.

797 References

- 799 1. Rajasingham R, Smith RM, Park BJ et al (2017) Global burden of disease of
800 HIV-associated cryptococcal meningitis: an
801 updated analysis. *Lancet Infect Dis* 17:873–
802 881
- 804 2. Lee SC, Dickson DW, Casadevall A et al (1996)
805 Pathology of cryptococcal meningoencephali-
806 tis: analysis of 27 patients with pathogenetic
807 implications. *Hum Pathol* 27:839–847
- 808 3. Jarvis JN, Bicanic T, Loyse A et al (2014)
809 Determinants of mortality in a combined
810 cohort of 501 patients with HIV-associated
811 Cryptococcal meningitis: implications for
812 improving outcomes. *Clin Infect Dis* 58:736–
813 745
- 814 4. Van Reeth E, Tham IWK, Tan CH et al (2012)
815 Super-resolution in magnetic resonance imag-
816 ing: a review. *Concepts Magn Reson*
817 40A:306–325
- 818 5. Mukaremera L, McDonald TR, Nielsen JN
819 et al (2019) The mouse inhalation model of
820 *Cryptococcus neoformans* infection recapitu-
821 lates strain virulence in humans and shows
822 that closely related strains can possess differ-
823 ential virulence. *Infect Immun* 87(5)
- 824 6. Tenor JL, Oehlers SH, Yang JL et al (2015)
825 Live imaging of host-parasite interactions in a
826 zebrafish infection model reveals Cryptococcal
827 determinants of virulence and central nervous
828 system invasion. *MBio* 6(5):e01425–e01415
- 829 7. Davis JM, Huang M, Botts MR et al (2016) A
830 zebrafish model of Cryptococcal infection
831 reveals roles for macrophages, endothelial
832 cells, and neutrophils in the establishment and
833 control of sustained Fungemia. *Infect Immun*
834 84(10):3047–3062
- 835 8. Bojarczuk A, Miller KA, Hotham R et al (2016)
836 *Cryptococcus neoformans* intracellular proliferation and
837 capsule size determines early macrophage control of
838 infection. *Sci Rep* 18(6):21489
- 839 9. Evans RJ, Pline K, Loynes CA et al (2019)
840 15-keto-prostaglandin E2 activates host perox-
841 isome proliferator-activated receptor gamma
842 (PPAR- γ) to promote *Cryptococcus neoformans*
843 growth during infection. *PLoS Pathog*
844 15(3):e1007597
- 845 10. Singulani JL, Oliveira LT, Ramos MD et al
846 (2021) The antimicrobial peptide MK58911-
847 NH2 acts on planktonic, biofilm, and Intrama-
848 crophage cells of *Cryptococcus neoformans*.
849 *Antimicrob Agents Chemother*
- 850 11. Gibson JF, Bojarczuk A, Evans RJ et al (2017)
851 Dissemination of *Cryptococcus neoformans* via
852 localised proliferation and blockage of blood
853 vessels. *PLoS Pathog*
- 854 12. van Leeuwen LM, Evans RJ, Jim KK et al
855 (2018) A transgenic zebrafish model for the
856 in vivo study of the blood and choroid plexus
857 brain barriers using claudin 5. *Biol Open* 7(2):
858 bio030494
- 859 13. Hamilton N, Rutherford HA, Petts JJ et al
860 (2020) The failure of microglia to digest devel-
861 opmental apoptotic cells contributes to the
862 pathology of RNASET2-deficient leukoence-
863 phalopathy. *Glia* 2020(68):1531–1545
- 864

- 865 14. Nüsslein-Volhard C, Dahm R (2002) Zebra- 881
866 fish: a practical approach. Oxford University 882
867 Press 883
- 868 15. Morrow CA, Lee IR, Chow EW et al (2012) A 884
869 unique chromosomal rearrangement in the 885
870 *Cryptococcus neoformans* var. *grubii* type 886
871 strain enhances key phenotypes associated 887
872 with virulence. *MBio* 3:e00310-e00311 888
- 873 16. Fouquet B, Weinstein BM, Serluca FC et al 889
874 (1997) Vessel patterning in the embryo of the 890
875 zebrafish: guidance by notochord. *Dev Biol* 891
876 183(1):37-48
- 877 17. Kugler E, Snodgrass R, Bowley G et al (2021) 892
878 The effect of absent blood flow on the zebra- 893
879 fish cerebral and trunk vasculature. *Vasc Biol* 894
880 3(1) 895
18. Isogai S, Lawson ND, Torrealday S et al (2003) 881
Angiogenic network formation in the develop- 882
ing vertebrate trunk. *Development* 130(21): 883
5281-5290 884
19. Quiñonez-Silvero C, Hübner K, Herzog W 885
et al (2020) Development of the brain vascula- 886
ture and the blood-brain barrier in zebrafish. 887
Dev Biol 457(2):181-190 888
20. Mork L, Crump G (2015) Zebrafish craniofa- 889
cial development. A window into early pattern- 890
ing. *Curr Top Dev Biol* 115:235-269 891
21. Krueger J, Liu D, Scholz K et al (2011) *Flt1* 892
acts as a negative regulator of tip cell formation 893
and branching morphogenesis in the zebrafish 894
embryo. *Development* 138(10):2111-2120 895

References

1. Aaron, P. A., et al. (2018). The blood–brain barrier internalises *Cryptococcus neoformans* via the EphA2-tyrosine kinase receptor. *Cellular Microbiology*.
2. Abassi, M., et al. (2015). "Cryptococcal Meningitis: Diagnosis and Management Update." *Current tropical medicine reports* 2(2): 90-99.
3. Abbott, N. J., et al. (2018). "The role of brain barriers in fluid movement in the CNS: is there a 'glymphatic' system?" *Acta Neuropathologica* 135(3): 387-407.
4. Abdelilah-Seyfried, S. (2010). "Claudin-5a in developing zebrafish brain barriers: another brick in the wall." *BioEssays* 32(9): 768-776.
5. Acharya, S., et al. (2021). Cryptococcal meningitis in an immunocompetent individual: A case report. *Clinical Case Reports*, Wiley-Blackwell. 9.
6. Adler-Moore, J., et al. (2019). "Preclinical Safety, Tolerability, Pharmacokinetics, Pharmacodynamics, and Antifungal Activity of Liposomal Amphotericin B." *Clinical infectious diseases* 68(Supplement_4): S244-S259.
7. AG, L., et al. (2004). Cerebral infarction related to cryptococcal meningitis in an HIV-infected patient: case report and literature review. *The Brazilian journal of infectious diseases : an official publication of the Brazilian Society of Infectious Diseases, Braz J Infect Dis.* 8: 175-179.
8. Aharon-Peretz, J., et al. (2004). Cryptococcal meningitis mimicking vascular dementia. *Neurology, Neurology.* 62: 2135.
9. AK, M., et al. (2018). Cerebrovascular injury in cryptococcal meningitis. *International journal of stroke : official journal of the International Stroke Society, Int J Stroke.* 13: 57-65.
10. Akagi, J., et al. (2015). Microfluidic device for a rapid immobilization of Zebrafish larvae in environmental scanning electron microscopy. *Cytometry Part A, Wiley-Liss Inc.* 87: 190-194.
11. Aktas, G., et al. (2019). "Spinal CSF flow in response to forced thoracic and abdominal respiration." *Fluids and Barriers of the CNS* 16(1).
12. Ala, T. A., et al. (2004). "Reversible dementia: a case of cryptococcal meningitis masquerading as Alzheimer's disease." *J Alzheimers Dis* 6(5): 503-508.
13. Ala, T. A., et al. (2004). "Reversible dementia: a case of cryptococcal meningitis masquerading as Alzheimer's disease." *J Alzheimers Dis* 6(5): 503-508.

14. Alani, A., et al. (2015). *Cryptococcus neoformans* Host Adaptation: Toward Biological Evidence of Dormancy. *MBio*, American Society for Microbiology. 6: e02580-02514.
15. Andreula, C. F., et al. (1993). "CNS Cryptococcosis in AIDS: Spectrum of MR Findings." *Journal of Computer Assisted Tomography* 17(3).
16. Antinori, S., et al. (2000). "The Role of Lumbar Puncture in the Management of Elevated Intracranial Pressure in Patients with AIDS-Associated Cryptococcal Meningitis." *Clinical infectious diseases* 31(5): 1309-1310.
17. Arnder, L., et al. (1996). "Unusual Pattern of Enhancement in Cryptococcal Meningitis: In Vivo Findings with Postmortem Correlation." *Journal of Computer Assisted Tomography* 20(6): 1023-1026.
18. Ashley, E. D. (2019). "Antifungal Drugs: Special Problems Treating Central Nervous System Infections." *J Fungi (Basel)* 5(4).
19. Awasthi, M., et al. (2001). "Cerebral cryptococcosis: atypical appearances on CT." *The British Journal of Radiology* 74(877): 83-85.
20. Bacynski, A., et al. (2017). "The Paravascular Pathway for Brain Waste Clearance: Current Understanding, Significance and Controversy." *Frontiers in Neuroanatomy* 11.
21. Baddley, J. W., et al. (2019). "Factors Associated with Ventriculo-peritoneal Shunt Placement in Patients With Cryptococcal Meningitis." *Open Forum Infect Dis* 6(6): ofz241.
22. Bahrami, N. and S. J. Childs (2020). *Development of vascular regulation in the zebrafish embryo*. Development (Cambridge), Company of Biologists Ltd. 147.
23. Bai, Y. and Q. Bai (2019). *Hydraulics*. *Subsea Engineering Handbook (Second Edition)*. Y. Bai and Q. Bai. Boston, Gulf Professional Publishing: 315-361.
24. Bain, J. M., et al. (2021). "Immune cells fold and damage fungal hyphae." *Proceedings of the National Academy of Sciences* 118(15): e2020484118.
25. Balasko, A. and Y. Keynan (2019). *Shedding light on IRIS: from Pathophysiology to Treatment of Cryptococcal Meningitis and Immune Reconstitution Inflammatory Syndrome in HIV-Infected Individuals*. *HIV Medicine*, John Wiley & Sons, Ltd (10.1111). 20: 1-10.
26. Barnes, H. A., et al. (1989). *An introduction to rheology*, Elsevier: 199.
27. Beardsley, J., et al. (2016). *Adjunctive Dexamethasone in HIV-Associated Cryptococcal Meningitis*. *New England Journal of Medicine*, Massachusetts Medical Society. 374: 542-554.

28. Benard, E. L., et al. (2012). "Infection of zebrafish embryos with intracellular bacterial pathogens." *J Vis Exp* (61).
29. Best, J. D., et al. (2007). "Non-Associative learning in larval zebrafish." *Neuropsychopharmacology* 33 (5), 1206–1215.
30. Bicanic, T. and T. S. Harrison (2005). "Cryptococcal meningitis." *British Medical Bulletin* 72(1): 99-118.
31. Bicanic, T., et al. (2007). "Fungal Burden, Early Fungicidal Activity, and Outcome in Cryptococcal Meningitis in Antiretroviral-Naive or Antiretroviral-Experienced Patients Treated with Amphotericin B or Fluconazole." *Clinical infectious diseases* 45(1): 76-80.
32. Bicanic, T., et al. (2009). "Independent Association between Rate of Clearance of Infection and Clinical Outcome of HIV-Associated Cryptococcal Meningitis: Analysis of a Combined Cohort of 262 Patients." *Clinical infectious diseases* 49(5): 702-709.
33. Bicanic, T., et al. (2009). Relationship of cerebrospinal fluid pressure, fungal burden and outcome in patients with cryptococcal meningitis undergoing serial lumbar punctures, *Wolters Kluwer Health | Lippincott Williams & Wilkins AIDS*. 23: 701-706.
34. Blank M., et al. (2009). A one-trial inhibitory avoidance task to zebrafish: rapid acquisition of an NMDA-dependent long-term memory. *Neurobiol Learn Mem*. 2009 Nov;92(4):529-34.
35. Bojarczuk, A., et al. (2016). *Cryptococcus neoformans* Intracellular Proliferation and Capsule Size Determines Early Macrophage Control of Infection. *Scientific Reports*, Nature Publishing Group. 6.
36. Bordoni, B., et al. (2018). The Influence of Breathing on the Central Nervous System. *Cureus*, Cureus Inc. 10: e2724.
37. Bothwell, S. W., et al. (2019). "Cerebrospinal fluid dynamics and intracranial pressure elevation in neurological diseases." *Fluids and Barriers of the CNS* 16(1): 9.
38. Bradley, W. G. (2015). CSF Flow in the Brain in the Context of Normal Pressure Hydrocephalus. *AJNR*. American journal of neuroradiology.
39. Bradley, W. G., et al. (2004). Increased intracranial volume: a clue to the etiology of idiopathic normal-pressure hydrocephalus? *AJNR*. American journal of neuroradiology, *American Journal of Neuroradiology*. 25: 1479-1484.
40. Brinker, T., et al. (2014). A new look at cerebrospinal fluid circulation. *Fluids and barriers of the CNS*, BioMed Central. 11: 10.
41. Bruno, S., et al. (2017). Magnetic resonance imaging findings in central nervous system cryptococcosis: comparison between immunocompetent and immunocompromised

- patients Achados de ressonância magnética em criptococose do sistema nervoso central: comparação entre pacientes imunoco. Nov/Dez. 50: 359-365.
42. Bunck, A. C., et al. (2011). "Magnetic resonance 4D flow characteristics of cerebrospinal fluid at the craniocervical junction and the cervical spinal canal." *European Radiology* 21(8): 1788-1796.
 43. Bussmann, J., et al. (2011). "Arterial-venous network formation during brain vascularization involves hemodynamic regulation of chemokine signalling." *Development* 138(9): 1717-1726.
 44. Casadevall, A., et al. (2018). The capsule of *Cryptococcus neoformans*.
 45. Cassot, F., et al. (2006). A Novel Three-Dimensional Computer-Assisted Method for a Quantitative Study of Microvascular Networks of the Human Cerebral Cortex. *Microcirculation*. 13: 1-18.
 46. Cerutti, D. and E. Levin (2008). *Behavioral Neuroscience of Zebrafish*, CRC Press/Taylor & Francis: 293-310.
 47. Chang, Y. C., and K. J. Kwon-Chung. 1994. Complementation of a capsule-deficient mutation of *Cryptococcus neoformans* restores its virulence. *Mol. Cell. Biol.* 14:4912-4919
 48. Chang, Y. C., and K. J. Kwon-Chung. 1998. Isolation of the third capsule-associated gene, *CAP60*, required for virulence in *Cryptococcus neoformans*. *Infect. Immun.* 66:2230-2236.
 49. Chang, Y. C., and K. J. Kwon-Chung. 1999. Isolation, characterization, and localization of a capsule-associated gene, *CAP10*, of *Cryptococcus neoformans*. *J. Bacteriol.* 181:5636-5643.
 50. Chang, Y. C., L. A. Penoyer, and K. J. Kwon-Chung. 1996. The second capsule gene of *Cryptococcus neoformans*, *CAP64*, is essential for virulence. *Infect. Immun.* 64:1977-1983.
 51. Chang, Y. C., B. L. Wickes, and K. J. Kwon-Chung. 1995. Further analysis of the *CAP59* locus of *Cryptococcus neoformans*: structure defined by forced expression and description of a new ribosomal protein-encoding gene. *Gene* 167:179-183.
 52. Chen, S. H. M., et al. (2003). *Cryptococcus neoformans* induces alterations in the cytoskeleton of human brain microvascular endothelial cells. *Journal of Medical Microbiology*, Microbiology Society. 52: 961-970.
 53. Chen, S., et al. (2011). "MRI findings of cerebral cryptococcosis in immunocompetent patients." *Journal of Medical Imaging and Radiation Oncology* 55(1): 52-57.

54. Cherian, J., et al. (2016). Shunting in cryptococcal meningitis. *Journal of Neurosurgery*. 125: 177-186.
55. Cherniak, R. and J. B. Sundstrom (1994). Polysaccharide antigens of the capsule of *Cryptococcus neoformans*. *Infection and immunity*. 62: 1507-1512.
56. Chico, T. J. A. and E. C. Kugler (2021). Cerebrovascular development: mechanisms and experimental approaches. *Cellular and Molecular Life Sciences* 2021 78:9, Springer. 78: 4377-4398.
57. Coady, G., et al. (2011). Pseudosubarachnoid hemorrhage in a 42-year-old male with meningitis. *Radiology Case Reports, Elsevier*. 6: 470.
58. Coelho, C., et al. (2019). "Intranasal Inoculation of *Cryptococcus neoformans* in Mice Produces Nasal Infection with Rapid Brain Dissemination." *mSphere* 4(4): e00483-00419.
59. Colombo, A. C., et al. (2015). Fungal colonization of the brain: anatomopathological aspects of neurological cryptococcosis. *Anais da Academia Brasileira de Ciências, Academia Brasileira de Ciências*. 87: 1293-1309.
60. Crilly, S., et al. (2018). Using zebrafish larval models to study brain injury, locomotor and neuroinflammatory outcomes following intracerebral haemorrhage. *F1000Research, NLM (Medline)*. 7: 1617.
61. Czosnyka, M. and J. D. Pickard (2004). Monitoring and interpretation of intracranial pressure. *Journal of Neurology, Neurosurgery and Psychiatry*. 75: 813-821.
62. Czosnyka, M., et al. (2017). Principles of intracranial pressure monitoring and treatment. *Critical Care Neurology, Pt I. E. F. M. Wijdicks and A. H. Kramer. Amsterdam, Elsevier Science Bv*. 140: 67-89.
63. Czosnyka, M., et al. (2017). Principles of intracranial pressure monitoring and treatment. *Handbook of Clinical Neurology, Elsevier*. 140: 67-89.
64. D’Gama, P. P., et al. (2021). "Diversity and function of motile ciliated cell types within ependymal lineages of the zebrafish brain." *Cell Reports* 37(1).
65. Dammert, P., et al. (2008). "Treatment of cryptococcal meningitis in Peruvian AIDS Patients using amphotericin B and fluconazole." *Journal of Infection* 57(3): 260-265.
66. Dandy, W. E. (1919). EXPERIMENTAL HYDROCEPHALUS. *Annals of surgery, Lippincott, Williams, and Wilkins*. 70: 129-142.
67. Dandy, W. E. and K. D. Blackfan (1913). An experimental and clinical study of internal hydrocephalus. *Journal of the American Medical Association, American Medical Association*. 61: 2216-2217.

68. de Almeida, S. M., et al. (2016). Blood-CSF barrier and compartmentalisation of CNS cellular immune response in HIV infection.
69. de Vedia, L., et al. (2013). "Relevance of intracranial hypertension control in the management of *Cryptococcus neoformans* meningitis related to AIDS." *Infection* 41(6): 1073-1077.
70. Del Bigio, M. R. (2010). "Ependymal cells: biology and pathology." *Acta Neuropathologica* 119(1): 55-73.
71. Denham, S. T., et al. (2017). Regulated release of cryptococcal polysaccharide drives virulence and suppresses immune infiltration into the central nervous system. *Infection and immunity, American Society for Microbiology Journals*. 86: e00662-00617.
72. Denham ST, Brown JCS. Mechanisms of Pulmonary Escape and Dissemination by *Cryptococcus neoformans*. *J Fungi (Basel)*. 2018 Feb 17;4(1):25.
73. Denning, D. W., et al. (1991). Elevated cerebrospinal fluid pressures in patients with cryptococcal meningitis and acquired immunodeficiency syndrome. *The American Journal of Medicine, Elsevier*. 91: 267-272.
74. Desban, L., et al. (2019). Regulation of the apical extension morphogenesis tunes the mechanosensory response of microvilliated neurons. *PLoS biology, NLM (Medline)*. 17: e3000235.
75. Dorand, R. D., et al. (2014). "Comparison of intravital thinned skull and cranial window approaches to study CNS immunobiology in the mouse cortex." *IntraVital* 3(2): e29728.
76. Dreha-Kulaczewski, S., et al. (2017). "Identification of the Upward Movement of Human CSF In Vivo and its Relation to the Brain Venous System." *J Neurosci* 37(9): 2395-2402.
77. Dreha-Kulaczewski, S., et al. (2018). "Respiration and the watershed of spinal CSF flow in humans." *Scientific Reports* 8(1): 5594.
78. Eftekhari, S., et al. (2020). "Long-term monitoring of intracranial pressure in freely-moving rats; impact of different physiological states." *Fluids and Barriers of the CNS* 17(1).
79. Ertürk, A., et al. (2014). Imaging cleared intact biological systems at a cellular level by 3DISCO. *Journal of Visualised Experiments, Journal of Visualised Experiments*.
80. Fame, R. M., et al. (2016). Directional cerebrospinal fluid movement between brain ventricles in larval zebrafish *Fluids and Barriers of the CNS* Directional cerebrospinal fluid movement between brain ventricles in larval zebrafish. *Fluids and Barriers of the CNS*. 13: 11.

81. Faul, F., et al. (2007). "G*Power 3: a flexible statistical power analysis program for the social, behavioral, and biomedical sciences." *Behav Res Methods* 39(2): 175-191.
82. Feldmesser, M., et al. (1996). "Serum cryptococcal antigen in patients with AIDS." *Clinical infectious diseases*: 827-830.
83. Frases, S., et al. (2008). Cryptococcus neoformans capsular polysaccharide and exopolysaccharide fractions manifest physical, chemical, and antigenic differences. *Eukaryotic cell, American Society for Microbiology (ASM)*. 7: 319-327.
84. Fries, B. C., et al. (2005). "Phenotypic switching of Cryptococcus neoformans can produce variants that elicit increased intracranial pressure in a rat model of cryptococcal meningoencephalitis." *Infect Immun* 73(3): 1779-1787.
85. Friese, S., et al. (2004). "The Influence of Pulse and Respiration on Spinal Cerebrospinal Fluid Pulsation." *Investigative Radiology* 39(2): 120-130.
86. Fritsche, R., et al. (2000). "Nitric oxide and vascular reactivity in developing zebrafish, *Danio rerio*." *Am J Physiol Regul Integr Comp Physiol* 279(6): R2200-2207.
87. Fromtling RA, Shadomy HJ, Jacobson ES. Decreased virulence in stable, acapsular mutants of cryptococcus neoformans. *Mycopathologia*. 1982 Jul 23;79(1):23-9.
88. Fronius, M., et al. (2012). Why do we have to move fluid to be able to breathe? *Frontiers in Physiology, Frontiers Media SA*. 3 MAY.
89. Galanternik, M. V., et al. (2017). A novel perivascular cell population in the zebrafish brain. *eLife, eLife Sciences Publications Ltd*. 6.
90. García-Lecea, M., et al. (2008). "In vivo Analysis of Choroid Plexus Morphogenesis in Zebrafish." *PLOS ONE* 3(9): e3090.
91. Gassiep, I., et al. (2018). Correlation between serum cryptococcal antigen titre and meningitis in immunocompetent patients. *Journal of Medical Microbiology, Microbiology Society*. 67: 1515-1518.
92. Gibson, J. F. and S. A. Johnston (2015). Immunity to Cryptococcus neoformans and *C. gattii* during cryptococcosis. *Fungal Genetics and Biology*.
93. Gibson, J. F., et al. (2017). Dissemination of Cryptococcus neoformans via localised proliferation and blockage of blood vessels. *bioRxiv, Cold Spring Harbor Laboratory*: 184200.
94. Gibson, J. F., et al. (2020). Blood vessel occlusion by Cryptococcus neoformans is a mechanism for haemorrhagic dissemination of infection. *bioRxiv, Cold Spring Harbor Laboratory*: 2020.2003.2017.995571.

95. Glavin, G. B. (1985). Stress and brain noradrenaline: A review. *Neuroscience & Biobehavioral Reviews*, Pergamon. 9: 233-243.
96. Goldman, D. L., et al. (1996). "Cryptococcus neoformans meningitis in the rat." *Laboratory investigation*. 75(6): 759-770.
97. Gomez-Garcia, M. J., et al. (2018). "Nanoparticle localization in blood vessels: dependence on fluid shear stress, flow disturbances, and flow-induced changes in endothelial physiology." *Nanoscale* 10(32): 15249-15261.
98. Góralaska, K., et al. (2018). Neuroinfections caused by fungi. *Infection*, Springer. 46: 443.
99. Goughenour, K. D., et al. (2021). "Murine Inducible Nitric Oxide Synthase Expression Is Essential for Antifungal Defenses in Kidneys during Disseminated Cryptococcus deneoformans Infection." *The Journal of Immunology* 207(8): 2096-2106.
100. Gow, N. A. R., et al. (2017). Microbe Profile: *Candida albicans*: a shape-changing, opportunistic pathogenic fungus of humans MICROBE PROFILE. *Microbiology*. 163: 1145-1147.
101. Graybill, J. R., et al. (2000). Diagnosis and Management of Increased Intracranial Pressure in Patients with AIDS and Cryptococcal Meningitis. *Clinical infectious diseases*, Oxford University Press. 30: 47-54.
102. Greene, C. and M. Campbell (2016). "Tight junction modulation of the blood brain barrier: CNS delivery of small molecules." *Tissue Barriers* 4(1): e1138017.
103. Greene, C., et al. (2019). "Claudin-5: gatekeeper of neurological function." *Fluids and Barriers of the CNS* 16(1): 3.
104. Griffith, B., et al. (2018). CSF Pressure Change in Relation to Opening Pressure and CSF Volume Removed. *AJNR*. American journal of neuroradiology, American Journal of Neuroradiology. 39: 1185-1190.
105. Groll, A. H., et al. (2000). "Comparative efficacy and distribution of lipid formulations of amphotericin B in experimental *Candida albicans* infection of the central nervous system." *The Journal of infectious diseases* 182(1): 274-282.
106. Gut, P., et al. (2017). "Little fish, big data: zebrafish as a model for cardiovascular and metabolic disease." *Physiological reviews* 97(3): 889-938.
107. Gutzman, J. H. and H. Sive (2009). Zebrafish Brain Ventricle Injection. *JoVE*. 26
108. Haddad-Tóvolli, R., et al. (2017). Development and function of the blood-brain barrier in the context of metabolic control. *Frontiers in Neuroscience*. 11

- 109.Hammoud, D. A., et al. (2017). "Choroid Plexitis and Ependymitis by Magnetic Resonance Imaging are Biomarkers of Neuronal Damage and Inflammation in HIV-negative Cryptococcal Meningoencephalitis." *Scientific reports* 7(1): 9184-9184.
- 110.Han, F., et al. (2021). "Reduced coupling between cerebrospinal fluid flow and global brain activity is linked to Alzheimer disease–related pathology." *PLOS Biology* 19(6): e3001233.
- 111.He, H., et al. (2016). *Perivascular Macrophages Limit Permeability. Arteriosclerosis, Thrombosis, and Vascular Biology*, Lippincott Williams and Wilkins. 36: 2203-2212.
- 112.Henriksen, J. R. and J. H. Ipsen (2004). Measurement of membrane elasticity by micropipette aspiration. *The European Physical Journal E*, Springer-Verlag. 14: 149-167.
- 113.Henson, H. E., et al. (2014). Functional and genetic analysis of choroid plexus development in zebrafish. *Frontiers in Neuroscience*.
- 114.Hill, J. O. (1992). "CD4+ T cells cause multinucleated giant cells to form around *Cryptococcus neoformans* and confine the yeast within the primary site of infection in the respiratory tract." *The Journal of experimental medicine* 175(6): 1685-1695.
- 115.Hladky, S. B. and M. A. Barrand (2016). "Fluid and ion transfer across the blood–brain and blood–cerebrospinal fluid barriers; a comparative account of mechanisms and roles." *Fluids and Barriers of the CNS* 13(1): 19.
- 116.Hochmuth, R. M. (2000). Micropipette aspiration of living cells. *Journal of Biomechanics*. 33: 15-22.
- 117.Howden, L., et al. (2008). *Computer Methods in Biomechanics and Biomedical Engineering Three-dimensional cerebrospinal fluid flow within the human ventricular system Three-dimensional cerebrospinal fluid flow within the human ventricular system. Computer Methods in Biomechanics and Biomedical Engineering*. 11: 123-133.
- 118.Howden, L., et al. (2008). Three-dimensional cerebrospinal fluid flow within the human ventricular system Three-dimensional cerebrospinal fluid flow within the human ventricular system. *Computer Methods in Biomechanics and Biomedical Engineering*. 11: 123-133.
- 119.Hu, Z., et al. (2017). "The use of mannitol in HIV-infected patients with symptomatic cryptococcal meningitis." *Drug Discov Ther* 10(6): 329-333.
- 120.Huang, L., et al. (2015). Analysis of cerebrospinal fluid protein concentrations of patients with cryptococcal meningitis treated with antifungal agents. *BMC Infectious Diseases*, BioMed Central Ltd. 15.

- 121.Hurtado, J. C., et al. (2019). "Mortality due to *Cryptococcus neoformans* and *Cryptococcus gattii* in low-income settings: an autopsy study." *Sci Rep* 9(1): 7493.
- 122.Iliff, J. J., et al. (2012). "A paravascular pathway facilitates CSF flow through the brain parenchyma and the clearance of interstitial solutes, including amyloid β ." *Sci Transl Med* 4(147): 147ra111.
- 123.Jarvis, J. N. and T. S. Harrison (2019). "Understanding Causal Pathways in Cryptococcal Meningitis Immune Reconstitution Inflammatory Syndrome." *The Journal of infectious diseases* 219(3): 344-346.
- 124.Jarvis, J. N., et al. (2014). Determinants of mortality in a combined cohort of 501 patients with HIV-associated Cryptococcal meningitis: implications for improving outcomes. *Clinical infectious diseases : an official publication of the Infectious Diseases Society of America*, Oxford University Press. 58: 736-745.
- 125.Jean., et al. (2002). Cryptococcaemia: clinical features and prognostic factors. *QJM: monthly journal of the Association of Physicians*, QJM. 95: 511-518.
- 126.Jeong, J.-Y., et al. (2008). "Functional and developmental analysis of the blood–brain barrier in zebrafish." *Brain Research Bulletin* 75(5): 619-628.
- 127.Jeroen Bussmann¹, S. A. W., ³ and Arndt F. Siekmann¹, (2011). Arterial-venous network formation during brain vascularization involves hemodynamic regulation of chemokine signaling.
- 128.Jiménez, A. J., et al. (2014). "Structure and function of the ependymal barrier and diseases associated with ependyma disruption." *Tissue Barriers* 2(1): e28426.
- 129.John CL., (1995). *Analytical Polymer Rheology – Structure-Processing-Property*
- 130.John Vassilouthis, A. R. (1979). Ventricular dilatation and communicating hydrocephalus following spontaneous subarachnoid hemorrhage. *Journal of Neurosurgery*.
- 131.Kambugu, A., et al. (2008). "Outcomes of Cryptococcal Meningitis in Uganda Before and After the Availability of Highly Active Antiretroviral Therapy." *Clinical infectious diseases* 46(11): 1694-1701.
- 132.Kanther, M., et al. (2019). Initiation and early growth of the skull vault in zebrafish. *Mechanisms of Development*: 103578.
- 133.Kasprowicz, M., et al. (2016). Intracranial pressure, its components and cerebrospinal fluid pressure-volume compensation. *Acta Neurologica Scandinavica*, John Wiley & Sons, Ltd (10.1111). 134: 168-180.

134. Kaufman-Francis, K., et al. (2018). "The Early Innate Immune Response to, and Phagocyte-Dependent Entry of, *Cryptococcus neoformans* Map to the Perivascular Space of Cortical Post-Capillary Venules in Neurocryptococcosis." *The American Journal of Pathology* 188(7): 1653-1665.
135. Kellie G. (1824). An account of the appearances observed in the dissection of two of three individuals presumed to have perished in the storm of the 3rd, and whose bodies were discovered in the vicinity of Leith on the morning of the 4th, November 1821: with some reflections on the pathology of the brain. *Transactions of the Medico-Chirurgical Society of Edinburgh* 1824; 1: 82–169.
136. Kharel et al. (2018). "Spectrum of Cryptococcal Meningoencephalitis in Tertiary Hospital in Nepal." *Journal of Institute of Medicine* 40(2).
137. Khan, S. F., et al. (2019). When ventricular cerebrospinal fluid assessment misleads basal meningitis and the importance of lumbar puncture sampling. *Open Forum Infectious Diseases*, Narnia. 6.
138. Khasawneh, A. H., et al. (2018). Cerebrospinal fluid circulation: What do we know and how do we know it? *Brain circulation*, Wolters Kluwer -- Medknow Publications. 4: 14-18.
139. Koch M (1999). The neurobiology of startle. *Prog Neurobiol* 59: 107–128.
140. Kochhan, E., et al. (2013). "Blood Flow Changes Coincide with Cellular Rearrangements during Blood Vessel Pruning in Zebrafish Embryos." *PLOS ONE* 8(10): e75060.
141. Kominsky, S. L., et al. (2007). "Clostridium perfringens enterotoxin as a novel-targeted therapeutic for brain metastasis." *Cancer research* 67(17): 7977-7982.
142. Kondo, R., et al. (2015). Neurogenic pulmonary edema following Cryptococcal meningoencephalitis associated with HIV infection.
143. Köster, S., et al. (2017). Mycobacterium tuberculosis is protected from NADPH oxidase and LC3-associated phagocytosis by the LCP protein CpsA. *Proceedings of the National Academy of Sciences*.
144. Koundal, S., et al. (2020). "Optimal Mass Transport with Lagrangian Workflow Reveals Advective and Diffusion Driven Solute Transport in the Glymphatic System." *Scientific Reports* 10(1): 1990.
145. Kramer-Zucker, A. G., et al. (2005). "Cilia-driven fluid flow in the zebrafish pronephros, brain and Kupffer's vesicle is required for normal organogenesis." *Development* 132(8): 1907-1921.

146. Kratzer, I., et al. (2012). "Complexity and developmental changes in the expression pattern of claudins at the blood–CSF barrier." *Histochemistry and cell biology* 138: 861-879.
147. Kuehne, L. K., et al. (2013). Cerebrospinal fluid neopterin is brain-derived and not associated with blood-CSF barrier dysfunction in non-inflammatory affective and schizophrenic spectrum disorders. *Journal of Psychiatric Research*. 47: 1417-1422.
148. Kugler, E. C., et al. (2019). Cerebrovascular endothelial cells form transient Notch-dependent cystic structures in zebrafish. *EMBO reports*, EMBO. 20.
149. Kugler, E. C., et al. (2022). "Zebrafish vascular quantification: a tool for quantification of three-dimensional zebrafish cerebrovascular architecture by automated image analysis." *Development* 149(3).
150. Kugler, E., et al. (2018). *Image Analysis in Light Sheet Fluorescence Microscopy Images of Transgenic Zebrafish Vascular Development*, Cham, Springer International Publishing.
151. Kugler, E., et al. (2019). "Enhancement and Segmentation Workflow for the Developing Zebrafish Vasculature." *Journal of Imaging* 5(1): 14.
152. Kugler, E., et al. (2021). "The effect of absent blood flow on the zebrafish cerebral and trunk vasculature." *Vascular Biology* 3(1): 1-16.
153. Kumari, R., et al. (2010). Cryptococcal choroid plexitis: rare imaging findings of central nervous system cryptococcal infection in an immunocompetent individual. *British Journal of Radiology*, British Institute of Radiology. 83: e014.
154. Lagendijk, A. K., et al. (2017). Live imaging molecular changes in junctional tension upon VE-cadherin in zebrafish. *Nature Communications*, Nature Publishing Group. 8.
155. Lawrence, D. S., et al. (2019). "Emerging concepts in HIV-associated cryptococcal meningitis." *Current Opinion in Infectious Diseases* 32(1): 16-23.
156. Lawson, N. D. and B. M. Weinstein (2002). "In vivo imaging of embryonic vascular development using transgenic zebrafish." *Developmental biology* 248(2): 307-318.
157. Lee., et al. (1996). Pathology of cryptococcal meningoencephalitis: analysis of 27 patients with pathogenetic implications. *Human pathology*, Hum Pathol. 27: 839-847.
158. Lee, H., et al. (2018). "Quantitative Gd-DOTA uptake from cerebrospinal fluid into rat brain using 3D VFA-SPGR at 9.4T." *Magnetic Resonance in Medicine* 79(3): 1568-1578.

- 159.Lee, S. C., et al. (1996). Immunohistochemical localization of capsular polysaccharide antigen in the central nervous system cells in cryptococcal meningoencephalitis. *The American journal of pathology*. 148: 1267-1274.
- 160.Lee, W. J., et al. (2021). "Enlarged periventricular space and periventricular lesion extension on baseline brain MRI predicts poor neurological outcomes in cryptococcus meningoencephalitis." *Sci Rep* 11(1): 6446.
- 161.Leinonen, V., et al. (2017). Raised intracranial pressure and brain edema. *Handbook of Clinical Neurology*, Elsevier B.V. 145: 25-37.
- 162.Lewis, M., Bromley, K., Sutton, C.J. et al. (2021) Determining sample size for progression criteria for pragmatic pilot RCTs: the hypothesis test strikes back!. *Pilot Feasibility Stud* 7, 40.
- 163.Liang, L., et al. (2021). A case–control study of human immunodeficiency virus-negative patients with cryptococemia and cryptococcal meningitis in a Chinese tertiary care hospital during 10 years. *Journal of International Medical Research*, SAGE Publications Ltd. 49.
- 164.Liechty, C.A., et al., 2007. Asymptomatic serum cryptococcal antigenemia and early mortality during antiretroviral therapy in rural Uganda. *Tropical medicine & international health*, 12(8), pp.929-935
- 165.Link A, et al., (2022). Delays in Cryptococcal Meningitis Diagnosis and Care: A Mixed Methods Study in Rural Uganda. *Ann Glob Health*. 2022 Mar 18;88(1):22.
- 166.Lister, J. A., et al. (1999). "Nacre encodes a zebrafish microphthalmia-related protein that regulates neural-crest-derived pigment cell fate." *Development* 126(17): 3757-3767.
- 167.Liu, J., et al. (2018). Ventriculoperitoneal shunts in non-HIV cryptococcal meningitis. *BMC neurology*, BioMed Central. 18: 58.
- 168.Liu, L., et al. (2014). "The use of ventriculoperitoneal shunts for uncontrollable intracranial hypertension in patients with HIV-associated cryptococcal meningitis with or without hydrocephalus." *Biosci Trends* 8(6): 327-332.
- 169.Lofgren, S., et al. (2017). "Recent advances in AIDS-related cryptococcal meningitis treatment with an emphasis on resource limited settings." *Expert review of anti-infective therapy* 15(4): 331-340.
- 170.Louveau, A., et al. (2015). Structural and functional features of central nervous system lymphatic vessels. *Nature*, Nature Publishing Group. 523: 337-341.

171. Lowery, L. A. and H. Sive (2005). Initial formation of zebrafish brain ventricles occurs independently of circulation and requires the *nagie oko* and *snakehead/atp1a1a.1* gene products. *Development*. 132: 2057-2067.
172. Loyse, A., et al. (2010). Histopathology of the arachnoid granulations and brain in HIV-associated cryptococcal meningitis: correlation with cerebrospinal fluid pressure. *AIDS (London, England), Europe PMC Funders*. 24: 405-410.
173. Loyse, A., et al. (2011). "Comparison of the Early Fungicidal Activity of High-Dose Fluconazole, Voriconazole, and Flucytosine as Second-Line Drugs Given in Combination With Amphotericin B for the Treatment of HIV-Associated Cryptococcal Meningitis." *Clinical infectious diseases* 54(1): 121-128.
174. Loyse, A., et al. (2015). Neurological, visual, and MRI brain scan findings in 87 South African patients with HIV-associated cryptococcal meningoencephalitis. *Journal of Infection, W.B. Saunders*. 70: 668-675.
175. Lui, G., et al. (2006). Cryptococcosis in apparently immunocompetent patients. *QJM: An International Journal of Medicine, Oxford Academic*. 99: 143-151.
176. Lun, M. P., et al. (2015). "Development and functions of the choroid plexus–cerebrospinal fluid system." *Nature Reviews Neuroscience* 16(8): 445-457.
177. Luo Y, Alvarez M, Xia L, Casadevall A. (2008). The outcome of phagocytic cell division with infectious cargo depends on single phagosome formation. *PLoS One*
178. MacAulay, N. (2021). "Molecular mechanisms of brain water transport." *Nature Reviews Neuroscience* 22(6): 326-344.
179. MacAulay, N., et al. (2022). "Cerebrospinal fluid production by the choroid plexus: a century of barrier research revisited." *Fluids and Barriers of the CNS* 19(1): 26.
180. Macosko, C. (1994). *Rheology : Principles Measurements and Applications*. . New York New York NY: VCH; 1994.
181. Madhok, D. Y., et al. (2018). Overview of Neurovascular Physiology. *Current Neurology and Neuroscience Reports*. 18.
182. Mahuzier, A., et al. (2018). "Ependymal cilia beating induces an actin network to protect centrioles against shear stress." *Nature Communications* 9(1): 2279.
183. Markicevic, M., et al. (2021). "Emerging imaging methods to study whole-brain function in rodent models." *Translational Psychiatry* 11(1).
184. Mathews, V. P., et al. (1992). AIDS-Related CNS Cryptococcosis: Radiologic-Pathologic Correlation.

- 185.Mato, M. (2001). Perivascular Cells of Small Cerebral Vessels (FGP, Mato cells) and Their Permeability Under Pathological Conditions. *Ischemic Blood Flow in the Brain*, Springer Japan: 83-88.
- 186.McCarthy, K. M., et al. (2006). Population-based surveillance for cryptococcosis in an antiretroviral-naive South African province with a high HIV seroprevalence. *AIDS*.
- 187.McFadden, D. C., et al. (2006). The physical properties of the capsular polysaccharides from *Cryptococcus neoformans* suggest features for capsule construction. *The Journal of biological chemistry, American Society for Biochemistry and Molecular Biology*. 281: 1868-1875.
- 188.Megson, G. M., et al. (1996). "D-mannitol in cerebrospinal fluid of patients with AIDS and cryptococcal meningitis." *Journal of Clinical Microbiology* 34(1): 218-221.
- 189.Mehta, N. H., et al. (2022). "Quantifying cerebrospinal fluid dynamics: A review of human neuroimaging contributions to CSF physiology and neurodegenerative disease." *Neurobiology of Disease* 170: 105776.
- 190.Meng, L., et al. (2015). "Cardiac Output and Cerebral Blood Flow: The Integrated Regulation of Brain Perfusion in Adult Humans." *Anesthesiology* 123(5): 1198-1208.
- 191.Messas, E., et al. (2013). "Arterial wall elasticity: State of the art and future prospects." *Diagnostic and Interventional Imaging* 94(5): 561-569.
- 192.Mestre, H., et al. (2018). "Flow of cerebrospinal fluid is driven by arterial pulsations and is reduced in hypertension." *Nature Communications* 9(1): 4878.
- 193.Mestre, H., et al. (2020). "The Brain's Glymphatic System: Current Controversies." *Trends Neurosci* 43(7): 458-466.
- 194.Mishra, A. K., et al. (2018). Cerebrovascular injury in cryptococcal meningitis. *International Journal of Stroke, SAGE PublicationsSage UK: London, England*. 13: 57-65.
- 195.Miszkiel, K. A., et al. (1996). "The spectrum of MRI findings in CNS cryptococcosis in AIDS." *Clinical Radiology* 51(12): 842-850.
- 196.Mitchison, H. M. and E. M. Valente (2017). "Motile and non-motile cilia in human pathology: from function to phenotypes." *The Journal of Pathology* 241(2): 294-309.
- 197.Mitsunori Matsumae M.D., P. D., Ron Kikinis M.D. 1 (1996). Age-related changes in intracranial compartment volumes in normal adults assessed by magnetic resonance imaging.

198. Molloy, S. F., et al. (2021). "Fungal Burden and Raised Intracranial Pressure Are Independently Associated With Visual Loss in Human Immunodeficiency Virus-Associated Cryptococcal Meningitis." *Open Forum Infectious Diseases* 8(4).
199. Monro A. (1783) *Observations on the structure and functions of the nervous system: illustrated with tables*, Edinburgh: Printed for, and sold by, William Creech.
200. Mork, L. and G. Crump (2015). *Zebrafish Craniofacial Development. A Window into Early Patterning*. *Current Topics in Developmental Biology*, Academic Press Inc. 115: 235-269.
201. Mover, E., et al. (2013). Using Patient Pathways to Accelerate the Drive to Ending Tuberculosis. *Journal of Infectious Diseases*, Oxford Academic. 208: 2025-2035.
202. Mukaremera, L., et al. (2019). "The Mouse Inhalation Model of *Cryptococcus neoformans* Infection Recapitulates Strain Virulence in Humans and Shows that Closely Related Strains Can Possess Differential Virulence." *Infect Immun* 87(5).
203. Mylonakis, E., et al. (2002). "Killing of *Caenorhabditis elegans* by *Cryptococcus neoformans* as a model of yeast pathogenesis." *Proceedings of the National Academy of Sciences of the United States of America* 99(24): 15675-15680.
204. Nedelsky, N. B. and J. P. Taylor (2022). "Pathological phase transitions in ALS-FTD impair dynamic RNA–protein granules." *RNA* 28(1): 97-113.
205. Nematollahi, S. and V. Dioverti-Prano (2020). *Cryptococcal infection in haematologic malignancies and haematopoietic stem cell transplantation*. *Mycoses*, Blackwell Publishing Ltd. 63: 1033-1046.
206. Newton, Paul N., et al. (2002). A Randomized, Double-Blind, Placebo-Controlled Trial of Acetazolamide for the Treatment of Elevated Intracranial Pressure in Cryptococcal Meningitis. *Clinical infectious diseases*, Oxford University Press. 35: 769-772.
207. North, T. E., et al. (2009). "Hematopoietic Stem Cell Development Is Dependent on Blood Flow." *Cell* 137(4): 736-748.
208. Nüsslein-Volhard, C. and R. Dahm (2002). *Zebrafish: A Practical Approach*, Oxford University Press.
209. O’Brown, N. M., et al. (2019). Suppression of transcytosis regulates zebrafish blood-brain barrier function. *eLife*, eLife Sciences Publications Ltd. 8.
210. Offiah, C. E. and A. Naseer (2016). "Spectrum of imaging appearances of intracranial cryptococcal infection in HIV/AIDS patients in the anti-retroviral therapy era." *Clinical Radiology* 71(1): 9-17.

- 211.Ohtsuki, S., et al. (2008). "mRNA expression levels of tight junction protein genes in mouse brain capillary endothelial cells highly purified by magnetic cell sorting." *Journal of neurochemistry* 104(1): 147-154.
- 212.Okagaki, L. H., et al. (2010). "Cryptococcal cell morphology affects host cell interactions and pathogenicity." *PLoS Pathog* 6(6): e1000953.
- 213.Olstad, E. W., et al. (2019). Ciliary Beating Compartmentalizes Cerebrospinal Fluid Flow in the Brain and Regulates Ventricular Development. *Current Biology*, Cell Press. 29: 229-241.e226.
- 214.Olszewski, M. A., et al. (2004). "Urease Expression by *Cryptococcus neoformans* Promotes Microvascular Sequestration, Thereby Enhancing Central Nervous System Invasion." *The American Journal of Pathology* 164(5): 1761-1771.
- 215.Orešković, D. and M. Klarica (2010). The formation of cerebrospinal fluid: Nearly a hundred years of interpretations and misinterpretations.
- 216.Orešković, D. and M. Klarica (2011). Development of hydrocephalus and classical hypothesis of cerebrospinal fluid hydrodynamics: Facts and illusions. *Progress in Neurobiology*, Pergamon. 94: 238-258.
- 217.Otsu, N. (1979). "A threshold selection method from gray-level histograms." *IEEE transactions on systems, man, and cybernetics* 9(1): 62-66.
- 218.Pai, M. P., et al. (2009). "Characterization of BBB permeability in a preclinical model of cryptococcal meningoencephalitis using magnetic resonance imaging." *J Cereb Blood Flow Metab* 29(3): 545-553.
- 219.Parady, B. (2018). Innate Immune and Fungal Model of Alzheimer's Disease. *Journal of Alzheimer's Disease Reports*, IOS Press. 2: 139-152.
- 220.Park, B. J., et al. (2008). Refocusing on a reemergent disease: the current global burden of cryptococcal meningitis among persons living with HIV/AIDS. *Aids*. 23: 525-530.
- 221.Park, B. J., et al. (2009). Estimation of the current global burden of cryptococcal meningitis among persons living with HIV/AIDS. *AIDS*. 23: 525-530.
- 222.Park, Matthew K., et al. (1999). Treatment of Hydrocephalus Secondary to Cryptococcal Meningitis by Use of Shunting. *Clinical infectious diseases*. 28: 629-633.
- 223.Passos-Neto, C. E. B., et al. (2022). "Normal pressure hydrocephalus: an update." *Arquivos de Neuro-Psiquiatria* 80(5 suppl 1): 42-52.
- 224.Pelster, B. and B. Bagatto (2010). 7 - Respiration. *Fish Physiology*. S. F. Perry, M. Ekker, A. P. Farrell and C. J. Brauner, Academic Press. 29: 289-309.

225. Peng, X., et al. (2021). Successful Intravenous Thrombolysis in Ischemic Stroke Caused by Tuberculous Meningitis: A Case Report. *Frontiers in Neurology, Frontiers Media SA.* 12: 676684.
226. Peter, G. P. (2005). "Managing Cryptococcal Meningitis Is about Handling the Pressure." *Clinical infectious diseases* 40(3): 480-482.
227. Phusoongnern, W., et al. (2017). Predictive Model for Permanent Shunting in Cryptococcal meningitis. *The American journal of tropical medicine and hygiene, The American Society of Tropical Medicine and Hygiene.* 97: 1451-1453.
228. Piyankarage, S. C., et al. (2012). "Nanoliter Hemolymph Sampling and Analysis of Individual Adult *Drosophila melanogaster*." *Analytical Chemistry* 84(10): 4460-4466.
229. Pollay, M. and F. Curl (1967). Secretion of cerebrospinal fluid by the ventricular ependyma of the rabbit. *American Journal of Physiology-Legacy Content, American Physiological Society.* 213: 1031-1038.
230. Popovich, M. J., et al. (1990). "CT of intracranial cryptococcosis." *American Journal of Roentgenology* 154(3): 603-606.
231. Quiñonez-Silvero, C., et al. (2020). "Development of the brain vasculature and the blood-brain barrier in zebrafish." *Developmental biology* 457(2): 181-190.
232. Rajasingham, R., et al. (2017). Global burden of disease of HIV-associated cryptococcal meningitis: an updated analysis. *The Lancet. Infectious diseases, NIH Public Access.* 17: 873-881.
233. Rajasingham R, et al., (2019). Cryptococcal Meningitis Diagnostics and Screening in the Era of Point-of-Care Laboratory Testing. *J Clin Microbiol.* 2019 Jan 2;57(1):e01238-18.
234. Ramirez, J., et al. (2016). Imaging the Perivascular Space as a Potential Biomarker of Neurovascular and Neurodegenerative Diseases. *Cellular and Molecular Neurobiology, Springer US.* 36: 289-299.
235. Rathore SS, Raman T, Ramakrishnan J. Magnesium Ion Acts as a Signal for Capsule Induction in *Cryptococcus neoformans*. *Front Microbiol.* 2016 Mar 15;7:325.
236. Ray, L., et al. (2019). "Analysis of convective and diffusive transport in the brain interstitium." *Fluids and Barriers of the CNS* 16(1): 6.
237. Redzic, Z. (2011). "Molecular biology of the blood-brain and the blood-cerebrospinal fluid barriers: similarities and differences." *Fluids and Barriers of the CNS* 8(1): 3.

- 238.Reemst K., Shanin H. and Shahar D. (2023). "Learning and memory formation in zebrafish: Protein dynamics and molecular tools.". *Front. Cell Dev. Biol.*, 09 March 2023. Sec. Molecular and Cellular Pathology. Volume 11 - 2023
- 239.Reiber, H. (1994). Flow rate of cerebrospinal fluid (CSF) - A concept common to normal blood-CSF barrier function and to dysfunction in neurological diseases. *Journal of the Neurological Sciences*. 122: 189-203.
- 240.Reiber, H. (2010). *2 Blood-Brain Barrier and Blood-CSF Barrier Function. Relationships* Hanser-Gardner Publishers.
- 241.Renshaw, S. A. and N. S. Trede (2012). A model 450 million years in the making: zebrafish and vertebrate immunity. *Disease models & mechanisms*, Company of Biologists. 5: 38-47.
- 242.Rigi, M., et al. (2017). Evaluation and management of the swollen optic disk in cryptococcal meningitis. *Survey of Ophthalmology*, Elsevier. 62: 150-160.
- 243.Roales-Buján, R., et al. (2012). "Astrocytes acquire morphological and functional characteristics of ependymal cells following disruption of ependyma in hydrocephalus." *Acta Neuropathol* 124(4): 531-546.
- 244.Robertson, E. J., et al. (2014). *Cryptococcus neoformans* ex vivo capsule size is associated with intracranial pressure and host immune response in HIV-associated cryptococcal meningitis. *The Journal of infectious diseases*, Oxford University Press. 209: 74-82.
- 245.Rodríguez-Boto, G., et al. (2015). Basic concepts about brain pathophysiology and intracranial pressure monitoring. *Neurología (English Edition)*, Elsevier. 30: 16-22.
- 246.Rolfes, M. A., et al. (2014). The effect of therapeutic lumbar punctures on acute mortality from cryptococcal meningitis. *Clinical infectious diseases: an official publication of the Infectious Diseases Society of America*, Oxford University Press. 59: 1607-1614.
- 247.Ropper, A. H. (2012). Hyperosmolar Therapy for Raised Intracranial Pressure. *N Engl J Med*. 367: 746-752.
- 248.Rosario, M., et al. (2012). An Unusual Case of Stroke. *The neurologist*, NIH Public Access. 18: 229.
- 249.Rosowski, E., et al. (2018). The Zebrafish as a Model Host for Invasive Fungal Infections. *Journal of Fungi*, Multidisciplinary Digital Publishing Institute. 4: 136.
- 250.Rudkin, F. M., et al. (2018). Single human B cell-derived monoclonal anti-*Candida* antibodies enhance phagocytosis and protect against disseminated candidiasis. *Nature Communications*. 9: 5288.

- 251.Sabiiti, et al. (2014). Efficient phagocytosis and laccase activity affect the outcome of HIV-associated cryptococcosis. *The Journal of Clinical Investigation* 2014 Vol. 124 Issue 5 Pages 2000-2008
- 252.Sakka, L., et al. (2011). "Anatomy and physiology of cerebrospinal fluid." *Eur Ann Otorhinolaryngol Head Neck Dis* 128(6): 309-316.
- 253.Saleem, S. and R. R. Kannan (2018). Zebrafish: an emerging real-time model system to study Alzheimer's disease and neurospecific drug discovery. *Cell Death Discovery*, Springer Nature. 4: 45.
- 254.Santiago-Tirado, F. H., et al. (2017). "Trojan horse transit contributes to blood-brain barrier crossing of a eukaryotic pathogen." *MBio* 8(1): e02183-02116.
- 255.Satishchandra, P., et al. (2007). Cryptococcal meningitis: Clinical, diagnostic, and therapeutic overviews. *Neurology India*, Medknow Publications. 55: 226.
- 256.Sato, Y., et al. (1997). 3D multi-scale line filter for segmentation and visualization of curvilinear structures in medical images. *CVRMed-MRCAS'97*, Springer.
- 257.Schindelin, J., et al. (2012). "Fiji: an open-source platform for biological-image analysis." *Nat Methods* 9(7): 676-682.
- 258.Schmid, B., et al. (2010). "A high-level 3D visualization API for Java and ImageJ." *BMC Bioinformatics* 11(1): 274.
- 259.Schwartz, S., et al. (2018). Advances in the diagnosis and treatment of fungal infections of the CNS. *The Lancet Neurology*, Elsevier. 17: 362-372.
- 260.Schwerk, C., et al. (2015). The choroid plexus-a multi-role player during infectious diseases of the CNS. *Frontiers in cellular neuroscience*, Frontiers Media SA. 9: 80.
- 261.Sharma, A. K., et al. (2008). Measurement of peak CSF flow velocity at cerebral aqueduct, before and after lumbar CSF drainage, by use of phase-contrast MRI: Utility in the management of idiopathic normal pressure hydrocephalus. *Clinical Neurology and Neurosurgery*.
- 262.Shi, M., et al. (2010). "Real-time imaging of trapping and urease-dependent transmigration of *Cryptococcus neoformans* in mouse brain." *The Journal of clinical investigation* 120(5): 1683-1693.
- 263.Shoham, S., et al. (2001). Toll-Like Receptor 4 Mediates Intracellular Signaling Without TNF- α Release in Response to *Cryptococcus neoformans* Polysaccharide Capsule *The Journal of Immunology*. 166: 4620-4626.
- 264.Silva, I., et al. (2021). "Glymphatic system, AQP4, and their implications in Alzheimer's disease." *Neurological Research and Practice* 3(1).

- 265.Simpson, I. A., et al. (2007). "Supply and demand in cerebral energy metabolism: the role of nutrient transporters." *Journal of Cerebral Blood Flow & Metabolism* 27(11): 1766-1791.
- 266.Sinclair, J. and I. Hamza (2015). "Lessons from bloodless worms: heme homeostasis in *C. elegans*." *BioMetals* 28(3): 481-489.
- 267.Skripuletz, T., et al. (2014). Importance of Follow-Up Cerebrospinal Fluid Analysis in Cryptococcal Meningoencephalitis.
- 268.Smith, A. F., et al. (2019). "Brain Capillary Networks Across Species: A few Simple Organizational Requirements Are Sufficient to Reproduce Both Structure and Function." *Front Physiol* 10: 233.
- 269.Sorrell, T. C., et al. (2016). "Cryptococcal transmigration across a model brain blood-barrier: evidence of the Trojan horse mechanism and differences between *Cryptococcus neoformans* var. *grubii* strain H99 and *Cryptococcus gattii* strain R265." *Microbes and infection* 18(1): 57-67.
- 270.Speake, T., et al. (2001). "Mechanisms of CSF secretion by the choroid plexus." *Microscopy Research and Technique* 52(1): 49-59.
- 271.Squizani, E. D., et al. (2018). Cryptococcal dissemination to the central nervous system requires the vacuolar calcium transporter Pmc1. *Cellular Microbiology*.
- 272.Srikanta, D., et al. (2014). "*Cryptococcus neoformans*: historical curiosity to modern pathogen." *Yeast* 31(2): 47-60.
- 273.Steffensen, A. B., et al. (2018). Cotransporter-mediated water transport underlying cerebrospinal fluid formation. *Nature Communications, Springer US*. 9: 2167.
- 274.Steinemann, A., et al. (2016). "Claudin-1, -2 and -3 Are Selectively Expressed in the Epithelia of the Choroid Plexus of the Mouse from Early Development and into Adulthood While Claudin-5 is Restricted to Endothelial Cells." *Frontiers in Neuroanatomy* 10.
- 275.Stie, J. and D. Fox (2012). Blood-brain barrier invasion by *Cryptococcus neoformans* is enhanced by functional interactions with plasmin. *Microbiology*.
- 276.Strickland, A. B. and M. Shi (2021). "Mechanisms of fungal dissemination." *Cellular and Molecular Life Sciences* 78(7): 3219-3238.
- 277.Sun, H.-Y., et al. (2004). "Management of Cryptococcal Meningitis with Extremely High Intracranial Pressure in HIV-Infected Patients." *Clinical infectious diseases* 38(12): 1790-1792.

278. Sweeney, M. D., et al. (2019). "Blood-Brain Barrier: From Physiology to Disease and Back." *Physiological reviews* 99(1): 21-78.
279. Takizawa, K., et al. (2017). Characterization of cardiac- and respiratory-driven cerebrospinal fluid motion based on asynchronous phase-contrast magnetic resonance imaging in volunteers. *Fluids and barriers of the CNS*, BioMed Central. 14: 25.
280. Tang, L.-M. (1990). Ventriculoperitoneal shunt in cryptococcal meningitis with hydrocephalus. *Surgical Neurology*, Elsevier. 33: 314-319.
281. Tenforde, M. W., et al. (2018). "Treatment for HIV-associated cryptococcal meningitis." *Cochrane Database Syst Rev* 7(7): Cd005647.
282. Tenforde, M. W., et al. (2018). "Treatment for HIV-associated cryptococcal meningitis." *The Cochrane database of systematic reviews* 7(7): CD005647-CD005647.
283. Tenor, J. L., et al. (2015). "Live Imaging of Host-Parasite Interactions in a Zebrafish Infection Model Reveals Cryptococcal Determinants of Virulence and Central Nervous System Invasion." *MBio* 6(5): e01425-01415.
284. Tenor, J. L., et al. (2015). "Live Imaging of Host-Parasite Interactions in a Zebrafish Infection Model Reveals Cryptococcal Determinants of Virulence and Central Nervous System Invasion." *MBio* 6(5): e01425.
285. This text introduces the subject of rheology in terms understandable to non-experts and describes the application of rheological principles to many industrial products and processes.
286. Thorsten Schwerte, D. Ü. a. B. P. (2003). Non-invasive imaging of blood cell concentration and blood distribution in zebrafish *Danio rerio* incubated in hypoxic conditions in vivo. *The Journal of Experimental Biology*
287. Thouvenin, O., et al. (2020). Origin and role of the cerebrospinal fluid bidirectional flow in the central canal. *eLife*, eLife Sciences Publications Ltd. 9.
288. Tien, R. D., et al. (1991). "Intracranial cryptococcosis in immunocompromised patients: CT and MR findings in 29 cases." *American Journal of Neuroradiology* 12(2): 283-289.
289. Tinevez, J.-Y., et al. (2017). "TrackMate: An open and extensible platform for single-particle tracking." *Methods* 115: 80-90.
290. Tomiyama, Y., et al. (2000). "Plasma viscosity and cerebral blood flow." *American Journal of Physiology-Heart and Circulatory Physiology* 279(4): H1949-H1954.
291. Trumbore, C. N. (2016). "Shear-Induced Amyloid Formation in the Brain: I. Potential Vascular and Parenchymal Processes." *J Alzheimers Dis* 54(2): 457-470.

292. Tsai, W.-C., et al. (2019). The clinical characteristics of adult cryptococcal meningitis patients who died within one year of treatment with a focus on those with early mortality. *Journal of Clinical Neuroscience*, Churchill Livingstone.
293. Ulrich, F., et al. (2011). Neurovascular development in the embryonic zebrafish hindbrain. *Developmental biology*, Academic Press Inc. 357: 134-151.
294. Umans, R. A., et al. (2017). "CNS angiogenesis and barrierogenesis occur simultaneously." *Developmental biology* 425(2): 101-108.
295. Van Leeuwen, L. M., et al. (2014). Modeling tuberculous meningitis in zebrafish using *Mycobacterium marinum*. *DMM Disease Models and Mechanisms*, Company of Biologists Ltd. 7: 1111-1122.
296. van Leeuwen, L. M., et al. (2018). A transgenic zebrafish model for the *in vivo* study of the blood and choroid plexus brain barriers using *claudin 5*. *Biology Open*. 7: bio030494.
297. Velagapudi, R., et al. (2009). "Spores as infectious propagules of *Cryptococcus neoformans*." *Infection and immunity* 77(10): 4345-4355.
298. Vinchon, M., et al. (2012). "Adult outcome of pediatric hydrocephalus." *Child's Nervous System* 28(6): 847-854.
299. Vu, K., et al. (2009). "Immortalized human brain endothelial cell line HCMEC/D3 as a model of the blood-brain barrier facilitates *in vitro* studies of central nervous system infection by *Cryptococcus neoformans*." *Eukaryotic cell* 8(11): 1803-1807.
300. Vu, K., et al. (2014). "Invasion of the central nervous system by *Cryptococcus neoformans* requires a secreted fungal metalloprotease." *MBio* 5(3): e01101-01114.
301. Wang, M., et al. (2021). "Investigating Migraine-Like Behavior Using Light Aversion in Mice." *J Vis Exp*(174).
302. Wang, Y., et al. (2021). Application and evaluation of nucleic acid sequence-based amplification, PCR and cryptococcal antigen test for diagnosis of cryptococcosis. *BMC Infectious Diseases*, BioMed Central. 21: 1020.
303. Weller, R. O. and R. O. Carare (2018). Lymphatic Drainage of the CNS and Its Role in Neuroinflammation and Neurodegenerative Disease. *Neuroinflammation*, Elsevier: 601-617.
304. West, J. A., et al. (2016). "Structural, super-resolution microscopy analysis of paraspeckle nuclear body organization." *Journal of Cell Biology* 214(7): 817-830.

305. Wijewardana, I., et al. (2011). "Large volume lumbar punctures in cryptococcal meningitis clear cryptococcal antigen as well as lowering pressure." *Journal of Infection* 63(6): 484-486.
306. Williamson, P. R., et al. (2016). Cryptococcal meningitis: Epidemiology, immunology, diagnosis and therapy. *Nature Reviews Neurology*, Nature Publishing Group. 13: 13-24.
307. Wirth, F., et al. (2018). Relationship between intracranial pressure and antifungal agents levels in the CSF of patients with cryptococcal meningitis. *Medical Mycology*, Oxford University Press. 56: 257-262.
308. World Health Organisation (2022, June 27th). "Guidelines for diagnosing, preventing and managing cryptococcal disease among adults, adolescents and children living with HIV"
309. Wolburg, H. and W. Paulus (2010). Choroid plexus: biology and pathology. *Acta Neuropathologica*, Springer-Verlag. 119: 75-88.
310. Wu, Y., et al. (2019). Microglia and amyloid precursor protein coordinate control of transient *Candida cerebritis* with memory deficits. *Nature Communications*, Nature Publishing Group. 10: 1-15.
311. Xia, S., et al. (2016). Imaging characterization of cryptococcal meningoencephalitis. *Radiology of Infectious Diseases*, Elsevier BV. 3: 187-191.
312. Xu, C.-Y., et al. (2014). "Increased permeability of blood–brain barrier is mediated by serine protease during *Cryptococcus meningitis*." *Journal of International Medical Research* 42(1): 85-92.
313. Xu, H. (2016). New concept of the pathogenesis and therapeutic orientation of acquired communicating hydrocephalus. *Neurological Sciences*, Springer Milan. 37: 1387-1391.
314. Xu, J., et al. (2014). Structural diversity requires individual optimization of ethanol concentration in polysaccharide precipitation. *International Journal of Biological Macromolecules*, Elsevier. 67: 205-209.
315. Yamada, S., et al. (2016). "Choroidal fissure acts as an overflow device in cerebrospinal fluid drainage: morphological comparison between idiopathic and secondary normal-pressure hydrocephalus." *Scientific Reports* 6(1): 39070.
316. Yang, G., et al. (2010). "Thinned-skull cranial window technique for long-term imaging of the cortex in live mice." *Nature Protocols* 5(2): 201-208.
317. Yang, M., Ji, R., Zhao, Z. et al. (2023). Detection of apoptotic cells based on in situ hybridization chain reaction using specific hairpins. *Apoptosis* 28, 222–232.

318. Yu CH, et al. (2021) Gene Expression of Diverse Cryptococcus Isolates during Infection of the Human Central Nervous System. *mBio.*;12(6):e0231321
319. Yunker, P. J., et al. (2011). Suppression of the coffee-ring effect by shape-dependent capillary interactions. *Nature*, Nature Publishing Group, a division of Macmillan Publishers Limited. All Rights Reserved. 476: 308.
320. Zhang, P., et al. (2019). "Magnetic resonance imaging features of gelatinous pseudocysts in cryptococcal meningoencephalitis." *Acta Neurologica Belgica* 119(2): 265-267.
321. Zhao, K., et al. (2022), Advances in the Understanding of the Complex Role of Venous Sinus Stenosis in Idiopathic Intracranial Hypertension. *J Magn Reson Imaging*, 56: 645-654.
322. Žikić, D. (2016). A mathematical model of pressure and flow waveforms in the aortic root. *European Biophysics Journal* 2016 46:1, Springer. 46: 41-48.